DYNAMICS OF VARIABLE DENSITY RATIO REACTING JETS IN UNSTEADY, VITIATED CROSSFLOWS

A Thesis
Presented to
The Academic Faculty

by

Benjamin R. Wilde

In Partial Fulfillment
of the Requirements for the Degree
Doctor of Philosophy in the
School of Mechanical Engineering

Georgia Institute of Technology
December 2014

DYNAMICS OF VARIABLE DENSITY RATIO REACTING JETS IN UNSTEADY, VITIATED CROSSFLOWS

Approved by:

Dr. Ben T. Zinn, Advisor
Regents Professor
School of Aerospace Engineering
Georgia Institute of Technology

Dr. David Scarborough
Senior Research Engineer
School of Aerospace Engineering
Georgia Institute of Technology

Dr. Tim C. Lieuwen
Professor
School of Aerospace Engineering
Georgia Institute of Technology

Dr. Ari Glezer
Professor
School of Mechanical Engineering
Georgia Institute of Technology

Dr. Jerry M. Seitzman
Professor
School of Aerospace Engineering
Georgia Institute of Technology

Date Approved: September 23, 2014

To my wife, Lauren

ACKNOWLEDGEMENTS

A number of individuals helped me immensely during my time at Georgia Tech. First, I would like to thank my advisor, Ben T. Zinn, for believing in me and for offering me a chance to work in the combustion lab. This dissertation would not have been possible without Professor Zinn's support, encouragement, and guidance. The lessons I learned from Professor Zinn will always be with me in the future. Professors Tim Lieuwen and Jerry Seitzman also worked closely with me for several years and have always treated me like one of their own students. Tim's deep understanding of shear flow dynamics, unwavering positive attitude, and goal-oriented approach will continue to be an inspiration for me. Jerry's razor-sharp intellect, deep probing questions, and passion for teaching made me a better student and a better researcher. David Scarborough's deep knowledge of physical acoustics and his willingness to tutor me on thermoacoustics significantly improved my research. David's ability to boil difficult engineering problems down to their essentials in reduced-order models is as rare as his ability to troubleshoot experimental hardware. I would like to thank Professor Ari Glezer for graciously agreeing to serve on my committee and for offering a number of suggestions that improved the quality of this work.

In addition to my committee members, a number of wonderful faculty and staff at Georgia Tech helped me along the way. Bobby Noble deserves special mention for going out of his way to make this research possible. His help was instrumental in securing initial funding to build the reacting jet in crossflow facility and for supporting the project over the years. It was a pleasure to share an office with Brad Ochs and to work on high pressure combustion systems with him. I learned a great deal about combustor design, Labview programming, and high pressure testing from Brad. I cannot thank Sasha Bibik enough for his help with optics and lasers. Sasha's expertise and his unbelievable knack for fixing almost anything in the lab are unmatched. I would like to thank and acknowledge the contributions of Scott Elliot, Scott Moseley, and Red Russell for their expert work in the Aerospace

Engineering machine shop. They have been both friends and colleagues throughout my time at Georgia Tech. Without their help and valuable advice on fabrication and material selection, the facility I used throughout this work may never have been developed or worked properly. Professor Jechiel Jagoda, Dr. Wayne Whiteman, and Professor Bill Wepfer helped me navigate the trials and tribulations of graduate school. Their student-first approach and compassionate professionalism are greatly appreciated. I would also like to thank Professor Ann Karagozian of UCLA, who graciously shared her wealth of expertise about jet in crossflow dynamics with me at the beginning of this work and generously shared the contoured nozzle design used in the experiments described in this thesis.

I have been fortunate to work with a number of very talented students at the combustion lab who have helped me with my research and have become great friends over the years. I would especially like to thank Ianko Chterev for volunteering to help me with laser diagnostics, even at the expense of his own work and sleep. His expertise and friendship made running experiments so much more efficient and enjoyable. In addition to being a great office mate and friend, Matt Quinlan generously shared his acoustics hardware with me and taught me the finer points of dynamic pressure measurements. My many discussions with Matt on thermoacoustic stability and dynamical systems have certainly influenced this work for the better. I want to thank Ben Emerson for never tiring of my questions about hydrodynamic stability and for graciously sharing the experimental facility with me during the last few years. Ben's work ethic, research excellence, and genuine personality are an inspiration that everyone at the combustion lab can aspire to. Andrew Marshall, Prabhakar Venkateswaran, and Chris Foley have been world-class office mates and great friends. They taught me a great deal about stretched flames, and my many discussions with them over the years definitely improved this work. Although I do not have the space to properly acknowledge everyone I should, I would also like to acknowledge a few members of the combustion lab community that I had the pleasure of working and studying with, including Jim Cornacchio, Justin Fernandez, Jackie O'Connor, Brandon Sforzo, Gina Magnotti, Jack Crawford, Julia Lundrigan, Michael Malanoski, Nishant Jain, Ben Knox, Tommy Slais, Sampath Adusumilli, Aimee Williams, Alex Damiao, Karthik Periagaram,

Arun Radhakrishnan, Matthew Clay, Tim Dawson, David Wu, and Anna Hotle.

I was also fortunate to work with several very talented undergraduate students who helped me at different points throughout my research. A few of those students that deserve special mention are Miguel Amador, David Ku, Joseph Blaeser, and Sebastian Cardona.

I am very grateful to the United States Department of Defense for funding the last three years of my graduate studies through the Science, Mathematics, and Research for Transformation Scholarship. I would especially like to thank Shere Tuckey and Eric Welle for patiently waiting on me to complete my graduate work and for offering me a chance to work at the Air Force Research Laboratory.

I would like to thank my family for their love and support. My parents have always set a great example for me to follow, and they have given me every opportunity to succeed in life. I cannot thank them enough for that. My dad taught me to take pride in my work and to never stop trying to improve. My mom taught me the value of hard work, determination, and compassion. I would like to thank my sister and brother-in-law for being a constant source of support and encouragement throughout graduate school.

Most importantly, I would like to thank my wife Lauren. She has been a constant and never ending source of strength, inspiration, love, and support throughout my time at Georgia Tech. I cannot imagine completing this dissertation without her, and I will forever be indebted to her for the many, many sacrifices she made so that I could pursue my doctorate at Georgia Tech.

TABLE OF CONTENTS

LIST OF TABLES

LIST OF FIGURES

NOMENCLATURE

α_{f}	Duty cycle of forcing.
χ	Mixture fraction scalar dissipation rate, [s^{-1}].
δ_f	Flame thickness, [mm].
δ_∞	Crossflow boundary layer thickness, [mm].
δ_ν	Viscous length scale of the crossflow, [mm].
$\lambda_{\infty,\mathrm{F}}$	Acoustic wavelength at f_{F} in the crossflow, [m].
$\lambda_{\mathrm{j,F}}$	Acoustic wavelength at f_{F} in the jet supply system, [m].
ϕ	Equivalence ratio.
ρ_{ad}	Equilibrium product density, [$\mathrm{kg/m}^3$].
ρ_∞	Mean crossflow density, [$\mathrm{kg/m}^3$].
ρ_{j}	Mean jet density, [$\mathrm{kg/m}^3$].
Σ	Area of a shear layer vortex, [mm^2].
τ_{chem}	Chemical timescale, [s].
τ_χ	Timescale derived from scalar dissipation rate, [s].
τ_{fluid}	Fluid mechanical timescale, [s].
τ_{j}	Characteristic jet timescale, [s].
τ_{w}	Shear stress at the wall, [Pa].
θ_{j}	Momentum thickness of the jet, [mm].
$\theta_{P_{\mathrm{j}}}$	Phase of the acoustic pressure signal in the jet supply plenum, [deg.].
ω_z	z-component of vorticity, [s^{-1}].
ω_z'	Amplitude of the fluctuating z-component of vorticity at f_{F}, [s^{-1}].
ζ_{c}	Instantaneous jet center streamline perturbation, [mm].
ζ_{c}'	Amplitude of jet center streamline perturbation at f_{F}, [mm].
ζ_{f}	Instantaneous windward flame edge perturbation, [mm].
ζ_{f}'	Amplitude of the windward flame edge perturbation at f_{F}, [mm].

A_{F}	Acoustic forcing amplitude, [A].
A_{j}	Area of the jet orifice, [mm^2].
c_{∞}	Speed of sound in the crossflow, [m/s].
c_{j}	Speed of sound in the jet, [m/s].
Da	Damköhler number.
d_{hyd}	Hydraulic diameter of the test section, [mm].
d_{j}	Diameter of the jet orifice, [mm].
f_{c}	Cutoff frequency of the test section, [Hz].
f_{F}	Acoustic forcing frequency, [Hz].
f_{M}	Fundamental mode frequency of the windward shear layer, [Hz].
h	Half-height of the test section, [mm].
H_{TS}	Height of the test section, [mm].
J	Jet-to-crossflow momentum flux ratio.
Ma	Mach number of the jet based on mean flow velocity, $U_{\mathrm{j}}/c_{\mathrm{j}}$.
p'_{∞}	Amplitude of the fluctuating crossflow pressure at the jet injector, $[Pa]$.
P_{j}	Acoustic pressure measured in the jet supply plenum, [Pa].
$P_{\infty,1}$	Acoustic pressure measured by crossflow sensor 1, [Pa].
$P_{\infty,2}$	Acoustic pressure measured by crossflow sensor 2, [Pa].
r	Mean jet-to-crossflow velocity ratio.
R	Mean density-weighted jet-to-crossflow velocity ratio.
Re_{j}	Bulk Reynolds number of the jet.
Re_{τ}	Friction Reynolds number.
S	Mean jet-to-crossflow density ratio.
s	Arc length distance along the mean jet center streamline, [mm].
s_{A}	Distance separating the two-microphone method sensors, [mm].
$S_{\infty,\mathrm{ad}}$	Mean crossflow-to-equilibrium product density ratio.
$S_{\mathrm{j,ad}}$	Mean jet-to-equilibrium product density ratio.
St_{j}	Strouhal number of the jet.
T_{ad}	Adiabatic flame temperature, [K].

T_∞	Temperature of the crossflow fluid, [K].
U_∞	Mean crossflow velocity, [m/s].
u'_∞	Amplitude of the fluctuating crossflow velocity at the jet injector, $[m/s]$.
U_j	Mean jet exit velocity, [m/s].
u'_j	Amplitude of the fluctuating jet exit velocity at f_F, [m/s].
U, V, W	Velocity component in the x, y, and z directions, [m/s].
$\langle U\rangle, \langle V\rangle, \langle W\rangle$	Mean velocity component in the x, y, and z directions, [m/s].
u, v, w	Unsteady velocity component in the x, y, and z directions, [m/s].
u_τ	Friction velocity of the crossflow, [m/s].
W_TS	Width of the test section, [mm].
x_i	Mole fraction of species i.
y_+	Wall coordinate, [mm].
z	Mixture fraction.
Z_j	JICF injector acoustic impedance, $[\mathrm{Pa}\cdot\mathrm{s/m^3}]$.
z_st	Stoichiometric Mixture fraction.

CI	Combustion Instability.
CRVP	Counter-Rotating Vortex Pair.
FWHM	Full width, half maximum.
HV	Horseshoe Vortices.
JICF	Jet in crossflow.
LP	Lean-Premixed.
RQL	Rich burn, Quick quench, Lean burn.
SF	Staged-Fuel.
SLV	Shear Layer Vortices.
SPIV	Stereoscopic Particle image velocimetry.
SPL	Sound Pressure Level.
WV	Wake Vortices.

$(\quad)_\infty$	Crossflow quantity.
$(\quad)_\mathrm{f}$	Flame quantity.
$(\quad)'$	Fluctuating quantity.
$(\quad)_\mathrm{F}$	Forced response quantity.
$(\breve{\quad})$	Fourier transformed quantity.
$(\quad)_\mathrm{j}$	Jet quantity.
$(\quad)_\mathrm{max}$	Maximum of the quantity.
$(\quad)_\mathrm{min}$	Minimum of the quantity.
$(\quad)_\mathrm{LSL}$	Leeward shear layer quantity.
$(\quad)_\mathrm{WSL}$	Windward shear layer quantity.
$(\quad)_{\hat{\mathrm{n}}}$	Projection in the direction normal to the jet center streamline.
$(\quad)_{\hat{\mathrm{s}}}$	Projection in the direction of the jet center streamline.
$\langle(\quad)\rangle$	Time-averaged quantity.
$(\hat{\quad})$	Unit vector.

SUMMARY

The jet in crossflow (JICF) is an important flow configuration that finds application in many combustion systems. This work is motivated by the application of a jet in crossflow for secondary fuel injection in a staged-fuel combustion system. The high temperature, vitiated air crossflow in these systems is inherently unsteady and is characterized by coherent, acoustic oscillations. The primary objective of this study is to understand the effects of near-field heat release and crossflow acoustic forcing on the time-averaged and unsteady dynamics of reacting JICF.

The first part of this work focuses on characterizing the flow structure and flame stabilization of fuel jets injected into high temperature, vitiated air crossflow. To this end, a new vitiated flow facility is developed, and a parametric study is performed to investigate the dependence of JICF on momentum flux ratio J, density ratio S, and the presence/absence of combustion heat release. Results obtained from simultaneous time-resolved stereoscopic particle image velocimetry (SPIV) and OH planar laser induced fluorescence (PLIF) are presented and analyzed.

The results show that, contrary to the behavior of reacting jets stabilized in low-to-moderate temperature air crossflow, vitiated crossflows stabilize attached flames anchored near the exit of the jet injector. SPIV results show that this near-field heat release significantly alters the time-averaged and instantaneous flow field of JICF. Notably, reacting jets are found to penetrate further into the crossflow than non-reacting jets. This finding is attributed to increased aerodynamic blockage of the crossflow due to the presence of the jet in reacting cases as well as combustion-induced flow acceleration. These effects are incorporated into a modified trajectory scaling law that successfully collapses measured jet trajectories for both non-reacting and reacting jets.

Instantaneous OH PLIF results show that the windward reaction zone is characterized by a thin, non-premixed flame front located in the shear layer between the jet core and the

stagnating crossflow. While the windward flame branch is attached to the jet injector in low J cases ($J \approx 5$), it intermittently lifts away from the jet injector in high J ($J \approx 25$) cases and pockets of local extinction are observed further downstream. The leeward reaction zone remains attached to the jet injector, but it is much broader and more diffuse than the windward reaction zone. The orientation of the leeward reaction zone relative to the shear layer depends on J, which is a key parameter controlling the amount of combustion products entrained into the leeward recirculation zone.

The second part of this work investigates the jet response to crossflow forcing. Acoustic drivers are used to excite natural acoustic resonances of the vitiated facility, and the jet response is measured using simultaneous SPIV, OH PLIF, and dynamic pressure measurements. A parametric study is performed to investigate the dependence of the jet response on forcing frequency f_{F}, forcing amplitude A_{F}, J, S, and the presence/absence of combustion heat release.

The results of this study indicate that the jet response to the fluctuating crossflow velocity is often negligible. On the other hand, the fluctuating crossflow pressure can induce large fluctuating jet exit velocities, which lead to large-scale, periodic jet flapping. While this periodic jet flapping exerts minimal influence on the time-averaged jet trajectory, the instantaneous jet trajectory varies significantly during each acoustic pressure cycle. The jet flapping amplitude increases with increasing arc length distance s until saturation occurs further downstream at a point whose location depends on the forcing frequency.

The dependence of the jet flapping amplitude on JICF parameters such as J and S is primarily a consequence of how those parameters affect the jet injector impedance. The resistive part of the jet injector impedance is smaller for low J test conditions and, thus, the jet flapping amplitude tends to be much larger in low J jets than in high J jets. Similarly, iso-density jets tend to flap with larger amplitude than low S jets with identical J. An analytical model is developed that predicts the dependence of the jet injector impedance and the fluctuating jet exit velocity upon J, S, f_{F}, and Mach number Ma_{j}. The model predictions are in good agreement with SPIV measurements and, thus, the model can be used to study the sensitivity of the injector impedance to important JICF parameters.

The final part of this work investigates the effect of near-field heat release on the shear layer dynamics of density stratified, reacting JICF. SPIV results reveal that the time-averaged jet/crossflow momentum transfer in the near-field can be significantly altered by combustion heat release. Results obtained from instantaneous Mie scattering flow visualization and vortex tracking suggest that this finding is related to combustion-induced modification of the shear layer vortices. Concepts from hydrodynamic stability theory are used to investigate this hypothesis, and a new phenomenological model for the density stratification in a reacting JICF is proposed. The jet-to-reaction zone density ratio is identified as an important parameter affecting the shear layer stability of reacting JICF, and the important connection between the location of flame stabilization and the shear layer stability of a reacting JICF is described. Lastly, the effect of crossflow forcing on the shear layer dynamics is investigated, and a quasi-steady interpretation is proposed based on a timescale separation argument.

CHAPTER I

BACKGROUND & MOTIVATION

Rapidly increasing worldwide demand for energy, reduced natural gas prices, and more stringent emissions regulations continue to stimulate development and installation of power-generating gas turbine engines. Utility companies increasingly use these engines to provide both base load power generation capacity and quick-response, load-balancing power capacity. Thus, gas turbine manufacturers must design and build more powerful, efficient, flexible, and reliable engines. Combustor design plays a critical part in achieving those goals, and the combustion engineer must find new methods to provide greater turn-down ratio, account for fuel variability, avoid thermo-acoustic instabilities, and reduce emissions. Three promising combustion technologies under development by industrial gas turbine manufacturers to address these challenges are Lean Premixed (LP) combustion, Rich-Quench-Lean (RQL) combustion, and Staged-Fuel (SF) combustion. An important commonality amongst all three of these combustion concepts is the need to rapidly and effectively mix different gaseous fluid streams.

This thesis focuses specifically on the jet in crossflow (JICF), which is a geometrically simple, but remarkably effective flow configuration that is commonly used in combustors for mixing two dissimilar gaseous fluid streams. The basic jet in crossflow consists of a jet with mean velocity U_{j} injected perpendicularly into a crossflow with mean velocity U_{∞}, as illustrated in Figure 1.1. The widespread adoption of JICF in many important industrial applications is a testament to their mixing performance. This fact combined with the rich, interesting physics associated with JICF has motivated more than 50 years of research on the topic. Recent comprehensive reviews are given by Karagozian [11] and Mahesh [12]. This thesis builds on that substantial body of work and extends the study of classical JICF to consider dynamics of both non-reacting and reacting jets injected perpendicularly into unsteady, vitiated crossflows. The application of JICF for fuel and air injection in gas

turbine combustors is the primary technological interest here.

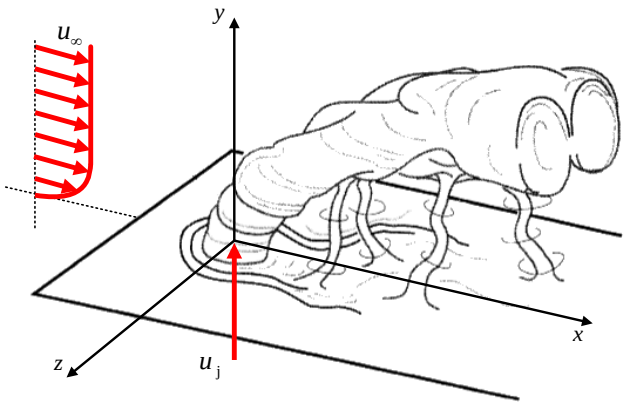

Figure 1.1: Diagram of the basic structure of a jet in crosflow (JICF). Adapted from Fric & Roshko [1].

The remainder of this chapter reviews the most pertinent results from the JICF literature and builds a foundation for the rest of the thesis. Section 1.1.1 gives an overview of the three gas turbine combustion technologies mentioned above and highlights the important role JICF play in each. Section 1.1.2 describes the acoustic environment inside gas turbine engines and introduces the topic of thermo-acoustic instability, thus motivating the study of jets in unsteady crossflows. Section 1.2 presents the basic trajectory and scaling laws for JICF. Coherent structures of JICF are discussed in Section 1.3, which leads naturally into a discussion of hydrodynamic instabilities in JICF in Section 1.4. Section 1.5 concerns reacting JICF, including their flame stabilization mechanisms and the influence of chemical heat release on the flow field. Section 1.6 concludes the chapter by looking at forced response of JICF.

1.1 JICF in Gas Turbine Combustors

1.1.1 Applications

JICF are utilized throughout modern ground-based and aviation gas turbines in situations where rapid mixing between two dissimilar fluid streams is required. Perhaps the most well-known example is that of JICF-style injectors used for fuel injection in the premixing section of lean-premixed burners. These injectors are intended to rapidly mix fuel and air

upstream of the entrance to the combustor and are often installed along stationary vanes just downstream of the compressor exit, as shown in Figure 1.2. An important secondary objective for JICF-type fuel injectors is avoiding flashback and flame stabilization in the premixing section. Flashback is always a serious concern when dealing with premixed reactants, and this is particularly true in modern gas turbines, which can have preheat temperatures exceeding 750K and are increasingly called upon to operate with a wide variety of fuel types. The ideal premixing section must thus avoid any chance of flashback while still providing rapid and uniform mixing between fuel and air. This is clearly a difficult design task that necessitates detailed understanding of JICF dynamics.

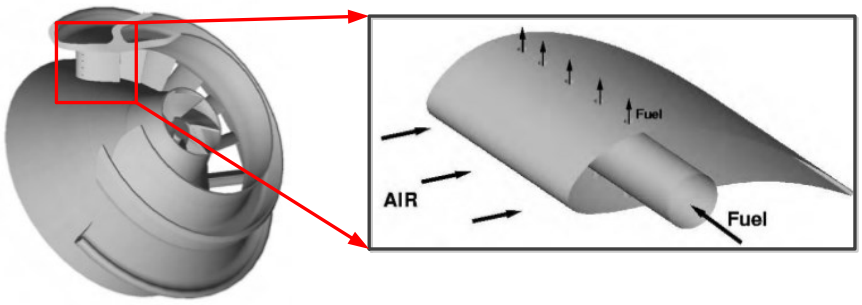

Figure 1.2: Application of multiple JICF along a single vane in the premixing section of a Lean-Premixed type burner. Adapted from Schlüter & Schönfeld [2].

Dilution air addition in gas turbine combustors is another important application of JICF. Rich-Quench-Lean (RQL) combustors commonly found in aero-engines utilize large JICF-type injectors to rapidly introduce additional combustion air downstream of a non-premixed, fuel-rich front-end combustion zone. The JICF configuration and the impact of dilution air addition in an RQL combustor are seen clearly in Figure 1.3, which shows a cross-sectional slice of the predicted temperature field inside a Pratt & Whitney combustor [3]. The additional air injected by the JICF injectors effectively partitions the combustor into two independent combustion zones, the fuel-rich zone upstream of the air injection and a fuel-lean zone downstream of the air injection. In other words, the dilution air injectors provide the oxidizer needed to fully react the leftover fuel from the upstream combustion zone, a task that much be accomplished on a timescale $\tau = \mathcal{O}(1\text{ms})$. The fuel-rich front end

provides robust flame stabilization, and the two-stage combustion process reduces thermal (Zeldovich) NO_x formation by avoiding the high flame temperatures associated with stoichiometric non-premixed combustion. Thus, the performance of RQL combustors depends heavily on the ability to design effective JICF injectors for dilution air addition.

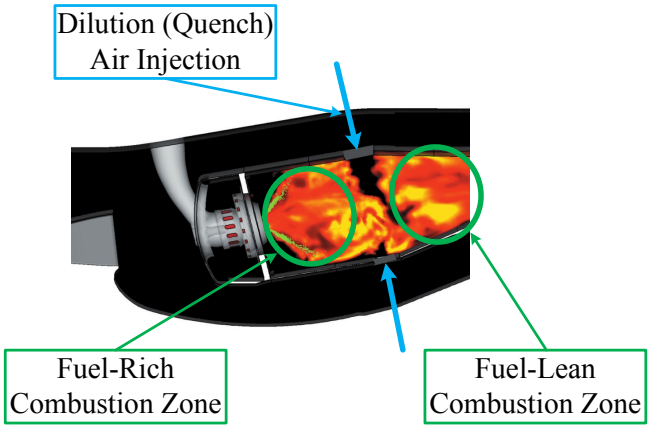

Figure 1.3: LES prediction of the temperature field inside a Rich-Quench-Lean combustor utilizing JICF for dilution air injection. Image adapted from Moin & Apte [3].

The final combustion concept discussed is the staged fuel combustion system, which is the technology most directly relevant to this thesis. Unlike conventional combustion systems, staged fuel combustors burn only part of their fuel in the primary combustor and rely on a secondary combustion zone downstream of the main burner to oxidize the remaining fuel. In practice, staged fuel combustion devices often use JICF-style injectors to add fuel and aerodynamically stabilize a flame in the secondary combustion zone. The distance separating the secondary combustion zone from the primary combustion zone can vary significantly in different designs. For example, staged fuel combustion can be implemented inside a single, annular combustion liner simply by using multiple, axially-staged fuel injection locations, or on the other hand, the secondary combustion zone may be located downstream of a high-pressure turbine stage, as seen in the reheat cycle engine shown in Figure 1.4. The key feature shared amongst all staged fuel designs is that the secondary fuel is injected into a vitiated flow, i.e., a flow containing combustion products and reduced O_2

relative to air. This distinction provides several potential advantages for staged fuel combustion devices: 1) Lower emissions levels can be achieved at a given specific power output by carefully controlling the local firing temperature and the reactants composition. 2) The type and quantity of fuel can be adjusted on an as-needed basis by changing the secondary fuel injection without adjusting the main burner, thus increasing turn-down ratio. 3) The presence of high-temperature vitiated products in the secondary combustion zone provides a robust flame stabilization mechanism, which translates into greater fuel-flexibility for the engine and the option of burning non-ideal fuels. 4) The existence of a second combustion zone leads to a more distributed heat release profile, which not only tends to reduce the onset of problems with thermo-acoustic instability but also provides additional means to "de-tune" instabilities that arise during operation.

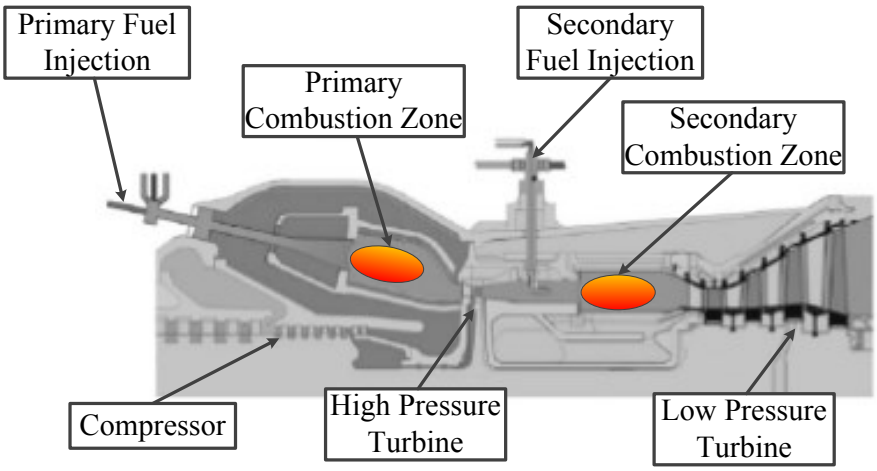

Figure 1.4: Schematic of staged fuel combustion concept used in a reheat cycle Alstom GT 24/26 gas turbine engine. Adapted from Güthe et al. [4].

A key challenge to designing these staged fuel devices concerns the ability to predict and control mixing and flame stabilization in the secondary combustion zone[13, 14]. Important engine performance metrics such as the spatial heat release uniformity and the amount of pollutant formation depend explicitly on the local mixing characteristics in the secondary combustion zone. This thesis focuses on the dynamics of a single reacting jet injected perpendicularly into a vitated crossflow, which serves as a simplified model problem for the technologically important class of flow configurations seen in many staged fuel combustion

devices.

1.1.2 Role of Acoustics and Combustion Instability

Internal flow passages in gas turbine engines are inherently noisy environments due to a combination of their rigid steel construction and an abundance of sound generating processes, including, e.g., aero-acoustically generated sound from high velocity nozzles, mechanically generated sound due to resonances in rotating parts, and combustion generated sound. The significance with respect to the study of JICF is that effectively *all* possible crossflows inside a gas turbine are inherently unsteady, both due to random turbulent fluctuations and coherent acoustic oscillations. This reality is in contrast to the majority of JICF studies reported in the literature, which primarily focus on steady and often laminar crossflows. A more realistic view of the acoustic environment inside a staged-fuel combustor is shown in Figure 1.5, where the magnitude and phase of the acoustic pressure and velocity fields depend on factors such as the unsteady heat release, the facility geometry, the working fluid properties, and the boundary conditions.

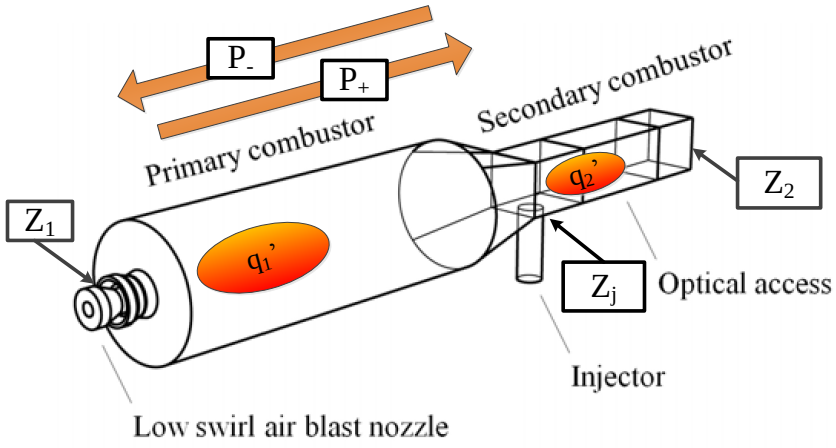

Figure 1.5: Simplified view of the acoustic environment inside a staged-fuel combustion device utilizing JICF for secondary fuel injection. Adapted from Galeazzo et al. [5].

Very high amplitude acoustics can occur as a result of coupling between the natural acoustic modes and the unsteady heat release inside a combustor, a phenomenon referred to as combustion instability (CI). CI are driven by a feedback cycle consisting of two critical

elements. First, a physical mechanism by which acoustic fields can excite oscillations in the heat release field is required. Completing the cycle then requires a return path by which those heat release oscillations can act as a source that drives the acoustic waves. If both elements of the CI cycle are present, the acoustic energy inside the combustor will grow until the system's acoustic damping (losses) balance the heat release source or until mechanical failure occurs. CI have historically plagued many combustion systems, including everything from industrial boilers [15] to liquid rocket engines [16]. Lean-premixed combustors in gas turbine engines have proven especially susceptible to CI due to their concentrated heat release distributions and relatively low acoustic damping [17]. The high-amplitude acoustic waves associated with CI are very detrimental to operating gas turbine engines. Combustion instabilities often lead to premature part failure due to high-cycle fatigue and enhanced heat transfer to hot-section parts. Flame stabilization issues can arise as well, including flashback and blow-off [18].

The connection between combustion instability and JICF injectors has not been emphasized previously but can be characterized by either a one-way or a two-way coupling process. One-way coupling emphasizes only the effect of the unsteady crossflow on the JICF. Thus, one-way coupling is identical to the normal interaction between a jet and an unsteady crossflow discussed previously, except that the unsteady crossflow will have very high amplitude acoustic oscillations during a CI. Two-way coupling is more complex and involves a cyclical interaction between the acoustic field and the unsteady heat release produced by the JICF. In this case, the JICF *actively* participates in the CI.

Understanding the effects of both one-way and two-way coupling necessitates a detailed understanding of the response of reacting JICF to acoustic excitation, which is lacking in the existing literature. Interestingly, studies of this sort have been conducted in other important free shear flows used in gas turbine engines, including bluff-body wakes [19, 20], swirling jets [21], and axial jets [22]. The physical response mechanisms to acoustic excitation for these various shear flows are numerous and complex. Two of the most important response mechanisms are injector-coupled (bulk) response and vorticity-coupled (hydrodynamic) response. Detailed discussion of these mechanisms with respect to JICF is deferred to Section 1.6

after coherent structures and hydrodynamic instabilities in JICF are presented in Sections 1.3 and 1.4, respectively.

1.2 Trajectory and Scaling of JICF

This section presents an overview of the trajectory and scaling laws used to describe JICF. Only subsonic, gas phase jets injected perpendicularly into a crossflow are considered. As illustrated in Figure 1.1, the JICF is an unsteady, three-dimensional flow field that develops as a consequence of the interaction of two canonical flows; namely, a boundary layer flow and an axial jet flow. The jet deflects into the crossflow direction as it entrains crossflow fluid due a combination of shear and pressure forces.

The first, fundamental metric used to describe JICF is the jet trajectory, which describes the penetration of the jet into the crossflow direction. Much of the early work on JICF, motivated largely by the need to understand dispersion of effluents from exhaust stacks, focused on understanding and scaling the trajectory and penetration of non-reacting JICF. One challenge is simply defining the jet trajectory. Among other choices, the trajectory can be defined based on the scalar concentration field [23], the locus of points of maximum velocity [24], or the jet center streamline [25]. The definition based on jet center streamline will be used throughout the present work because it is equally applicable in non-reacting and reacting flows. Pratte & Baines [26] investigated the trajectory of JICF over a wide range of different jet-to-crossflow momentum flux ratios, J , where

$$J = \frac{\rho_{\mathrm{j}} U_{\mathrm{j}}^2}{\rho_\infty U_\infty^2}, \tag{1.1}$$

and found that their measured trajectory profiles were well-approximated by the correlation

$$\frac{y}{R d_{\mathrm{j}}} = 2.05 \left(\frac{x}{R d_{\mathrm{j}}} \right)^{0.28} \tag{1.2}$$

where $R = J^{1/2}$ is a density-weighted jet-to-crossflow velocity ratio and d_{j} is the jet diameter. The subscript "j" refers to a jet quantity and subscript "∞" refers to a crossflow quantity. J is an important quantity in JICF that represents the ratio of the initial transverse momentum of the jet to the initial axial momentum of the crossflow. J can also be reformulated as the product of the jet-to-crossflow density ratio, $S = \rho_{\mathrm{j}}/\rho_\infty$, and the square

of the velocity ratio, $r = U_\mathrm{j}/U_\infty$. As expected, jets with higher J penetrate further into the crossflow because they have greater transverse momentum. Broadwell & Breidenthal [27] later confirmed the empirical scaling law given in Equation (1.2) and derived the expression for jet trajectory

$$\frac{y}{Rd_\mathrm{j}} = A\left(\frac{x}{Rd_\mathrm{j}}\right)^{1/3} \tag{1.3}$$

by modeling the JICF as a point source of transverse momentum that gives rise to two counter-rotating vortices, similar to those created by the lift force on a wing. The coefficient A is a constant that must be measured. A number of experimental, theoretical, and computational studies conducted since have generally confirmed the Rd_j scaling in Equations (1.2) and (1.3). Measurements spanning a wide range of different JICF conditions have been used to parameterize equations with the slightly more generic form

$$\frac{y}{Rd_\mathrm{j}} = A\left(\frac{x}{Rd_\mathrm{j}}\right)^{b} \tag{1.4}$$

where both A and b are coefficients obtained from measurements. Coefficient values given in the literature exhibit a good amount of scatter and span $1.2 \leq A \leq 2.6$ and $0.28 \leq b \leq 0.34$ [28]. The significant scatter is not too surprising considering the number of important flow parameters not accounted for in Equation (1.4).

Hasselbrink Jr. & Mungal [29] suggest that perhaps a single trajectory scaling is not appropriate for JICF. They note that the near-field of JICF is essentially jet-like, while the far-field more closely resembles a wake. This interpretation follows directly from the observation that the jet fluid contains no time-averaged axial momentum prior to interacting with the crossflow and thus has a velocity defect in the axial direction. Based on this reasoning, they derived different trajectory scaling laws for each region, given by

$$\frac{y}{Rd_\mathrm{j}} = \left(\frac{2}{c_{ej}}\frac{x}{Rd_\mathrm{j}}\right)^{1/2} \quad (\mathrm{Near-Field}) \tag{1.5a}$$

$$\frac{y}{Rd_\mathrm{j}} = \left(\frac{3}{c_{ew}}\frac{x}{Rd_\mathrm{j}}\right)^{1/3} \quad (\mathrm{Far-Field}) \tag{1.5b}$$

where c_{ej} and c_{ew} are mass entrainment coefficients for the jet-like and the wake-like regions, respectively.

The jet injector geometry can also alter the jet trajectory. Jet injectors that protrude into the crossflow, for example, force a portion of the flow below the nozzle injection plane ($y/d_\mathrm{j} = 0$) to deflect upward [7]. This upward flow increases the effective transverse momentum of the jet and thus tends to increase penetration. This effect is offset, however, by the fact that jets issuing from elevated nozzles interact with crossflow fluid at the freestream velocity rather than the lower-velocity fluid present in the boundary layer.

Muppidi & Mahesh [30] showed that the trajectory of JICF are sensitive to both the jet inlet velocity profile and the crossflow velocity profile. Fully-developed laminar jets penetrate further than corresponding fully-developed turbulent jets with identical J (note that J is defined based on the mass-weighted average velocity so the laminar profile has greater average transverse momentum). Muppidi & Mahesh [30] demonstrated that jets penetrate further into crossflows with greater boundary layer thickness, δ_∞, and they proposed an additional length scale, h, to account for these effects. The resulting trajectory scaling law is given as

$$\frac{y}{Rd_\mathrm{j}} = A\left(\frac{x}{Rd_\mathrm{j}}\right)^b\left(\frac{h}{d_\mathrm{j}}\right)^C \tag{1.6}$$

where $C = 0.15$ and h/d_j is approximated as

$$\frac{h}{d_\mathrm{j}} = \begin{cases} \left\{\dfrac{3}{4}\pi C_m R^2 \dfrac{\delta_\infty^2 D^2}{d_\mathrm{j}^4}\right\}^{1/3} & \text{if} \quad h \le \delta_\infty \\ \dfrac{2}{3}\dfrac{\delta_\infty}{d_\mathrm{j}} + \dfrac{\pi}{4} C_m R^2 \dfrac{D^2}{d_\mathrm{j}^2} & \text{if} \quad h > \delta_\infty \end{cases} \tag{1.7}$$

with $C_m \approx 0.05$ and the effective jet diameter, D, defined by

$$\rho_\mathrm{j} \int_{A_\mathrm{j}} \langle V_{y=0}^2 \rangle^2 \, \mathrm{d}A_\mathrm{j} = \frac{\pi D^2}{4} \rho_\mathrm{j} U_\mathrm{j}^2. \tag{1.8}$$

A subtle but important difference between Equation (1.6) and all the other trajectory scaling laws presented is the implicit assumption that the near-field pressure affects the jet trajectory. Pressure effects in the jet near-field are less important at high J, but can be significant for low-to-moderate J [23].

Interestingly, the effect of the jet Reynolds number, $Re_\mathrm{j} = U_\mathrm{j} d_\mathrm{j}/\nu_\mathrm{j}$, on the jet trajectory is relatively small and manifests itself primarily through changes in the inlet velocity profile,

as demonstrated by the detailed experimental measurements of Shan & Dimotakis [31] on JICF with $1.0 \times 10^3 \leq Re_{\mathrm{j}} \leq 20.0 \times 10^3$. Presumably, the effect of the crossflow Reynolds number, $Re_\infty = U_\infty d_{\mathrm{hyd}}/\nu_\infty$, is also minimal outside of its effect on δ_∞. Additional high-fidelity experimental or computational data are needed, however, at high Re_{j} and Re_∞ for a range of different J to fully validate these conclusions. The findings of Shan & Dimotakis [31] and the success of scaling laws derived using momentum integral approaches suggest that the deflection of the jet into the crossflow direction is dominated by crossflow entrainment rather than small-scale viscous transport. Crossflow entrainment is in turn controlled by large-scale, coherent structures whose formation is primarily attributed to inviscid mechanisms [1, 6]. These coherent structures and their important influence on the JICF are the focus of the next section.

1.3 Coherent Structures in JICF

The interaction between a jet and a crossflow gives rise to four large-scale, coherent vortical structures that play an important role in controlling the time-averaged and instantaneous behavior of the JICF [1, 6]. Those structures are: (i) the horseshoe vortices (HV), (ii) the upright wake vortices (WV), (iii) the counter-rotating vortex pair (CRVP), and (iv) the shear layer vortices (SLV), see Figure 1.6. The remainder of this section discusses the key aspects of each vortex system. Insight into the origin of the coherent vortex structures shown in Figure 1.6 comes from tracking the "initial" vorticity, i.e., the vorticity present in the jet flow and the crossflow prior to their interaction. Both the jet and the crossflow contain vorticity in their respective boundary layers. The jet vorticity is primarily azimuthal, while the crossflow boundary layer is dominated by out-of-plane z-component vorticity, ω_z. The vorticity distribution and magnitude depends on Re_{j}, Re_∞, and the geometry of the facility. From this perspective, the four vortex systems shown in Figure 1.6 are responsible for the re-organization and evolution of that initial vorticity.

Consider the horseshoe vortices (HV) first. These vortices form in the boundary layer region immediately upstream of the jet column and resemble the necklace vortices that form upstream of a column, despite significant differences in boundary conditions [32]. Their

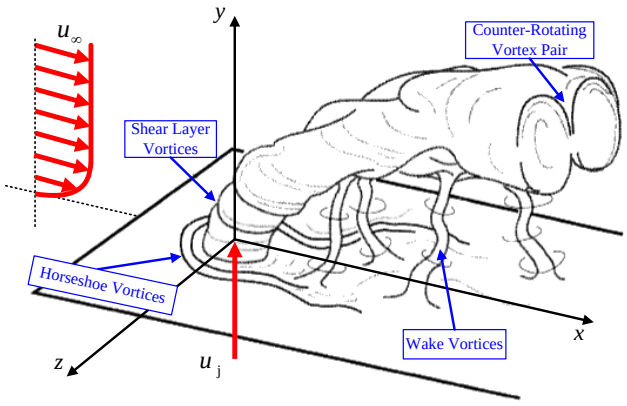

Figure 1.6: Sketch detailing the four large-scale, coherent vortical structures found in the jet in crossflow. Adapted from Fric & Roshko [1] and shown with the coordinate system for the present work overlaid.

formation is attributed to the adverse pressure gradient caused by the jet's aerodynamic blockage, which causes boundary layer separation and roll-up. Advection by the crossflow fluid bends the horseshoe vortices around the jet core and gives them their namesake horseshoe shape. The presence of the horseshoe vortices is generally observable in time-averaged measurements, although Kelso & Smits [32] showed that the horseshoe vortices can intermittently switch between "steady, oscillating, or coalescing" behavior. Interestingly, oscillatory-type HV exhibit the same frequency of oscillation as the upright wake vortices [32].

The wake vortices (WV) are upright column-like vortical structures that shed periodically and asymmetrically from the leeward side of the jet. The WV are an inherently unsteady feature of the flow. Obvious similarities exist between the WV in a JICF and the asymmetric shedding of vorticity behind a bluff-body. In particular, the jet column can be viewed as an aerodynamic blockage impeding the approaching crossflow. Fric & Roshko [1] show convincingly, however, that the origin of the shed vorticity is fundamentally different in the two situations. Vorticity shed into the bluff-body wake is generated in the boundary layer of the bluff-body. No equivalent source of vorticity exists in the JICF. Instead, the WV are formed by bursts of boundary layer vorticity that connect the deflected jet column to the boundary layer as they convect downstream. Experimentally measured

shedding frequencies of the WV in terms of jet Strouhal number, $St_\mathrm{j} = fU_\mathrm{j}/d_\mathrm{j}$, range from $0.05 \leq St_\mathrm{j} \leq 0.20$ [1, 32].

The counter-rotating vortex pair (CRVP) is the most well-known feature of the JICF and has been studied extensively [24, 33, 34]. The CRVP dominates the far-field of the JICF and is widely attributed as a key reason for the strong mixing performance of JICF relative to other common shear flows, e.g., axial jets, mixing layers, and wakes. The formation of the CRVP begins in the near-field due a combination of shear-driven and pressure-driven mechanisms. The shear-driven mechanism proposed by Kelso et al. [6] is illustrated in Figure 1.7. The essential feature is the transport of concentrated (initially azimuthal) shear layer vorticity towards the leeward side of the jet by the crossflow. Simultaneously, the wall-normal velocity of the jet sweeps these regions of concentrated vorticity upwards, resulting in tilting and folding of the shear layer vortices as they convect along the jet trajectory, as shown in Figure 1.7c. Muppidi & Mahesh [35] later proposed a pressure-driven mechanism based on an elegant two-dimensional model problem. They showed that the net pressure gradient across the jet in the axial direction causes deformation of the jet column in the near-field that contributes directly to the formation of a CRVP. This mechanism is essentially independent of the shear layer vortices and, significantly, also explains the observation that CRVP formation is generally delayed in jets with higher J [23].

The shear layer vortices seen clearly in Figure 1.7a are attributed to a Kelvin-Helmholtz type instability in the near-field shear layer, not unlike the shear layer roll-up seen in axial jets [6, 7]. The key distinction between SLV in JICF and axial jets being the asymmetric transport of the vortices. The asymmetry of the SLV in JICF arises, in fact, even before the fluid exits the pipe due to the presence of reverse flow into the jet injector, which is a manifestation of the strong adverse pressure gradient in the jet near-field [6]. Furthermore, note that the relative vertical shear velocity between the crossflow and the jet depends on the azimuthal location, with the highest shear occurring along the $z = 0$ jet centerplane. The SLV grow as they convect in the streamwise direction before eventually undergoing vortex pairing and breakdown to turbulence. The dynamics of the SLV are influenced both by Re_j, J , and the jet exit velocity profile. Vortex pairing, in particular, is seen to occur

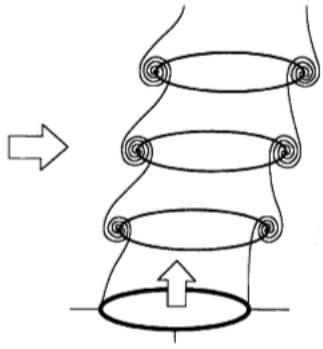

(a) Concentrated azimuthal vorticity in jet shear layer

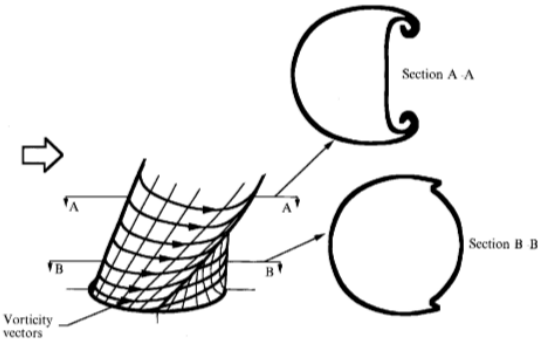

(b) Distortion and transport of the jet shear layer vorticity

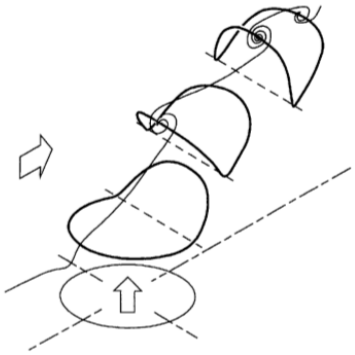

(c) Tilting and folding of the shear layer vortices

Figure 1.7: Illustration of shear-driven CRVP formation mechanism. Adapted from Kelso et al. [6].

less frequently and further from the jet injector at lower J [6]. New et al. [36] examined the effect of jet exit velocity profile on the formation of the shear layer vortices using flow visualization and PIV measurements. Their results showed conclusively that formation and growth of the SLV is suppressed in jets with parabolic velocity profiles and augmented by jets with tophat velocity profiles. This result is not surprising based on the much more concentrated vorticity distribution in the tophat profile.

1.4 Hydrodynamic Instability in JICF

The previous discussion concerning coherent vortical structures in JICF is incomplete without considering the hydrodynamic stability of JICF. Many shear flows used in combustion systems are linearly unstable under certain conditions, e.g., bluff-body wakes above a certain Re_D [37], swirling jets with sufficiently high swirl-number, and axisymmetric jets with low

density relative to the surroundings. An unstable flow will amplify an initial perturbation to the flow field, whereas the same perturbation would decay in a stable flow. The initial perturbation in a combustor could be a turbulent eddy, an acoustic wave, or an autoignition event. Unstable shear flows are further classified as either convectively unstable or globally unstable [38]. A convectively unstable flow amplifies a perturbation as it convects. In an open flow, the perturbation will eventually leave the domain of interest unless continuous excitation is provided, thus explaining why these flows are often called "noise amplifiers." On the other hand, globally unstable flows behave as self-excited oscillators and do not require continuous external excitation for the instability to persist.

Unlike combustion instabilities, hydrodynamic instabilities are not necessarily bad. In fact, hydrodynamic instability may be highly desirable in certain situations, e.g., fuel injectors, where the instability can accelerate the transition to turbulent flow and enhance mixing. On the other hand, shear layer dynamics associated with a flow instability can also drive combustion instabilities in certain circumstances, which is referred to as a vorticity-coupled combustion instability mechanism [39]. Since all practical combustion devices utilize turbulent flows, it is worthwhile to note that prior studies (e.g., Emerson et al. [20]) have shown that hydrodynamic stability concepts, developed exclusively for laminar flows, are also useful for understanding the dynamics of turbulent flows. This is true because turbulent flows are dominated by large-scale, vortical structures whose origin can often be traced to an underlying hydrodynamic instability present in the flow [40–42].

Recent experimental investigations suggest that the stability of JICF undergoes a transition from convectively unstable to globally unstable at sufficiently low R [7]. Single component hot-wire measurements in the windward shear layer showed that the spectral characteristics of the flow were altered dramatically when R was reduced below approximately 3.2 (or $J \approx 10.2$ for the unity S case). Representative power spectral density measurements for jets with $R = \infty$ (axial jet), $R = 6.4$, and $R = 2.0$ are shown in Figure 1.8. Note that the ordinate, s/d_j, is the non-dimensional streamwise coordinate, which is simply y/d_j in the free jet case. The low J case (Figure 1.8c) has strong, narrow-band oscillations along the entire shear layer that originate close to the jet injector. On the other hand, the $R = 6.4$

case shown in Figure 1.8b shows evidence of frequency-hopping about the fundamental mode frequency, staring near $s/d_\mathrm{j} = 1.5$. The fundamental mode frequency, f_M, occurs near $St_\mathrm{j} = 0.70$ in this case, although in general the frequency of the global mode depends on J and S. A Strouhal number, St_θ, based on the momentum thickness, $St_\theta = f\theta/U_\mathrm{j}$, can also be defined and does a slightly better job collapsing the J dependence. It is also interesting to note that f_M is roughly three times the frequency of oscillation usually observed in the HV and WV. Thus, the characteristic timescale for the SLV, $1/f_\mathrm{M}$, is easily the shortest fluid mechanical timescale of any large-scale structure in the flow. Davitian et al. [8] provide additional evidence for the transition to global instability at low J . They note that the low J jets exhibit a reduction in the transfer of energy to subharmonic modes, and that the low J jets are resistant to low-level acoustic forcing. Resistance to low-level forcing is a characteristic of many globally unstable flows, which prefer to oscillate at their own natural frequency.

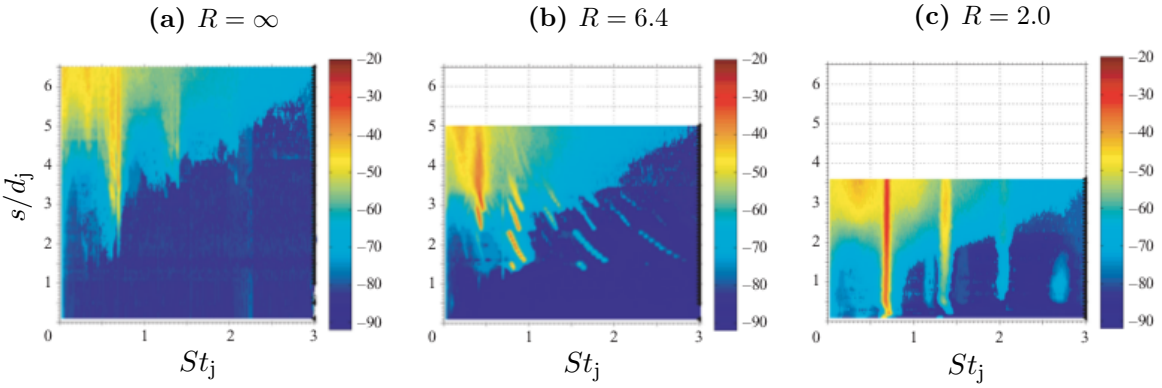

Figure 1.8: Contour plots of the power spectral density of vertical velocity as a function of s/d_j at three different values of R measured in the windward shear layer of a flush-injected JICF with $Re_\mathrm{j} = 3000$. Adapted from Megerian et al. [7].

Bagheri et al. [43] performed a global linear stability analysis on a non-reacting JICF with $R = 3$. They found two linearly unstable global modes in the flow, including a high frequency mode associated with the SLV and a lower frequency mode in the wake of the jet. Subsequent DNS and global linear stability analysis by Schlatter et al. [44] suggested that the high-frequency shear layer mode is non-axisymmetric and its mechanism may be similar to the elliptic, short-wave instability observed in vortex pairs. The low frequency

mode is particularly interesting from a mixing enhancement perspective because it caused the instantaneous jet trajectory to oscillate. This bulk oscillation occurred with the same frequency as the spanwise oscillation of the separated (low-pressure) region in the wake of the jet, suggesting that the WV may be more important to JICF dynamics than previously thought.

Getsinger et al. [9] extended the previous experimental work on unity S JICF to consider variable density ratio JICF. The motivation for these studies stems from previously observed transitions in the stability of variable density axial jets, including both heated jets [45] and low molecular weight jets [46]. The experiments reported by Getsinger et al. [9] varied the jet density by controlling the concentration of He and N_2 used in the jet. Single component hot-wire measurements in the shear layer, identical to those described above, suggest that the JICF stability transitions from convective to global instability when $S \leq 0.45$. However, regardless of the magnitude of S, the JICF always becomes globally unstable at sufficiently low J, which was also associated with the complete elimination of vortex pairing in the near-field of the low J jets. Interestingly, the low S jets exhibited enhanced energy transfer to the subharmonic mode ($f = f_M/2$), a result that was not expected based on the unity S measurements. Getsinger et al. [9] suggest that this may be indicative of a change in the nature of the shear layer instability for low S jets. These findings are summarized in the J and S hydrodynamic stability map for the JICF shown in Figure 1.9.

The stability of a reacting JICF has not been considered previously, and caution must be used before extrapolating the non-reacting results since chemical heat release is known to modify global stability boundaries of shear flows [20]. Juniper et al. [47] studied a globally unstable axial jet under both non-reacting and reacting conditions. They found that the global instability is significantly enhanced in the reacting case, but this result may be limited solely to the buoyancy-driven instabilities considered in that study. Physically, the combustion process can modify the stability either through active participation in the instability mechanism or by altering the base flow. The detailed analysis by Mahalingam et al. [48] showed that the latter effect is much more important. This conclusion is not surprising given the large changes in density and velocity associated with combustion heat

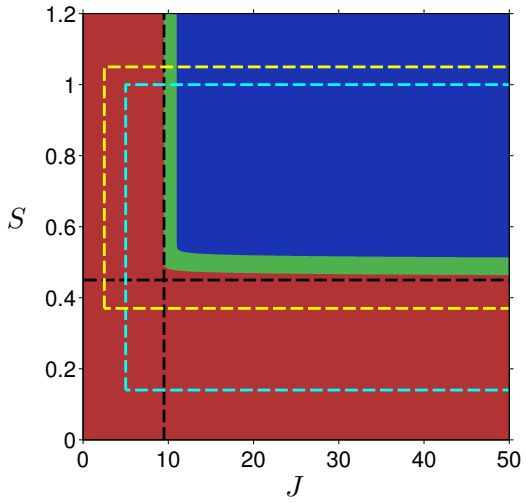

Figure 1.9: Sketch of the stability boundaries in non-reacting JICF based on experimental results obtained at UCLA's Energy & Propulsion Research Laboratory [7–9]. Blue: Convectively Unstable Region, Green: Transitional Stability Region, Red: Globally Unstable Region. Parameter space explored by Getsinger et al. [9] denoted by dashed turquoise line. Accessible parameter space for the present facility (see Chapter 2) denoted by dashed yellow line.

release. The *relative* position of the shear layer and the flame (i.e., the density gradient) were also shown to be important in a premixed, bluff-body stabilized flame [20]. In variable density axial jets, Lesshafft & Marquet [49] found that steep velocity gradients in low-velocity regions combined with abrupt density variation near the location of maximum shear promote absolute instability.

1.5 Entrainment, Mixing, and Flame Stabilization in JICF

Coherent vortical structures are believed to cause much of the enhanced mixing performance observed in JICF relative to axial jets [23]. These coherent structures deform and distort the jet/crossflow interface, leading to rapid entrainment of crossflow fluid into the jet. The increased interfacial surface area and strong gradients in the mixture fraction field ultimately contribute to enhanced molecular diffusion. Smith & Mungal [23] used acetone PLIF to measure the scalar concentration field in the $x-y$ and $y-z$ planes of high J JICF ($25 \leq J \leq 625$). Their results indicate that the scalar concentration along the jet center streamline is constant in the potential core and then decays with a rate proportional to $(s/d_{\mathrm{j}})^{-1.3}$ in the near-field, which is faster than the rate $(s/d_{\mathrm{j}})^{-1}$ observed in free jets.

The far-field concentration decay rate is notably lower and is generally less than that of the free-jet. The streamwise distance at which the mixing decay rate shifts lower seems to scale with J, with lower J jets showing decreased mixing rates at locations closer to the jet injector. This led Smith & Mungal [23] to suggest $s/d_\mathrm{j} = 0.3J$ as a transition point between near-field and far-field scaling in JICF.

Su & Mungal [25] collected simultaneous velocity and scalar field measurements for a $J = 32.49$ jet. They showed that both the velocity field and the scalar field became asymmetric very near the jet injector, but the asymmetry of the scalar field persisted much further into the far-field relative to the velocity field. A detailed comparison of their dataset, which considered jets with fully-developed pipe flow at the injection plane, with the earlier results of Smith & Mungal [23], who used a "top-hat" velocity profile, suggests that the inlet velocity profile strongly affects mixing in the jet near-field and can be more important than J (at least over the range spanned by those experiments). Muppidi & Mahesh [10] used DNS to study scalar transport in a non-reacting JICF at the conditions studied by Su & Mungal [25]. They caution against using centerplane measurements to quantify JICF mixing and suggest that global entrainment metrics, such as volumetric scalar fluxes, should be used to quantify mixing in fully three-dimensional flows like JICF. They compute the volumetric flux of scalar-containing fluid at different cross sections along the jet trajectory and compare with corresponding data for an axial jet. The results, shown in Figure 1.10a, indicate that the JICF entrainment surpasses that of the axial jet by $s/d_\mathrm{j} = 2$ and grows to nearly $3\times$ that of the axial jet by $s/d_\mathrm{j} = 10$. Interestingly, the streamwise location where the JICF becomes more effective than the free jet coincides very well with the location where entrainment by the JICF is dominated by the leeward side of the jet, as shown in Figure 1.10b.

Mixing dynamics are critically important in non-premixed reacting JICF, where the fuel/air mixing controls flame stabilization, heat release distribution, and pollutant formation. Despite its widespread application, research on reacting JICF has generally lagged well-behind that of the non-reacting JICF, and many open questions remain concerning the dynamics of reacting JICF. A key distinction can immediately be made, however, between

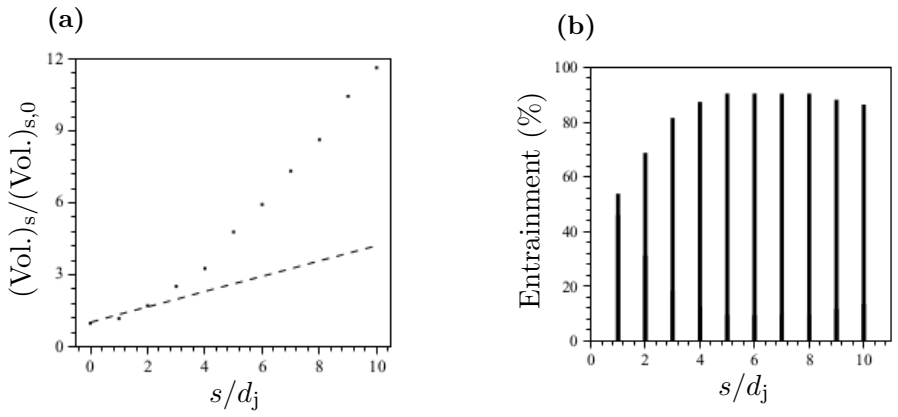

Figure 1.10: Entrainment characteristics of a non-reacting JICF. (a) Volumetric flux of scalar-containing fluid, $(\mathrm{Vol.})_s$, at different streamwise locations normalized by the initial flux, $(\mathrm{Vol.})_{s,0}$, for JICF (symbols) and axial jets (dashed line). (b) Percentage of the total entrainment occurring on the leeward side of the JICF. Adapted from Muppidi & Mahesh [10].

reacting JICF stabilized in low-temperature, air crossflows and those stabilized in high-temperature, vitiated crossflows. This distinction can be qualitatively understood through a simple Damköhler scaling argument, where $Da = \tau_{\mathrm{fluid}}/\tau_{\mathrm{chem}}$. τ_{fluid} and τ_{chem} are characteristic timescales associated with the fluid dynamic and combustion processes, respectively. Conceptually, flame stabilization in a non-premixed JICF occurs at a point where the rate of mixing ($\approx 1/\tau_{\mathrm{fluid}}$) between fuel and oxidizder is roughly balanced by the rate ($\approx 1/\tau_{\mathrm{chem}}$) of chemical reactions. The exponential dependence of reaction rates on temperature means that τ_{chem} in a vitiated crossflow ($T_\infty > 1000$K) is significantly decreased (often by several orders of magnitude) relative to τ_{chem} in a low-temperature, air crossflow. Thus, in vitiated flows, entirely different flame stabilization mechanisms, sometimes involving autoignition, are possible and reaction zones can be stabilized at flow velocities and in locations that are not possible in a jet injected into a low-temperature, air crossflow.

Consider flame stabilization in jets injected into low temperature, air crossflows first. Hasselbrink Jr. & Mungal [50] studied high J CH_4 jets injected into low temperature, air crossflows using simultaneous planar PIV and OH PLIF. They observed lifted jet flames and proposed a partially-premixed flame stabilization mechanism based on the characteristics of their OH PLIF measurements. Flame stabilization occurred in a low velocity region on the lee side of the jet, several jet diameters removed from the wall. The majority of

the fuel burned in a non-premixed flamelet regime downstream of a premixed stabilization region. This finding suggests that the CRVP likely controls the heat release rate through its effect on far-field mixing and entrainment. Hasselbrink Jr. & Mungal [50] found that the jet center streamline trajectory was only slightly affected by combustion heat release in their experiments. It is noteworthy that these observations pertain exclusively to very high J, lifted jet flames with combustion occurring in the far-field. Interestingly, despite the relatively small change in trajectory, there were significant regions of the flow that were strongly accelerated by the heat release processes. One possible explanation for this apparent contradiction is that heat release generally does not radically alter turbulent jet flame width [51] and thus momentum conservation requires flow acceleration to balance the large reduction in density due to combustion [50]. The simultaneous PIV and CH PLIF measurements by Han & Mungal [52] provide additional evidence for a partially-premixed flame stabilization mechanism in low temperature, non-premixed JICF. In particular, they found that the local flow velocity at the flame front closely matched the stoichiometric laminar flame speed, and contrary to the expected behavior of a non-premixed jet flame in co-flow, high 2D dilatation occurred upstream of the CH layer.

Recent DNS reported by Kolla et al. [53] studied flame stabilization of a slightly pre-heated (420K), diluted fuel jet (70% H_2 and 30% N_2 by volume) in a turbulent, 750K air crossflow. The simulation parameters were $J = 11.56$, $S = 0.57$, $Re_{\mathrm{j}} = 4000$, $Re_{\delta_{99\%}} = 8900$, $U_{\mathrm{j}} = 254$m/s, and $U_\infty = 57$m/s. The jet injector was not simulated, and a laminar top-hat velocity profile was prescribed for the jet inlet condition. Despite the preheating and the high-reactivity of H_2, flame stabilization occurred on the leeward side of the jet near the location where the potential core breaks down and the jet substantially deflects into the crossflow direction, which was near $(x/d_{\mathrm{j}}, y/d_{\mathrm{j}}) = (1.75, 4)$. The lack of flame stabilization along the windward shear layer, where rapid fuel/air mixing occurs, demonstrates the importance of coherent structures such as the SLV, which are ultimately responsible for the intense shear forces at the jet/crossflow interface. The flame stabilization location was further characterized by near stoichiometric mixture fraction and relatively low scalar

dissipation, χ, given by

$$\chi = 2D\left(\nabla z \cdot \nabla z\right) \tag{1.9}$$

where z is the local mixture fraction and D is the mixture-averaged mass diffusivity. χ is closely related to the strain-rate field in diffusion flames and can also be used to construct a timescale, $\tau_\chi = 1/\chi$, for mixing in diffusion flames. Additional analysis of the DNS database by Grout et al. [54] revealed that broken flamelets intermittently appear in the highly-strained JICF shear layer and that the slower WV modulate the bulk heat release distribution in the flow. They suggest that the primary role of the SLV, for their simulation conditions at least, is to mix fuel and air upstream of the flame stabilization location, leading to pockets of very high heat release as soon as the magnitude of χ drops. Lastly, they note that combustion occurred along the windward edge of the jet only after substantial jet deflection caused the CRVP axis to be nearly aligned with the crossflow direction.

High-temperature, vitiated crossflows greatly accelerate chemical kinetics and allow flame stabilization to occur much closer to the jet injector, even at high J and very large Re_j [55]. Autoignition phenomena are thought to play a more important role in flame stabilization for these cases [56] and can sometimes anchor a reaction zone even in the highly-strained windward jet shear layer [57]. The autoignition delay time can be viewed as an additional chemical timescale, τ_ign, of the flow and may be compared with, for example, convective timescales in the jet near-field or the scalar dissipation based mixing timescale, τ_χ. Autoignition timescales are extremely sensitive to temperature and local mixture composition. The minimum autoignition time for a given temperature occurs at the most-reactive mixture fraction, which tends to be very lean and far from the near-stoichiometric mixture fraction preferred by non-premixed flames [58]. Thus, the location of flame stabilization for a jet injected into a high-temperature, vitiated crossflow differs from that in a low-temperature air crossflow because of both the much shorter τ_chem and the fact that autoignition occurs preferentially at non-stoichiometric mixture fractions.

Recently, Mörtberg et al. [57] studied flame stabilization of high J ($390 \leq J \leq 420$) fuel

jets comprised of either CH_4 or C_3H_8 under both standard ($T_\infty = 298$K) and high temperature ($T_\infty = 1173$K) crossflow conditions. They used a custom reheat facility to vary the temperature and O_2 content of the crossflow, albeit at very low U_∞. The high temperature reacting jets penetrated further into the crossflow, exhibited reduced turbulence intensity at the jet/crossflow interface relative to non-reacting jets, and demonstrated larger flame volumes due to reduced entrainment and mixing. Reduced turbulence and laminarization due to combustion heat release has also been observed in attached axial jet flames [59]. Reduced O_2 levels in vitiated flows tend to increase the flame volume in JICF, consistent with basic notions of the stoichiometric mixture fraction, z_{st}, in diluted fuel jets [60].

The critical role of autoignition in flame stabilization for high temperature crossflows is seen clearly in the study reported by Micka & Driscoll [61]. They investigated flame stabilization and heat release distribution in non-premixed fuel jets injected into high temperature air crossflows ($T_\infty = 1390$K) with very high crossflow velocity ($U_\infty \approx 470$m/s). They propose a three-region model in these highly-strained JICF, referred to as an "autoignition-assisted flame," for the combustion process based on CH, OH, and CH_2O PLIF measurements. An initial lifted region of the flame is dominated by autoignition phenomena. The autoignition kernels support a secondary region characterized as a premixed flame base further downstream that has high instantaneous heat release. The remainder of the fuel is then burnt in a non-premixed thickened and broken flamelet regime downstream of the flame base. Interestingly, they observe a linear increase in flame length as a function of fuel mass flow rate, suggesting that their jet ($J = 4.84$) acts more like a wake with respect to mixing. This result agrees with the observations of Smith & Mungal [23], who showed that mixing in low J non-reacting JICF transitions to wake-like scaling relatively quickly.

Schmitt et al. [62] considered flame stabilization in premixed jets injected into a vitiated crossflow ($T_\infty = 1776$K) for a range of equivalence ratios, ϕ, between $0.05 \leq \phi \leq 0.77$ and J between $4 \leq J \leq 10$. Premixed flames were fully-attached around the entire periphery of the jet at all conditions, and penetration increased for the reacting jets relative to non-reacting jets. Jets with higher ϕ exhibited much shorter flame lengths compared to lower ϕ jets, and OH^* chemiluminescence imaging suggested that the flame structure in the low ϕ

jets was significantly more affected by the near-field turbulence. The flow/flame interaction at high T_∞ and in premixed flames are indicative of the highly turbulent flow conditions in the JICF near-field. Also note that premixed flames are generally an order of magnitude less sensitive to flame stretch and velocity perturbations relative to non-premixed flames, which are dependent on mixing and therefore cannot easily propagate into lower strain-rate regions [63].

Lastly, it is worth noting that additional work on reacting jets in vitiated crossflows is found in the RQL literature [64]. RQL combustors, as shown in Figure 1.3, involve so-called "inverse flames" where the jet contains the oxidizer and the crossflow contains the fuel. These studies are usually concerned with the interaction of multiple JICF, often at very high J and with significant confinement. The structural differences between these inverse flames and the more conventional reacting fuel jet discussed previously is not well-understood.

1.6 Forced Response of JICF

Forcing the JICF as a means to increase jet penetration and enhance mixing has been investigated by a number of researchers [65–69]. These studies focus exclusively on forcing the jet rather than the crossflow and can be partitioned into two types based on their forcing methodology, partially-modulated jet studies and fully-modulated jet studies. Partially-modulated studies generally rely on a loud speaker located in the jet supply system to excite acoustic oscillations and impose a fluctuating jet exit velocity, similar to earlier work on forced response of axial jets and mixing layers [70, 71]. Fully-modulated studies use solenoid valves or rotating valves to periodically stop and start the flow.

Eroglu & Breidenthal [67] were able to increase penetration by 70% in a high Re_j JICF relative to a steady jet using a fully-modulated strategy. Narayanan et al. [68] observed smaller increases in penetration but cited $30-46\%$ enhancement of near-field entrainment as a result of forcing. Interestingly, the "optimal" forcing conditions required to achieve maximum penetration vary widely between different studies [69]. This is perhaps not surprising since the parameter space in forced response studies is quite large and includes, in

addition to the usual JICF parameters, the forcing frequency (f_{F}), forcing amplitude (u'_{j}), duty cycle (α_{F}), and pulse shape. The greatest increase in jet penetration is always found for f_{F} less than the fundamental mode of the SLV [72], but reported values span a wide range from $0.004 \leq St_{\mathrm{j}} \leq 0.5$ [68]. Square-wave forcing is consistently more effective than sinusoidal forcing, and small values of α_{F} are more effective [66] because they create more intense vortex rings. Sau & Mahesh [73] present DNS of pulsed jets and show that optimal penetration for their simulations and much of the experimental data in the literature can be collapsed on a single line in (L/d_{j},R_{ring}) space, where L/d_{j} is the stroke ratio and R_{ring} is the ring velocity ratio. This result suggests that the forced response of JICF can be understood primarily through the evolution of toroidal vortex rings formed at the jet exit as a result of the applied forcing, similar to starting vortices. Maximum penetration occurs when the forcing creates vortex structures lying at the transition between independent vortex rings and vortex rings with trailing columns of vorticity.

The effect of jet pulsing on hydrodynamic instabilities in the JICF has also been investigated [7–9]. Low J and low S jets in the globally unstable regime are resistant to low amplitude forcing, while the shear layer structures of convectively unstable jets respond sensitively to the same low amplitude forcing. The globally unstable jets did respond to high-amplitude sinusoidal forcing near the fundamental mode, and the critical amplitude of excitation required to cause "lock-in" scaled linearly with the difference between f_{F} and f_{M}, as would be expected near a Hopf bifurcation. MCloskey et al. [72] found that forcing at subharmonics of the fundamental shear layer mode can be particularly effective in increasing penetration and spread, but forcing at frequencies above the fundamental was not effective. DNS of a $J = 36$ case by Muldoon & Acharya [74] also found that the SLV were strongly affected by jet pulsing. They tracked the evolution of a passive scalar in an unforced jet and in forced jets with sinusoidal forcing applied at $St_{\mathrm{j}} = 0.2,\ 0.4, \mathrm{and} 0.6$. The $St_{\mathrm{j}} = 0.2$ case bifurcated in the vertical ($x - y$) plane, and the $St_{\mathrm{j}} = 0.4$ case trifurcated in the vertical plane. Both $St_{\mathrm{j}} = 0.2$ and $St_{\mathrm{j}} = 0.4$ cases penetrated further into the crossflow and had enhanced jet spread. Interestingly, the $St_{\mathrm{j}} = 0.6$ case bifurcated in the horizontal ($x - z$) plane and suppressed WV formation/shedding.

Marr et al. [75] recently explored the effect of forcing on jet flames stabilized in low-temperature air crossflows. Similarly to the earlier non-reacting studies, periodic forcing created toroidal ring vortices that penetrated further into the crossflow. They found that acoustic forcing drastically decreased the overall flame length in non-premixed flames. Eroglu & Breidenthal [67] measured the flame length decrease using reactive LIF of a forced JICF in a water tunnel and found a 50% reduction at the optimal pulsing conditions. They attributed the enhanced mixing to interaction of the ring vortices in the far-field after the jet breaks down. Interestingly, Marr et al. [75] report that the forcing also drew air directly into the leading edge of the nozzle, thus introducing a degree of partial-premixing in the near-field and potentially affecting the flame stabilization mechanism. The overall effect of the near-field mixing due to forcing in nominally non-premixed jets is similar to partially-premixing an unforced jet, as demonstrated by very similar CH^* luminescence profiles and NO_x emissions. The partial-premixing at the injector is particularly significant since non-premixed flames, which do not have a propagation velocity, are much more sensitive to velocity fluctuations than premixed flames [63].

The effect of crossflow forcing on a JICF appears to have been considered only twice in the reported literature [76, 77] and perhaps never for a reacting jet. Note that acoustically forcing the jet generally results in axisymmetric excitation, which is consistent with the formation of ring vortices at the nozzle exit plane. Crossflow forcing, on the other hand, is inherently asymmetric and has many similarities with the type of forcing used to study transverse excitation in swirl flames [78] and in liquid rocket engines [16]. Kremer et al. [76] used LES to study the dynamics of a $J = 32.49$ water jet injected perpendicularly into a sinusoidallly oscillating crossflow. They found that the jet plume was strongly modified by the oscillatory crossflow and showed much less contiguity relative to an identical jet injected into a steady crossflow. The jet penetration was more sensitive to variation in forcing frequency over the range ($0.025 \leq St_\mathrm{j} \leq 0.137$) than variations in forcing amplitude spanning ($0.10 \leq u'_\infty/U_\infty \leq 0.40$). Zhang et al. [77] recently investigated the effect of oscillatory crossflow in a gas-phase environment using LES. They considered frequencies in the range $0.0635 \leq St_\mathrm{j} \leq 0.3175$ and forcing amplitudes spanning $0.10 \leq u'_\infty/U_\infty \leq$

0.50. Significantly, they find that both dominant spectral features in the unforced JICF, namely the WV with $St_{\mathrm{j}} \approx 0.10$ and the SLV with $St_{\mathrm{j}} \approx 0.70$, are suppressed by the crossflow forcing. Instead, the crossflow forcing causes "flapping and detaching movements" at the forcing frequency that become increasingly dominant as the amplitude of forcing is increased. POD analysis of velocity and scalar fields extracted from the forced LES results reveals a longer, narrower jet plume and a lower "center-of-gravity" in scalar field. The forcing appears to improve the spatial mixedness but negatively impacts the temporal mixedness. In other words, the flapping of the jet helps spatially distribute jet fluid on a time-averaged basis but also leads to greater instantaneous variation in the jet mixing processes. It is worth noting that these authors, unlike many other JICF studies, actively model a substantial region *upstream* of the jet injection location in order to properly account for the jet/crossflow coupling. Ignoring the details of the injector dynamics is problematic even in steady JICF but would absolutely invalidate any computational or experimental study concerning forced response of JICF.

The remainder of this section pivots slightly in order to emphasize the connection between forced response of JICF and the earlier discussion of acoustics and combustion instability in gas turbine combustors. The natural acoustics present throughout gas turbines can be viewed simplistically as a built-in forcing mechanism. The JICF can often be considered acoustically compact since natural mode frequencies tend to be in the range $100\mathrm{Hz} \leq f_{\mathrm{F}} \leq 1000\mathrm{Hz}$, preheating leads to high sound speed ($500\mathrm{m/s} \leq c_{\infty} \leq 1250\mathrm{m/s}$), and the jet diameters are generally quite small ($5 \times 10^{-4}\mathrm{m} \leq d_{\mathrm{j}} \leq 0.04\mathrm{m}$). The oscillatory acoustic field will drive a time-varying mass flow rate through the JICF injector. The amplitude and phase of this time-varying mass flow rate through the injector is a function of the local acoustic field and the nozzle impedance Z_{j}, which in turn depends on the mean flow rate through the injector, the local fluid properties, and the injector geometry. The amplitude of the acoustic field is, of course, strongly dependent on the mode shape of the acoustic standing waves inside the combustor. Note that even relatively low amplitude acoustic oscillations in the combustion chamber can cause a large time-varying mass flux because JICF-style injectors used in gas turbine combustors tend to be low pressure drop

(i.e., low impedance) devices in order to minimize pressure losses, which reduce the engine's thermodynamic efficiency. The unsteady mass flow rate issuing from a JICF-style injector can, especially in the case of JICF-style *fuel* injectors, lead to additional unsteady heat release and the potential for enhanced combustion instability. Thus, any open- or closed-loop control for JICF in a gas turbine system will have to account for *crossflow* oscillations.

Coupling between jet injectors and acoustically unsteady crossflows can adversely affect the performance of JICF by altering the jet penetration and mixing, even when the unsteady mass flow rate does not drive thermo-acoustic instability. Consider, for example, a JICF-type fuel injector used in the premixing vanes of a power-generating gas turbine. This injector and whatever ducting may exist between the fuel mixing location and the combustor must never stabilize a flame because the premixing hardware is not designed to withstand flame temperatures. A JICF-type injector designed for- and operating in a steady crossflow may maintain velocity and scalar fields that do not allow flashback or flame stabilization. The same injector operating in an unsteady acoustic field may, however, exhibit decreased exit velocity at some point in the acoustic cycle and the combination of low fuel exit velocity and altered fuel distribution in the premixing ducts that may allow flashback/flame stabilization to occur in an otherwise flashback-safe premixing section.

1.7 Research Questions and Thesis Outline

This thesis focuses on understanding the dynamics of non-reacting and reacting jets injected into unsteady, vitiated air crossflow. The primary technological motivation is the application of JICF in staged fuel combustion systems. The crossflow composition, temperature, and velocity field in these systems differ considerably from the classical JICF, which has been the focus of extensive research for many years. These differences raise the following three fundamental research questions that have been addressed by this thesis:

1. What are the effects of near-field chemical heat release on the structure and dynamics of a jet injected into a vitiated crossflow?

2. How does an acoustically excited crossflow modify the dynamics of non-reacting and reacting JICF?

3. Do JICF parameters that control the convective/global stability of non-reacting JICF have a measurable impact on the dynamics of reacting JICF at gas turbine relevant conditions?

The remainder of this thesis is organized around these three central research questions. First, Chapter 2 describes the unique, optically accessible facility developed to investigate jets injected into very high temperature, vitiated air crossflows. The design of experiments is presented next, including a detailed description of the test conditions and parameter space. Chapter 2 concludes with a discussion on the experimental methodology and the optical diagnostics used throughout this thesis.

Chapter 3 focuses on characterizing the effects of near-field heat release on unforced JICF. Non-reacting and reacting jets at otherwise identical conditions are compared in order to understand the structural changes in the flow field due to large volumetric dilatation and local flow acceleration. Instantaneous and time-averaged results extracted from simultaneous high-speed, stereoscopic particle image velocimetry (SPIV) measurements, OH Planar Laser Induced Fluorescence (OH PLIF) imaging, Mie scattering flow visualization, and dynamic pressure measurements are presented and analyzed. The trajectory, penetration, and spread of reacting JICF is quantified and compared against existing models. The inability of the existing scaling laws to fully-collapse the measured jet trajectories leads to the development of a new trajectory scaling law that accounts for the effects of near-field heat release. OH PLIF imaging provides insight into the flame stabilization mechanisms at high temperatures and reveals important differences between the windward and leeward reaction zones.

Chapter 4 examines the response of jets injected into acoustically excited crossflow. Loud speakers are used to excite the crossflow near natural acoustic modes of the system, and the jet response is studied using time-resolved diagnostics at several different forcing frequencies and forcing amplitudes. Based on these measurements, structural differences between unforced and forced JICF are evaluated. The role of injector coupling, in particular, is found to be particularly important, and a model is developed to predict the injector-coupled response in jets with different J and S. Flame edge tracking is used to extract the

spatio-temporal dynamics of the windward reaction zone, including the fluctuating flame length and flame flapping amplitude.

Chapter 5 considers the influence of density ratio on the shear layer dynamics of non-reacting and reacting JICF. Statistical measures extracted along the jet centerline show significant and non-intuitive dependency on J and S. Simultaneous OH PLIF images and Mie scattering flow visualization reveal further evidence that the shear layer structure is sensitive to changes in S and the presence/absence of combustion. Concepts from linear stability theory are utilized to develop a phenomenological model to explain these observations. A quasi-steady interpretation of the shear layer dynamics is postulated based on a timescale separation argument to extend the proposed phenomenological model to jets in oscillatory crossflows. Chapter 6 concludes with a summary of the key findings and a discussion of recommendations for future work.

CHAPTER II

EXPERIMENTAL METHODOLOGY

This chapter describes the experimental methods used to investigate the key research questions outlined in Section 1.7. Details of the reacting JICF facility developed and utilized in this study are presented in Section 2.1.1. Section 2.1.2 covers flow measurement, process control, and data acquisition in the new facility. Acoustic forcing hardware and methodology are discussed in Section 2.1.3. The design of experiments and the selection of test conditions are described in Section 2.2. Section 2.3 focuses on the diagnostics and measurements used in this study. Details concerning the relevant optical diagnostics are presented first, including stereoscopic particle image velocimetry (SPIV) in Section 2.3.1, Mie scattering in Section 2.3.2, and OH planar laser induced fluorescence (OH-PLIF) in Section 2.3.3. Dynamic pressure measurements used to characterize the acoustic velocity and pressure are described in Section 2.3.4. Timing and synchronization between all the various hardware are discussed in Section 2.3.5. Section 2.3.6 covers the hot-wire anemometry system used to characterize the jet exit condition in the absence of crossflow. The chapter concludes with a detailed characterization of the jet and crossflow inlet conditions, including the background acoustics present in the facility during the unforced experiments.

2.1 Reacting JICF Facility

2.1.1 Overview

The facility developed for this study was designed specifically to study reacting jets injected perpendicularly into subsonic, vitiated crossflow. A rendering of the facility is shown in Figure 2.1. The vitiated crossflow simulates the composition, temperature, and velocity field that might be encountered in the secondary combustion zone of a staged fuel combustion system. The facility runs in a blow-down mode of operation with the test section at atmospheric pressure. The primary distinction between this new facility and the standard experimental facility for studying JICF, i.e., a low-speed wind tunnel, is the high-temperature, vitiated

crossflow. The reacting JICF facility provides a "hot wind-tunnel" capable of continuous operation at temperatures up to 1900 K. The facility, shown in more detail in Figure 2.2, consists of three main components: a vitiator section, a flow conditioning section, and an optically accessible test section.

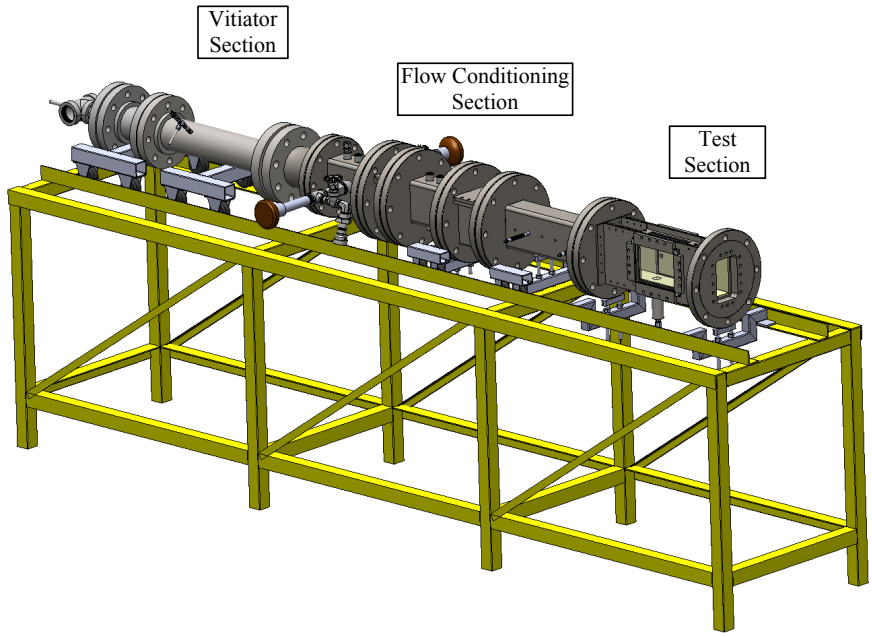

Figure 2.1: Rendering of the reacting jet in crossflow facility developed as part of this study.

The vitiator section (detailed in Figure 2.3) consists of a swirl-stabilized, partially-premixed natural gas burner coupled to a cylindrical, refractory-lined combustion chamber. The inner diameter of the vitiator is 76mm, and the slip cast refractory (Cotronics Corp. Rescor 780) lining is 12.7mm thick. Strong swirl, minimal thermal losses, and a non-premixed pilot combine to stabilize a robust, compact flame within the first third of the combustor, even at equivalence ratios as low as $\phi = 0.4$. This was visually verified by operating the primary combustor attached to a quartz tube of the same inner diameter as the actual vitiator. The overall hot-section length of the vitiator is 597mm, which translates to a total vitiator residence time of $\approx$ 25ms at standard operating conditions. The lengthy primary combustion chamber and relatively low mean axial velocity at normal operating conditions ensures that complete combustion occurs within the vitiator section. The vitiator

generally operates at lean overall equivalence ratios in the range $0.45 \leq \phi \leq 0.95$, depending on the desired test section temperature, velocity, and O_2 content.

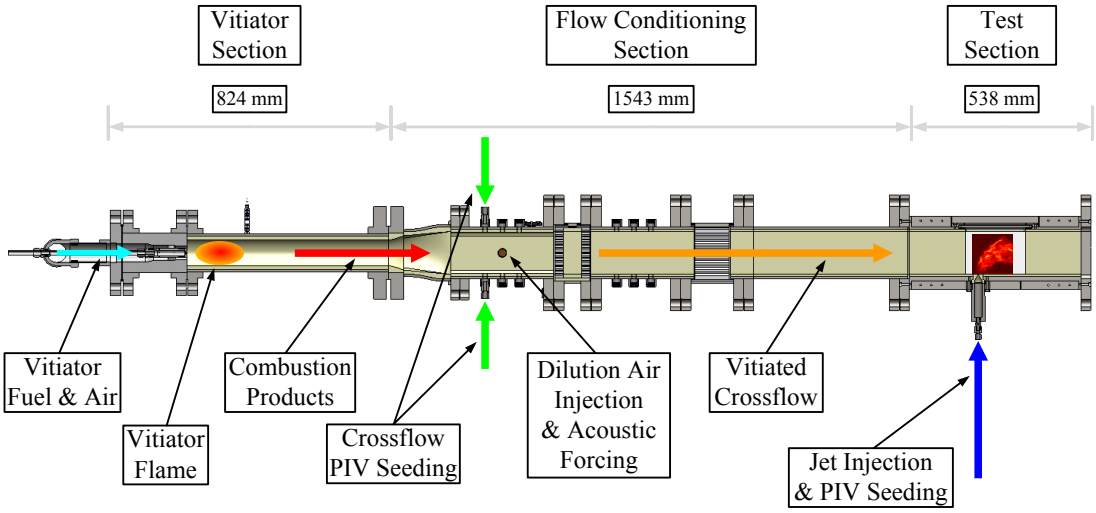

Figure 2.2: Schematic detailing key components of the reacting JICF facility.

At the end of the vitiator section, hot product gases from the primary combustion zone expand into the rectangular (76.2mm × 127mm) flow conditioning section via a smooth round-to-rectangular transition section. A diagram of the flow conditioning section is provided in Figure 2.4. Immediately after the round-to-rectangular transition, large opposed air inlets inject a metered quantity of room-temperature dilution air to reduce the temperature of the vitiated combustion products. The dilution air inlets have inner diameter of 32mm and double as the connection point for the acoustic drivers, which are described in greater detail in Section 2.1.3. The appropriate vitiator and dilution flow rates are determined using an integrated Matlab/Chemkin optimization tool that computes the required vitiator air flow rate, vitiator fuel flow rate, and dilution air flow rate based on a specified J, S, T_∞, Re_∞, and jet composition. We assume that the vitiator generates equilibrium combustion products at the adiabatic flame temperature and that these hot products mix uniformly and adiabatically with the room temperature dilution air.

Downstream of the dilution air location, a series of settling chambers and ceramic flow straighteners promote gas mixing and velocity field homogenization. The flow straighteners are Mullite Versagrid units manufactured by Applied Ceramics with cell density of 16

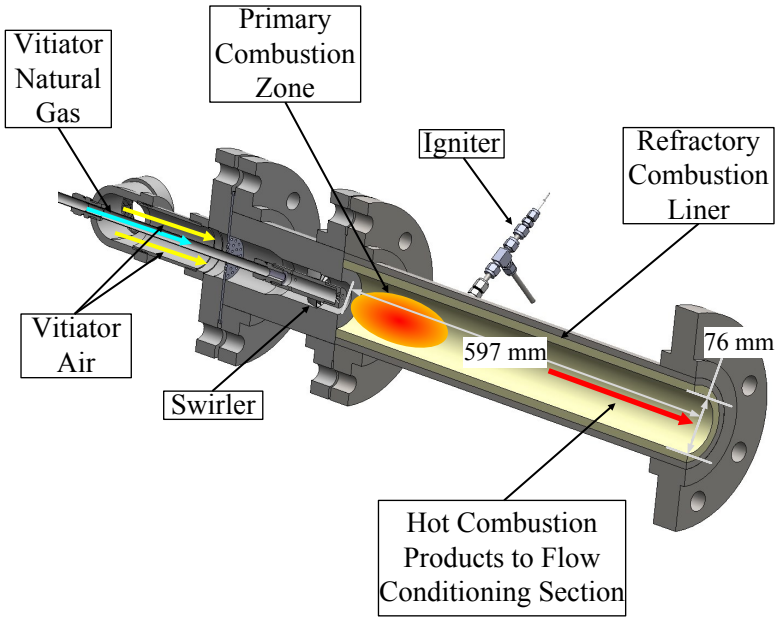

Figure 2.3: Diagram of the vitiator section

per inch (i.e., 6.35mm square flow passages). The last flow straightener is located 0.73m upstream of the jet injection location to minimize the influence of any grid generated turbulence. All the hot-section flow passages in the flow conditioning section are lined with a 9.5mm thick slip-cast refractory layer to minimize thermal losses upstream of the test section. The last settling chamber in the flow conditioning section doubles as an acoustic measurement section. Two dynamic pressure transducers mounted on stand-off tubes are installed along the flow path, as shown in Figure 2.4. Additional details on the acoustic measurements are provided in Section 2.3.4. It is important to note that the reacting jet in crossflow facility, unlike a conventional wind-tunnel, does not contain a large area contraction section upstream of the test section. Hence, the test section flow profile most closely approximates a well-mixed, fully-developed turbulent channel flow. In addition to being more practical in a reacting facility, this configuration better approximates the flow field found in the secondary combustion zone of staged-fuel combustion devices utilizing the reacting JICF for fuel injection and flame stabilization.

The test section is located immediately downstream of the flow conditioning section and is shown in Figure 2.5. The rectangular test section spans 127mm ($40d_{\mathrm{j}}$) from top-to-bottom

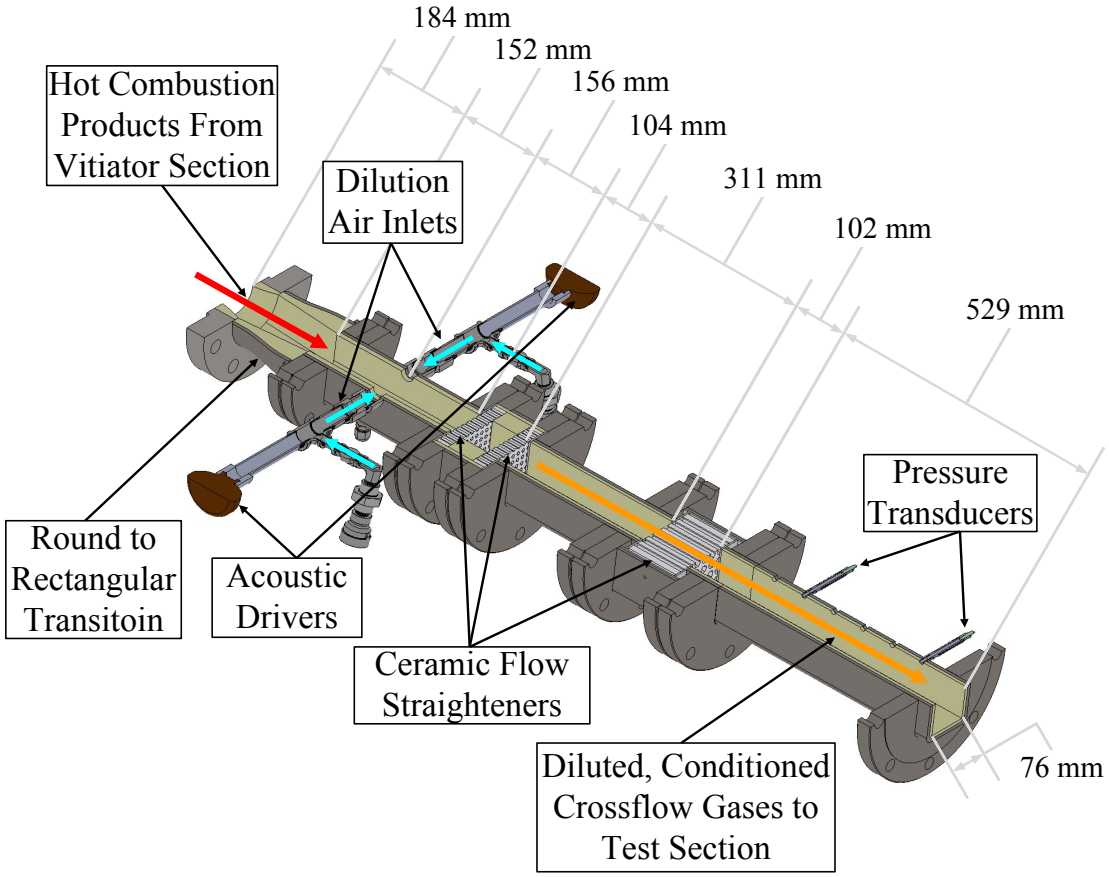

Figure 2.4: Diagram of the flow conditioning section

and 76.2mm ($24d_j$) side-to-side. Confinement effects are minimal since jet penetration does not exceed $y = 25d_j$ in the vertical direction for any test condition investigated in this study. The test section provides optical access for laser diagnostics via large UV-grade quartz windows located on the top and both sides of the test section. The viewable area extends $12d_j$ upstream of the jet and $44d_j$ downstream of the jet. The interior walls of the test section are insulated from combustion gases by a 6.35mm thick slip-cast ceramic lining. The lining reduces wall-quenching, minimizes thermal expansion of the facility, and provides a better-defined thermal boundary condition for comparison with computational modeling. Furthermore, the back end of the test section is rigidly clamped to the test stand (see Figure 2.1) in order to mitigate the tendency of the facility to expand axially once heated. Both the vitiator section and the flow conditioning section, on the other hand, float freely on wheeled supports thus allowing the facility to thermally expand in the upstream

direction without affecting optical alignment/calibration in the test section.

The contoured jet injector is fabricated from machinable ceramic (Cotronics Rescor 960-9) for similar reasons. The nozzle contour is similar to the one used by Megerian et al. [7], and the nozzle diameter at the injection location is $d_j = 3.175$mm. In the absence of crossflow, the fifth order smooth contraction nozzle generates a thin, nearly top-hat velocity profile at the exit plane. The jet is injected flush with the lower wall of the test section and normal to the crossflow direction at a location $73d_j$ downstream of the entrance to the test section. The center of the jet injector is taken as the coordinate system origin, and the coordinate axes are defined as was shown previously in Figure 1.6.

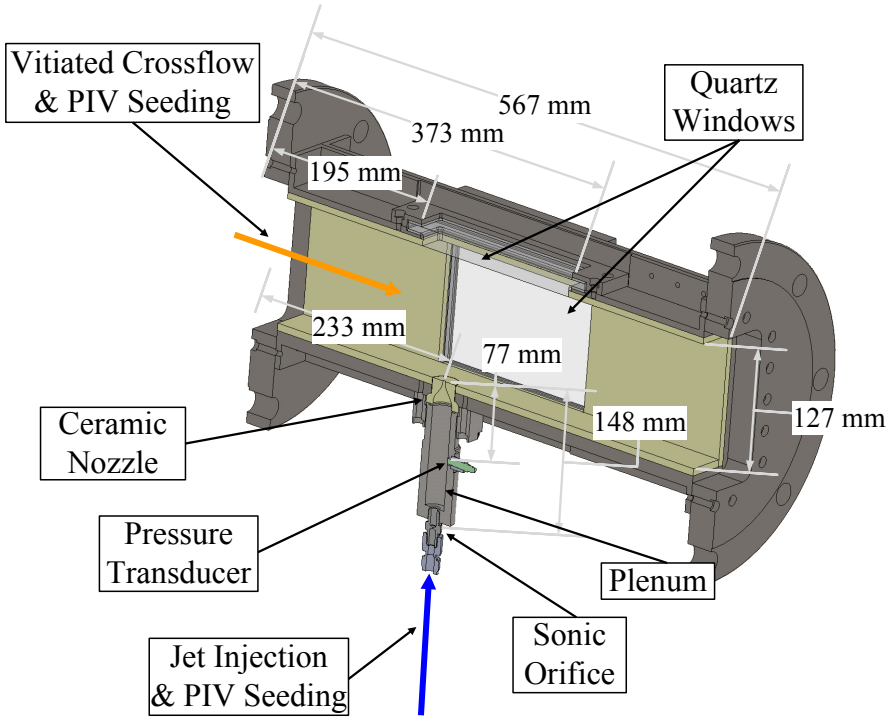

Figure 2.5: Schematic of the optically accessible test section

Although often neglected, the details of the jet injection assembly upstream of the nozzle are also very important in JICF studies, and particularly so when studying jet dynamics. In the case of low Mach number jets, the jet injection assembly and the crossflow/test section should be viewed as an acoustically coupled system rather than as separate, independent components. This is true even for very small nozzle diameters, as evidenced by recent

work demonstrating the detrimental effect that acoustics can have on the performance of $\mathcal{O}(500\mu\text{m})$ film cooling jets in gas turbine flow passages [79]. From this perspective, there are two primary objectives for the jet injection assembly in this study. First, the injection system should supply approximately uniform laminar flow to the inlet of the contoured nozzle since any flow non-uniformities will negatively affect the jet exit velocity profile. This objective is achieved by providing a sufficiently large plenum upstream of the nozzle contraction. The plenum in the present work has a diameter of 22.9mm ($\approx 7.2d_\text{j}$) and a length of 127mm ($40d_\text{j}$). The second objective for the jet injection assembly is to provide well-defined acoustic boundary conditions. This is accomplished by installing a choked orifice immediately upstream of the jet injector plenum, which eliminates the propagation of acoustic pressure/velocity waves from the test section into the jet supply system. Note, however, that acoustic waves originating in the jet supply system (i.e., upstream of the choked orifice) may still affect the instantaneous flow rate through the choked orifice but this effect is much less important since typical acoustic pressures are very small compared to the stagnation pressure required to choke a flow. The dynamic pressure inside the jet plenum is monitored during all tests using a sensor located $20d_\text{j}$ upstream of the jet injection location. Additional discussion of the jet injector dynamics are deferred until Section 2.1.3.

The exit of the test section is located $105d_\text{j}$ downstream of the jet injector. Exhaust gases flow out of the test facility, briefly expand and entrain ambient air for approximately 0.5 m, and then enter the building's vacuum exhaust gas system. Dynamic pressure measurements in the test section confirm that the test section is negligibly affected by small fluctuations in the exhaust system due to the periodic exhaust fan motion.

2.1.2 Flow Metering and Measurement

Operation of the reacting JICF facility requires controlling a number of different gas flow rates. A process and instrumentation diagram for the entire facility is provided in Figure 2.6. The vitiator is supplied with metered primary air and natural gas via calibrated sub-critical orifice assemblies. Natural gas is supplied by the building's 25psig system, and primary air is supplied by the building's regulated 250psig air system. Each sub-critical

orifice assembly consists of a static pressure transducer (Omega PX-309), an ungrounded K-type thermocouple, a high-accuracy differential pressure transducer (Omega PX-771A), and an appropriately sized calibrated orifice plate (Imperial Flange Company). Needle valves located downstream of the sub-critical orifice assemblies are used to control the gas flow rate. The differential pressure across each of the needle valves is sufficiently large to decouple any thermo-acoustic oscillations in the reacting JICF from the fuel and air supply lines.

Secondary (dilution) air is supplied by the building's 250psig air line and is independently metered by an additional sub-critical orifice assembly. A bypass line can be used to divert a portion of the metered secondary air through the crossflow PIV seeder (described in Section 2.3.1) to introduce seeding particles into the crossflow. The flow rate of secondary air through both the dilution air ports and the crossflow seeder is manually controlled using needle valves. Lastly, two additional needle valves (shown in Figure 2.7) are located immediately adjacent to the dilution air injection ports. These valves are adjusted on a case-by-case basis to maintain a choked flow condition and thus eliminate acoustic coupling between the facility and the secondary air supply system.

The jet supply system provides mixtures of up to four different gases. The present work, however, considers jet gas mixtures comprised of only H_2, N_2, and He. The jet gases are supplied by compressed gas bottles, and each gas is independently metered using a calibrated critical orifice assembly. Each critical orifice assembly consists of a static pressure transducer (PX-209), a K-type thermocouple, and a precision micro-orifice (O'Keefe Flow Controls). The flow rate through each critical orifice assembly is controlled by manually adjusting two-stage pressure regulators mounted on each gas bottle. The metered jet gases are combined in a mixing plenum several meters upstream of the test section to provide plenty of time for the gases to mix. The back pressure in the mixing plenum is continuously monitored to insure that the flow through each critical orifice assembly remains choked. The mixed jet fluid leaves the plenum and flows through a seeding assembly where anywhere from 0% to 100% of the jet fluid can be seeded with PIV particles. The seeded flow is then routed to the test section where it passes through a final choked orifice before entering the jet supply

plenum, as shown in Figure 2.5.

All the flow rates, temperatures, and pressures describing a specific JICF test are continuously monitored and recorded using a custom Labview application. A National Instruments (NI) Labview 6024E board is used to read in all the pressure signals associated with the primary air, primary natural gas, and secondary air. The jet pressure measurements are recorded using a NI Labview 6034E board. Thermocouple temperatures are monitored using a NI 9213 module attached to a NI cDAQ 9174 chassis. All the Labview boards are operated at 300Hz and average calculated flow rates, temperatures, and pressures are output at 4Hz.

The flow rates measured by the sub-critical orifice assemblies are accurate to within $\pm 1.79\%$ of the measured values. Details of the uncertainty analysis are available in Appendix A. At normal operating conditions in the primary combustion zone, these uncertainties translate to a ± 0.011 uncertainty in equivalence ratio, or an equivalent maximum variation in vitiator flame temperature of $\pm \Delta T_{\text{vitiator}} = 44.1\text{K}$. With a secondary air flow rate of $\dot{m}_{\text{secondary}} = 10\text{g/s}$ the propagated measurement errors result in a crossflow temperature uncertainty in the test section of $\pm \Delta T_{\infty} = 19.6\text{K}$. Flow rates measured by each of the critical orifice assemblies are accurate to within $\pm 1.67\%$ of the measured value. The propagated uncertainty in the jet gas density and total jet mass flow rates are $\pm 2.24\%$ and $\pm 1.10\%$, respectively. Assuming that the crossflow density depends primarily on changes in the crossflow temperature rather than changes in the crossflow composition, the cumulative uncertainty in density ratio for the experiments reported in the present study is 2.77%, and the uncertainty in J is 9.34%. Uncertainties for additional JICF parameters such as Re_{j} and Re_{∞} can be found in Appendix A.

The uncertainty estimates given above for parameters such as T_{∞}, J, and S implicitly require that the reacting JICF facility has reached a steady-state operating condition. This requirement primarily concerns the crossflow since the unheated jet gases reach steady-state in a matter of seconds. To insure that the crossflow reached steady-state as well, the vitiator was run for 10 minutes prior to starting the jet for every test condition. This warm-up time was sufficiently long to limit the temperature variation at the exit of the test section to less

than 1K per minute, as measured by a shielded, ungrounded K-type thermocouple. It is also worth noting that the natural acoustic modes of the facility (and presumably their response to applied forcing) can change considerably during the rig warm-up period. Thus, acoustic pressure measurements were performed at the end of each warm-up period and prior to the start of data acquisition to verify that the rig had reached a steady thermo-acoustic condition as well.

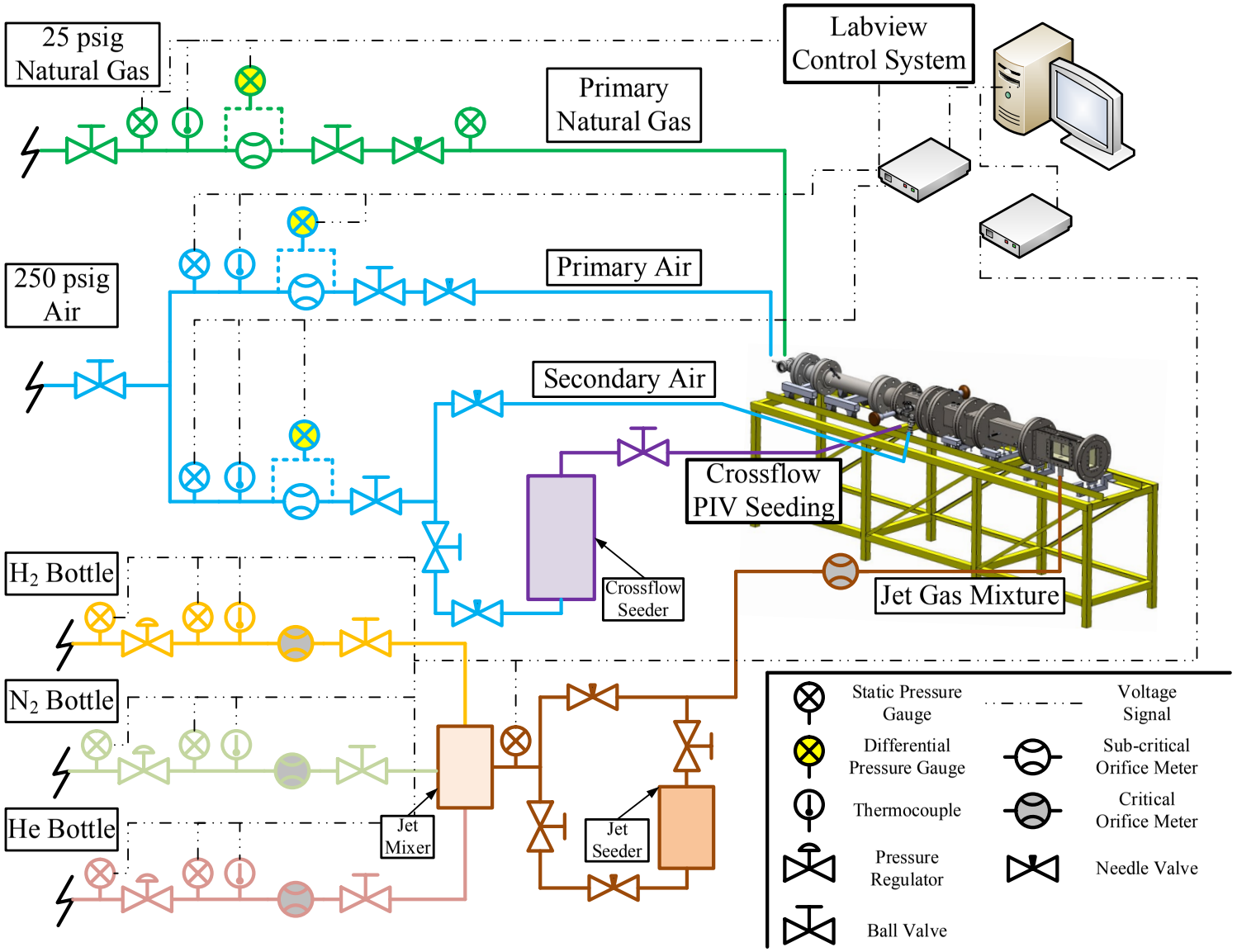

Figure 2.6: Flow Controls

2.1.3 Acoustic Forcing

A major objective of this study is to examine the response of non-reacting and reacting jets when injected into unsteady crossflow. This objective requires a method for exciting the crossflow. A diagram of the acoustic forcing setup utilized in this study is provided in Figure 2.7. Acoustic excitation is provided by a pair of symmetrically located 5.5 inch, 100W speakers that are integrated into the secondary air supply system. Each speaker is mounted at the end of a rigid 1 inch NPT pipe that extends 0.36m from the sidewall of the conditioning section. Secondary air is injected into the pipe roughly halfway between the speaker and the conditioning section. The mean flow of room temperature secondary air thus prevents vitiated crossflow gases from back-filling into the acoustic forcing assembly and damaging the speakers.

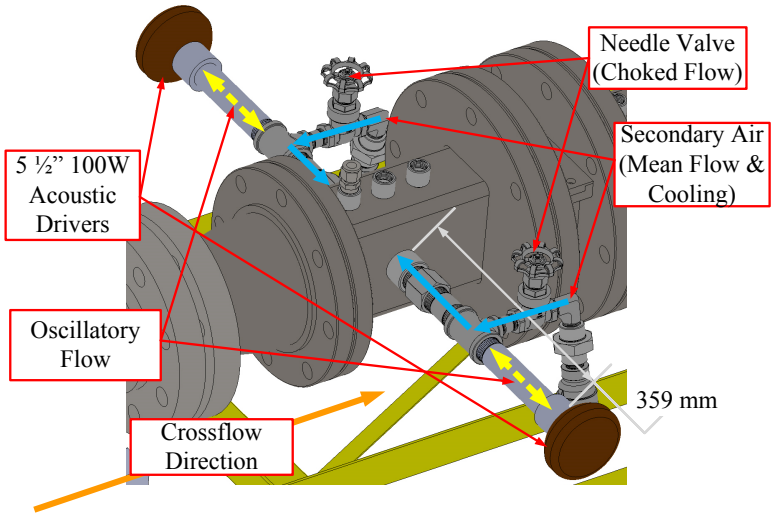

Figure 2.7: Diagram of the acoustic forcing setup

This study considers only sinusoidal excitation and focuses on low frequency acoustic waves (100Hz $\leq f_F \leq$ 500Hz). This frequency range is representative of the longitudinal modes found in staged-fuel combustion systems. Selecting excitation frequencies is slightly more complicated since the reacting JICF facility has its own natural acoustic modes, which vary in amplitude and frequency depending on the vitiator equivalence ratio and the secondary air flow rate. To mitigate the variability in the natural acoustic modes, a single

vitiated crossflow condition is used for all the experiments reported in this thesis. Additional details on the crossflow and jet conditions are presented below in Section 2.2. The sound pressure level (SPL) of the natural (unforced) acoustics inside the flow conditioning section with the vitiator operating are shown in Figure 2.8a. The natural modes are broad and relatively closely spaced. This result motivates the decision in the present work to force the facility at the natural mode frequencies rather than in between the natural modes. There are two advantages associated with this choice. First, forcing at a natural mode frequency provides the greatest possible frequency separation between the forcing frequency and the other natural mode frequencies present in the facility. Secondly, and more importantly, the strong response of the facility at these frequencies enables a wide range of crossflow excitation amplitudes.

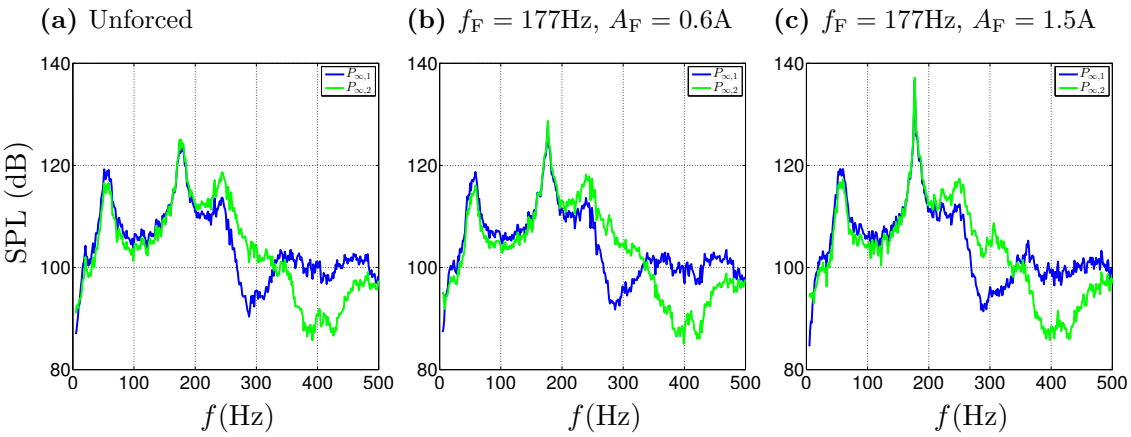

Figure 2.8: Sound pressure levels ($P_{\text{ref}} = 20\,\mu$Pa) measured in the flow conditioning section with no forcing, low-amplitude forcing, and high-amplitude forcing. $P_{\infty,1}$ and $P_{\infty,2}$ correspond to the pressure signals measured by the upstream and downstream pressure transducers, respectively, located in the flow conditioning section (see Figure 2.4).

Accordingly, forcing frequencies $f_F = 177$Hz, 250Hz, and 340Hz were used throughout this study. Note that the first longitudinal mode of the facility ($f \approx 52$Hz) is intentionally neglected since the speakers do not function well at this low frequency. A signal generator (Agilent 33120A) and a linear power amplifier (AE Techron LVC608) operating in constant current mode were used to drive the speakers. The amplitude of excitation at each frequency was varied by adjusting the driving current, which generally ranged from 0.6A to 1.5A. The lowest excitation level corresponded to a $\approx 50\%$ increase in the crossflow acoustic pressure

amplitude at the driving frequency, p'_{∞}, and the highest excitation level provided roughly an order of magnitude increase in the acoustic pressure at the excitation frequency. Examples of low amplitude and high amplitude forcing cases are shown in Figures 2.8b and 2.8c, respectively.

2.2 Design of Experiments

This section describes the experimental design and methods used to investigate the research questions identified in Section 1.7. The experiments conducted in this study can be broadly classified into four types of JICF experiments: unforced non-reacting studies, unforced reacting studies, forced non-reacting studies, and forced reacting studies. The key factor differentiating all of these studies from the many JICF studies reported in the literature is the turbulent vitiated crossflow. A complete test matrix is provided in Table 2.3, where test cases corresponding to each of the four types of experiments are denoted by a different color. Note that non-reacting cases are denoted by "NR," and reacting cases are denoted by "R." At each test condition the velocity field was interrogated using time-resolved SPIV measurements, and the acoustic field was monitored using dynamic pressure measurements. Simultaneous OH-PLIF reaction zone imaging was used to study the flame dynamics in the reacting cases.

J and S are the primary JICF parameters varied in Table 2.3. In general, J and S can be varied either by adjusting the crossflow, adjusting the jet, or adjusting both the jet and the crossflow simultaneously. The choice has subtle but important consequences. In particular, adjusting the jet to effect a change in J and/or S also affects Re_{j}. Similarly, altering the crossflow will lead to a change in Re_{∞}. The natural choice in a standard wind-tunnel facility is to fix Re_{j} and use the tunnel to vary J by increasing or decreasing U_{∞}. This choice has the primary advantage of fixing the jet exit velocity profile, which in turn fixes the momentum thickness of the jet, $\theta_{\mathrm{j}}/d_{\mathrm{j}}$. There are two problems with this approach in a vitiated facility. First, arbitrarily varying the crossflow velocity requires arbitrarily varying the mass flow rate of the vitiator. This is not possible because the vitiator cannot operate stably at either very low or very high flow rates. Furthermore, as mentioned earlier in the acoustic forcing

discussion, varying the crossflow condition alters the natural acoustics of the facility, which is clearly undesirable. Thus, in these experiments, a single crossflow condition is specified, while the jet velocity and jet density are varied to cover a range of J and S values.

Fluid dynamic and thermodynamic properties of the nominal crossflow condition used throughout this thesis are given in Table 2.1. The values for U_∞ and T_∞ are characteristic of the secondary reaction zone in a staged-fuel combustion system. The crossflow is fully turbulent based on the mean Reynolds number, and the speed of sound is roughly double that of room temperature air. The major chemical species in the crossflow are O_2, N_2, CO_2, and H_2O. The O_2 concentration is slightly more than half that of air. OH is a minor species in the crossflow, but its concentration is obviously significant for the OH-PLIF studies. Note that this concentration is about 0.15% of the super-equilibrium OH concentration found in a stoichiometric H_2-air flame at atmospheric conditions.

Table 2.1: Nominal properties of the vitiated crossflow. Calculations were performed using Chemkin. Vitiator products are assumed to reach equilibrium and dilution air mixing is treated as an adiabatic process.

Fluid Dynamic Properties	
$\dot{m}_{\text{vitiator,fuel}}$	1.103 g/s
$\dot{m}_{\text{vitiator,air}}$	41.96 g/s
$\dot{m}_{\text{secondary,air}}$	10.23 g/s
U_∞	19.1 m/s
Re_∞	11070
Thermodynamic Properties	
MW	28.38 kg/kmol
ρ_∞	0.288 kg/m^3
μ_∞	4.738E−5 kg/m · s
T_∞	1200 K
c_∞	677.5 m/s
Chemical composition	
x_{O_2}	0.1291
x_{N_2}	0.7611
x_{CO_2}	0.0366
x_{H_2O}	0.0732
x_{OH}	1.9629E−5

The effect of near-field heat release on the jet dynamics is investigated by considering non-reacting and reacting test conditions with identical J and S . In particular, cases 1, 9, 17, 24, 31, and 38 (see Table 2.3) are utilized for this purpose. These are all unforced test

conditions with J values of either 5 or 25. The presence/absence of heat release in the jet is controlled simply by the presence/absence of fuel in the jet. Note that the temperature of the vitated crossflow, approximately $T_\infty = 1200$K in all the experiments reported here, exceeds the autoignition threshold and thus does not require an external ignition source to initiate chemical reactions. The non-reacting jets consist of a mixture of N_2 and He, while the reacting jets also contain H_2. The mole fraction of H_2 in all reacting jet experiments is held fixed at 70%. The concentration of N_2 relative to He is adjusted in each case such that the overall density ratio remains fixed at $S = 1.00$. Details of the jet composition are given in Table 2.2. The jet supply system is actively cooled using forced convection to maintain the temperature of the jet fluid at approximately $T_\mathrm{j} = 300$K in all the experiments. H_2 was selected as the jet fuel due to its relevance for practical applications, low molecular weight (i.e., ability to reach low S), and because its fast kinetics promote flame stabilization in the near-field. H_2 chemistry is also much simpler and better understood than that of typical hydrocarbon fuels, which enables the possibility of comparing the present experimental results with reactive DNS studies [53, 54].

Table 2.2: Jet composition (by volume) corresponding to test conditions given in Table 2.3

Case	NR/R	x_{H_2}	x_{N_2}	x_{He}
$1 \rightarrow 16$	R	0.7000	0.0087	0.2913
$17 \rightarrow 30$	R	0.7000	0.1849	0.1151
$31 \rightarrow 42$	NR	0.0000	0.1270	0.8730

The second major research objective for this work focuses on the response of a jet injected into an acoustically excited crossflow. This topic is explored in both non-reacting and reacting jets. Test conditions for forced non-reacting and forced reacting jets are shown in Table 2.3 in blue and orange, respectively. Both the forcing frequency, f_F, and the excitation amplitude, A_F, are varied in these studies. The six unforced test conditions, shown in green and yellow in Table 2.3, provide a baseline for comparison. It is worth noting that the term "unforced" does not mean a "steady crossflow." The natural acoustics of the facility, although substantially lower in amplitude than any of the forced studies, are still present. The jet response to applied crossflow forcing is studied in greater depth for the

low S jets. This choice is driven by practical limitations on the size of the test matrix and the greater applicability of low S jets in staged-fuel devices, where low molecular weight fuels such as H_2, syngas, and CH_4 are more common. $S = 0.40$ jets were studied with momentum flux ratios of $J = 5$ and $J = 25$ at seven different combinations of forcing frequencies and excitation amplitudes. Jets with density ratio approximately $S = 1.00$ were considered at three different combinations of forcing frequencies and excitation amplitudes.

The choice of J and S in both the forced and unforced experiments is motivated by the previously observed change in the hydrodynamic stability of non-reacting JICF as a function of those two parameters. Recent experimental [7, 9] and computational [43, 44] studies suggest that the windward shear layer of jets with J less than approximately 10 or S less than roughly 0.50 transition from convective to global instability. The present study is believed to be the first attempt to systematically vary these hydrodynamic parameters in a reacting JICF. The high J cases ($J = 25$) described in Table 2.3 lie in the convectively unstable parameter space, while the low J cases ($J = 5$) are in the globally unstable parameter space. Similarly, based on previous non-reacting studies, the iso-density cases ($S = 1.00$) in Table 2.3 are expected to be convectively unstable, while global instability is anticipated in the low S cases ($S = 0.40$). The vitiated crossflow plays an important role in these investigations because it allows for near-field heat release. Near-field heat release introduces strong density gradients into the high shear region of the flow and alters the mean velocity profile. Both of these effects are known to substantially alter the stability of reacting wakes [20, 80]. The stability of reacting jets injected into low temperature air crossflows is less interesting because flame stabilization occurs far from the windward shear layer in those cases and thus is less likely to substantially alter the stability of the jet.

The fixed crossflow condition in the present experiments complicates the design of the parameter study slightly. In particular, changes in J and S affect Re_j and θ_j/d_j, which can have a large impact on the shear layer dynamics. The work by Megerian et al. [7], however, found no significant difference in the shear layer stability for transitional jets with $Re_j = 2000$ or $Re_j = 3000$. Accordingly, the crossflow in the present experiments was selected such that the low J test conditions had Re_j in this range, with the unity S cases

having about a 20% larger Re_{j} than their low S counterparts. Re_{j} in the $J = 25$ jets is larger by a factor of $\sqrt{5}$. Both the low J and high J jets are laminar when they enter the test section and then become turbulent under the influence of the crossflow.

Table 2.3: Key JICF parameters for each test case. ■ : Unforced, non-reacting experiment. ■ : Forced, non-reacting experiment. ■ : Unforced, reacting experiment. ■ : Forced, reacting experiment.

Case	R/NR	J	S	Re_j	Re_∞	T_∞ [K]	f_F [Hz]	A_F [A]
1	R	5.05	0.41	1980	10520	1241	0	0.0
2	R	4.72	0.40	1990	11500	1186	177	0.6
3	R	4.69	0.40	1980	11480	1187	177	1.2
4	R	4.84	0.41	1980	10970	1218	177	1.5
5	R	4.83	0.41	1980	11060	1211	250	0.9
6	R	4.78	0.40	1990	11280	1203	250	1.5
7	R	4.60	0.39	1990	11770	1179	340	0.6
8	R	4.67	0.40	1980	11490	1191	340	1.5
9	R	23.23	0.40	4420	11480	1191	0	0.0
10	R	22.40	0.40	4400	11780	1179	177	0.6
11	R	25.19	0.42	4400	10420	1247	177	1.2
12	R	23.59	0.41	4380	11200	1203	177	1.5
13	R	23.75	0.40	4400	11150	1206	250	0.9
14	R	23.89	0.40	4400	11230	1199	250	1.5
15	R	23.38	0.40	4400	11430	1192	340	0.6
16	R	23.67	0.40	4400	11330	1197	340	1.5
17	R	5.08	1.04	2590	10660	1236	0	0.0
18	n/a	n/a	n/a	n/a	n/a	n/a	n/a	n/a
19	R	4.64	0.97	2590	11900	1171	177	1.5
20	R	4.68	1.00	2560	11490	1189	250	0.9
21	R	4.63	0.98	2550	11680	1178	250	1.5
22	n/a	n/a	n/a	n/a	n/a	n/a	n/a	n/a
23	R	4.97	1.02	2550	10810	1219	340	1.5
24	R	25.32	1.04	5750	10610	1236	0	0.0
25	n/a	n/a	n/a	n/a	n/a	n/a	n/a	n/a
26	R	23.49	1.01	5700	11350	1196	177	1.5
27	R	23.77	1.02	5720	11220	1203	250	0.9
28	R	24.44	0.99	5760	11310	1190	250	1.5
29	n/a	n/a	n/a	n/a	n/a	n/a	n/a	n/a
30	R	23.38	1.00	5740	11510	1192	340	1.5
31	R	4.74	1.00	1920	11460	1186	0	0.0
32	n/a	n/a	n/a	n/a	n/a	n/a	n/a	n/a
33	n/a	n/a	n/a	n/a	n/a	n/a	n/a	n/a
34	NR	5.02	1.03	1910	10600	1237	250	0.9
35	NR	4.82	1.00	1920	11230	1206	250	1.5
36	n/a	n/a	n/a	n/a	n/a	n/a	n/a	n/a
37	n/a	n/a	n/a	n/a	n/a	n/a	n/a	n/a
38	NR	25.14	1.03	4270	10680	1226	0	0.0
39	n/a	n/a	n/a	n/a	n/a	n/a	n/a	n/a
40	n/a	n/a	n/a	n/a	n/a	n/a	n/a	n/a
41	NR	23.08	0.98	4310	11880	1169	250	0.9
42	NR	24.24	1.02	4290	11060	1215	250	1.5
43	n/a	n/a	n/a	n/a	n/a	n/a	n/a	n/a
44	n/a	n/a	n/a	n/a	n/a	n/a	n/a	n/a

2.3 Diagnostics and Measurement Techniques

2.3.1 Stereoscopic Particle Image Velocimetry

A high-speed stereoscopic particle image velocimetry (SPIV) system was used to characterize the velocity field in the $x - y$ centerplane. Illumination for the SPIV system was provided by a dual head, frequency doubled Nd:YLF laser (Litron LDY303-HE) operated at 10kHz, with measured pulse energy of about 2mJ. The laser beam was expanded, collimated, formed into a $\sim$ 1mm thick sheet, and guided into the test section using a series of mirrors and converging/diverging lenses (Lattice Electro Optics) suspended above the test section (see Figure 2.9). The laser sheet was aligned with the jet centerplane using a pin-located jig, shown in Figure 2.10a, containing two vertical 0.50 mm slits spaced 100mm apart in the y-direction. The laser pulse separation was adjusted based on the jet and crossflow velocity for each test condition in order to achieve a nominal particle displacement of 8 pixels, which yielded pulse separation times in the range $5.0\mu\text{s} \leq \Delta t_{\text{SPIV}} \leq 17.0\mu\text{s}$. The pulse separation was recorded during each experiment using an oscilliscope.

SPIV images were captured by two Photron SA5 cameras mounted in a side-scatter configuration. The cameras were each positioned at an angle of approximately 30° relative to the jet centerplane normal coordinate ($z - axis$). Each camera was equipped with a 105mm focal length Tokina macro lens at $f/8$ mounted on Scheimpflug adapters (LaVision) and viewed the test section through a narrow band interference filter (Semrock Brightline 527/20). Standard corrections for perspective and distortion were made using a 3D dot target (LaVision 058-5). The 3D dot target was positioned inside the test section using a custom-made, pin-located jig as illustrated in Figure 2.10b. The absolute positioning of the calibration plate relative to the jet injector was accurate to within $\pm$0.25mm. The camera resolution was 512 x 512 and the viewable area was approximately 45mm square. About 11000 double-framed images were recorded at each test condition, which equated to $\sim$ 1.1s.

Both the crossflow and the jet were seeded with Dupont R-960 TiO_2 particles, which have a mean particle diameter of 0.50μm. The crossflow seeding system consisted of a passively agitated swirling seeder operated with about 2g/s of air flow, which was diverted from the metered secondary dilution air as discussed previously. The seeded crossflow air was injected

through the dilution air ports shown in Fig.2.4. The jet flow was seeded approximately 2m upstream of the jet injection location using a small, custom-made surface spray type seeder. The seeding density of both the crossflow and the jet were manually balanced to achieve optimal seeding levels. The best velocity measurements were obtained by slightly over-seeding the jet fluid relative to the crossflow so that sufficient particle density was still present in jet wake after combustion occurred.

Velocity vectors were computed using LaVision DaVis 8.1.6 software with multi-pass processing and adaptive interrogation windows. Before processing the vector fields, the raw Mie scattering images were digitally masked below $y/d_{\mathrm{j}} = 0$ to reduce the quantity of spurious vectors computed due to strong laser light reflection by the ceramic walls of the test section. Particle intensity normalization with a scale length of 3 pixels was used to reduce the influence of intensity fluctuations in the images. The actual velocity fields were computed using a total of 5 velocity calculation passes, including 2 initial passes using 24 x 24 interrogation windows with 50% overlap and 3 final passes using 16 x 16 interrogation windows with 50% overlap, resulting in final vector spacing of about 0.48mm. Normalized correlation functions were used for all passes, and DaVis' median-filter-based universal outlier detection algorithm was used to remove spurious vectors in between passes on a 3×3 neighborhood. Groups containing less than 5 vectors were also removed in between passes, and a single pass of a 3×3 Gaussian smoothing filter was applied. Finally, any missing vectors were added using interpolation, which was never required for more than 0.1% of the total number of vectors. A representative instantaneous SPIV velocity field is plotted in Figure 2.11. The color contour denotes the velocity magnitude, and two-dimensional streamlines are overlaid in white. The streamlines have been computed using the Matlab® routine *streamslice*, which produces geometrically well-spaced streamlines from vector field data. Although streamlines computed in this manner are useful for flow visualization, it is important to note that they are really two-dimensional pseudo-streamlines since the flow is fully three-dimensional. The velocity field is cropped along the x-direction to match the region illuminated by the laser and vectors below $y/d_{\mathrm{j}} = 0.50$ are not reported due to the large errors associated with reflections off the lower wall of the test section.

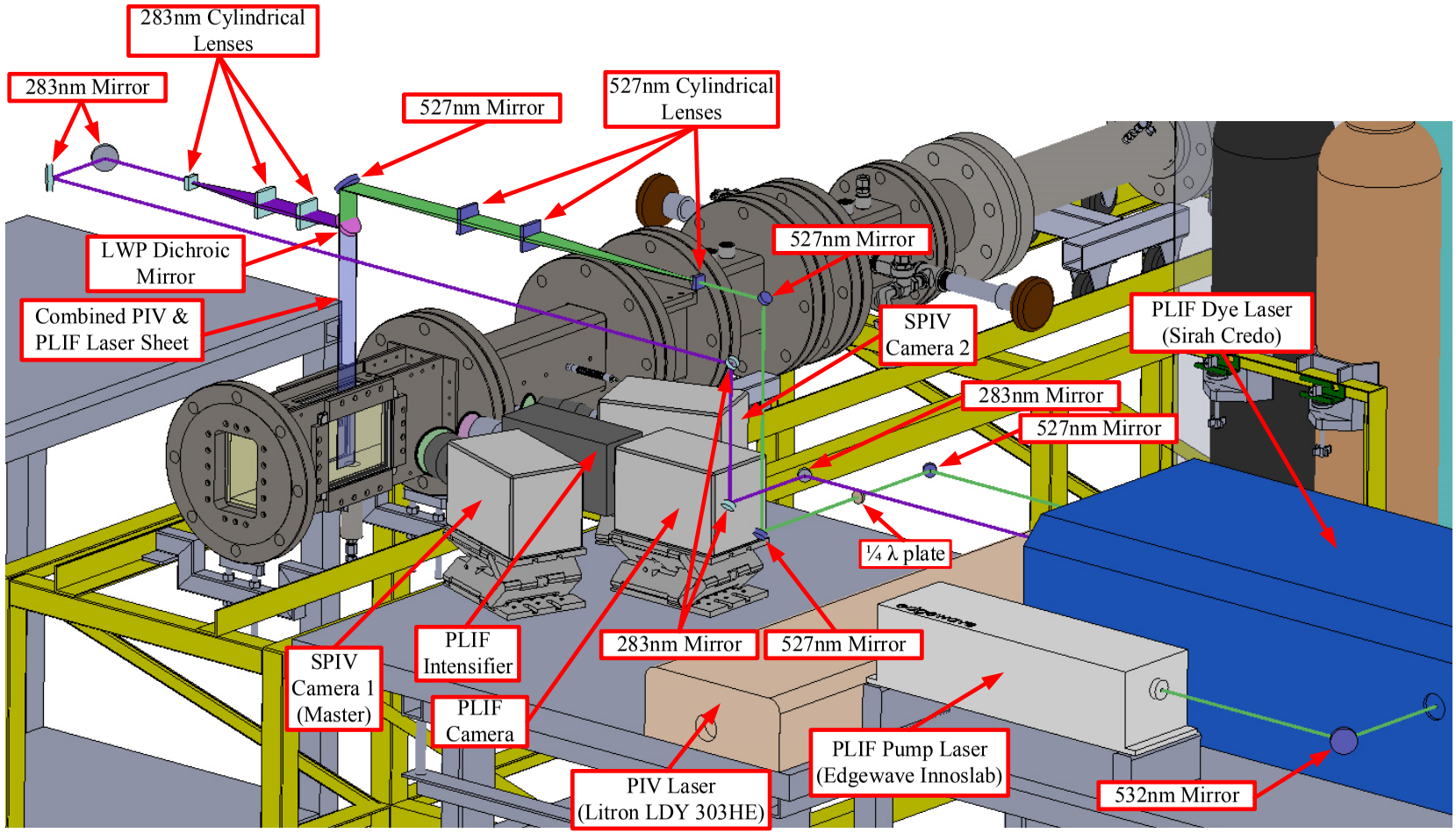

Figure 2.9: Overview of the SPIV and OH PLIF systems.

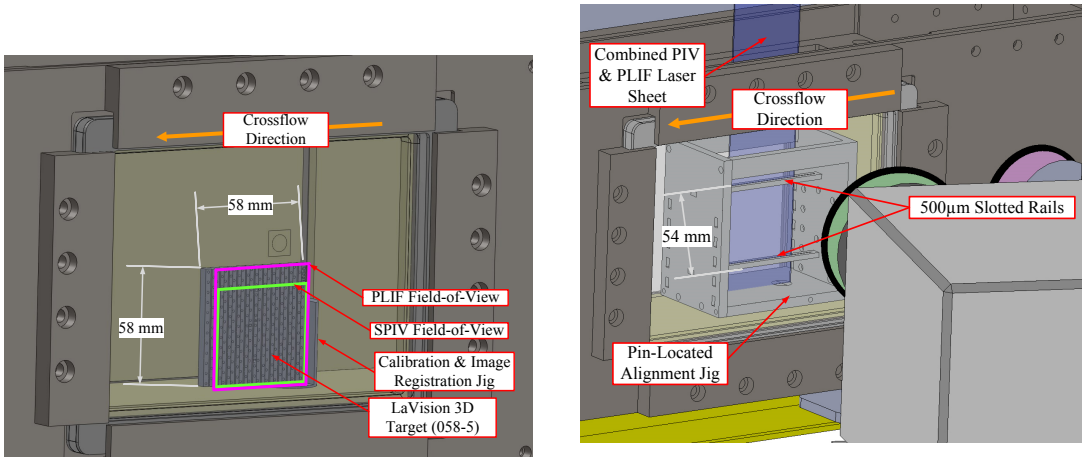

(a) Image calibration jig **(b)** Laser sheet alignment jig

Figure 2.10: Rendering illustrating the hardware used for image calibration and laser sheet alignment.

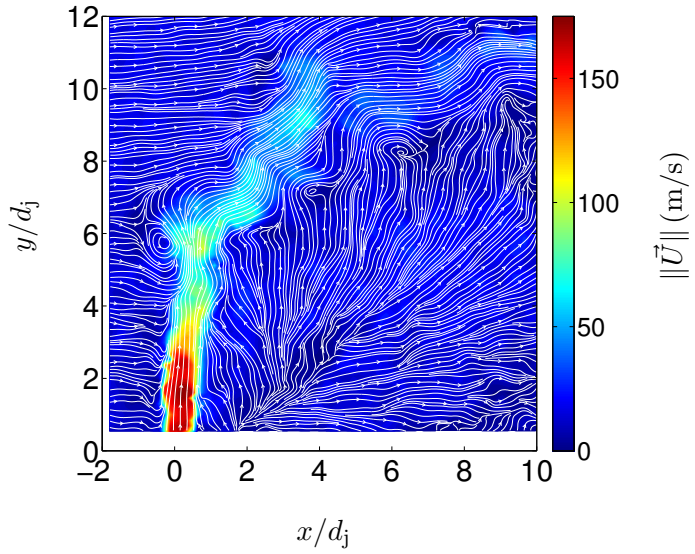

Figure 2.11: Representative instantaneous SPIV velocity field for a $J = 25$, $S = 0.40$ reacting JICF. Color contour represents velocity magnitude and 2D streamlines are shown in white.

2.3.2 Mie Scattering Flow Visualization

The raw Mie scattering images used to compute the SPIV velocity fields can also be used for flow visualization purposes. The data rate and sample size of the Mie scattering data thus exactly correspond to that of the SPIV measurements. More specifically, the Mie scattering flow visualization images presented in this thesis correspond to the intensity image illuminated by the first SPIV laser pulse and recorded by SPIV camera 1. The raw intensity image is corrected for distortion and perspective using the calibration procedure utilized in the SPIV measurements. Two representative Mie scattering images are shown in Figure 2.12.

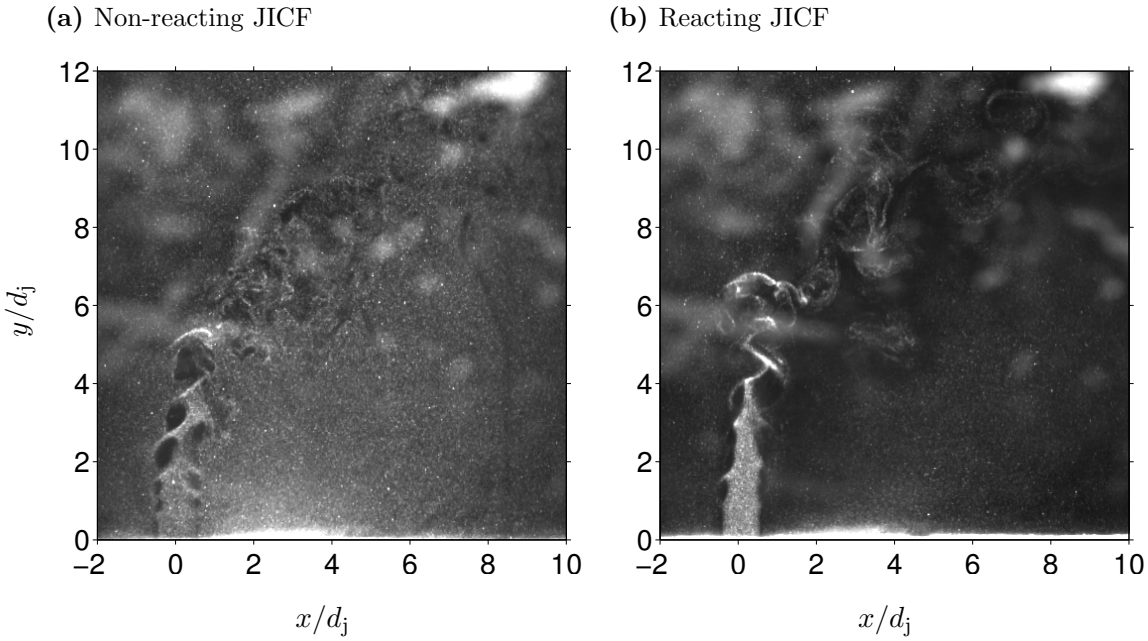

Figure 2.12: Representative instantaneous Mie scattering images for a $J = 25$ JICF with and without heat release. Vitiated crossflow is identical in both cases.

Two interesting observations about the Mie scattering technique can be made using the example images shown in Figure 2.12. First, the particle density (and Mie scattering intensity) is very low in the innermost core of the shear layer vortices. The SPIV particles used in this study are 0.5μm TiO_2 particles. These metal oxide seeding particles are able to survive the 2500K flame temperatures in the present experiments but are also much more dense ($\rho_{TiO_2} \approx 3.9\text{g/cm}^3$) than the gaseous flows being investigated ($\rho_\infty = 2.88\text{E}{-4}\text{g/cm}^3$). Despite the disparity in density, the small size of these particles insures that the frequency

response safely exceeds the Nyquist sampling frequency of the 10kHz SPIV system for all test conditions. The shear layer frequency, however, is approximately $St_{\mathrm{j}} \approx 0.75$, which corresponds to very high frequencies in the range $6.6\mathrm{kHz} \leq f_{\mathrm{M}} \leq 43.1\mathrm{kHz}$ for the present test conditions. The centrifugal forces due to the high frequency shear layer vortices are large, and a significant fraction of the seeding particles are ejected from the vortex cores. This effect is detrimental, of course, in the SPIV measurements but provides a useful vortex tracking capability in the windward shear layer. Features such as the instantaneous shear layer vortex location, size/growth, and pairing are easily discerned from Mie scattering images. The second observation from the Mie scattering images concerns the scattering intensity in the reacted regions of the flow, which is substantially decreased due to the large volumetric dilatation from combustion and the corresponding reduction in local particle seeding density. This effect is particularly apparent in both the windward shear layer and in the jet wake, as illustrated by Figure 2.12b. The Mie scattering images thus provide some insight into the instantaneous temperature field and can be compared with simultaneous OH PLIF images to further characterize the reaction zone dynamics.

2.3.3 Planar Laser Induced Fluorescence

OH PLIF reaction zone imaging is used to study the flame dynamics of reacting JICF. The 10kHz OH PLIF system consisted of a frequency doubled Nd:YAG laser (Edgewave InnoSlab IS811-E) with output power of 40W pumping a tunable dye laser (Sirah Credo LG24). The UV output at approximately 283 nm had pulse width of about 9ns and pulse energy of 0.2mJ. The dye laser wavelength was tuned to the $Q_1(9)$ transition of OH in the $\nu'' = 0$, $\nu' = 1$ band of the $A^2\Sigma^+ - X^2\Pi$ system. The laser beam was expanded and collimated in a parallel optical path analogous to the SPIV beam. The OH-PLIF sheet had a width of approximately 40 mm and was combined with the SPIV laser sheet using a LWP dichroic mirror (Lattice Electro Optics). The dichroic mirror and the sheet forming optics were mounted on linear translation stages to allow precise positioning of the laser sheet within the test section. The OH-PLIF laser sheet was focused to a thickness of approximately 0.4 mm inside the test section.

The fluorescence signal near 310 nm was collected using a Photron SA1.1 camera optically coupled to an image intensifier (Lambert Instruments HiCatt 25) and a 45 mm focal length Cerco $f/1.8$ UV lens. The OH-PLIF camera was located in between the two SPIV cameras and was positioned for a normal viewing angle relative to the jet centerplane. The intensifier was gated to 200ns and the intensifier gain was fixed at 755V in all the experiments. Care was taken to insure that these settings did not cause saturation of the OH PLIF signal. The timing of the camera, intensifier, and lasers were adjusted so that the OH PLIF laser pulse bisected the SPIV laser pulse separation time at each test condition. Background flame luminescence was blocked using a high transmission ($> 80\%$) narrowband interference filter (custom fabrication by Omega Optical Inc.). About 9,700 images were recorded per OH PLIF data set and the image resolution was 768 x 768 pixels. The viewable area was slightly larger than that of the SPIV measurements and resulted in a spatial resolution of about 0.081mm. Thus, the thickness of the laser sheet, $\approx$ 0.4mm, limited the effective spatial resolution, particularly in the wake of the jet where the flame is less likely to be aligned perpendicularly relative to the laser sheet.

Standard corrections for perspective and distortion errors were applied using the same 3D dot target and alignment jig discussed previously. A total of 200 calibration/image registration images was acquired prior to each test campaign with the intensifier operating at 100Hz, gain set to 755V, and the gating set to 100μs. Variations in the laser sheet intensity along the x-direction where corrected using an acetone imaging calibration procedure. The jet nozzle was replaced with a plug nozzle and the back-end of the test section was sealed to perform this procedure. After sealing the test section, roughly 150mL of acetone was sprinkled along the lower wall of the test section and allowed to evaporate. A sequence of 2000 PLIF images was acquired once the test section was uniformly filled with evaporated acetone. The intensifier and gain settings were identical to those used in the OH PLIF studies. The images were temporally averaged and cropped to remove the regions outside the laser sheet. The averaged image (shown in Figure 2.13a) was integrated along the vertical direction, and the resulting intensity profile was normalized to 1. This profile, shown in Figure 2.13b, was replicated along the vertical direction to create an acetone correction grid,

such that each raw OH PLIF image could be corrected for axial sheet variation simply by dividing the raw image by the acetone correction grid. Note that regions on the periphery of the acetone correction grid where laser sheet intensity was less than 15% of the maximum are set to 1 so that no correction is applied in those regions. The final OH PLIF images were also corrected for background OH level in the vitiated crossflow by subtracting the average OH PLIF signal obtained when the vitiator was operating without a jet. This correction was not particularly important, however, since very low (< 5 counts) OH PLIF signal was seen when the jet was off. This is consistent with the fact that the equilibrium OH mole fraction in the crossflow is $\mathcal{O}(10^{-3})$ smaller than the super-equilibrium OH levels in a stoichiometric H_2-Air flame.

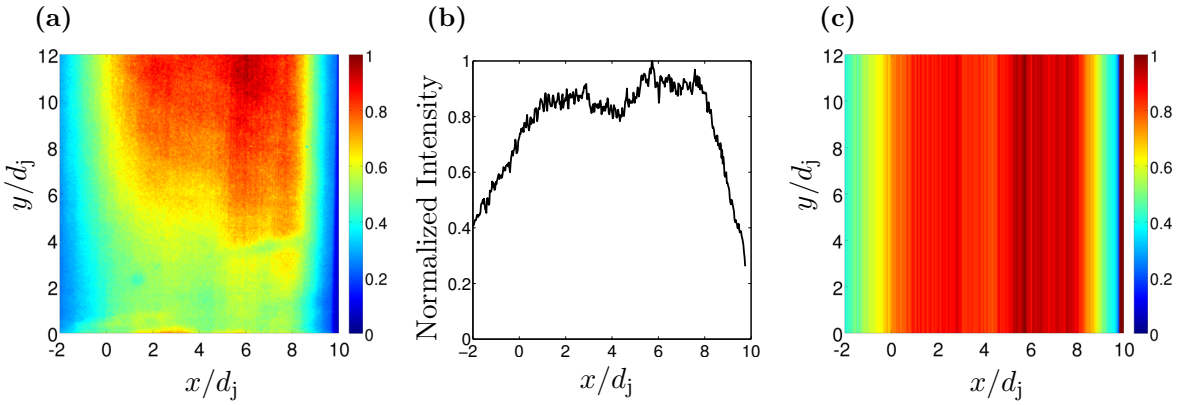

Figure 2.13: Images illustrating the steps used in the acetone correction procedure. (a): Average acetone image, (b): Vertically integrated and normalized average acetone profile, (c): Final applied acetone correction image.

Representative raw (uncorrected) and final (corrected) instantaneous OH PLIF images are shown in Figure 2.14. Note that the OH PLIF signal in these images cannot not be directly interpreted as a flame marker although it does provide much useful information about the flame structure and dynamics. Special care is required to interpret differences in the mean OH PLIF signal. The OH PLIF level is an indication of where high concentrations of hot OH exist. The OH PLIF signal increases with local temperature and concentration [81]. Super-equilibrium levels of OH occur inside the flame, but OH is also an equilibrium product of H_2 combustion. Similarly, the temperature of the mixture is highest in the flame

zone, but the temperature is also high in regions containing high concentrations of combustion products. Flame temperature depends on mixture composition, but fortunately the adiabatic flame temperature varies by less than 25K for stoichiometric mixtures of jet and crossflow fluid for the $S = 0.40$ and $S = 1.00$ cases considered here. Also note that the maximum temperature of a non-premixed flamelet decreases with increasing local scalar dissipation(CITE), which also has a strong influence on both the thickness of a non-premixed flamelet. Sharp gradients between regions with no OH PLIF signal and regions with high OH PLIF signal, as seen along the windward edge of the jet in Figure 2.14, can only be caused by a flame front. In addition to the influence of OH concentration and local temperature, the OH PLIF signal is also sensitive to shot-to-shot variation in laser intensity, laser sheet extinction along its propagation direction, and absorption and scattering of the PLIF signal. These additional complexities do not cause a problem in the present experiments since the objective is not to obtain quantitative OH concentration measurements but rather understand the dynamics of the reaction zone, which is well described by the spatio-temportal evolution of the OH PLIF signal.

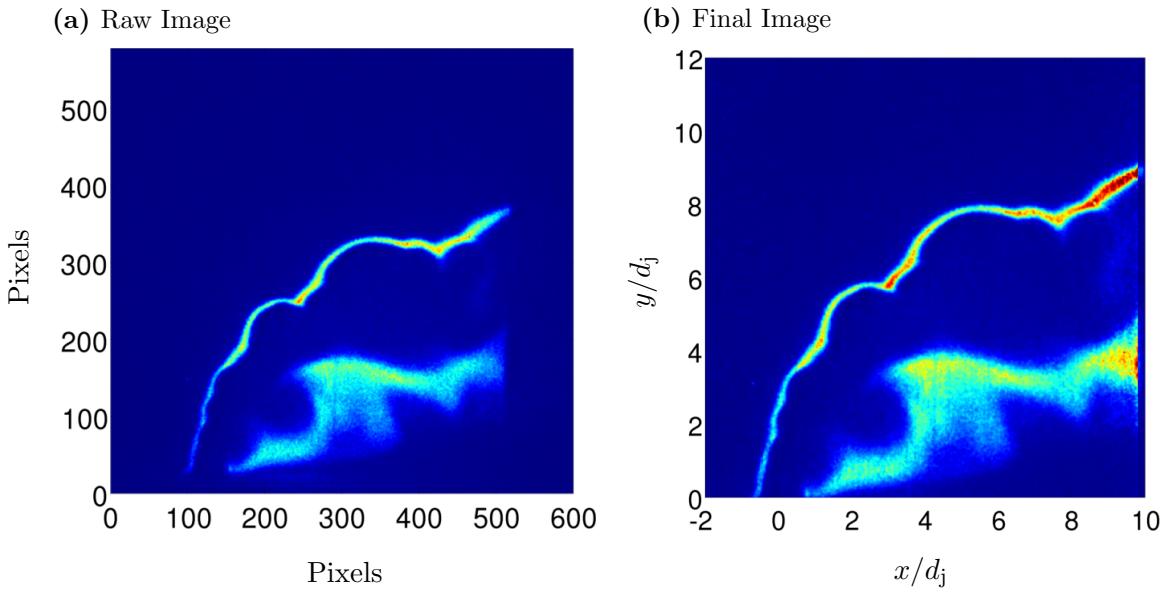

Figure 2.14: Representative instantaneous OH PLIF images obtained from the reacting JICF facility.

2.3.4 Dynamic Pressure Measurements

Dynamic pressure measurements were performed in order to characterize the acoustic field in the test section of the reacting JICF facility. A pair of Kistler 211B5 pressure transducers, referred to as $P_{\infty,1}$ and $P_{\infty,2}$, were located just upstream of the test section as shown in Figure 2.15. The sensors were installed on standoff tubes to prevent damage due to heat transfer from the high temperature crossflow. The standoff tubes were flush-mounted on the sidewall of the facility and were actively cooled using compressed air. The total length of the standoff tubes was 99.2mm and the inner diameter was 5.6mm. The geometry of the standoff tubes was selected to assure that the first resonance of the standoff tube ($\approx$ 1000Hz) was more than twice the highest frequency of interest in the present study. An additional pressure transducer, which will be referred to as P_{j}, was located $20d_{\mathrm{j}}$ upstream of the jet injector in the jet supply plenum, as shown in Figure 2.5. The jet sensor was flush-mounted directly in the sidewall of the supply plenum since the jet fluid was not heated.

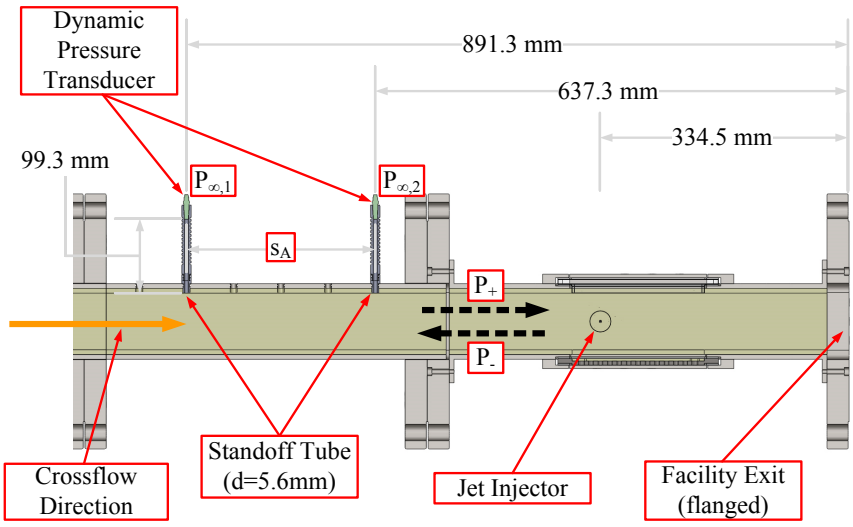

Figure 2.15: Schematic detailing the setup used to characterize the crossflow acoustics of the reacting JICF facility.

The raw piezotron transducer signals were amplified and conditioned using a Kistler model 5010 amplifier. Each signal was low-pass filtered at $f = 5$kHz using a 4^{th} order Butterworth filter implemented on a 4-channel Krohn 3364 analog filter. The output signal was digitized and stored at 20kHz using a National Instruments 9215 analog input module

and a cDaq-9174 system. A little more than 8 seconds worth of acoustic data was recorded during each test.

The pressure measurements were used to estimate the sound pressure level in the test section and compute the standing wave mode shapes in the facility. Sound pressure levels were estimated using Welch's method [82] to compute the power spectral density of each recorded pressure signal with 20 ensembles and 50% overlap of the windowed time series, yielding a frequency resolution of about 1Hz. The two-microphone method [83, 84] was used to compute the mode shapes based on crossflow pressure measurements at sensor locations $P_{\infty,1}$ and $P_{\infty,2}$, which were separated by a distance $s_\mathrm{A} = 254\mathrm{mm}$. For the frequencies of interest in the present work, this distance lies within the recommended range $0.1\pi \leq 2\pi f s_\mathrm{A}/(c_\infty \pm U_\infty) \leq 0.8\pi$ determined by Bodén & Åbom [85]. Note that the effect of the mean crossflow velocity, U_∞, has been considered in the analysis that follows.

The acoustic field is decomposed into right and left traveling acoustic waves. Thus, the Fourier transform of the pressure, $\check{p}(x_\mathrm{A}, f)$, in the test section is given by

$$\check{p}(x_\mathrm{A}, f) = a\exp(ik_\mathrm{A}^+ x_\mathrm{A}) + b\exp(-ik_\mathrm{A}^- x_\mathrm{A}) \tag{2.1}$$

where x_A is the axial distance measured in the crossflow direction from the location of $P_{\infty,1}$, which is taken as the origin of the coordinate system (i.e., $x_\mathrm{A} = 0$). a and b are complex coefficients, and the longitudinal acoustic wavenumbers, k_A^+ and k_A^-, for acoustic waves traveling in the positive and negative directions, respectively, are defined in terms of the mean crossflow velocity, U_∞, as

$$k_\mathrm{A}^+ = \frac{2\pi f}{c_\infty + U_\infty} \qquad k_\mathrm{A}^- = \frac{2\pi f}{c_\infty - U_\infty} \tag{2.2}$$

where c_∞ is the speed of sound in the vitiated crossflow. It is important to note that the cutoff frequency of the duct based on the height of the test section is $f_\mathrm{c} = 2665\mathrm{Hz}$, indicating that only longitudinal acoustic waves propagate at the low frequencies of interest in the present experiments (i.e., $f \leq 500\mathrm{Hz}$). The Fourier transforms of the pressure

measurements $P_{\infty,1}$ and $P_{\infty,2}$ can be expressed using Equation (2.1) as

$$\check{P}_{\infty,1}(f) = a + b \tag{2.3a}$$

$$\check{P}_{\infty,2}(f) = a\exp(ik_{\mathrm{A}}^{+}s_{\mathrm{A}}) + b\exp(-ik_{\mathrm{A}}^{-}s_{\mathrm{A}}) \tag{2.3b}$$

Thus, the reflection coefficient at $x_{\mathrm{A}} = 0$ can be defined as

$$R(x_{\mathrm{A}} = 0, f) = \frac{a}{b} \tag{2.4}$$

and the ratio of the Fourier transforms of the pressure measurements $P_{\infty,1}$ and $P_{\infty,2}$ is expressed as a transfer function, $H_{s_{\mathrm{A}}}$,

$$H_{s_{\mathrm{A}}} = \frac{\check{P}_{\infty,1}(f)}{\check{P}_{\infty,2}(f)} = \frac{a+b}{a\exp(ik_{\mathrm{A}}^{+}s_{\mathrm{A}}) + b\exp(-ik_{\mathrm{A}}^{-}s_{\mathrm{A}})} \tag{2.5}$$

Rearranging equation (2.5) yields an expression for R in terms of measured quantities,

$$R(x_{\mathrm{A}} = 0, f) = \frac{1 - H_{s_{\mathrm{A}}}\exp(-ik_{\mathrm{A}}^{-}s_{\mathrm{A}})}{H_{s_{\mathrm{A}}}\exp(ik_{\mathrm{A}}^{+}s_{\mathrm{A}}) - 1}. \tag{2.6}$$

Finally, the unknown coefficients, a and b, which fully-determine the standing wave mode shape, are calculated by combining Equations (2.4), (2.6), and (2.3a).

The accuracy of this method is sensitive, however, to the amplitude and phase response of both pressure transducers. Accordingly, both sensors were calibrated over the frequency range 150Hz $\leq f \leq$ 1000Hz beforehand using an impedance tube. Each of the pressure transducers was flush-mounted on a flange at one end of an impedance tube and an acoustic driver was mounted at the opposite end. The acoustic driver was excited with a sinusoidal chirp signal and the response of each sensor was recorded. The upstream pressure sensor, $P_{\infty,1}$, was taken as the reference sensor and the amplitude and phase of $P_{\infty,2}$ was corrected following the approach outlined by Seybert & Ross [83].

$$\check{P}_{\infty,1} = \check{P}_{\infty,1,\mathrm{raw}} \qquad \check{P}_{\infty,2} = \check{P}_{\infty,2,\mathrm{raw}}/H_{12} \qquad \check{P}_{\mathrm{j}} = \check{P}_{\mathrm{j,raw}}/H_{1\mathrm{j}} \tag{2.7}$$

The measured frequency response functions, $H_{1\mathrm{x}}$, used in Equation (2.7) are shown in Figure 2.16. Although it is not used in the two microphone method, the jet pressure transducer, P_{j}, was also calibrated relative to $P_{\infty,1}$ for consistency.

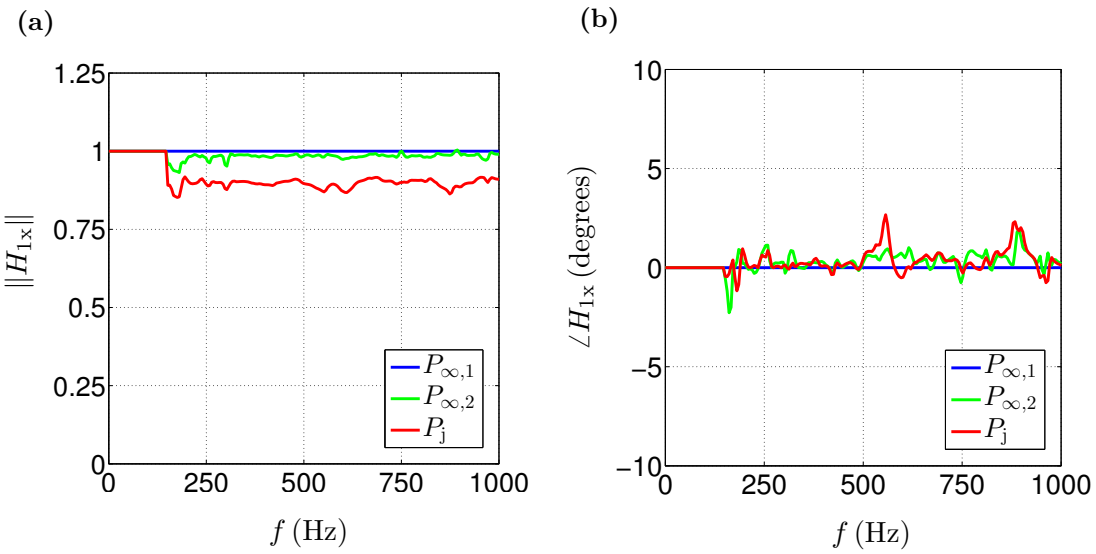

Figure 2.16: Frequency response function, H_{1x}, used to calibrate each sensor relative to reference sensor $P_{\infty,1}$. (a): Magnitude, (b): Phase angle.

2.3.5 Timing and Synchronization

This section briefly describes the timing and synchronization protocol used to control the various diagnostics discussed previously in this chapter. In all the experiments, SPIV camera 1 served as the system master clock and generated a 20kHz sync signal. SPIV camera 2 was operated in slave mode and was synced using the master clock signal output from SPIV camera 1. The master clock signal was also supplied to a Berkeley Nucleonics Corp. 575-8C timing unit. The timing unit's divide-by-N capability was used to downsample the master clock signal to 10kHz, which was the data acquisition rate for both the SPIV and the PLIF measurements. The 10kHz clock signal was replicated and appropriately time-shifted using five BNC 575-8C channels in order to control the PLIF camera, the PLIF intensifier, the Q-switches for both heads of the SPIV laser, and the PLIF pump laser Q-switch. The two channels controlling the SPIV laser Q-switches were adjusted in order to achieve the desired Δt_{SPIV}. The PLIF laser Q-switch timing was adjusted such that the PLIF pulse bisected the two frames of the SPIV system. The 200ns PLIF intensifier pulse was configured to straddle the PLIF laser pulse. The channel used to control the PLIF intensifier was gated using the "Record Positive" signal output from the PLIF camera to force the intensifier to fire only during image acquisition. A push-button TTL pulse generator connected to SPIV camera 1

was used to trigger the "Record Positive" signal once the desired test condition was achieved and the SPIV seeding levels were optimized, which then initiated the entire data acquisition sequence. The setup allowed the SPIV laser, the SPIV cameras, and the PLIF laser to fire continuously prior to receiving the "Record Positive" signal. This allowed all the lasers to reach a steady operating condition before data acquisition, and enabled careful visual adjustment of both the jet and the crossflow SPIV seeding levels. Both SPIV cameras and the PLIF camera recorded data until they ran out of memory (8Gb), which corresponded to about 1s worth of raw data for each test condition. The Labview-based flow measurements and dynamic pressure measurements were similarly triggered using the "Record Positive" signal output from SPIV camera 2 so that the acquired data was synchronized with the high-speed optical diagnostics.

2.3.6 Hot-Wire Anemometry

Hot-wire anemometry was used to characterize the jet exit velocity in the absence of crossflow. For these measurements, the nozzle was supplied with room temperature air from a compressed gas bottle. A calibrated critical orifice assembly was used to meter the flow, and for consistency with the JICF experiments, a choked orifice was installed just upstream of the jet supply plenum (see Figure 2.5). Two different jet exit velocities were investigated, which corresponded to $Re_{\mathrm{j}} = 2000$ and $Re_{\mathrm{j}} = 5000$. The Reynolds numbers were selected to match the low and high J JICF experiments, respectively.

The hot-wire system was comprised of a single-component Dantec 55P01 probe and a Dantec Dynamics StreamLine 90N10 chassis. The probe was calibrated using a laminar free jet from 0.5m/s to 35m/s. The probe was mounted on a two-axis linear translation stage and positioned at a height $y/d_{\mathrm{j}} = 1$. This allowed for movement in the $x - z$ plane (perpendicular to the jet axis) with accuracy of $\pm 1\mu$m. The sampling frequency was fixed at 30kHz, and the frequency response of the hot-wire system was evaluated using a square wave test for each test condition.

Two different types of measurements were conducted using the hot-wire system. The first set of experiments quantified the mean and fluctuating jet exit velocity profiles for each

Re_j condition. In these experiments, the jet centerline was traversed using 30 points spaced 0.005in ($0.04d_j$) apart. Data was recorded for 10 seconds at each location. The second set of experiments investigated the spectral content of jet. In these experiments, the probe was positioned along the jet centerline, and data was acquired for 80 seconds. This sampling time allowed for 5Hz spectral resolution with 400 individual data records.

2.4 Inlet Conditions and Background Acoustics

JICF are sensitive to the inlet conditions of both the jet and the crossflow. The jet trajectory, the jet/crossflow mixing rate, and the jet shear layer dynamics can change as a result of differences in the jet and crossflow inlet conditions, even when key parameters such as J and S are unchanged. This section presents measurements characterizing the jet and crossflow inlet conditions in this study. The jet was characterized using calibrated hot-wire measurements of the jet exit velocity profile in the absence of crossflow. SPIV was used to study the vitiated crossflow without the influence of the jet. Lastly, dynamic pressure measurements with and without the jet are used to quantify the background acoustics in the facility.

Calibrated hot-wire measurements of an air jet at room temperature issuing into a stagnant ambient environment are used to characterize the jet exit velocity profile. Figure 2.17 presents measurements of the mean velocity, RMS velocity, and centerline velocity spectra for jets with two different Reynolds numbers. The selected Reynolds numbers span the range investigated in this study. The $Re_j = 2000$ hot-wire results correspond to low J JICF test conditions, and the $Re_j = 5000$ hot-wire results correspond to high J JICF test conditions. The mean velocity profiles shown in the top row of Figure 2.17 are nearly symmetric with respect to the jet origin, and the shape of the velocity profiles closely resembles those reported by Megerian et al. [7], which is expected since the nozzle contour in the present work is nearly identical to the one used in that study. The momentum thickness is approximately $\theta_j/d_j = 0.0562$ in the $Re_j = 2000$ case and $\theta_j/d_j = 0.0515$ in the $Re_j = 5000$ case. θ_j/d_j is estimated by integrating the velocity profiles from the jet origin to the radial location where mean velocity drops to 20% of its centerline value.

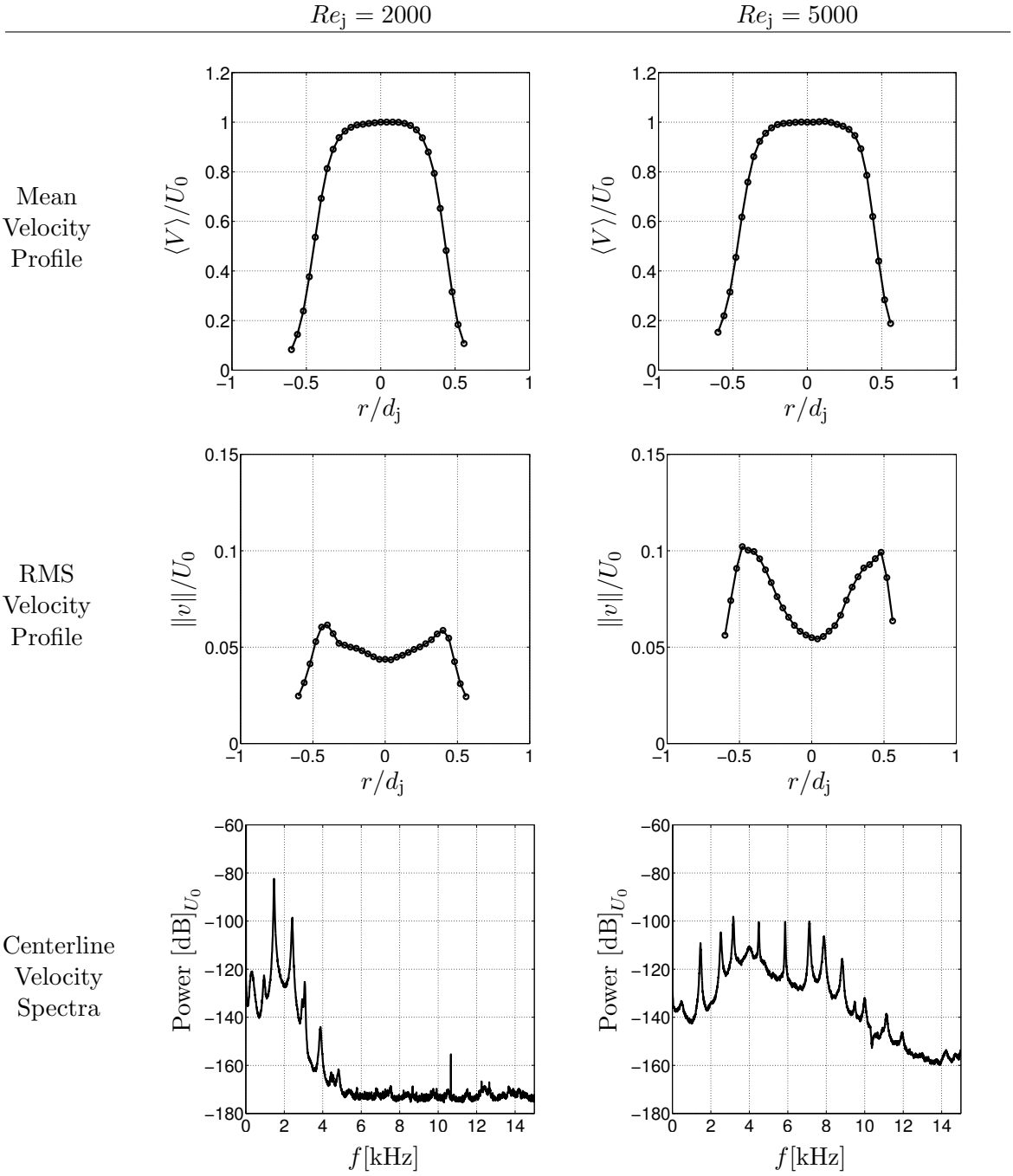

Figure 2.17: Jet exit velocity profiles measured for room temperature air jets in the absence of the crossflow. Measurements performed using a single-component hot-wire anemometer located at $y/d_j = 1$. Reference velocity for decibel scale used in centerline velocity spectra is $V_{ref} = U_0$.

The RMS velocities shown in middle row of Figure 2.17 are higher than those reported by Megerian et al. [7], presumably because the measurements were made at $y/d_j = 1$ in the present study (as opposed to $y/d_j = 0.1$). The RMS velocity in the jet core is close to 5% in the $Re_j = 2000$ case, although slightly lower values are seen along the jet centerline and higher values are found in the shear layers. The RMS velocities are higher in the $Re_j = 5000$ case, and the velocity fluctuations in the shear layer are roughly twice as large as the RMS velocity measured along the jet centerline.

Centerline velocity spectra are presented at the bottom of Figure 2.17 to validate that the jet supply system (see Figure 2.5) does not introduce strong spectral content in the absence of the crossflow that could potentially alter the jet dynamics. The results indicate that no strong resonances are present at the jet exit. The power of the strongest narrow-band features is four to five orders of magnitude smaller than that of the mean flow. The strongest narrow-band peak in the velocity spectrum obtained for the $Re_j = 2000$ case is located at $f \approx 1465$Hz. Higher frequency peaks with much lower amplitude are located at $f \approx 2420$Hz and $f \approx 3060$Hz. These narrow-band peaks are presumably due to the natural acoustic modes of the jet supply plenum, although aeroacoustic sound generation by the choked orifice at the entrance of jet supply plenum (see Figure 2.5) may also be partially responsible. Peaks with nearly identical frequencies appear in the velocity spectrum obtained in the $Re_j = 5000$ case, but the largest amplitude is found at $f \approx 3060$Hz. While very little spectral content is observed beyond $f = 5$kHz in the $Re_j = 2000$ case, the $Re_j = 5000$ case contains low amplitude spectral content out to at least $f = 12$kHz.

The crossflow velocity profile was quantified using SPIV measurements made in the test section while the jet was disabled (see Case 49 in Table 2.3). The vitiator and dilution air flow rates were identical to those used for all the JICF studies. A ceramic plug nozzle was installed in place of the usual jet nozzle for this case to prevent resonant coupling between the jet injector plenum and the unsteady crossflow. The mean crossflow velocity profile is shown in Figure 2.18 and is overlaid by a log law approximation of the velocity profile in fully-developed turbulent channel flow. The measured crossflow velocity profile, $\langle U(y) \rangle$, deviates from the fully-developed velocity profile but the deviation is never more

than 6.2% of the local mean velocity within the field of view of the diagnostic system. The fully-developed axial velocity profile increases more rapidly with y in the near-wall region $y/d_\mathrm{j} \leq 4$, but this trend is reversed further away from the wall where the experimentally measured velocity profile overtakes the log law profile. The $y_+ = 30$ line in Figure 2.18a denotes the lower limit at which the log law is still considered a good estimate of a fully-developed channel flow [86]. The viscous length scale, δ_ν, is approximately 0.15mm. The friction velocity, u_τ, is about 1.11 m/s, and the friction Reynolds number, Re_τ, is 429. The mean experimental velocity profile is quite flat beyond $y/d_\mathrm{j} \sim 6$ and resembles that of a plug flow.

The measured fluctuating velocity field clearly deviates more significantly from the expected values for fully-developed channel flow. In particular, the axial and transverse fluctuating velocity profiles are double-peaked. The peak closest to the wall, near $y_+ = 15$, is only partially-resolved but must exist since the fluctuating velocity is zero at the wall. This near-wall peak in fluctuating velocity is expected in a fully-developed channel flow, but the second, much broader peak, located near $y_+ \sim 80$, is not. Furthermore, the measured fluctuating transverse component, $\langle w^2 \rangle$, is quite large away from the wall. The second peak in the Reynolds stresses corresponds closely with the nearly linear mean velocity profile in the range $1 \leq y/d_\mathrm{j} \leq 6$. There are two plausible explanations for these observations. First, the distance after the last flow conditioning element may be insufficient to achieve fully-developed channel flow in the test section. Alternatively, the crossflow acoustics may be responsible for modifying the fluctuating velocity fields near the wall. In either case, the key objective here is to characterize the crossflow inlet conditions to assure that the data reported in subsequent chapters can be accurately and fairly compared with previous JICF studies in the literature.

The Reynolds stresses shown in Figure 2.18b represent the effects of both random turbulent fluctuations and coherent acoustic fluctuations. The spatial and temporal coherence of the acoustic oscillations can affect shear flows, including JICF, in ways that random fluctuations cannot. Thus, dynamic pressure measurements in the flow conditioning section are used to quantify the acoustic environment inside the reacting JICF facility. Figure 2.19

(a) Mean axial velocity **(b)** Reynolds stresses

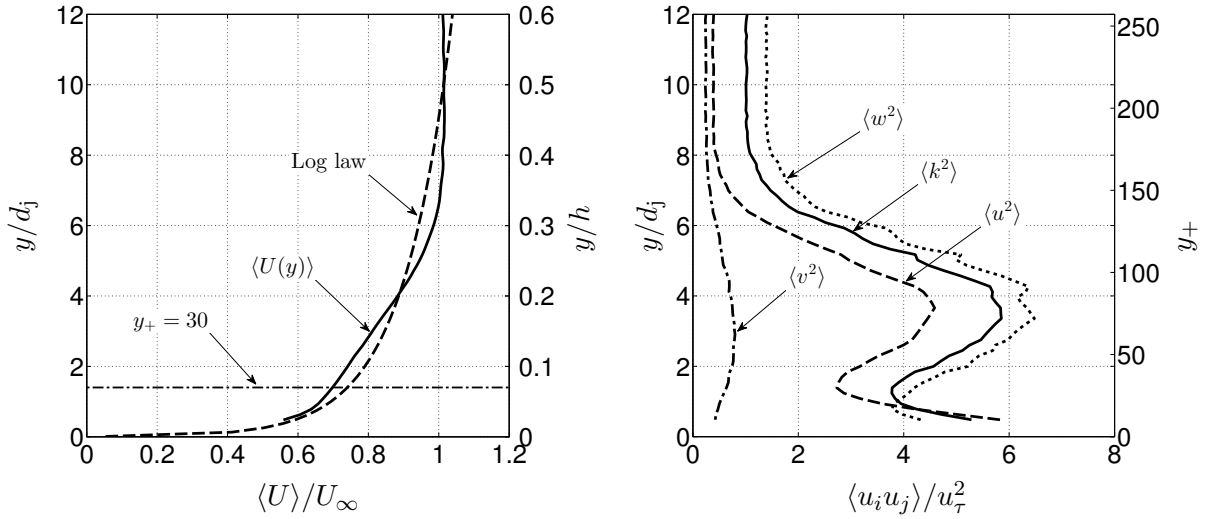

Figure 2.18: Velocity profiles measured in the vitiated crossflow at $x/d_j = 0$ in the absence of the jet.

shows sound pressure level (SPL) measurements acquired simultaneously with the SPIV data presented in Figure 2.18. Pressure measurements are reported for two locations in the crossflow conditioning section, $P_{\infty,1}$ and $P_{\infty,2}$ (see Figure 2.15). The spectra reveal three broad peaks below 300Hz, roughly corresponding to the $\lambda/4$, $3\lambda/4$, and $5\lambda/4$ longitudinal acoustic modes of the facility. The lowest frequency mode is centered near $f = 54$Hz, while the largest amplitude mode is located near $f = 177$Hz. The $5\lambda/4$ mode near $f = 249$Hz is broader and has lower amplitude. The sound pressure level falls off steeply beyond $f \approx 250$Hz and only very low amplitude content exists for $f > 500$Hz. Hence, the acoustic spectra presented throughout the remainder of this thesis are truncated to the range $0\text{Hz} \leq f \leq 500\text{Hz}$. Note that the sound pressure levels reported in Figure 2.19 are representative of the background acoustics that are present in most stable combustion systems. Great care was taken to operate the vitiator at thermoacoustically stable conditions. The fluctuating acoustic velocity associated with the dominant $3\lambda/4$ mode is only ~ 0.08m/s.

The influence of the jet on the background acoustics in the reacting JICF facility should also be considered. The addition of the jet modifies the acoustic boundary conditions, and in the case of a reacting jet, introduces an additional unsteady heat source. These effects must be quantified to insure that results obtained for jets with varying amounts

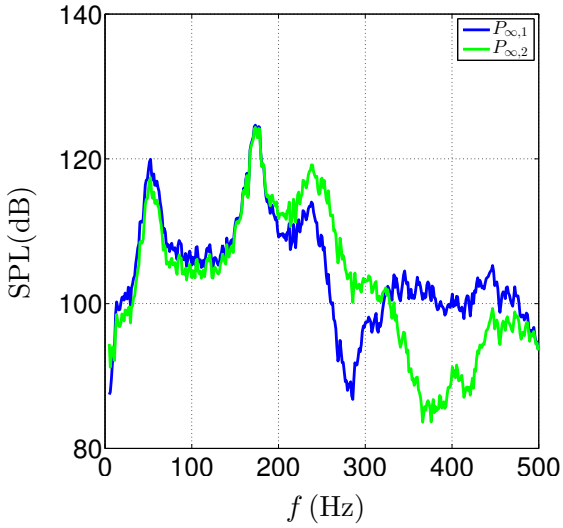

Figure 2.19: Sound pressure level ($P_{\text{ref}} = 20\,\mu$Pa) measured in the vitiated crossflow at two different locations inside the reacting JICF facility. $P_{\infty,1}$: $(x/d_{\text{j}}, y/d_{\text{j}}) = (-160, 20)$, $P_{\infty,2}$: $(x/d_{\text{j}}, y/d_{\text{j}}) = (-80, 20)$.

of heat release (e.g., jets with different J or S) can be compared without concern that any observed differences are simply due to changes in the crossflow acoustics. Accordingly, dynamic pressure measurements in the conditioning section were acquired during each of the unforced JICF experiments. The results of those measurements are presented in Figure 2.20. The spectra from the upstream sensor, $P_{\infty,1}$, and the downstream sensor, $P_{\infty,2}$, indicate that there is little difference in the crossflow acoustics for non-reacting (Figures 2.20e & 2.20f) and reacting jets (Figures 2.20a-2.20d). Similarly, reacting JICF with different S or J, both of which can affect the unsteady heat release, do not have a strong effect on the crossflow acoustics. There is more variation in the SPL in the jet plenum, P_{j}, for different test conditions but these differences can be attributed to changes in the jet injector impedance, Z_{j}, with J and S rather than changes in the crossflow acoustics. Note that the amplitude of P_{j} is generally lower than in the crossflow, which indicates a non-zero resistive component of the jet nozzle acoustic impedance. Comparing the low J results in the left column of Figure 2.20 with the high J cases on the right suggests that the resistive part of the jet impedance tends to increase with J , which is especially apparent at higher frequencies. The importance of the jet injector impedance and its sensitivity to changes in J and S will be discussed in much more detail in Chapter 4.

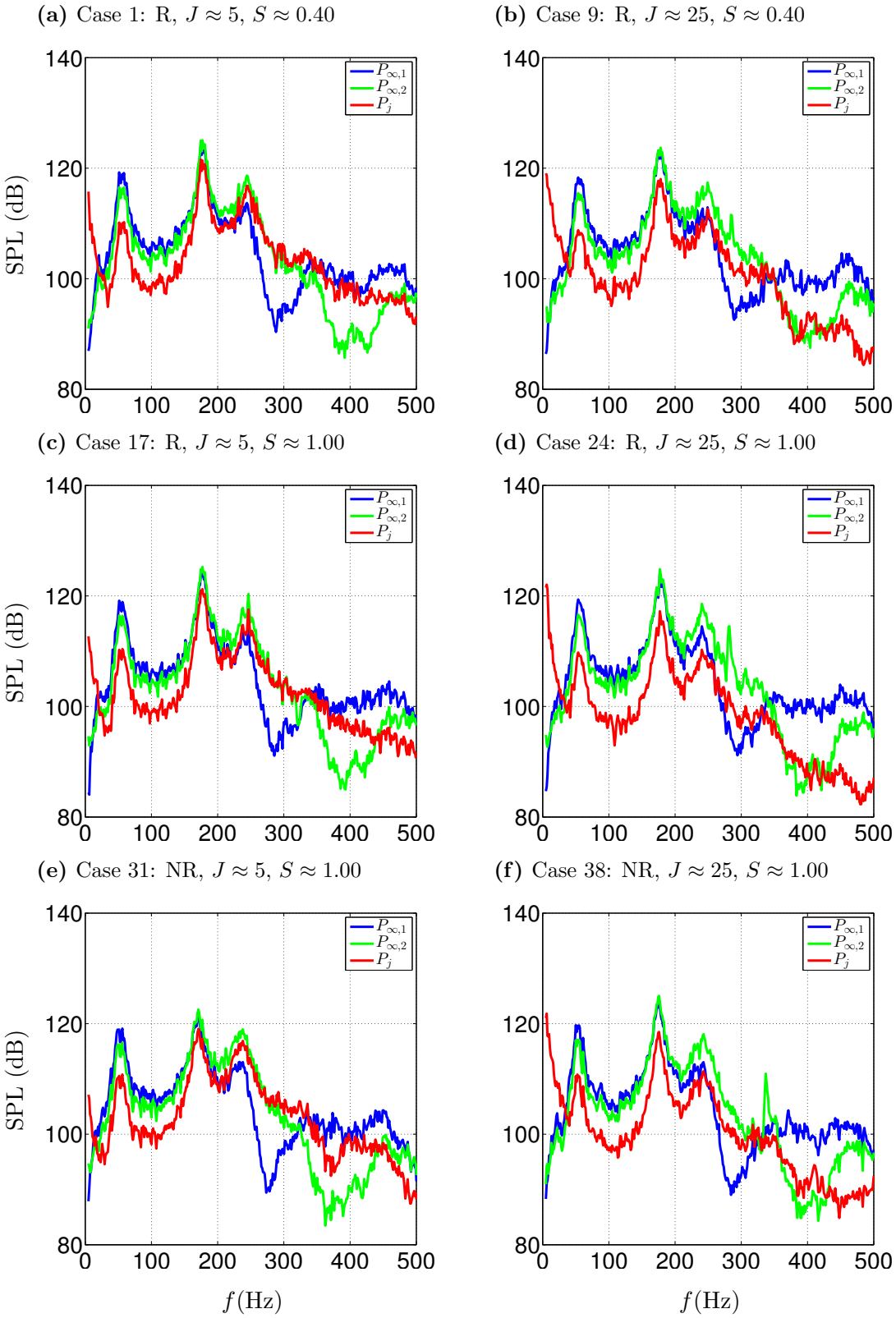

Figure 2.20: Sound pressure level ($P_{\text{ref}} = 20\,\mu$Pa) at three different locations inside the reacting JICF facility. $P_{\infty,1}$: $(x/d_{\text{j}}, y/d_{\text{j}}) = (-160, 20)$, $P_{\infty,2}$: $(x/d_{\text{j}}, y/d_{\text{j}}) = (-80, 20)$, and P_{j}: $(x/d_{\text{j}}, y/d_{\text{j}}) = (0, -20)$.

The jet SPL measurements also contain very low frequency content (i.e., $f < 15$Hz) for all the test conditions. These oscillations are likely due to resonances in the long jet fuel supply system, including the gas bottle regulators, the jet gas mixer, and the jet seeder. Although the entrance to the jet supply plenum is choked, these fuel supply system oscillations can still modulate the jet flow rate by influencing the supply side pressure. Nevertheless, the low frequency content is of relatively little importance since the time scales in question are several orders of magnitude larger than any fluid mechanical time scale of interest in the JICF. The very low frequency content essentially modulates the steady flow rate of the jet but only by a small amount since the acoustic velocities are small relative to the mean jet exit velocity.

CHAPTER III

UNFORCED JETS IN VITIATED CROSSFLOW

This chapter discusses time-averaged and instantaneous features of unforced jets injected perpendicularly into a turbulent, vitiated crossflow. Simultaneous time-resolved SPIV, OH PLIF, and dynamic pressure measurements are presented for both non-reacting and reacting jets. The primary objective of these measurements is to characterize the effect of near-field heat release on unforced JICF with different J and S. A secondary objective is to provide baseline results for the unforced JICF that can be compared with the forced response data presented in Chapter 4. Thus, this chapter focuses on the six unforced test conditions shown in Table 2.3. For convenience, the values of key JICF parameters for these six test conditions are duplicated in Table 3.1.

Table 3.1: Key JICF parameters for the unforced test conditions. Case numbers correspond to those given in Table 2.3.

Case	R/NR	J	S	Re_{j}	Re_{∞}	T_{∞}[K]	f_{F}[Hz]	A_{F}[A]
1	R	5.05	0.41	1980	10520	1241	0	0.0
9	R	23.23	0.40	4420	11480	1191	0	0.0
17	R	5.08	1.04	2590	10660	1236	0	0.0
24	R	25.32	1.04	5750	10610	1236	0	0.0
31	NR	4.74	1.00	1920	11460	1186	0	0.0
38	NR	25.14	1.03	4270	10680	1226	0	0.0

The chapter begins with a detailed characterization of the time-averaged flow features. The sensitivity of the time-averaged flow field with respect to changes in J and S is investigated in both non-reacting and reacting jets. Jet trajectories are then extracted from the SPIV measurements and modifications to the classical JICF scaling laws are explored. The time-averaged structure of the jet shear layer is presented and shear layer trajectories are defined. The time-averaged discussion concludes with a presentation of OH PLIF results. Instantaneous velocity, vorticity, and two-dimensional streamline fields corresponding to the six different unforced test conditions are presented and analyzed next. Key similarities and

differences are highlighted with respect to the time-averaged flow fields. Results from simultaneous OH PLIF and Mie scattering measurements are used to explore the instantaneous reaction zone structure of jet flames in vitiated crossflow. Lastly, edge tracking is used to quantify the probability of flame liftoff and/or local extinction in the windward shear layer.

3.1 Time-Averaged Characteristics of the Flow Field

3.1.1 Velocity Field

This section describes the time-averaged dynamics of jets injected into a vitiated crossflow obtained from 10kHz SPIV measurements in the jet near-field. Results obtained for both non-reacting and reacting jets are compared to better understand the effect of chemical heat release in the near-field of JICF. Contour plots of the time-averaged velocity magnitude, $\langle \|\vec{U}\| \rangle$, for six different unforced test conditions are shown in Figure 3.1. These measurements were made along the jet centerplane ($z/d_\mathrm{j} = 0$) and the measured velocities have been normalized by the mean jet exit velocity, U_j. The crossflow is from left to right in all cases and the jet enters the field of view perpendicular to the crossflow direction at $(x/d_\mathrm{j}, y/d_\mathrm{j}) = (0, 0)$. The time-averaged jet trajectory is defined as the mean jet center streamline and is shown with a bold, dashed line in Figure 3.1. Two-dimensional, time-averaged velocity streamlines are overlaid with thin white lines. Test conditions with $J \approx 5$ are shown in the left column of Figure 3.1 and $J \approx 25$ cases are in the right column. Throughout this work the $J \approx 5$ cases will be referred to as low J cases, and the $J \approx 25$ cases will be referred to as high J cases. The top two rows correspond to reacting cases, while the bottom row describes non-reacting cases. The top row describes low S ($S \approx 0.40$) results, while the bottom two rows describe unity S ($S \approx 1$) results. The time-averaged crossflow, which was discussed in Section 2.4, is nominally identical for each of the unforced cases. Velocities and streamlines for $y/d_\mathrm{j} < 0.5$ are not plotted due to high uncertainty associated with computing vectors near the intense elastic scattering caused by the impingement of the SPIV laser sheet on the lower refractory wall of the test section. Similarly, the region $x/d_\mathrm{j} \leq -1.5$ is omitted because of poor laser sheet intensity and uniformity beyond that point.

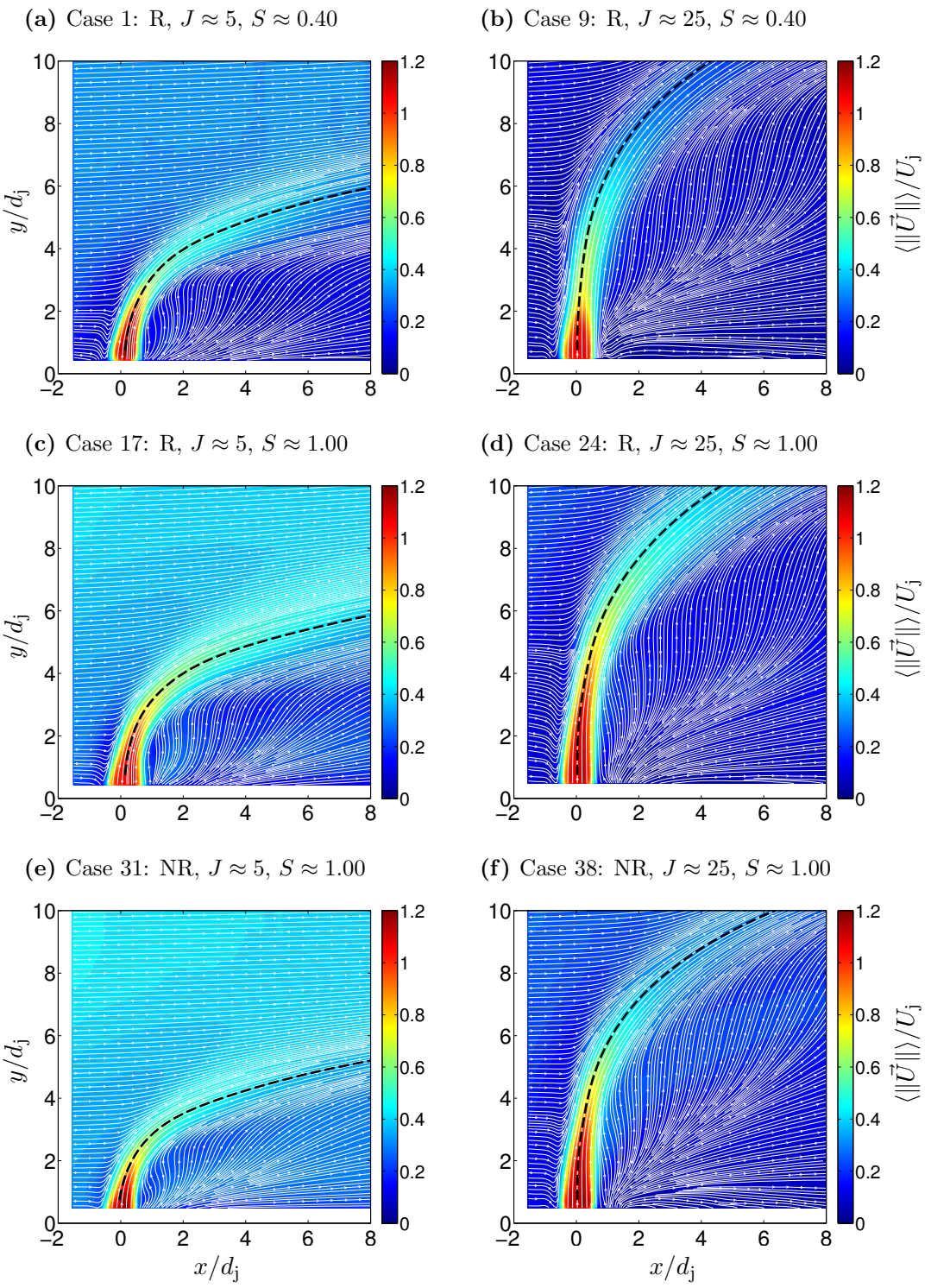

Figure 3.1: Time-averaged velocity magnitude, $\langle \|\vec{U}\| \rangle$, normalized by the mean jet exit velocity, U_j, measured on the $z/d_j = 0$ jet centerplane. (---): Mean jet center streamline trajectory.

The higher momentum flux ratio jets in the right-hand column penetrate significantly further into the crossflow. The low J jets in the left-hand column, on the other hand, never fully escape the boundary layer of the turbulent channel flow, which extends to approximately $y/d_\mathrm{j} = 6$ (see Figure 2.18). The maximum time-averaged velocity magnitude is found near the jet origin and has a value roughly $1.2U_\mathrm{j}$ for all the cases. The reacting cases (Figures 3.1a-3.1d) penetrate further than the non-reacting cases (Figures 3.1e-3.1f), although not dramatically. There is relatively little difference in penetration between reacting cases with the same J, which suggests that the effect of S is not significant for estimating the jet trajectory beyond its contribution to J (recall that $J = Sr^2$, where $r = U_\mathrm{j}/U_\infty$).

Closer inspection of the streamlines in Figure 3.1 reveals several interesting features of the time-averaged flow field. First, a two-dimensional velocity node exists near the wall on the leeward side of the jet for each of the six test conditions. The existence of a two-dimensional velocity node on the leeward side of the jet has been observed previously in non-reacting JICF studies by other researchers (e.g., [6, 29]) as well as in a recent study of premixed jets injected into a vitiated crossflow [62]. The interesting finding here is that the location of the velocity node is sensitive to changes in both J and S. At low J, the node appears close to the wall ($y/d_\mathrm{j} \leq 0.75$) and about $2d_\mathrm{j}$ downstream of the jet injection location. The position of the velocity node shifts upstream at higher J , although more significantly for the low S case. Note that the velocity node sits essentially in the leeward shear layer for the case shown in Figure 3.1b, which indicates that changes in S can alter the near-field structure of reacting jets with otherwise identical parameters. The position of the velocity node does not, however, change significantly for the two unity S, high J cases. This rules out the possibility that the axial shift in the velocity node is solely due to combustion heat release occurring on the leeward side of the jet.

The streamlines emanating from the leeward side velocity node tend to follow one of two divergent paths. Streamlines to the left (upstream) of the node bend back towards the jet and are ultimately entrained into the jet flow. Streamlines to the right (downstream) of the velocity node continue moving downstream along the wall and are not entrained into jet, at least within the present field-of-view. This effect is particularly apparent in the high

J jets, where the jet flow clearly separates from the lower wall and the divergent streamline paths seem to be separated by an imaginary slip line extending from the location of the velocity node at an angle of roughly 30° relative to the lower wall of the test section.

Shifting focus to the region upstream of the jet, note that all the time-averaged streamlines below a certain threshold value of y/d_j flow downwards toward the lower wall for $-1.5 \leq x/d_\mathrm{j} \leq -0.5$. Visual inspection shows that the threshold value of y/d_j for reverse flow depends on J and the presence/absence of combustion heat release. The streamlines bend most aggressively towards the lower wall and the spatial extent of the reverse flow region is most expansive for reacting cases with high J. For example, all the streamlines upstream of the jet and below $y/d_\mathrm{j} \sim 5.5$ deflect strongly downwards in Figure 3.1b. The streamlines in this region of flow turn increasingly towards the lower wall until they finally enter the windward shear layer where they are entrained into the jet and deflect sharply upward. The critical y/d_j value for the reacting low J cases is around $y/d_\mathrm{j} \sim 2$, while the streamlines in the non-reacting low J case in Figure 3.1e barely deflect towards the lower wall at all and only for streamlines below $y/d_\mathrm{j} \sim 0.75$.

Collectively, these observations point to the important influence of pressure (and ∇P) in the JICF near-field. The influence of gravity is negligible due to the small Richardson number of the present flows ($Ri = gd_\mathrm{j}/U_\mathrm{j}^2 < 3.0 \times 10^{-5}$). The dominant mean shear stress in the JICF near-field is due to the introduction of the jet and would tend to deflect the crossflow away from the wall rather than towards the wall. Thus, the pressure gradient must be responsible for the counterintuitive deflection of the streamlines toward the wall. This is noteworthy since the influence of pressure is routinely neglected in the development of JICF scaling laws. Physically speaking, a high pressure region is established upstream of the jet as the crossflow slows and is forced to deflect around the jet. On the leeward side, the jet creates a strong low pressure region due to the aerodynamic blockage of the jet and the rapid entrainment and convection of fluid away from the lower wall. The cumulative effect of the high pressure region upstream of the jet and the low pressure region behind the jet drives crossflow fluid down and around the jet core to fill the "vacuum" behind the jet. From this perspective, it is not surprising that the low J jets have a smaller,

weaker negative velocity region upstream of the jet since the low J jets create less of an aerodynamic blockage and never fully separate from the lower wall. The tendency of combustion heat release to augment the negative velocity region upstream of the jet points to the influence of combustion-induced volumetric dilatation in altering the near-field pressure field. Additional discussion on this point is reserved until after the time-averaged OH PLIF results are introduced in Section 3.1.4.

Examination of the individual velocity components of the time-averaged flow field can provide additional insight into the structure of JICF and the influence of combustion heat release. The time-averaged y-component of velocity, $\langle V \rangle$, is plotted in Figure 3.2. The $\langle V \rangle$ velocity fields are normalized by the local velocity magnitude rather than the mean jet exit velocity to emphasize the direction of the flow. The jet center streamline is shown with a dashed black line, and the $\langle V \rangle = 0$ velocity contour is drawn with a solid black line. The zero velocity contours confirm the observations made previously regarding negative wall-normal velocity upstream of the jet, and the color contour shows that the extent and intensity of the negative $\langle V \rangle$ velocity increases in the reacting cases. The most interesting aspect of the contour plots is the two lobes of high normalized $\langle V \rangle$ velocity. The first lobe is just the jet potential core, which of course contains predominantly vertical velocity. The second lobe of high normalized vertical velocity occurs in the wake region and is particularly apparent in the low J cases. The velocity magnitude in the wake region is relatively low but is dominated by positive vertical velocity inside the second lobe. Note that the second lobe remains attached to the lower edge of the jet core in the high J cases. In both the low J and the high J cases, however, the lower edge of the second lobe closely coincides with the slip line observed previously in the two-dimensional streamlines. This observation reinforces the notion that there is a demarcation in the mean flow above which fluid is entrained into the jet and below which the flow continues to flow in a direction parallel to the lower wall.

Figure 3.3 shows the time-averaged x-component of velocity, $\langle U \rangle$, which is normalized by the mean crossflow velocity, U_∞, in this case. In general, U_j can be interpreted as a global vertical velocity scale, whereas U_∞ is the more appropriate axial velocity scale. Since timescale based arguments will be utilized later to explain flame stabilization trends, it is

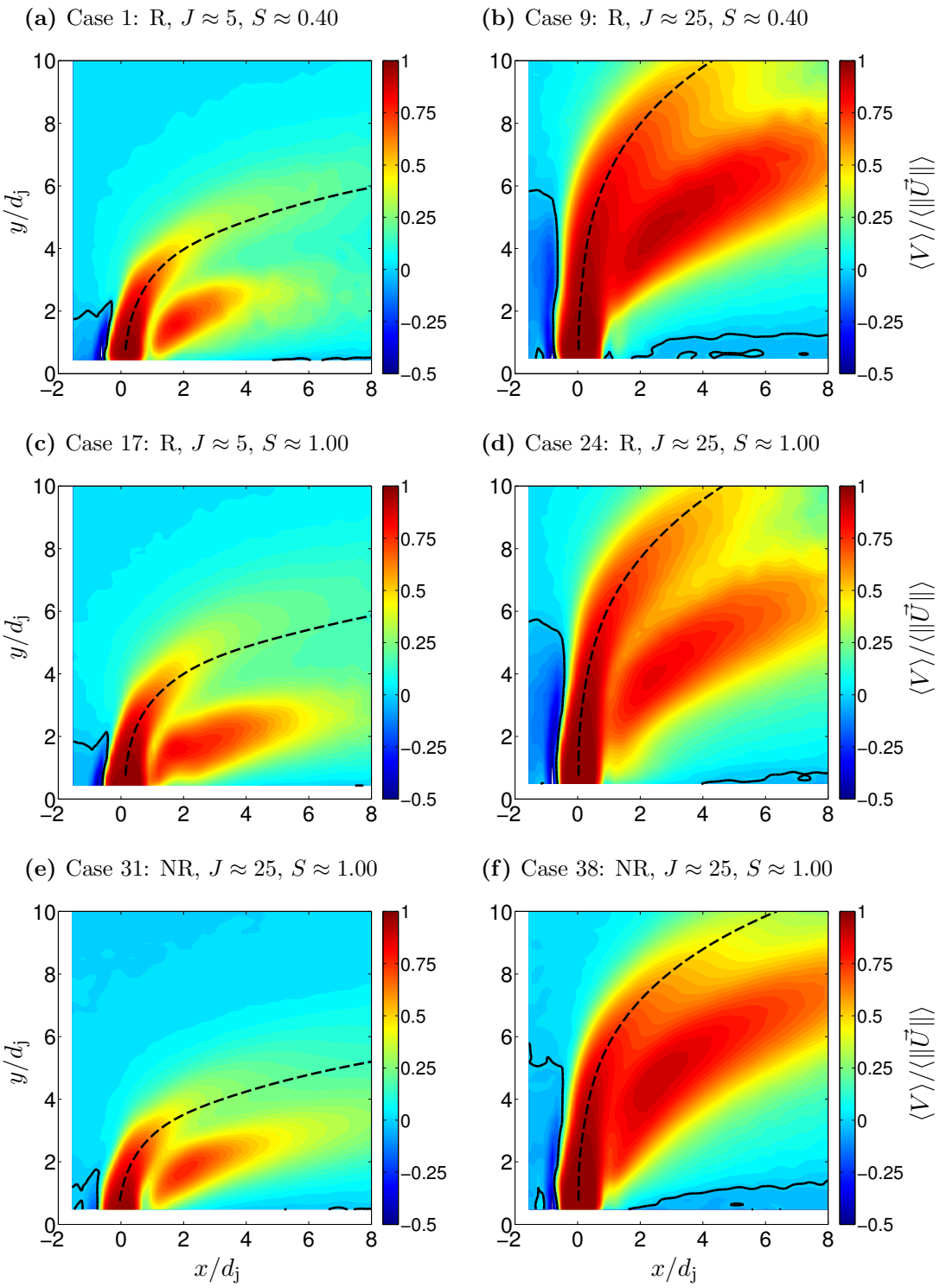

Figure 3.2: Time-averaged y-component of velocity, $\langle V \rangle$, measured on the $z/d_j = 0$ jet centerplane normalized by local velocity magnitude, $\langle \|\vec{U}\| \rangle$. (---): jet center streamline trajectory, (—): zero y-velocity contour.

worthwhile to note that these convective velocity scales can be combined with a length scale, e.g., the jet diameter, d_j, or the arc length distance, s, to estimate convective timescales in the flow. The ratio of the vertical to axial timescale is r^{-1} and depends on J and S . Values for r lie in the range $2.24 \leq r \leq 7.91$ in the present experiments. Thus, even for low J cases, the characteristic vertical convective timescale is less than half the value of the axial convective time scale.

The choice of U_∞ as the scaling factor for $\langle U \rangle$ in Figure 3.3 emphasizes the effect of the jet on the crossflow velocity profile. The $\langle U \rangle / U_\infty = 1$ contour is overlaid to delineate regions of the flow with axial velocity exceeding U_∞, which can only be the result of interaction with the jet and/or combustion heat release. Intuitively, we expect the jet to act as an aerodynamic blockage, leading to a deceleration of the crossflow fluid upstream of the jet along the $z/d_j = 0$ plane. This description accurately reflects the measured axial velocity profiles in the high J cases. The two reacting, high J cases are very similar in that the only region of the flow with $\langle U \rangle / U_\infty \geq 1$ is found inside the jet core and after the jet has partially deflected into the crossflow direction. The non-reacting, high J case does not decelerate the crossflow as strongly, and the axial velocity in the jet core never reaches the values seen for the two reacting, high J cases. Note that this observation holds despite the fact that the non-reacting jet actually deflects into the crossflow direction more rapidly and despite the fact that the non-reacting jet has exactly the same J, S, and U_j as Case 24. Combustion heat release alters the aerodynamic blockage due to the jet at high J conditions and leads to local flow acceleration in the jet core, particularly after the jet has begun to deflect in the crossflow direction.

The influence of the low J jets on the axial velocity field is more complex. In particular, the non-reacting, low J jet appears to cause the greatest deceleration of the crossflow for $y/d_j \geq 6$ while the crossflow velocity is accelerated in the reacting, low S, low J jet. This counter-intuitive result is repeatable and is also seen in the forced response studies reported in Chapter 4. The explanation lies in the very different jet trajectories in the low J and high J cases. Since the trajectory of high J jets is almost vertical for $y/d_j < 4$, the jet core resembles a cylindrical column of fluid. Although some crossflow fluid is entrained into

the jet in this near-field region, most of the crossflow fluid deflects around the jet in the z-direction (out-of-plane). On the other hand, low J jets never separate from the lower wall of the test section and rapidly deflect into the crossflow direction. Thus, the crossflow fluid approaching the upstream side of a low J jet can deflect either above the jet in the positive y-direction or around the jet in the $\pm z$-direction. In either case, conservation of mass requires that the aerodynamic blockage felt by the crossflow due to the jet must be compensated by a corresponding acceleration of the crossflow fluid. The magnitude of the crossflow acceleration is directly related to the amount of aerodynamic blockage due to the presence of the jet, which is largest in the reacting, low S cases.

The mean axial velocity fields are re-plotted in Figure 3.4 with $\langle U \rangle$ normalized by $\langle \|\vec{U}\| \rangle$ rather than U_∞ to demonstrate the sensitivity of the flow to changes in J, S, and the presence/absence of combustion heat release. Note that the isoline in this case denotes $\langle U \rangle = 0$. Comparing the three low J cases in the left-hand column reveals that the rate of recovery of axial velocity in the wake of the jet depends on the test condition. In particular, the low S, low J test condition shown in Figure 3.4a has a noticeably larger low axial velocity region on the leeward side of the jet relative to the unity S reacting (Figures 3.4c) and non-reacting (Figures 3.4e) counterparts. The unity S, low J cases have compact low $\langle U \rangle$ regions anchored immediately downstream of the jet injection location and extending roughly at a 30° angle away from the lower wall until about $6d_\mathrm{j}$. The $\langle U \rangle$ velocity outside of this region and near the lower wall recovers more quickly in the unity S cases, while the axial velocity in the low S case is still only about 25% of U_∞ at $x/d_\mathrm{j} = 8$.

The non-reacting, unity S, low J jet recovers axial velocity in the wake region fastest among the test conditions considered here. The difference in axial velocity recovery between the non-reacting and reacting unity S, low J cases shows that combustion tends to delay velocity recovery in the wake. The differences between reacting low J jets with different S points to the effect of density ratio on axial velocity recovery. The effect of S has not been linked, however, with significant variation of the wake velocity profile in recent non-reacting JICF studies that systematically varied S [9]. Therefore, the wake velocity effect is dominated by the presence/absence of combustion heat release, and the effect of S is felt

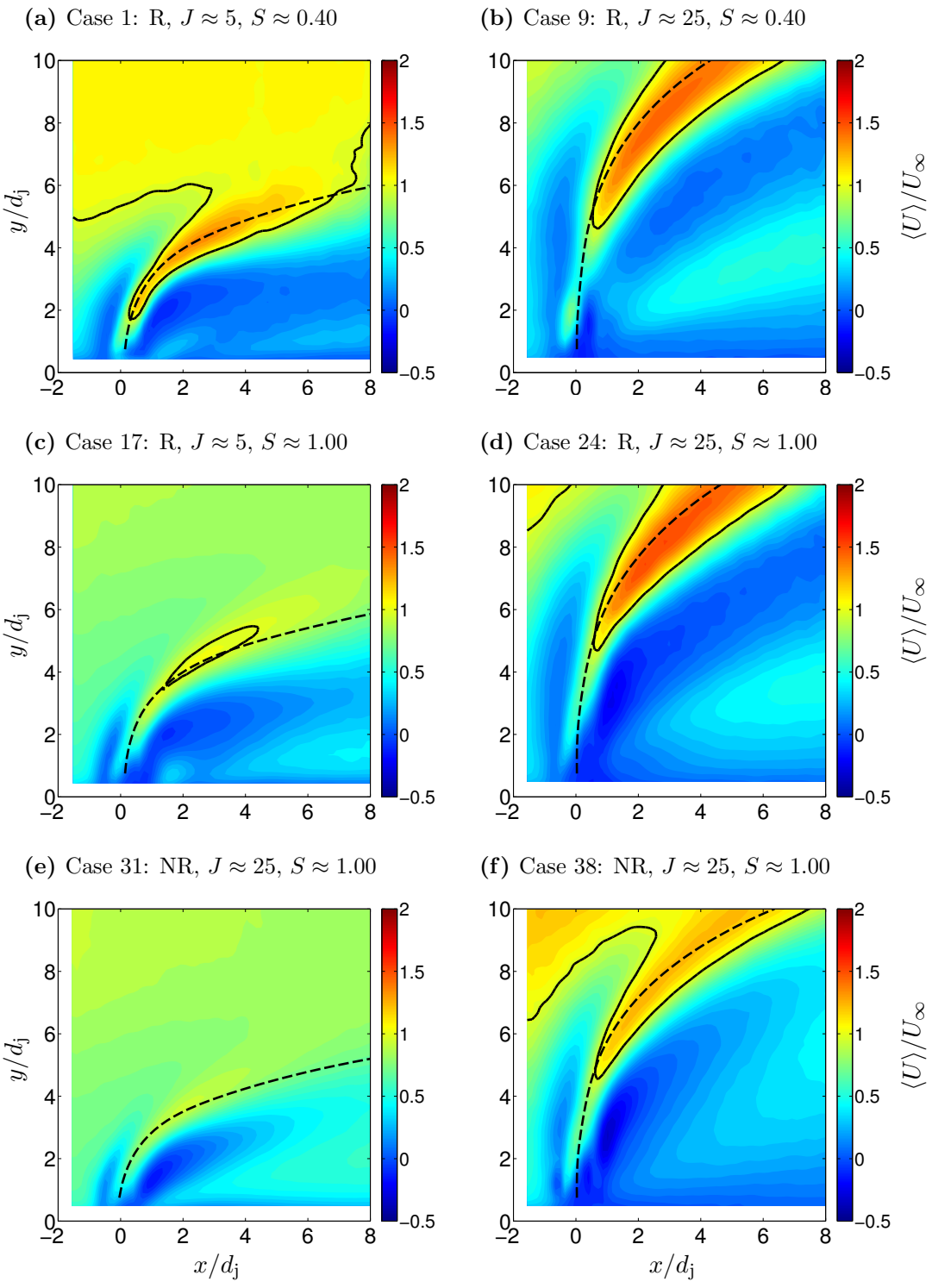

Figure 3.3: Time-averaged x-component of velocity, $\langle U \rangle$, measured on the $z/d_j = 0$ jet centerplane normalized by mean crossflow velocity, U_∞. (---): mean jet center streamline trajectory; (—): $\langle U \rangle / U_\infty = 1$ contour.

due to the fact that S influences the combustion heat release.

There are direct and indirect mechanisms by which combustion can modify the wake velocity profile. The direct mechanism is active when combustion occurs in the wake and causes volumetric dilatation and local flow acceleration. The direction of the flow acceleration depends on the orientation of the reaction zone . In the low J cases, the jet is nearly parallel to the lower wall of the test section by $x/d_{\mathrm{j}} = 2$, which results in predominantly wall-normal mixture fraction gradients in the wake region. In other words, the mean reaction zone in the wake of a low J jet is likely to be nearly parallel to the wall, and consequently, the combustion-induced dilatation preferentially accelerates the flow in the wall-normal direction rather than in the axial direction. The time-averaged OH PLIF images shown in Figure 3.13 support this interpretation of the reaction zone orientation in the low J wake. The indirect mechanism by which combustion modifies the wake structure is active when the combustion occurs upstream of the wake region (i.e., in the jet shear layer). The associated dilatation in this case results in increased aerodynamic blockage of the crossflow and entrainment of combustion products into the wake region. The reasoning in support of the increased aerodynamic blockage argument follows from a simple interpretation of the jet as a column-like obstruction in the near-field. The jet has much higher velocity than the crossflow in this region and shear forces have not yet significantly affected the jet width, thus forcing the crossflow to move around the jet core. The OH PLIF results (see Figure 3.13) indicate that a non-premixed flame is attached to the jet injector and wraps around the jet plume in the low J JICF cases. Thus, the combustion-induced dilatation acts to increase the effective diameter of the jet column. Assuming a flame thickness of $\delta_f = \mathcal{O}(1\mathrm{mm})$, the difference between the effective and the actual jet diameters is not negligible, particularly in the present experiments where $d_{\mathrm{j}} = 3.175\mathrm{mm}$. This observation suggests that the change in aerodynamic blockage due to combustion may be more important in small jets than in large diameter jets where $\delta_f/d_{\mathrm{j}} \ll 1$.

Explaining the difference in the axial velocity recovery in the wake region between the two reacting, low J jets requires a closer look at how volumetric dilatation might vary with S . The effective diameter of the jet column depends on the amount of combustion-induced

volumetric dilatation in the near-field, which is controlled by the rate of jet/crossflow mixing in the near-field and the jet composition. The rate of mixing is directly proportional to volumetric dilatation under the assumption that the near-field reactions occur in the mixing limited, infinitely fast chemistry regime, which is a reasonable assumption for low J jets in a vitiated $T_\infty = 1200$K crossflow. Since the rate of mixing cannot be easily estimate here, the jet composition effect is considered first.

The jet composition affects volumetric dilatation because the density of the combustion products varies as a function of the jet composition. The relative importance of the jet composition effect can be understood by computing the equilibrium products for stoichiometric mixtures of jet fluid and crossflow fluid corresponding to the two S values considered here. Stoichiometric mixture fractions were used in these calculations based on the assumption of non-premixed flame structure in the jet near-field. The resulting thermo-physical properties for combustion products in the low S and unity S cases are presented in Table 3.2. Despite the large discrepancy ($\sim 250\%$) in jet density, ρ_j, for the two different S values, the difference in the equilibrium product density, ρ_ad, is only $\sim 6.5\%$. The near-field dilatation due to a unit mass of reacted low S fluid is not very different than that of a unit mass of reacted unity S fluid. This follows directly from the low stoichiometric mixture fractions, z_st, which translates to equilibrium products comprised primarily of diluted crossflow gases that only weakly depend on the jet composition. Note that while this statement is true for the present study where H_2 is the only fuel, it may not be true in general for jets with very different z_st. The relatively small direct effect of jet composition on near-field dilatation suggests that variability in the near-field mixing rate may be the more important parameter controlling the volumetric dilatation in the near-field. Chapter 5 will discuss the dependence of near-field mixing on S in more detail.

Interestingly, the axial velocity (and velocity recovery) in the wake of the high J jets shows the opposite trend relative to that observed in the low J cases. Specifically, the fastest axial velocity recovery occurs in the reacting, low S case. The conceptual model for the influence of combustion heat release on the wake velocity recovery developed for the low J jets can be applied to the high J jets as well, although only after properly accounting

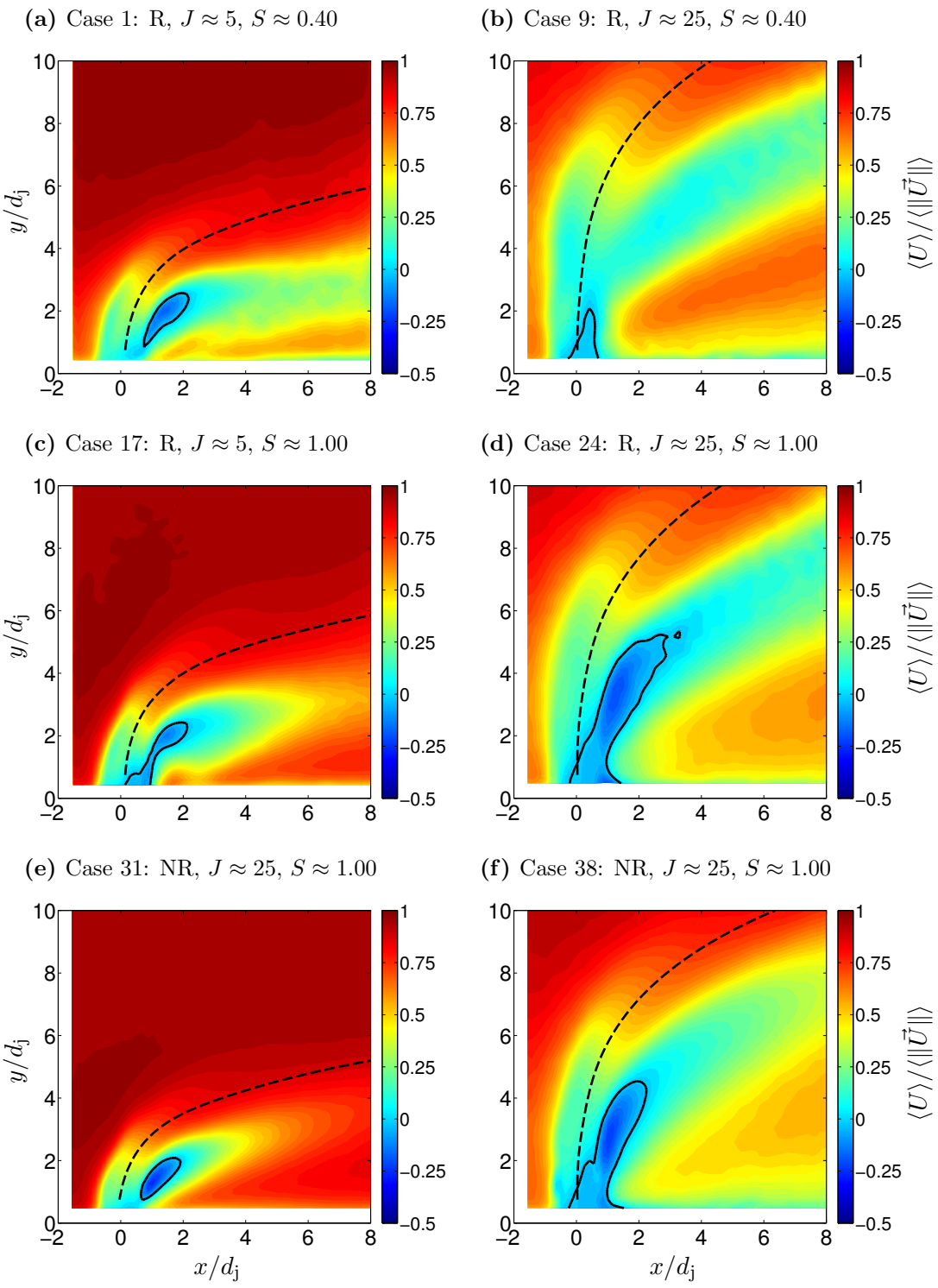

Figure 3.4: Time-averaged x-component of velocity, $\langle U \rangle$, measured on the $z/d_j = 0$ jet centerplane normalized by local velocity magnitude, $\langle \|\vec{U}\| \rangle$. (---): jet center streamline trajectory, (—): zero x-velocity contour.

Table 3.2: Thermo-physical properties of jet fluid, vitiated crossflow fluid, and equilibrium products of stoichiometric mixtures of jet fluid and vitiated crossflow fluid for different S.

	$S = 0.40$	$S = 1.00$
ρ_{j}	$0.1154\,\mathrm{kg/m^3}$	$0.2884\,\mathrm{kg/m^3}$
ρ_{∞}	$0.2884\,\mathrm{kg/m^3}$	$0.2884\,\mathrm{kg/m^3}$
z_{st}	0.0367	0.0916
ρ_{ad}	$0.1270\,\mathrm{kg/m^3}$	$0.1352\,\mathrm{kg/m^3}$
T_{ad}	2262 K	2239 K
$S_{\mathrm{j,ad}}$	0.9087	2.1331
$S_{\infty,\mathrm{ad}}$	2.2709	2.1331

for the differences in the orientation of the reaction zone in the wake region for low J and high J jets. The time-averaged OH PLIF images in Figure 3.13 show that the leeward side reaction zone generally follows the curvature of the jet trajectory in the high J jets, or equivalently, the mean mixture fraction gradient is primarily aligned in the axial direction. Therefore, the combustion-induced dilatation in these cases tends to accelerate the wake region in the axial direction.

Lastly, the $\langle U \rangle = 0$ velocity contours plotted in Figure 3.4 merit some discussion, especially since this flow feature turns out to be important in flame stabilization and in understanding the response of JICF to crossflow forcing. A region with $\langle U \rangle < 0$ exists in all six of the test conditions, but the size and strength of the reverse flow region varies with J and S. The low J cases have relatively small, compact, reverse flow regions immediately downstream of the jet potential core on the leeward side of the jet. The non-reacting cases exhibit the strongest reverse flow (relative to both U_{∞} and $\langle \|\vec{U}\| \rangle$). The reverse flow region in the reacting, low S, high J case (Figure 3.4b) is weak and is confined to a small region near the leeward shear layer. This is in sharp contrast to the reacting, unity S, high J case, which has the largest reverse flow region of all the test conditions. The reason for this discrepancy is related to differences in the near-field flame stabilization, which can be better understood by analyzing temporal data as is discussed in Section 3.2.2.

3.1.2 Trajectory and Scaling

This section focuses on developing a scaling law that describes the experimentally determined jet center streamline trajectories. Jet trajectories extracted from each of the six

unforced test conditions are shown in Figure 3.5a. It shows that cases with higher J values and cases with combustion penetrate further into the crossflow direction. The J dependence can be partially collapsed by using the standard Rd_{j} scaling employed in most JICF scaling laws [27, 29]. However, the inability of the standard Rd_{j} scaling to fully collapse the data shown in Figure 3.5b suggests that additional physical processes need to be considered. Note that the slope of the jet trajectory, when scaled by Rd_{j}, does not change much for any of the cases beyond $x/Rd_{\mathrm{j}} = 1.5$. This finding indicates that the unaccounted for physical processes affecting the jet trajectory act primarily in the jet near-field.

The scatter in the Rd_{j}-scaled jet trajectories can be quantified by fitting each measured trajectory to a scaling law of the form

$$\frac{y}{Rd_{\mathrm{j}}} = A\left(\frac{x}{Rd_{\mathrm{j}}}\right)^{b} \tag{3.1}$$

where the A and b coefficients have been determined using a least squares fit to the experimentally determined jet trajectories and are reported in Table 3.3. The coefficients in an optimal scaling law would be constants that are independent of the specific test condition. In contrast, the calculated coefficients extracted from the present experiments show a $\sim 30\%$ variation in A and a $\sim 13\%$ variation in b. Although this variability is substantial, it is noteworthy that the calculated coefficients are still within the ranges reported in the literature for non-reacting JICF trajectories [28]. As anticipated from the previous discussion, the largest differences in the calculated coefficients are found between cases with different J and between cases with/without combustion.

Table 3.3: Trajectory scaling law coefficients determined based on a least squares fit of Equation (1.4) to the measured jet center streamline trajectories.

Case	R/NR	J	S	A	b
1	R	5.05	0.41	1.736	0.333
9	R	23.23	0.40	2.139	0.307
17	R	5.08	1.04	1.735	0.324
24	R	25.32	1.04	2.037	0.321
31	NR	4.74	1.00	1.628	0.295
38	NR	25.14	1.03	1.863	0.305

The first step towards developing an improved JICF scaling law is selecting which additional physical processes need to be considered. The time-averaged flow field data presented

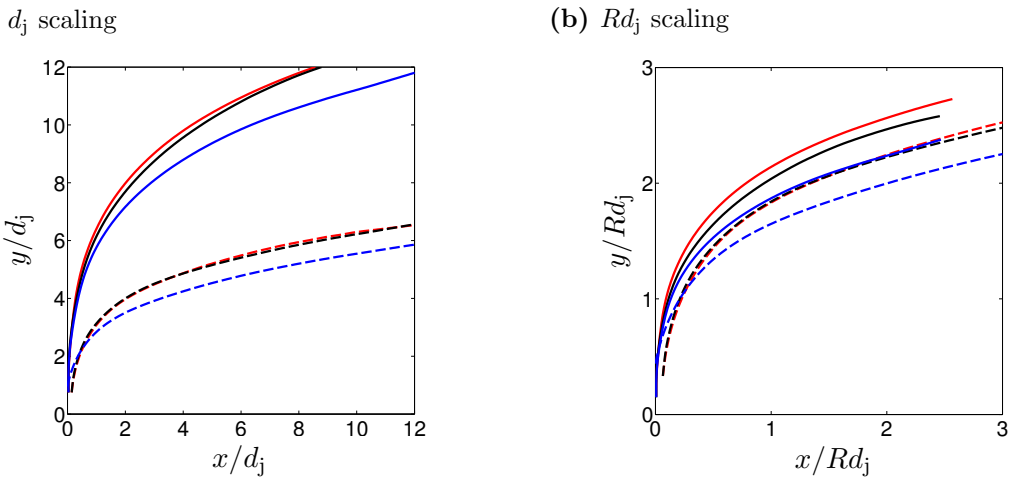

Figure 3.5: Scaled jet center streamline trajectories extracted from SPIV measurements of unforced non-reacting and reacting JICF. (---): Case 1, Reacting, low S, low J; (---): Case 17, Reacting, unity S, low J; (---): Case 31, Non-reacting, unity S, low J; (—): Case 9, Reacting, low S, high J; (—): Case 24, Reacting, unity S, high J; (—): Case 38, Non-reacting, unity S, high J.

previously is helpful in this regard. In particular, the importance of both the near-field pressure gradient and the combustion heat release was demonstrated through their influence on the x- and y-component velocity fields. Yet, the derivation of Equation (3.1) does not account for combustion and generally neglects the effect of pressure forces on the jet trajectory [29]. Generally, trajectory scaling laws such as Equation 3.1 treat the jet deflection as a consequence of crossflow entrainment. These scaling laws tend to be very successful in capturing the far-field behavior of the jet because the far-field is dominated by entrainment. The near-field is not dominated, however, by entrainment. Instead, as shown in Figure 3.6a, it experiences strong acceleration due to the local pressure gradient, and in the reacting case, due to combustion-induced dilatation. Thus, the objective in the remainder of this section is to investigate the development of a scaling approach that accounts for both near-field pressure effects and combustion-induced flow acceleration.

The recent work on JICF scaling reported by Muppidi & Mahesh [30] serves as the starting point for development of a modified scaling law that accounts for near-field pressure gradient effects and combustion effects. Muppidi & Mahesh [30] were motivated by their observation that standard Rd_j-scaling could not fully collapse non-reacting jet trajectories when J was held constant and the boundary layer thickness of the crossflow was varied.

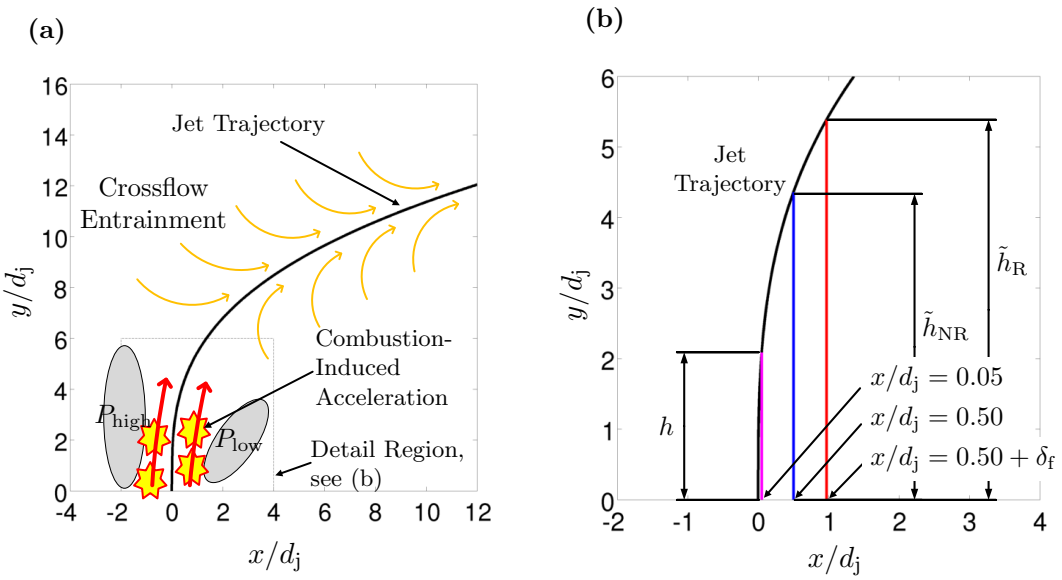

Figure 3.6: (a) Sketch of phenomena affecting the jet trajectory, including factors not accounted for in standard scaling laws such as the near-field pressure gradient and combustion-induced flow acceleration. (b) Detail view of the near-field illustrating definition of h, $\tilde{h}_{\text{NR}}$, and $\tilde{h}_{\text{R}}$ parameters.

They found that pressure forces acting in the jet near-field were sensitive to changes in J as well as changes in the crossflow boundary layer profile. They postulated that the pressure gradient force should scale with the crossflow momentum flux and since the jet is nearly vertical in the near-field, this force acts on a column with width, d_j, and height, h. The new parameter, h, represents the height of the vertical portion of the jet that experiences the pressure gradient force in the near-field. h is large for a crossflow with a thick crossflow boundary layer relative to a crossflow with a thin boundary layer because the lower momentum fluid in the thicker boundary layer creates a smaller stagnation pressure upstream of the jet.

The important practical questions are: (1) how to specify h and (2) how to incorporate h into a trajectory scaling law. Regarding the latter, Muppidi & Mahesh [30] demonstrated improved trajectory scaling for a large set of jet trajectories extracted from DNS results using the following, modified scaling law:

$$\frac{y}{Rd_j} = A\left(\frac{x}{Rd_j}\right)^b \left(\frac{h}{d_j}\right)^C \tag{3.2}$$

where A and b are constant coefficients, $C = 0.15$, and h is the y value where the jet

trajectory intersects the vertical line $x/d_\mathrm{j} = 0.05$. A schematic illustrating the definition of h is provided in Figure 3.6b. This definition of h is not particularly useful, however, because it requires *a priori* knowledge of the jet trajectory. Fortunately, Muppidi & Mahesh [30] found that h was well approximated by the analytical expression,

$$\rho_\infty d_\mathrm{j} \int_0^h \langle U(x^*, y, 0)\rangle^2 \,\mathrm{d}y = C_m \rho_\mathrm{j} \int_{A_\mathrm{j}} \langle V(x, 0, z)\rangle^2 \,\mathrm{d}A \tag{3.3}$$

where $C_m = 0.05$ and x^* denotes a location far upstream of the jet where the crossflow is not affected by the presence of the jet. This equation is a modified momentum flux balance between the crossflow and the jet, where the jet momentum flux is multiplied by the constant C_m and the crossflow momentum flux is evaluated only from $0 \leq y \leq h$. Thus, h can be interpreted as the height of a column with diameter d_j where the crossflow momentum flux incident on the projection of the column on the $y-z$ plane is equivalent to 5% (because they took $C_m = 0.05$) of the jet exit momentum flux. Equation (3.3) can now be evaluated to determine h, assuming that the boundary layer profile is known or can be approximated.

Two modifications to the scaling law given in Equation (3.2) are incorporated into the proposed scaling law, and their effect is introduced by replacing h with either $\tilde{h}_\mathrm{NR}$ or $\tilde{h}_\mathrm{R}$ for non-reacting or reacting jets, respectively. The parameter $\tilde{h}_\mathrm{NR}$ is defined as the y value where the jet trajectory intercepts the vertical line $x/d_\mathrm{j} = 0.5$, as shown in Figure 3.6b. This definition is similar to the definition used by Muppidi & Mahesh [30] with the exception that those authors used $x/d_\mathrm{j} = 0.05$ instead of $x/d_\mathrm{j} = 0.50$. Following the discussion on h presented above, $\tilde{h}_\mathrm{NR}$ is interpreted as the height of a column with diameter d_j that experiences a force as a result of the near-field pressure gradient. A sketch illustrating this interpretation is provided in Figure 3.7. The blue cylinder, which corresponds to $\tilde{h}_\mathrm{NR}$, represents the column on which the pressure gradient forces act in the non-reacting case. Note that the diameter is d_j and the height of the cylinder, $\tilde{h}_\mathrm{NR}$, is defined by the intersection of the jet trajectory with the vertical $x/d_\mathrm{j} = 0.50$ line. This definition of $\tilde{h}_\mathrm{NR}$ gives values that approximate the height at which the jet potential core was observed to breakdown in the SPIV measurements. The underlying implication is that pressure gradient forces are

assumed to act on the larger potential core region of the jet instead of just the vertical region considered by Muppidi & Mahesh [30]. This reasoning is consistent from a physical perspective because pressure forces alone are responsible for deflecting the jet potential core in the near-field where very little entrainment of crossflow fluid has occurred.

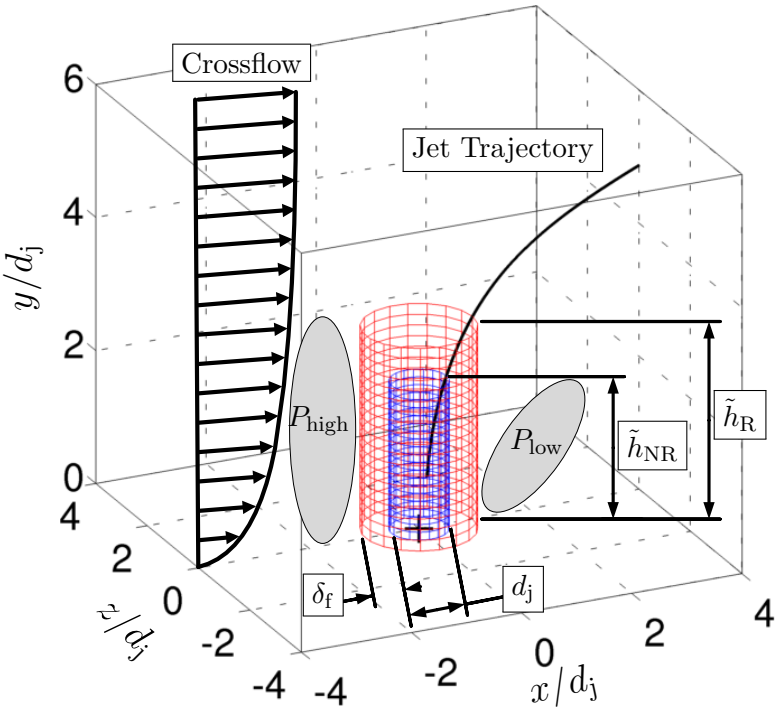

Figure 3.7: Sketch illustrating trajectory scaling procedure.

In reacting cases, the near-field pressure gradient will be stronger because volumetric dilatation will increase the aerodynamic blockage seen by the approaching crossflow. This effect is captured in the proposed scaling law by using $\tilde{h}_R$ instead of $\tilde{h}_{NR}$ to replace h in Equation (3.2). $\tilde{h}_R$ is defined as the y value where the jet trajectory intercepts the vertical line $x/d_j = 0.50 + \delta_f$, where δ_f is the flame thickness. As seen in Figure 3.6b, $\tilde{h}_R$ for a reacting jet is always larger than $\tilde{h}_{NR}$ for an identical non-reacting jet. Similar to $\tilde{h}_{NR}$, $\tilde{h}_R$ can be interpreted as the height of a column that experiences a pressure gradient force in the near-field. In the reacting case, however, Figure 3.7 shows that both the height of the column, $\tilde{h}_R$, and the width of the column, $d_j + 2\delta_f$, are larger than in the non-reacting case. Assuming a constant flame thickness of $\delta_f \sim 1.5$mm, the width of the column in the

reacting case is $\sim 1.95d_{\mathrm{j}}$. An interesting implication of the definition of $\tilde{h}_{\mathrm{R}}$ is that the ratio δ_f/d_{j} controls the extent to which combustion may be expected to modify the jet trajectory. Small jets, such as those used in the present work, should be more sensitive to the added blockage associated with combustion-induced dilatation, while the effective blockage of a large diameter jet will be relatively unchanged by the addition of a thin flame around its periphery. This reasoning may explain why the trajectory of large, reacting jets in crossflow appear to be relatively insensitive to the presence/absence of combustion [62]. Similarly, the trajectory in reacting jets stabilized in low-to-moderate temperature air crossflow, such as the configurations recently studied by Steinberg et al. [87] and Grout et al. [54], are unlikely to deviate much from the trajectory measured in non-reacting JICF since the flame is stabilized much further downstream and presumably does not contribute to an enhanced aerodynamic blockage in the near-field.

Jet trajectories scaled according to Equation (3.2) using either $\tilde{h}_{\mathrm{NR}}$ or $\tilde{h}_{\mathrm{R}}$ in place of h are shown in Figure 3.8b. Note that the collapse of the data is significantly improved relative to the standard Rd_{j}-scaling, which is shown for reference in Figure 3.8a. Optimum values for the A and b coefficients were determined using least squares regression, and those values as well as the corresponding values for $\tilde{h}_{\mathrm{NR}}$, $\tilde{h}_{\mathrm{R}}$, and C are reported in Table 3.4. The A parameter in the revised scaling law varies by only $\sim 11\%$ while the b parameter varies by $\sim 13\%$. It is worth noting that the variance in A and b across all the experimental conditions drops to a minimum for $C = 0.15$, which is the value found by Muppidi & Mahesh [30] in their DNS study. Since those authors were also trying to account for pressure effects on JICF trajectories, the fact that the same exponential factor is found in this study supports the hypothesis that jets with different J and jets with/without combustion experience different pressure gradient forces, leading to different jet penetration.

Despite their effectiveness as scaling parameters, the usefulness of $\tilde{h}_{\mathrm{NR}}$ and $\tilde{h}_{\mathrm{R}}$ is limited without a capability to estimate their value without *a priori* knowledge of the jet trajectory. As described above, the study by Muppidi & Mahesh [30] was able to analytically estimate h by assuming a crossflow boundary layer profile and using that profile to determine the crossflow momentum flux contributing to the pressure gradient acting on the jet core. While

(a) Standard scaling based on Rd_j

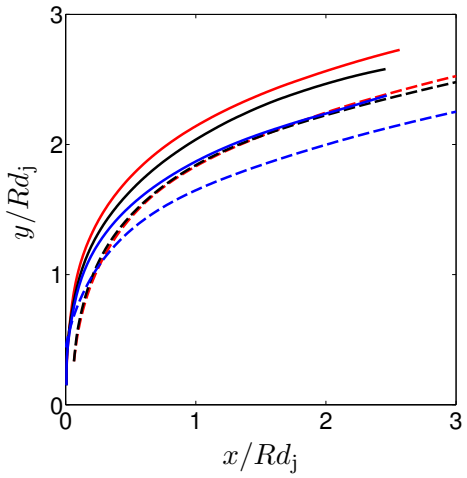

(b) Revised scaling based on Equation (3.2) where h has been replaced by $\tilde{h}_\mathrm{NR}$ or $\tilde{h}_\mathrm{R}$

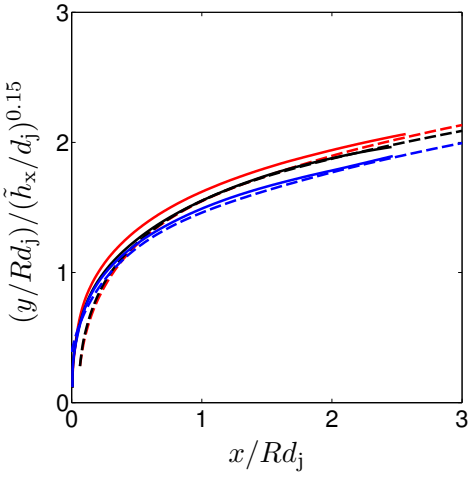

(c) Revised scaling identical to that used in (b) except R has been replaced by $\tilde{R}$

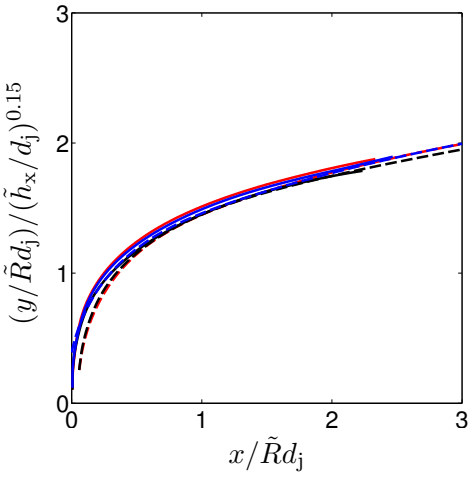

Figure 3.8: Experimentally determined jet center streamline trajectories scaled using different approaches. (---): Case 1, Reacting, low S, low J; (---): Case 17, Reacting, unity S, low J; (---): Case 31, Non-reacting, unity S, low J; (—): Case 9, Reacting, low S, high J; (—): Case 24, Reacting, unity S, high J; (—): Case 38, Non-reacting, unity S, high J.

this approach was well-suited for approximating the influence of different known, boundary layer profiles, it is not as applicable when the aerodynamic blockage of the jet itself is changing, as is the case in the present work. As an alternative, $\tilde{h}_{\mathrm{NR}}$ and $\tilde{h}_{\mathrm{R}}$ can be approximated by the y value predicted using a standard, two-coefficient JICF trajectory scaling law where x/d_{j} is taken as the radius of the appropriate jet column, i.e., $x/d_{\mathrm{j}} = 0.50$ in a non-reacting case or $x/d_{\mathrm{j}} = 0.5 + \delta_{\mathrm{f}}$ in a reacting case. The calculated y value can then be substituted for $\tilde{h}_{\mathrm{NR}}$ or $\tilde{h}_{\mathrm{R}}$ in the revised scaling law. Given an initial estimate for $\tilde{h}_{\mathrm{NR}}$ or $\tilde{h}_{\mathrm{R}}$, the revised scaling law can then be used to iteratively improve the estimate of $\tilde{h}_{\mathrm{NR}}$ or $\tilde{h}_{\mathrm{R}}$ until satisfactory convergence is achieved. To demonstrate the usefulness of this approximate approach, estimated values for $\tilde{h}_{\mathrm{NR}}$ and $\tilde{h}_{\mathrm{R}}$, which we will refer to as $\tilde{h}_{\mathrm{est.}}$, were computed using only the analytical expression given by Equation (3.1). The results are tabulated and compared against the values extracted from the SPIV results in Table 3.5. The values for $\tilde{h}_{\mathrm{est.}}$ are within 10% of measured values for $\tilde{h}_{\mathrm{NR}}$ and $\tilde{h}_{\mathrm{R}}$.

Table 3.4: Proposed trajectory scaling law coefficients extracted from SPIV measurements for use with a modified form of Equation (1.6). Note that $C = 0.15$.

Case	R/NR	J	S	R	$\tilde{h}_{\mathrm{NR}}/d_{\mathrm{j}}$	$\tilde{h}_{\mathrm{R}}/d_{\mathrm{j}}$	A	b	C
1	R	5.05	0.41	2.247	n/a	3.081	1.467	0.343	0.15
9	R	23.23	0.40	4.820	n/a	6.408	1.604	0.297	0.15
17	R	5.08	1.04	2.254	n/a	3.136	1.464	0.330	0.15
24	R	25.32	1.04	5.032	n/a	6.145	1.540	0.313	0.15
31	NR	4.74	1.00	2.178	2.245	n/a	1.442	0.296	0.15
38	NR	25.14	1.03	5.014	4.525	n/a	1.477	0.298	0.15

The physical significance of $\tilde{h}_{\mathrm{NR}}$ and $\tilde{h}_{\mathrm{R}}$ can be better understood by post-processing the time-averaged SPIV data to extract other length scales associated with the near-field pressure gradient. Recall that the following two features of the time-averaged flow field upstream of the jet were very clearly associated with the near-field pressure gradient: (1) the strong deceleration in the x-component of the crossflow velocity upstream of the jet core and (2) the region of negative y-component velocity upstream of the jet core. Consider the deceleration of the x-component of crossflow velocity first. It is postulated that the vertical centroid of the axial crossflow momentum deficit should scale similarly to $\tilde{h}_{\mathrm{NR}}$ or $\tilde{h}_{\mathrm{R}}$ since both length scales are controlled by the near-field pressure gradient. The y/d_{j} value of the

centroid of the x-momentum deficit, which we will refer to as $(y/d_j)_C$, can be computed using the equation

$$\left(\frac{y}{d_j}\right)_C = \frac{\iint [y/d_j][\langle U_{cf}(x,y)\rangle - \langle U(x,y)\rangle]^2 \, dA}{\iint [\langle U_{cf}(x,y)\rangle - \langle U(x,y)\rangle]^2 \, dA} \tag{3.4}$$

where $\langle U_{cf}\rangle$ is the crossflow velocity profile measured in the absence of the jet (i.e., Case 49) and only the area upstream of the jet is considered in the integration. The results of this calculation are included in Table 3.5. It shows that $(y/d_j)_C$ scales similarly to the previously determined values of $\tilde{h}_{NR}$ and $\tilde{h}_R$. $\tilde{h}_{NR}$ and $\tilde{h}_R$ can also be compared with the maximum y/d_j value, which we will refer to as $(y/d_j)_{max}$, where negative y-component velocities are observed upstream of the jet core. This method is only valid in the region just upstream of the jet, although the result did not vary much in the present work when $(y/d_j)_{max}$ was anywhere in the range $-3 \leq x/d_j \leq -0.75$. Thus $x/d_j = -0.75$ was selected for the present purposes and the extracted values for $(y/d_j)_{max}$ are tabulated in Table 3.5 to facilitate comparison with the previously determined values for $\tilde{h}_{NR}$ and $\tilde{h}_R$. The reasonable agreement again supports the hypothesis that near-field pressure effects are a key factor affecting the jet trajectory in the vicinity of the jet injector and that trajectory scaling laws can be improved by incorporating these effects.

Table 3.5: Comparison of scaling coefficients $\tilde{h}_{NR}$ and $\tilde{h}_R$ extracted directly from the measured jet trajectories against a simple analytical approximation, $\tilde{h}_{est.}/d_j$, and two length scales extracted from the time-averaged SPIV velocity fields, $(y/d_j)_C$ and $(y/d_j)_{max}$.

Case	R/NR	J	S	R	$\tilde{h}_{NR}/d_j$	$\tilde{h}_R/d_j$	$\tilde{h}_{est.}/d_j$	$(y/d_j)_C$	$(y/d_j)_{max}$
1	R	5.05	0.41	2.247	n/a	3.081	3.195	2.041	1.946
9	R	23.23	0.40	4.820	n/a	6.408	5.400	5.388	5.628
17	R	5.08	1.04	2.254	n/a	3.136	3.202	1.818	1.642
24	R	25.32	1.04	5.032	n/a	6.145	5.560	4.918	5.476
31	NR	4.74	1.00	2.178	2.245	n/a	2.540	1.484	1.539
38	NR	25.14	1.03	5.014	4.525	n/a	4.509	3.989	5.324

The modified trajectory scaling law given in Equation 3.2 properly accounts for the effect of combustion heat release on the near-field pressure gradient when h is replaced by $\tilde{h}_R$. However, the effect of combustion-induced flow acceleration (see Figure 3.6a) on the jet trajectory is not yet included, and thus, the scaled trajectories for reacting and non-reacting jets in Figure 3.8b do not fully collapse. Combustion-induced flow acceleration can be

incorporated into the trajectory scaling law by replacing R with a modified jet-to-crossflow velocity ratio $\tilde{R}$, which is equivalent to an increase in the effective J for the reacting cases. Comparing velocity field measurements of non-reacting and reacting jets with $S = 1.00$ indicates that the appropriate modified velocity ratio, $\tilde{r} = \tilde{U_{\mathrm{j}}}/U_{\infty}$, in the reacting cases is approximately $\tilde{r} = 1.10r$. This amounts to a 21% increase in the effective J for the reacting cases. $\tilde{R}$ values for the present test conditions are listed in Table 3.6. Figure 3.8c shows the experimentally determined jet trajectories scaled using the final modified scaling law, where h has been replaced by $\tilde{h}_{\mathrm{NR}}/\tilde{h}_{\mathrm{R}}$ and R has been replaced by $\tilde{R}$. The results indicate that the scaling law successfully collapses jet trajectories for non-reacting and reacting jets with different J and S. The fit coefficients obtained based on a least squares fit of the data are presented in Table 3.6. Note that the A coefficients vary by $\sim 8.5\%$ using the revised scaling law, which can be compared against the $\sim 30\%$ variation in A for the standard Rd_{j} scaling (reference Table 3.3).

Table 3.6: Optimal trajectory scaling law coefficients determined based on a least squares fit of the experimental data to a modified form of Equation (3.2) where R has been replaced with $\tilde{R}$ and h has been replaced with either $\tilde{h}_{\mathrm{NR}}$ or $\tilde{h}_{\mathrm{R}}$.

Case	R/NR	J	S	A	b	$\tilde{h}_{\mathrm{x}}/d_{\mathrm{j}}$	$\tilde{R}$	C
1	R	5.05	0.41	1.378	0.329	3.081	2.472	0.15
9	R	23.23	0.40	1.493	0.290	6.408	5.302	0.15
17	R	5.08	1.04	1.373	0.321	3.136	2.479	0.15
24	R	25.32	1.04	1.433	0.304	6.145	5.535	0.15
31	NR	4.74	1.00	1.442	0.295	2.245	2.178	0.15
38	NR	25.14	1.03	1.471	0.292	4.525	5.014	0.15

3.1.3 Shear Layer Structure

While the jet trajectory describes the penetration of jet fluid into the crossflow direction, the jet shear layer controls the mixing and the flame stabilization of JICF, particularly in the near-field. This section examines the time-averaged characteristics of the windward and leeward shear layers in non-reacting and reacting JICF. Figure 3.9 shows contour plots of the time-averaged z-component of vorticity, $\langle\omega_z\rangle$, non-dimensionalized by the inverse characteristic jet time-scale, $1/\tau_{\mathrm{j}} = U_{\mathrm{j}}/d_{\mathrm{j}}$. As expected, the highest mean vorticity is found in the jet shear layers. The right-handed coordinate system gives positive values of

vorticity in the windward shear layer and negative values in the leeward shear layer. The jet center streamline trajectory is shown as a spatial reference by the dashed black line, and the two additional curves shown with blue and red dashed lines correspond to the windward and leeward shear layer trajectories, respectively. The windward (leeward) shear layer trajectory is defined as the locus of points of maximum (minimum) time-averaged z-component vorticity extracted from a set of lines drawn normal to the jet center streamline trajectory at equal arc length intervals. Unlike the jet center streamline, however, the windward (leeward) shear layer trajectory is defined only for $s/d_\mathrm{j} \leq 8$ because clear maxima (minima) in $\langle \omega_z \rangle$ are not found past that point due to the increasing three dimensionality of the flow.

Differences in the mean vorticity decay rate along the windward and leeward shear layer trajectories point to the sensitivity of JICF to changes in J, S, and the presence/absence of combustion. Mean shear layer vorticity in the windward and leeward shear layers is plotted as a function of s/d_j in Figure 3.10. The windward (leeward) shear layer vorticity has been normalized by the maximum (minimum) vorticity to emphasize the rate of vorticity decay in the shear layer. Note that the curves in Figure 3.10 start at $s/d_\mathrm{j} = 0.75$ because the vorticity field is not resolved below that point. The solid lines reflect high J cases and the dashed lines correspond to low J cases. Windward shear layer vorticity drops to less than 20% of its peak value in the first $3-4d_\mathrm{j}$ for the low J cases. The leeward shear layer vorticity decays slightly slower, requiring up to $5d_\mathrm{j}$ to reach the same threshold. The two reacting, low J cases exhibit very similar behavior, while the mean vorticity decay is slightly faster in the non-reacting, low J case. The high J cases initially follow the low J results before shifting to a lower rate of decay around $s/d_\mathrm{j} = 2.5$. The high J cases are also more sensitive to changes in S and the presence/absence of combustion. Mean shear layer vorticity drops fastest in the low S case, followed by the non-reacting, unity S case. The reacting, unity S case exhibits the slowest decay, which is also apparent by visual inspection of Figure 3.9.

The windward and leeward shear layers also contain the peak RMS velocity, as shown by the contour plots of RMS velocity normalized by U_j in Figure 3.11. Interestingly, the peak RMS velocity does not usually occur right at the jet exit, which is where the highest

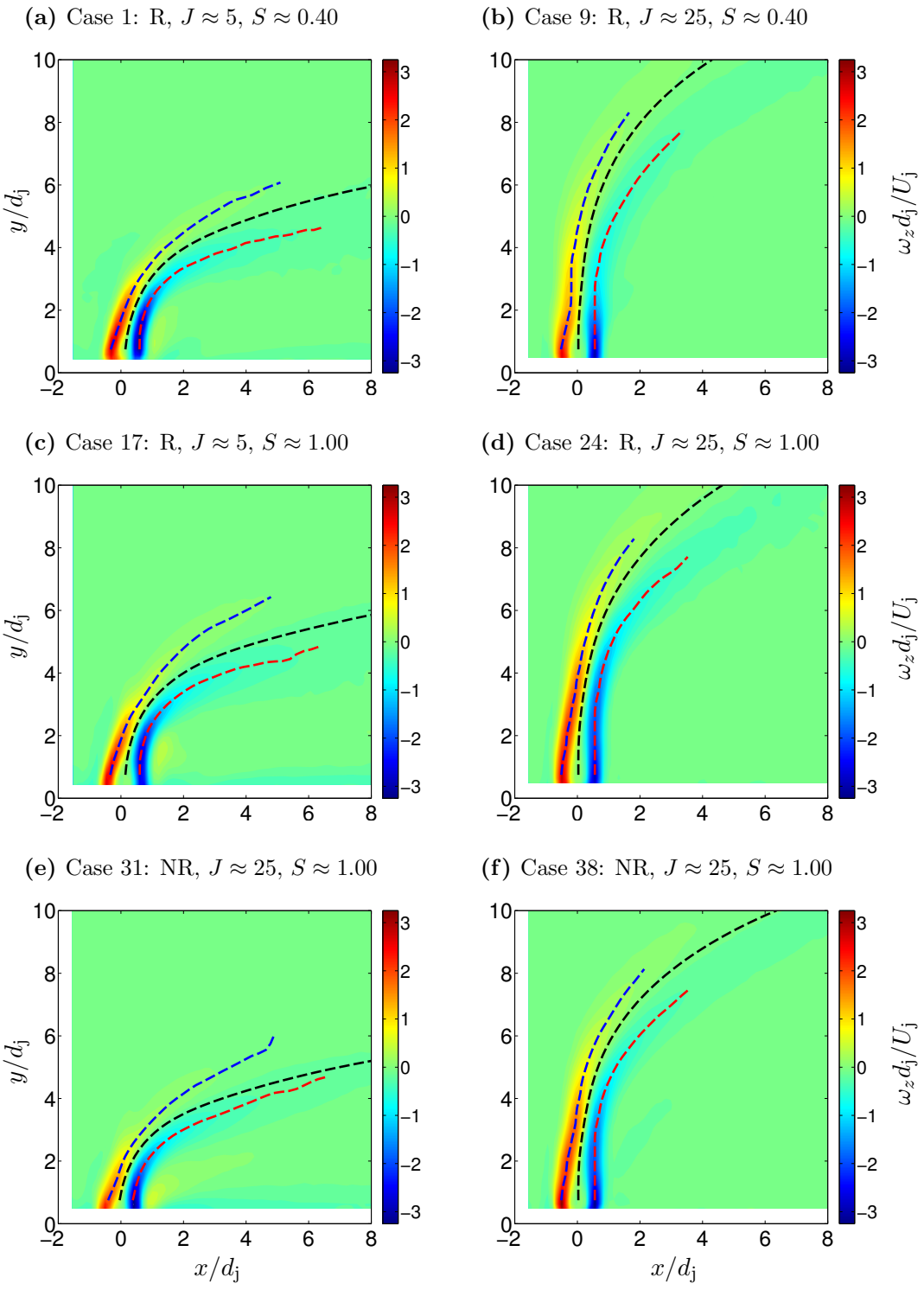

Figure 3.9: Time-averaged windward and leeward shear layer trajectories overlaid on non-dimensional, time-averaged z-component vorticity measured on the $z = 0$ jet centerplane. (---): mean windward shear layer trajectory, (---): mean jet center streamline trajectory, (---): mean leeward shear layer trajectory.

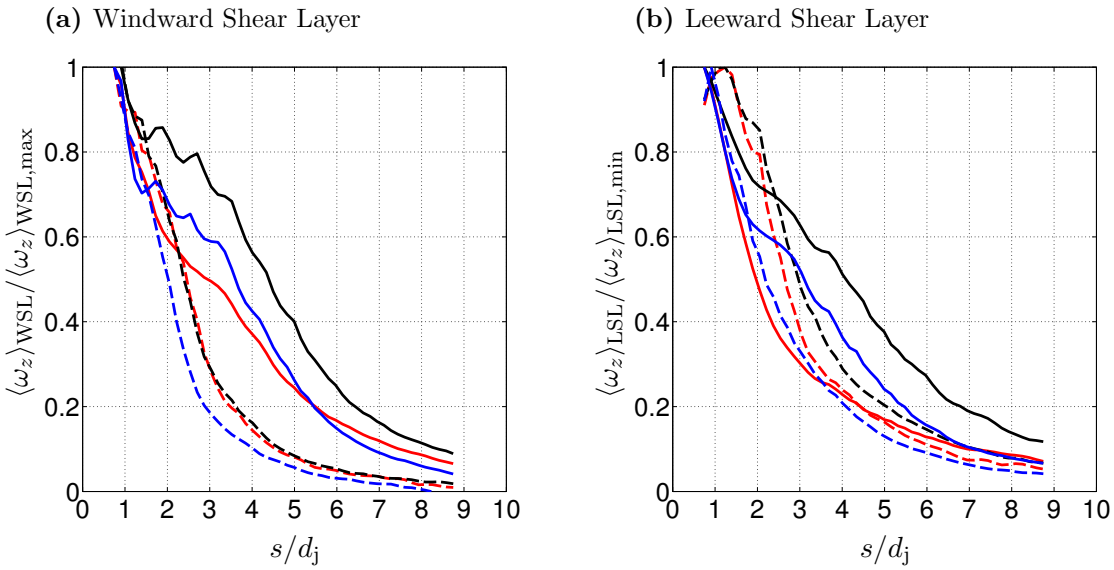

Figure 3.10: Normalized mean z-component vorticity decay in the windward and leeward shear layers as a function of arc length along the jet center streamline trajectory. (---): Case 1, Reacting, low S, low J, (---): Case 17, Reacting, unity S, low J, (---): Case 31, Non-reacting, unity S, low J, (—): Case 9, Reacting, low S, high J, (—): Case 24, Reacting, unity S, high J, (—): Case 38, Non-reacting, unity S, high J.

mean vorticity was found due to the thin shear layers and high mean velocities in that region. Rather, the RMS velocity tends to peak 3 to 5 d_{j} downstream after the jet has begun to deflect into the crossflow direction. The RMS velocities are generally higher in the windward shear layer relative to the leeward shear layer. Further downstream, after the shear layers merge, a broad region of high RMS velocity straddles the jet trajectory before ultimately decaying. The highest RMS velocities (relative to U_{j}) are always found in the low J cases. The low J, reacting jets have roughly 50% higher peak RMS velocities than the non-reacting, low J case. The effect of combustion is less obvious at high J. High RMS values persist further downstream in the reacting, unity S cases (for both low and high J) relative to the either the reacting, low S cases or the non-reacting, unity S cases.

Figure 3.12 re-plots the RMS velocities normalized by the local mean velocity instead of the jet exit velocity to emphasize the local intensity of the fluctuating velocity field. This scaling shows that the wake region has high relative RMS velocities even though the absolute RMS fluctuations are on the order of that found in the turbulent crossflow. The RMS velocity fluctuations in the jet core are very low relative to the mean velocity. The low

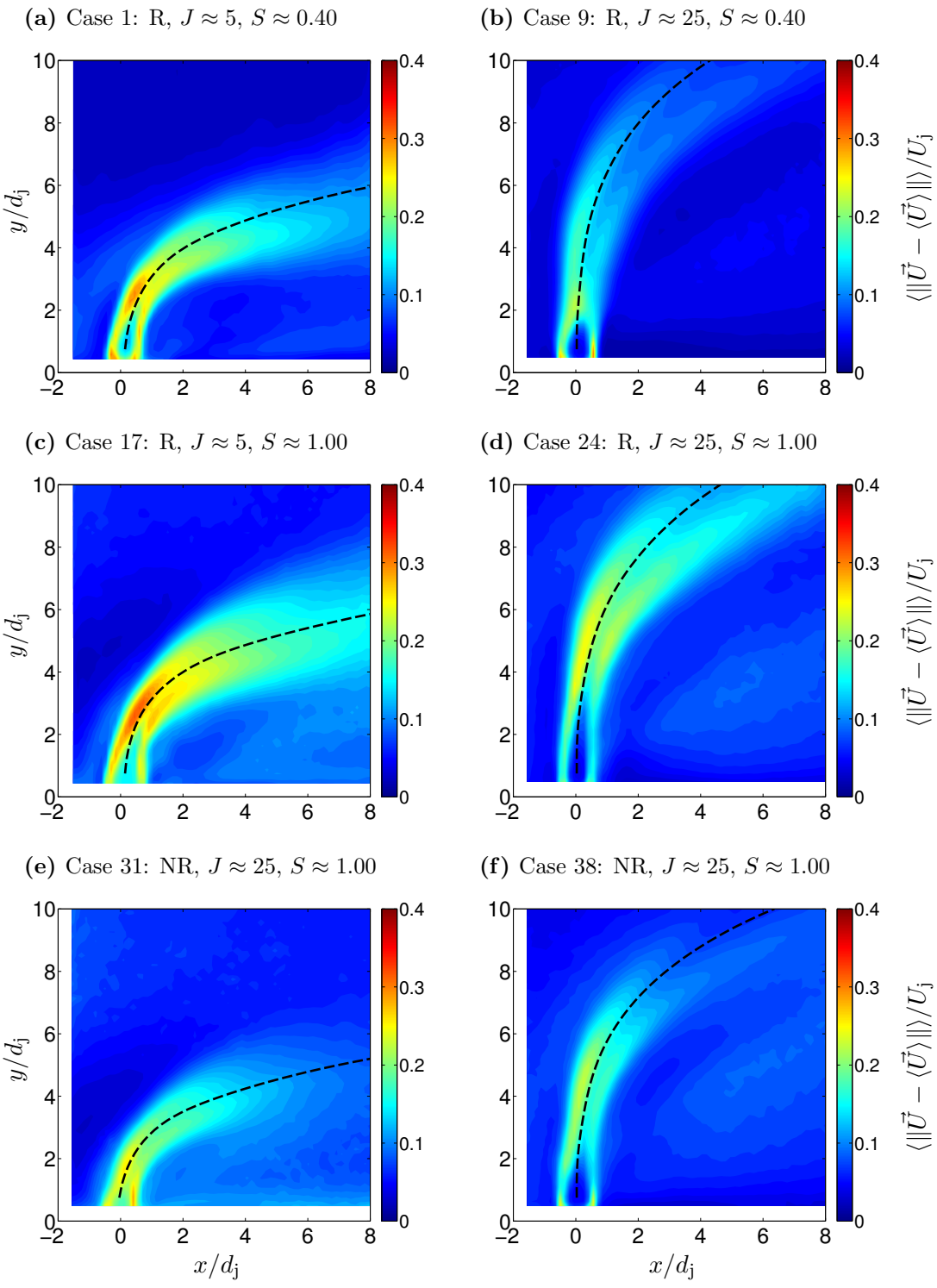

Figure 3.11: Non-dimensional RMS velocity fluctuations measured on the $z/d_j = 0$ jet centerplane overlaid with time-averaged, two-dimensional streamlines. (---): jet center streamline trajectory.

J reacting cases have significantly higher relative RMS velocity in the wake region, while the wake region in the high J jets is less affected by combustion. In all cases, a region of high relative RMS is found upstream of the jet, away from the wall, and just outside the windward shear layer. This region is in close proximity to the location where the sign of $\langle V \rangle$ transitions from positive to negative upstream of the jet (see Figure 3.2). This holds for both low and high J cases but is more pronounced in the reacting cases. The RMS velocities in this upstream stagnation region are on the order of the mean flow velocity. Both of the reacting, low J jets have a region of high relative RMS velocity on the leeward side of the jet near the end of the jet potential core. Note that this region coincides with the location identified by Grout et al. [88] as critical to partially-premixed flame stabilization in the JICF. A region of very low RMS velocity is sandwiched between the aforementioned region of high relative RMS velocity and the lower wall in these reacting, low J jets. This low relative RMS velocity region is noteworthy since the mean velocity is very low as well in this region, seemingly providing an ideal flame stabilization location if the local mixture fraction was suitable. The high J jets also contain a pocket of low relative RMS velocity in the wake region but the location is quite different than in the low J jets. In particular, the pocket of low relative RMS velocity in the high J cases is removed from the wall and follows the jet trajectory. Comparison with the mean x and y-component velocity fields in Figures 3.4 and 3.2 shows that this region of low relative RMS velocity almost exactly corresponds to the region of low $\langle U \rangle$ and high $\langle V \rangle$ described previously. Collectively, this information suggests that the region of low relative RMS velocity in these high J cases is due to unburnt crossflow fluid entrained into the leeward-side of the jet that has not yet entered the leeward shear layer. The higher relative RMS velocity fluid below this region is due to unsteady wake vortices shed from the back side of the jet core, and the region of higher relative RMS velocity above is due to combustion occurring in the leeward shear layer.

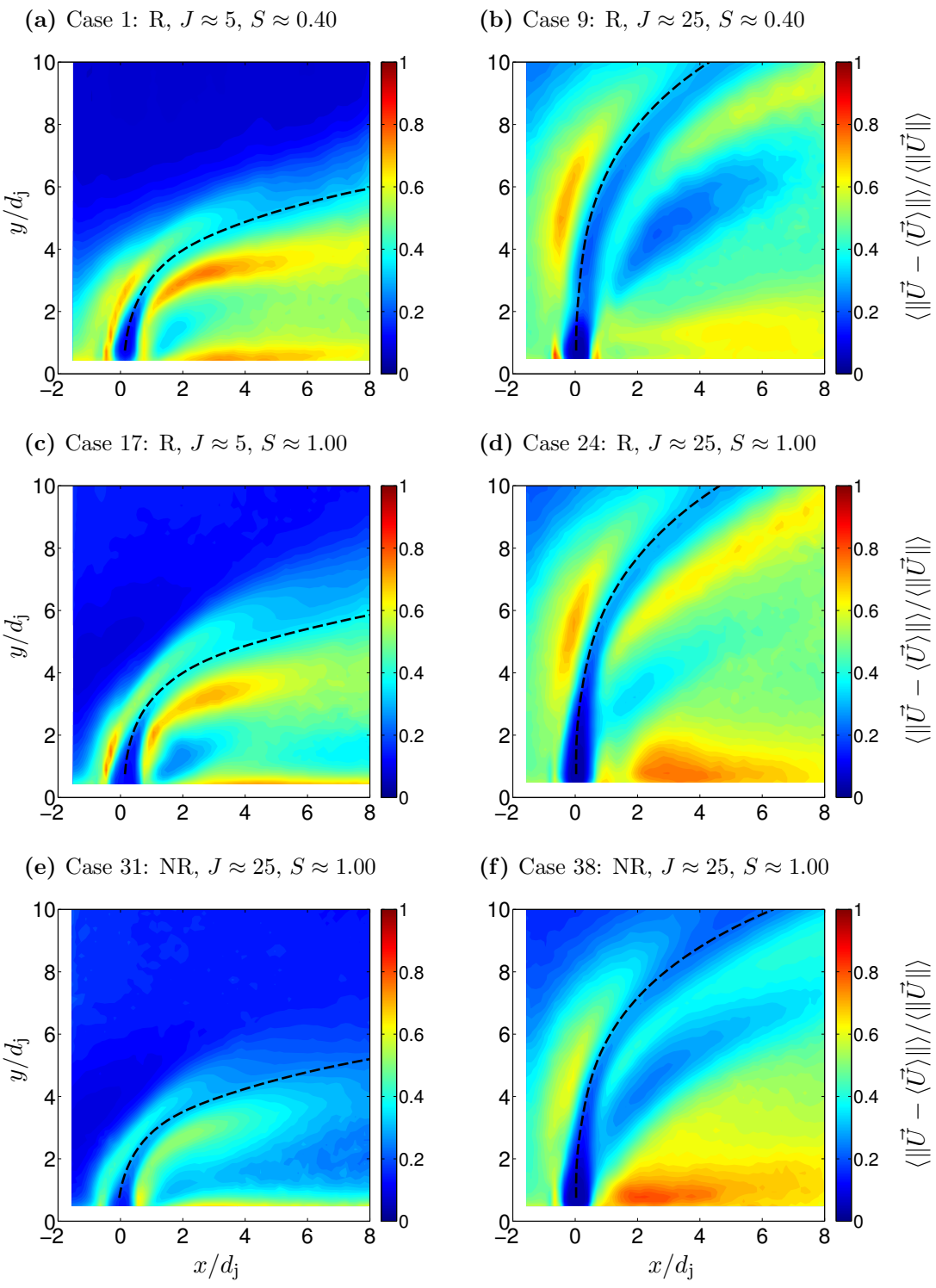

Figure 3.12: RMS velocity fluctuations measured on the $z/d_j = 0$ jet centerplane normalized by local velocity magnitude and overlaid with time-averaged, two-dimensional streamlines. (**---**): jet center streamline trajectory.

3.1.4 Reaction Zone Structure

This section presents time-averaged OH PLIF results and discusses the reaction zone structure of non-premixed jets with different J and S injected into high-temperature, vitiated crossflow. Contour plots of normalized OH PLIF intensity are shown in Figure 3.13 for the four unforced, reacting cases considered throughout this chapter. The dashed white line shows the jet center streamline trajectory, while the solid white and solid magenta lines denote the $\langle U \rangle = 0$ and $\langle V \rangle = 0$ contours, respectively. A few general observations regarding the OH PLIF images can be made that hold for each of the four cases regardless of J or S. First, the crossflow and the jet potential core have close to zero OH PLIF signal. The region of low OH PLIF signal associated with the jet core, which will be referred to as the dark core region, persists further downstream and remains roughly aligned with the jet center trajectory. Secondly, regions of high OH PLIF signal are located at the jet periphery on both the windward and the leeward sides of the jet. The high OH PLIF region on the windward side of the jet sits closer to the jet center streamline trajectory than the region of high OH PLIF intensity on the leeward side of the jet. Thirdly, the highest mean OH PLIF signal is always found on the leeward side of the jet and generally has a value about $3\times$ the peak OH PLIF signal observed in the windward shear layer.

The superposition of the $\langle U \rangle = 0$ velocity contour on top of the mean OH PLIF field reveals a surprising result concerning the composition of the fluid on the leeward side of the low J jets. Specifically, we can infer that the reverse flow region contains a non-flammable mixture of jet gases and combustion products. This is the only explanation for the existence of a low velocity, low strain rate region with very low OH PLIF signal near a 70% H_2 jet in a 1200K crossflow. The reverse flow region in the low S, high J case also contains negligible OH PLIF signal, but this is less noteworthy since the reverse flow region sits inside the jet core. The recirculation of burnt combustion products into the wake of the low J jets is also consistent with the wider dark core region in these cases as compared to the high J jets. The high J jets have much higher wall-normal velocity relative to U_∞ and thus tend to convect burnt products away from the wall before they can be swept around the jet and into the wake region. The increased inclination angle of the low J jets relative to the lower

wall also impedes the ability of fresh oxidizer in the crossflow to reach the wake region. This effect can be visually interpreted by treating the jet as column oriented at some angle into the crossflow direction. A unit of crossflow fluid at a given y/d_{j} has to travel further in the axial direction to reach the backside of the column when the column is tilted away from the wall-normal direction.

The reverse flow region in the unity S, high J case, on the other hand, not only coincides with non-zero OH PLIF signal but also overlaps the region containing peak OH PLIF signal. This observation is in contrast to the low S, high J case where the highest OH PLIF intensity is located further downstream and is centered about $6d_{\mathrm{j}}$ away from the wall. The region containing high OH PLIF signal in the low S, high J case is, however, well-correlated with the region of low axial velocity magnitude (see Figure 3.4b). It is important to remember that a low S case will tend to exhibit higher local strain rates when J is held constant because the low S case will have a higher U_{j}. In the low S, high J case, the combination of a much smaller reverse flow region and the increased local strain rate are sufficient to shift the location of maximum mean OH PLIF signal downstream (relative to the unity S case) despite the fact that the low S mixture is the more stretch resistant mixture. The difference in stretch sensitivity is due to the different diluents used in the low S and unity S cases; i.e., the diluent (30% by volume) is primarily He in the low S cases and is primarily N_2 in the unity S cases.

The time-averaged structure of the high OH PLIF region in the windward shear layer is quite different from that in the leeward region. Most notably, the windward OH region is narrower and has lower peak OH PLIF signal. It is instructive to explore the physical mechanisms that contribute to these differences between the windward and leeward reaction zones. The jet/crossflow mixing dynamics on the leeward side of the jet are quite different from those in the windward shear layer. The windward shear layer is dominated by the SLV, while the CRVP and the upright WV are also important on the leeward side of the jet. The characteristic time scale (period) for the SLV is $\sim 1/2$ that of a CRVP turnover time and $\sim 1/10$ that of the period for WV shedding [54]. Thus, the windward region on average experiences higher strain rates. More highly strained flames have lower flame temperatures,

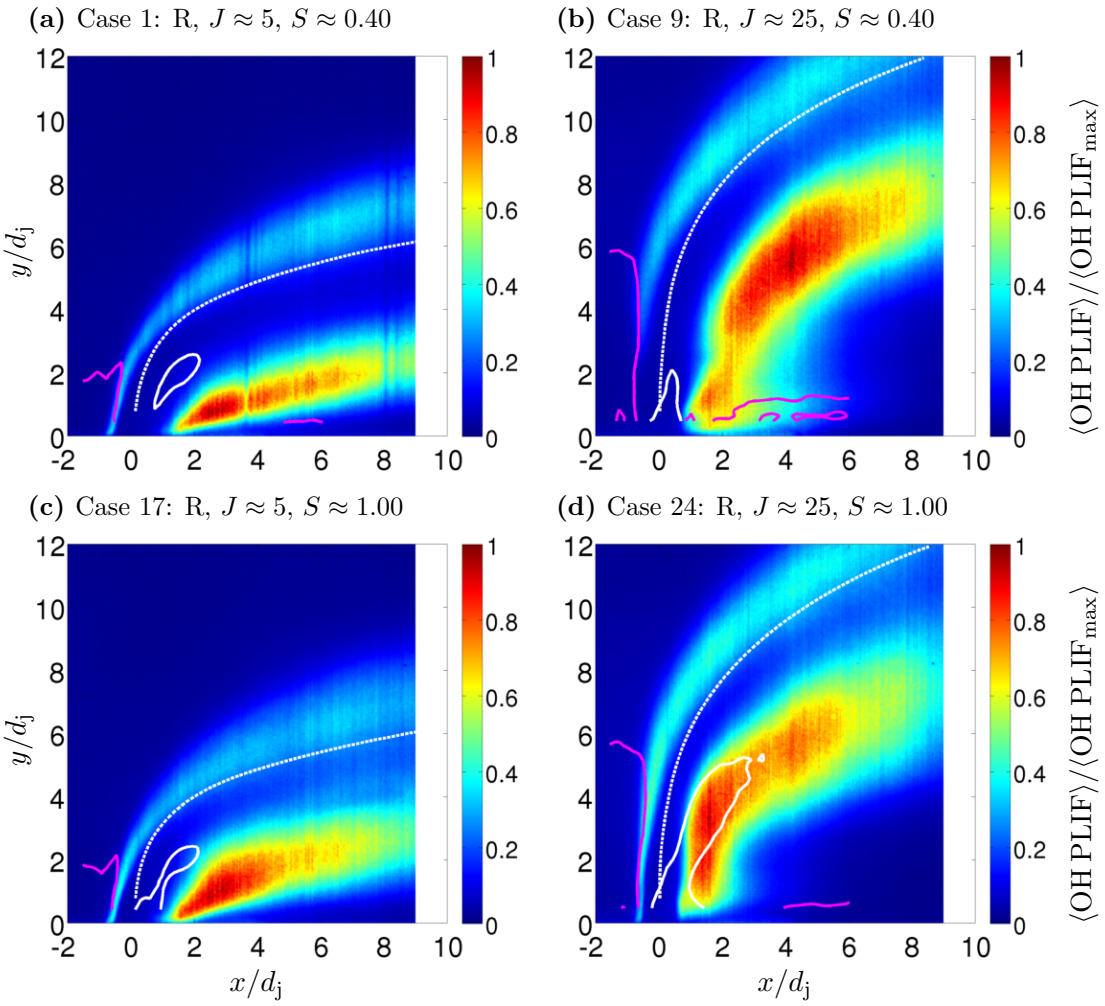

Figure 3.13: Normalized time-averaged OH PLIF intensity for four different unforced test conditions. (—): Zero y-velocity contour, (▬): Zero x-velocity contour (▬ ▬): Mean jet center streamline trajectory.

which reduces OH concentration. Note that flame flapping on the windward side of the jet is responsible for spreading out the time-averaged OH PLIF intensity downstream, but the low OH PLIF signal near the jet injector in the windward shear layer cannot be explained by a similar mechanism since the OH PLIF layer is very narrow. In addition to the important differences in coherent structures, the basic geometry of the JICF leads to key differences in the mixture composition in the windward and leeward regions. The windward reaction zone can be considered as a thin interface separating fuel in the jet from oxidizer in the crossflow. The situation is more complex on the leeward side since the resulting burnt combustion products are continuously entrained into the wake of the jet. The entrainment

of combustion products complicates the interpretation of the OH PLIF measurements, but more importantly, the combustion products further dilute the already vitiated oxidizer mixture. This effectively decreases z_{st} in the wake region and forces fuel molecules on the leeward side of the jet to travel further away from the jet core to find O_2. The combustion products generated in the wake are likely to remain trapped in the wake and thus serve to further dilute the oxidizer mixture.

In the low J cases, the location of peak OH PLIF signal in the windward shear layer is found roughly $1d_{\mathrm{j}}$ away from the jet injector, and the FWHM thickness near the peak OH PLIF signal is $\mathcal{O}(1\mathrm{mm})$. The OH PLIF layer in this region is sandwiched between the $\langle V \rangle = 0$ contour (shown in magenta) and the jet potential core. The thickness of the windward OH PLIF layer grows with increasing arc length distance, s, along the jet trajectory. This effect is primarily related to increasing flame flapping amplitude, which will be discussed in Section 3.2.2 after edge tracking the instantaneous OH PLIF images. Note that local scalar dissipation, χ, also tends to decrease with s and could contribute to broader OH PLIF regions further downstream.

The unity S, high J case also appears to support an attached flame in the windward shear layer, although the flame is narrower than in either of the low J cases. The maximum OH PLIF signal in the windward shear layer is located further downstream near $y/d_{\mathrm{j}} = 5$. These observations reflect the higher local χ found in the windward shear layer of the high J case. Further downstream, the width of the high OH PLIF region on the windward side remains narrower than the high OH PLIF region on the leeward side of the jet. This is in contrast with the low J cases where both the windward and leeward OH PLIF regions have similar thicknesses further downstream.

No OH PLIF signal is found in the windward shear layer below $y/d_{\mathrm{j}} \sim 2$ in the low S, high J case, which clearly indicates the existence of a lifted flame and the potential for a different flame stabilization mechanism. The absence of combustion in the first few jet diameters along the windward shear layer affects the composition of the gases swept around the jet core and entrained into the wake of the jet. The mixture transported into the wake will not contain combustion products and will be partially-premixed. The dark core without

any OH PLIF signal is also noticeably wider in the low S, high J case relative to the unity S, high J case. Note that the stoichiometric mixture fraction for the low S cases (see Table 3.2) is a factor of 3 smaller than z_{st} in the unity S jets. The smaller z_{st} value means that more oxidizer must be entrained to achieve a stoichiometric mixture fraction. Conceptually, the jet shear layer must transport the jet fluid further into the crossflow before combustion will occur, which agrees well with the experimental observation of wider dark core regions in the low S cases.

Figure 3.14 shows OH PLIF isocurves superimposed on contour plots of $\langle \omega_z \rangle$ to investigate the location of the reaction zone relative to the shear layer. The low J results confirm the presence of a thin windward flame front anchored in the jet shear layer. The 15% isocurve overlaps more of the windward shear layer in the unity S case than in the low S case. This is consistent with the differences in z_{st} mentioned above as well as the fact that the low S case is more highly strained. The region of high OH PLIF intensity on the leeward side of the low J jets does not follow the curvature of the leeward shear layer in a similar manner as is seen in the windward shear layer. Clearly, the near-wake region is starved of O_2 and, thus, cannot support the same type of flame front seen in the windward shear layer. The O_2 deficiency stems from the entrainment of products into the the jet wake and the tendency of those products to remain trapped in the low velocity region between the lower wall and the bottom edge of the jet. Interestingly, the high OH PLIF region on the leeward side is actually anchored in the leeward shear layer right at the wall. The local mixture fraction in this location is more favorable for combustion because combustion products generated immediately adjacent to the lower wall are transported away by the predominantly wall-normal jet flow velocity, while combustion products generated a few d_{j} downstream where the jet has significantly deflected into the crossflow direction experience a much lower wall-normal velocity and tend to remain trapped in the wake of the jet. The high J cases, on the other hand, maintain a much larger wall-normal velocity over a larger area, which serves to convect burnt products in the jet wake out of the crossflow boundary layer and enables fresh oxidizer to reach the trailing edge of the jet. Hence, the leeward shear layer anchors a very robust reaction zone in the high J cases. Note that the 60%

mean OH PLIF isocurve actually sits closer to the leeward shear layer in the high J cases than in the low J cases even though the strain rates are much higher in the high J cases.

The low S, high J case in Figure 3.14b merits further discussion since the lifted flame in this case makes it an outlier. The 15% isocurve in the windward shear layer is removed from the wall and sits outside the region of high $\langle\omega_z\rangle$. The scalar dissipation in the windward shear layer, at least in the first few d_j, for this case presumably exceeds the maximum value at which a non-premixed flamelet can survive even in a 1200K crossflow. The shear layer evolution is also altered since combustion heat release is no longer present (on average) in the initial development region, which will be explored in more depth in Chapter 5.

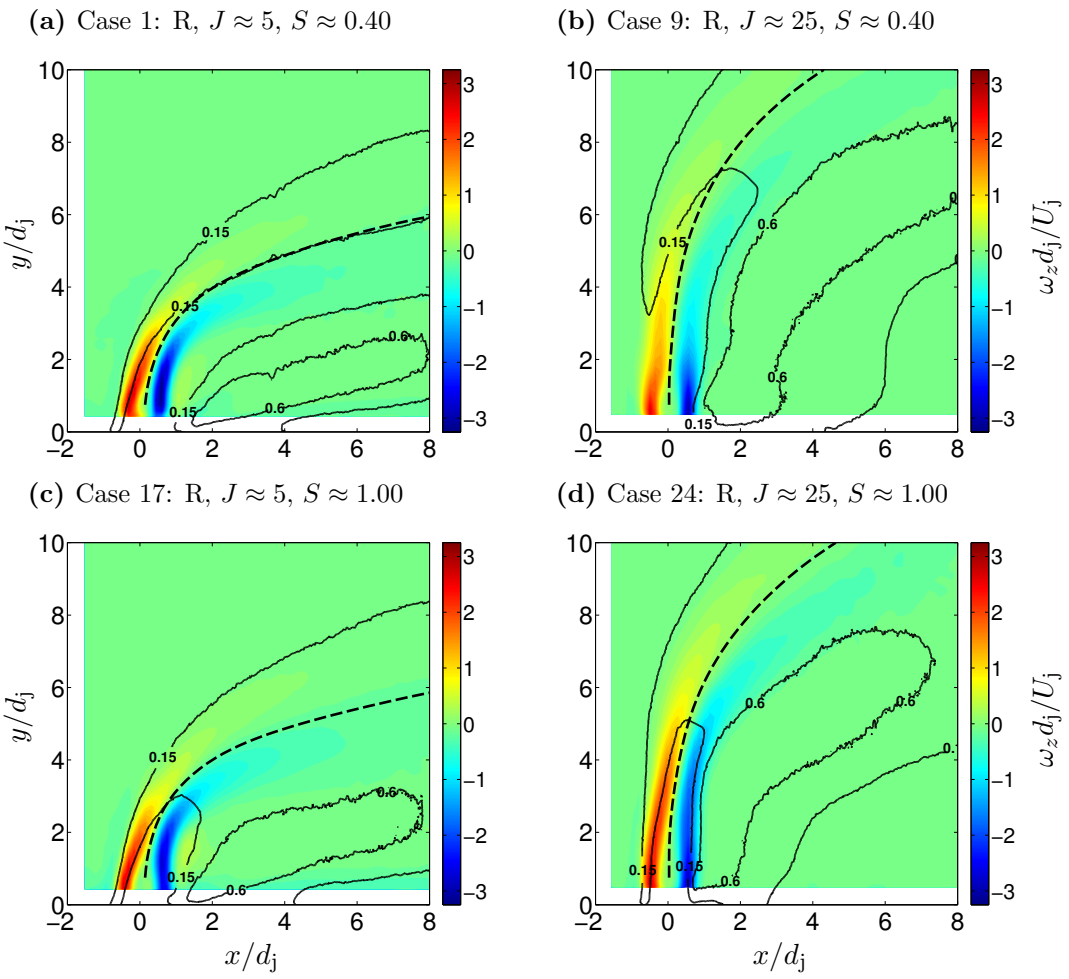

Figure 3.14: Non-dimensional, time-averaged z-component of vorticity overlaid with 15% and 60% mean OH PLIF intensity contour lines. (——): OH PLIF intensity contours, (- - -): Jet center streamline trajectory.

The largest fluctuations in the OH PLIF signal are also found in the jet shear layers, as shown in Figure 3.15, although generally several d_{j} removed from the jet injection point. The left-hand column of Figure 3.15 shows the RMS fluctuations normalized by the maximum fluctuation in the field of view, while the right-hand column shows RMS fluctuations normalized by the mean OH PLIF signal. The strength of the RMS fluctuations are similar between the windward and the leeward shear layers, but the the windward shear layer fluctuations are much stronger relative the local mean OH PLIF signal. The primary reason for this discrepancy is that the windward flame branch is more unsteady and is more likely to flap into a region with very low mean OH PLIF signal. The RMS plots also indicate a sensitivity to changes in S. In particular, the dark core region with near zero RMS fluctuations is wider and extends further in the low S cases, for both low and high J.

$\langle$**RMS OH PLIF**$\rangle/\langle$**RMS OH PLIF**$\rangle_{\mathbf{max}}$

(a) Case 1: R, $J \approx 5$, $S \approx 0.40$

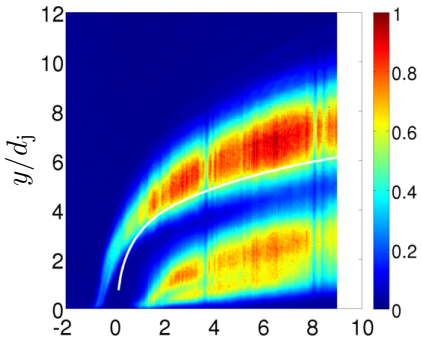

(c) Case 9: R, $J \approx 25$, $S \approx 0.40$

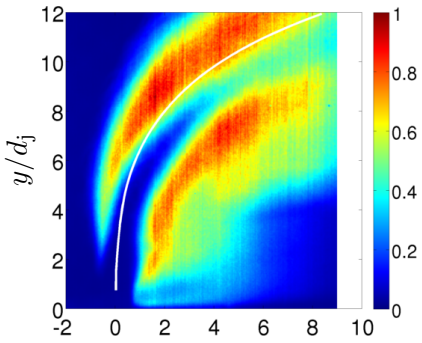

(e) Case 17: R, $J \approx 5$, $S \approx 1.00$

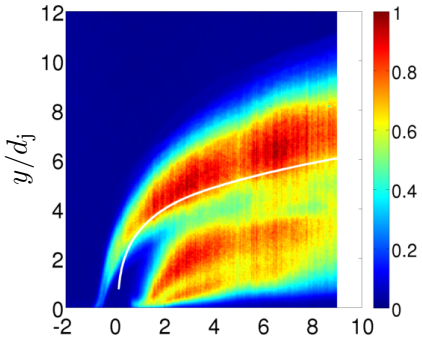

(g) Case 24: R, $J \approx 25$, $S \approx 1.00$

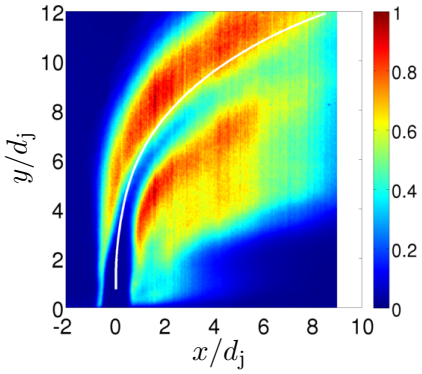

$\langle$**RMS OH PLIF**$\rangle/\langle$**OH PLIF**$\rangle$

(b) Case 1: R, $J \approx 5$, $S \approx 0.40$

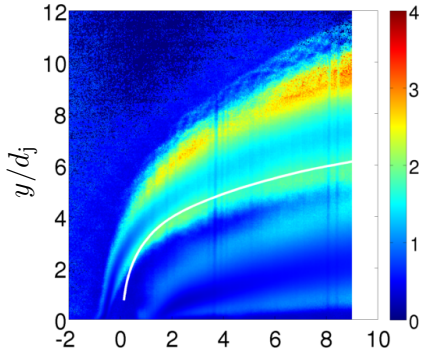

(d) Case 9: R, $J \approx 25$, $S \approx 0.40$

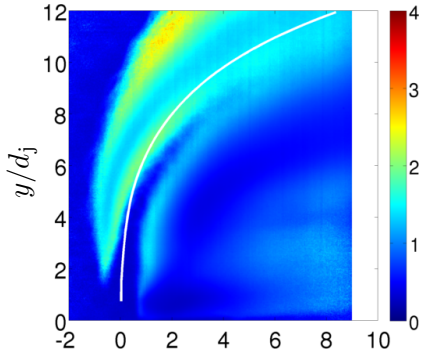

(f) Case 17: R, $J \approx 5$, $S \approx 1.00$

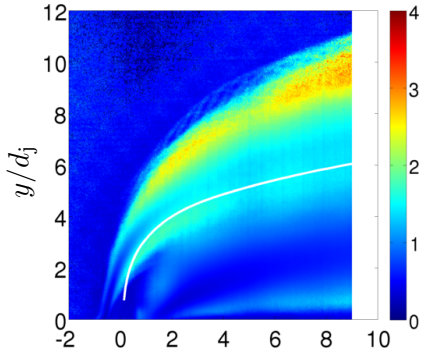

(h) Case 24: R, $J \approx 25$, $S \approx 1.00$

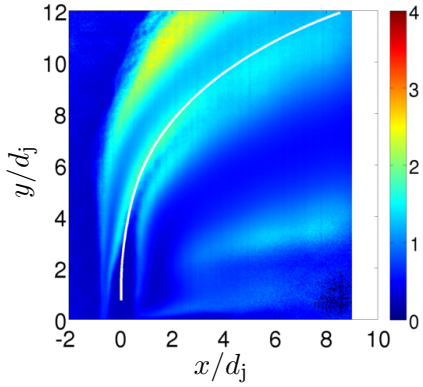

Figure 3.15: Normalized RMS OH PLIF intensity. (▬): Mean jet center streamline trajectory.

3.2 Instantaneous Features of the Flow Field

3.2.1 Velocity Field

This section discusses instantaneous features of unforced JICF. Figure 3.16 presents contour plots of the instantaneous velocity magnitude on the jet centerplane normalized by the mean jet exit velocity, U_j. Two-dimensional streamlines are overlaid with thin white lines. Each subfigure corresponds to a single instantaneous SPIV measurement at one of the unforced test conditions listed in Table 3.1. The representative time instances were selected randomly from each of the full time sequences, which contained approximately 10^4 instantaneous measurements. For consistency, the same six instantaneous time instances will be used throughout the remainder of this chapter when discussing other aspects of the instantaneous flow field.

The largest instantaneous velocity magnitudes are approximately $1.3U_\mathrm{j}$ and are found near the jet injector and inside the jet potential core. The instantaneous velocity magnitude decays non-monotonically along the jet center streamline, which is the result of the high-velocity jet core moving in and out of plane. Two-dimensional streamlines upstream of the jet injection location indicate that the higher J jets cause a greater disruption in the crossflow, while the crossflow fluid beyond $y/d_\mathrm{j} \sim 6$ is relatively undisturbed in the low J cases. Streamlines on the windward side of the jet near the interface between the jet and the crossflow tend to wrinkle and roll-up into concentrated vortices. The leeward side of the jet is characterized by relatively low velocity magnitudes and streamlines that tend to be highly irregular. Recall that both the CRVP and the upright WV exert greater influence on the leeward side of the jet.

Contour plots of the U velocity component are shown in Figure 3.17. The U velocity field in the low J cases beyond $y/d_\mathrm{j} \geq 6$ is relatively unaffected by the presence of the jet and remains close to the nominal crossflow velocity, U_∞. The U velocity is appreciably slowed at all y/d_j values upstream of the jet injection location in the high J cases. On the other hand, U is close to zero for all cases near the jet injector and inside the potential core of the jet. Larger U values are found further downstream of the jet injection location (i.e., $x/d_\mathrm{j} > 1$) after the jet begins to deflect into the streamwise direction. This is particularly

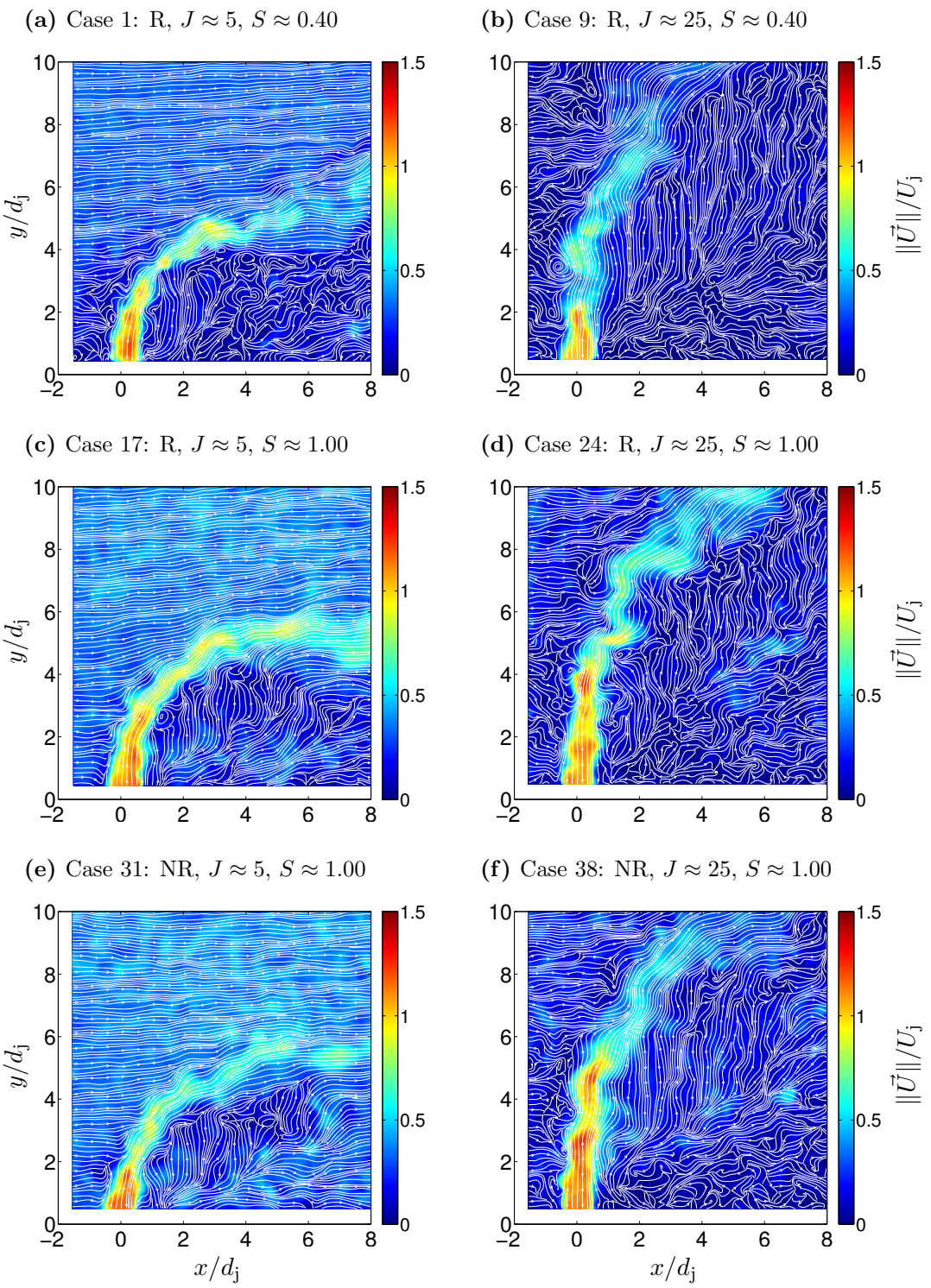

Figure 3.16: Non-dimensional instantaneous velocity magnitude, $|\vec{U}|$, measured on the $z/d_j = 0$ jet centerplane. Two-dimensional streamlines overlaid by thin white lines.

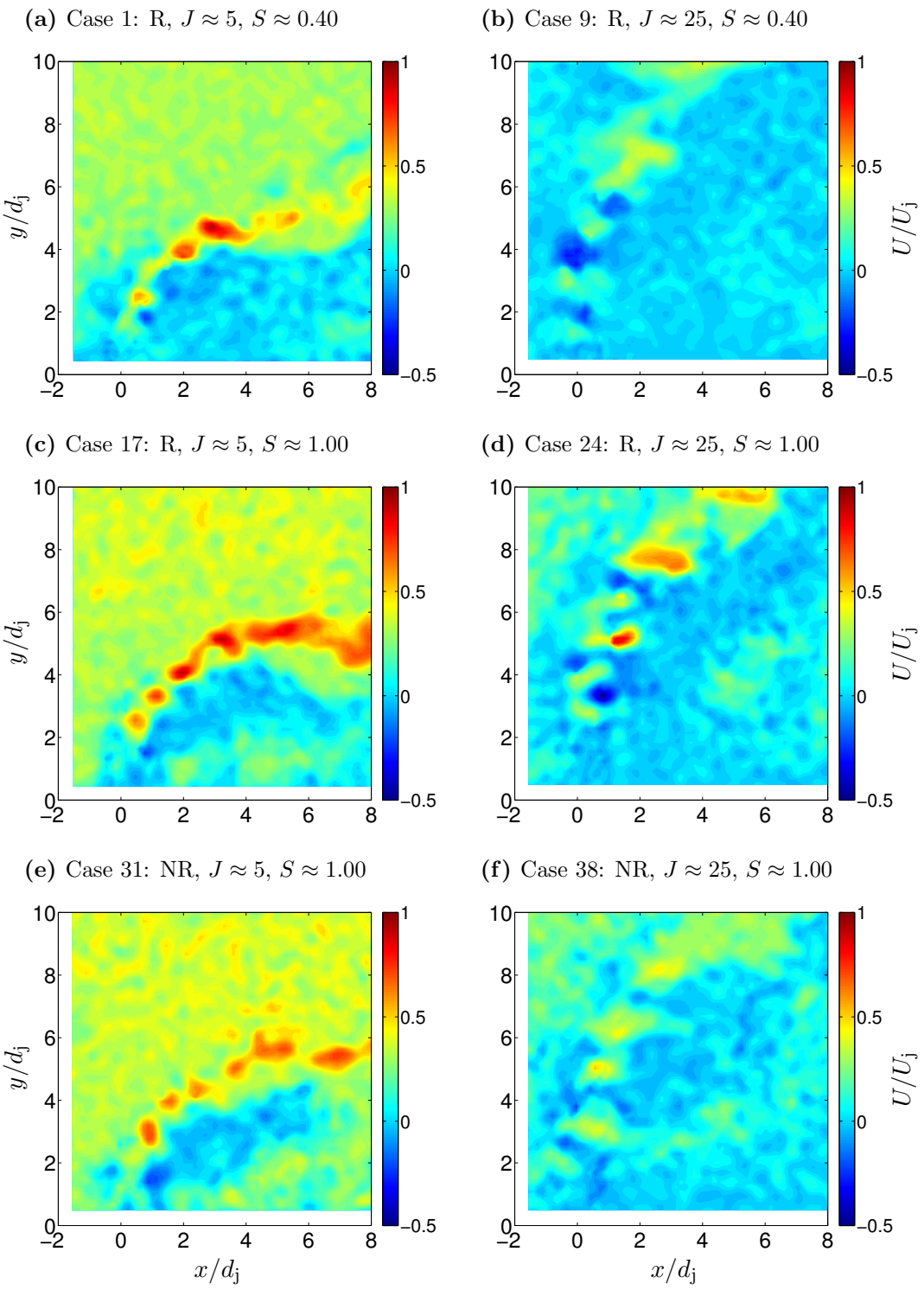

Figure 3.17: Non-dimensional instantaneous x-component of velocity, U, measured on the $z/d_j = 0$ jet centerplane.

evident at low J where U/U_j instantaneously achieves values of $\mathcal{O}(1)$ at axial distances as small as $x/d_\mathrm{j} = 2$.

An interesting pattern of alternating positive and negative velocity is observed in the contour plots of the U velocity beginning approximately $2 - 3d_\mathrm{j}$ downstream of the jet injection location. The initial appearance of this pattern in the U velocity field coincides with the location of the breakdown of the jet core (see Figure 3.16). The spatial proximity suggests that both the breakdown of the jet core and the formation of these alternating regions of positive and negative U velocity may be linked to the same near-field flow structures. The SLV are the dominant coherent structures in the JICF near-field, and their evolution along the jet shear layer may explain the distinctive banded structure seen in the U velocity field. Recall that Kelso et al. [6] proposed a mechanism by which the SLV grow, stretch, distort, and ultimately fold over on themselves along an axis parallel to the z-axis as they convect along the jet shear layer (see Figure 1.7). This folding process causes regions with large positive ω_z from the windward shear layer to interact with regions with large negative ω_z from the leeward shear layer. As a result of this interaction, the region sandwiched between the two opposite-signed vortex structures acquires either an enhanced positive or an enhanced negative U velocity depending on the orientation of the folded shear layer vortex. The resulting regions of positive and negative U velocity are then essentially stacked one on top of the other along the jet trajectory and are seen to persist until the JICF breaks down into turbulence. Note that these regions of alternating positive and negative U velocity are essentially centered along the jet trajectory rather than in either the windward or leeward shear layer, which is consistent with the notion that their formation depends on the collective interaction of both the windward and leeward shear layers.

Contour plots of the instantaneous y-component of velocity, V, shown in Figure 3.18, indicate that V velocity varies much more smoothly in the near-field compared to the irregular U velocity field. The influence of the SLV on the V velocity field is clearly seen in the wavy interface separating regions of high and low V velocity along the windward and leeward shear layers, but there is little evidence of the distinctive banded velocity structure seen along the jet centerline in the U field. Rather, the magnitude of V gradually decreases

as the jet bends into the crossflow direction. The V velocity field primarily convects jet fluid, entrained crossflow fluid, and shear layer structures in the wall-normal direction. The SLV affect the V velocity field because they transport wall-normal jet momentum into the crossflow fluid, but the SLV are not able to wholly alter the structure of the V velocity field, particularly along the jet centerline, in a manner similar to that seen in the U field. This difference reflects the fact that the jet fluid has zero mean x-momentum when the jet enters the crossflow.

The instantaneous shear layer structure is revealed more clearly through contour plots of the instantaneous z-component of vorticity, ω_z, as shown in Figure 3.19. Shear layer vortices become apparent downstream of the jet injection location once the initial vorticity contained in the jet shear layer rolls-up into concentrated vortex cores. Shear layer roll-up occurs preferentially along the windward shear layer, while the leeward vorticity tends to be more irregularly spaced and less likely to roll-up into coherent vortices. Note that the two-dimensional vortex cores seen in Figure 3.19 are really slices through a three-dimensional vortex ring structure that wraps around the jet core. These ring vortices form due to a Kelvin-Helmholtz type instability mechanism near the jet exit and evolve significantly as they are convected along the jet trajectory.

The low J cases shown in Figure 3.19 exhibit enhanced shear layer roll-up relative to the high J cases, which results in a train of independent, regularly spaced vortices in the low J cases. The high J jets also show clear evidence of vortex roll-up but the resulting regions of concentrated vorticity tend to be more amorphous and less regularly spaced. In the high J cases neighboring vortices interact more strongly and undergo vortex pairing in the jet near-field, particularly along the windward shear layer. The windward and leeward shear layer vortices progressively stagger relative to each other as they are convected along the jet trajectory. This observation is consistent with the vortex ring folding mechanism proposed by Kelso et al. [6] and results in concentrated regions of positive and negative vorticity, which were initially aligned horizontally, stacked one on top of the other. The interaction between these vertically stacked regions of opposed vorticity is ultimately responsible for the alternating regions of positive and negative U velocity previously mentioned.

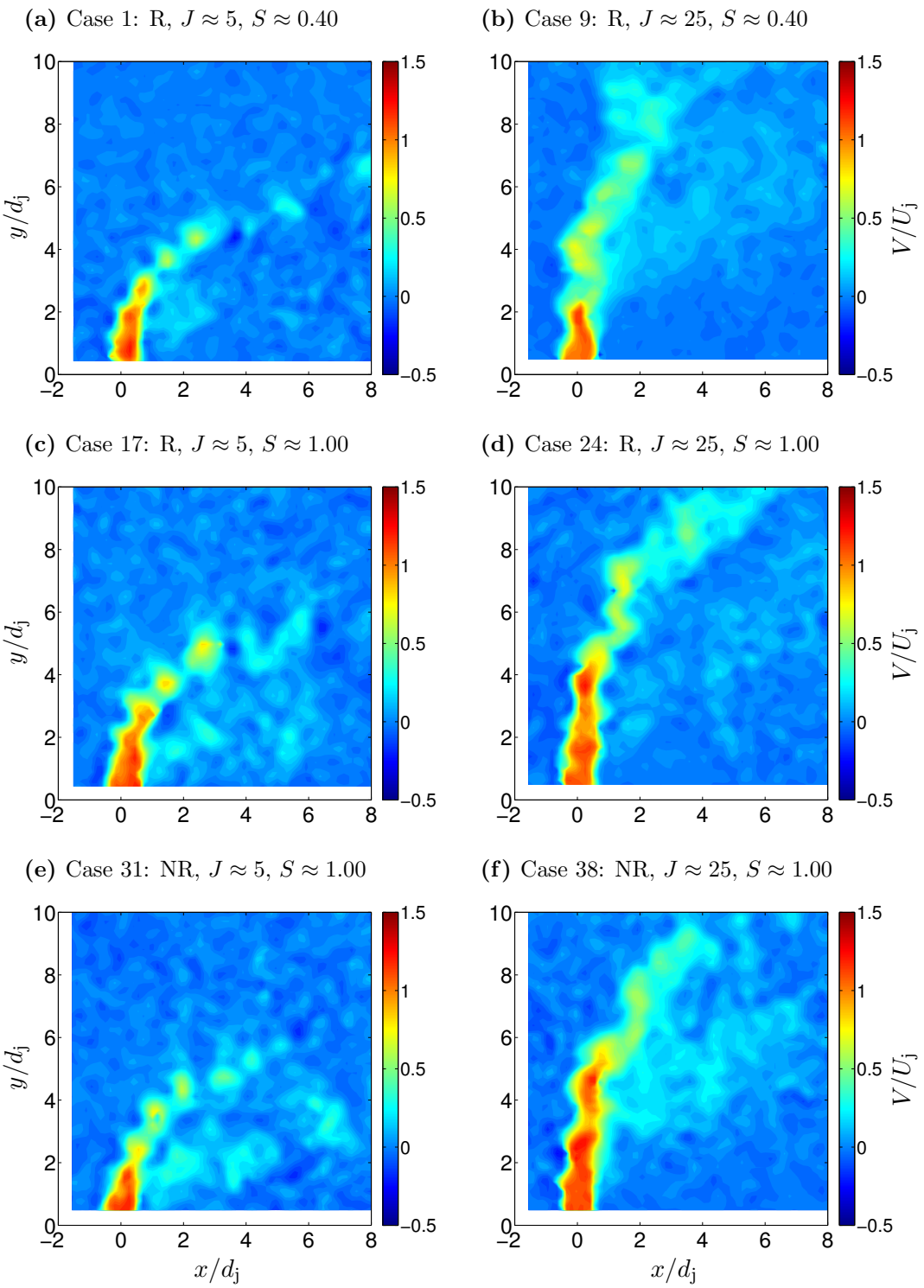

Figure 3.18: Non-dimensional instantaneous y-component of velocity, V, measured on the $z/d_j = 0$ jet centerplane.

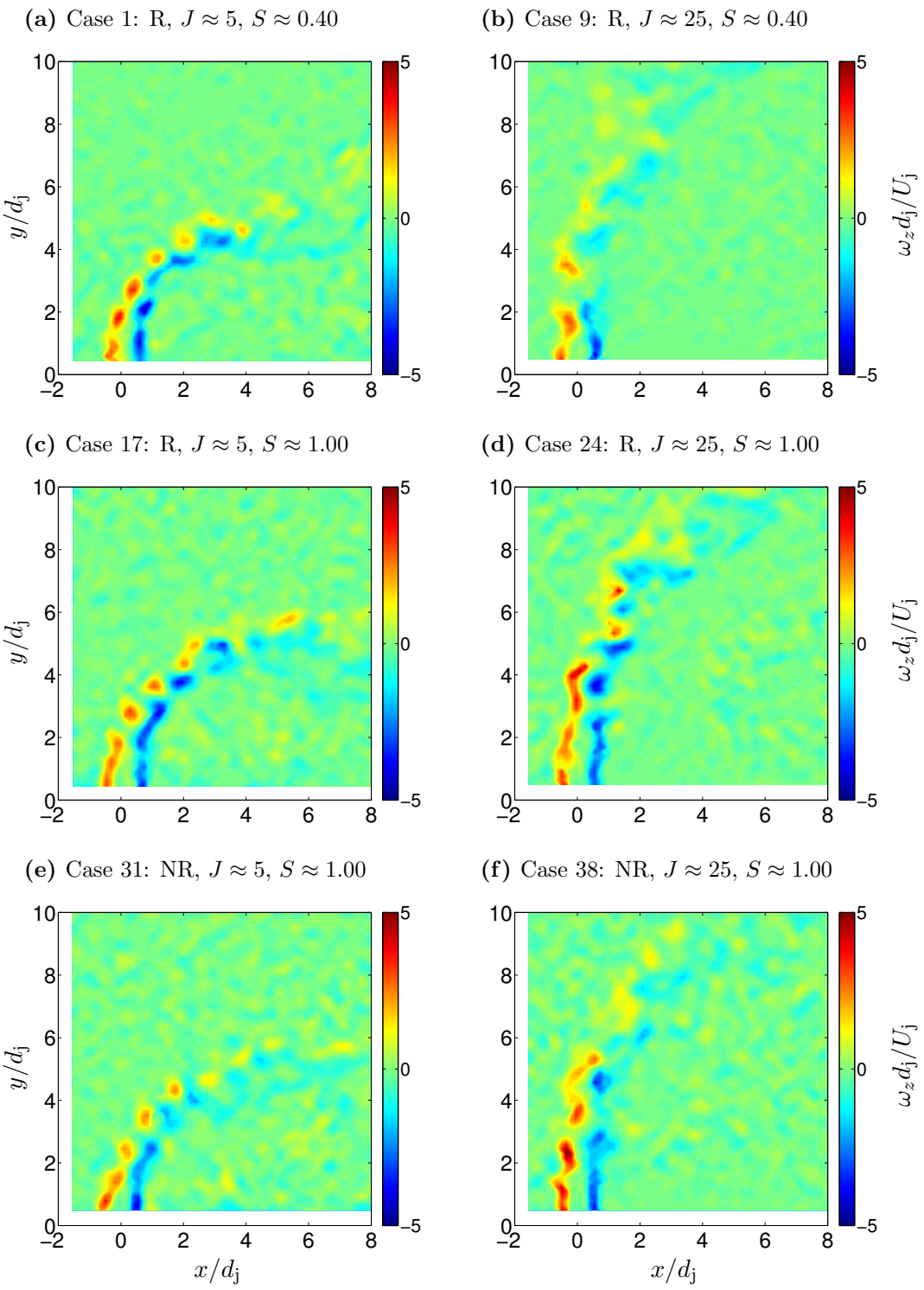

Figure 3.19: Non-dimensional instantaneous z-component of vorticity measured on the $z/d_j = 0$ jet centerplane.

3.2.2 Reaction Zone Structure

Section 3.1.4 discussed time-averaged features of reacting JICF. This section revisits the reaction zone structure of jets injected into vitiated crossflow from an instantaneous perspective using OH PLIF imaging as well as Mie scattering and flame edge tracking. Figure 3.20 presents OH PLIF images obtained simultaneously with the velocity fields discussed in the previous section. The color contour denotes the corrected OH PLIF intensity normalized by the maximum corrected PLIF intensity occurring within the field of view at a specific time instance. In each of the four test conditions, a narrow region with high OH PLIF signal on the windward side of the jet separates the jet core (containing fuel) from the crossflow (containing oxidizer). This observation can only be explained by the presence of a flame front and will be thus referred to as the windward flame branch. The windward flame branch is attached near the jet injector lip at the lower wall of the test section in three out of the four test conditions shown in Figure 3.20. The lone exception is the low S, high J case, which has a lifted windward flame branch.

The region of high OH PLIF signal on the leeward side of the jet is, however, much broader and more diffuse. In the low J cases, the signal strength of the high OH PLIF region on the leeward side is also more uniform relative to the windward side. Conversely, the leeward side of the high J cases is more irregular and shows greater variation in the OH PLIF signal. Regions containing low, but non-zero, OH PLIF signal tend to surround the regions of high OH PLIF signal on the leeward side for both low and high J cases. This low-level OH PLIF signal points to the presence of combustion products, which are entrained into the leeward side of the jet and are also generated by reactions occurring on the leeward side of the jet.

The strength of the instantaneous OH PLIF signal varies significantly along the windward flame branch, and generally increases in the downstream direction. Notably, the peak OH PLIF signal is at least as likely to occur along the windward flame branch as it is to occur on the leeward side of the jet. This is in contrast to the situation in the time-averaged OH PLIF images where the peak PLIF signal is always located on the leeward side of the jet. The thickness of the windward flame branch tends to increase with distance from the jet

injector, although non-monotonically. To illustrate this trend, Figure 3.21 shows enlarged views of both a near-field and a far-field region of the windward flame branch that were extracted from Figure 3.20a. The colorbar scaling of both enlarged views is identical to that of Figure 3.20a to avoid biasing the comparison. The thickness of the downstream OH PLIF region, $\delta_{\mathrm{OH,downstream}}$, is drawn in both images to illustrate the difference. The downstream flame thickness is approximately twice as thick as the flame thickness near the jet injector, and the OH PLIF signal is roughly three times stronger. Both the change in flame thickness and the increase in PLIF signal are consistent with a less strained, higher temperature flame at the downstream location. These findings are also in agreement with the recent DNS study of a H_2/N_2 jet burning in a 750K air crossflow by Grout et al. [88]. Those authors attributed a decrease in conditional progress variable gradient with downstream distance to an increase in local flame thickness.

The interaction between the reaction zone structure and the underlying fluid dynamics can be better understood by superimposing the instantaneous OH PLIF field on top of the instantaneous vorticity field, as shown in Figure 3.22. The windward flame branch is seen to sit just outside the shear layer and closely follow the instantaneous shear layer trajectory. In the three cases with an attached windward flame branch, the windward OH layer remains thin, relatively straight, and does not wrap around the shear layer vortices. The windward OH layer wrinkles more significantly further downstream after the SLV start to pair and breakdown into three dimensional structures. The positioning of the leeward OH PLIF layer relative to the leeward shear layer varies substantially between the low J and the high J cases. In the low J cases, the leeward reaction zone is displaced from leeward shear layer. Conversely, at high J, the leeward reaction zone essentially follows the leeward shear layer trajectory.

The J dependence of the leeward reaction zone structure can be further explored using simultaneous Mie scattering and OH PLIF imaging, as shown in Figure 3.23. Recall that both the jet and the crossflow fluid are seeded with 0.5μm TiO_2 particles, although the jet fluid is more heavily seeded. The seed density of the jet fluid drops as the jet mixes and reacts with the crossflow fluid. The most dramatic drop in seed density, however, occurs

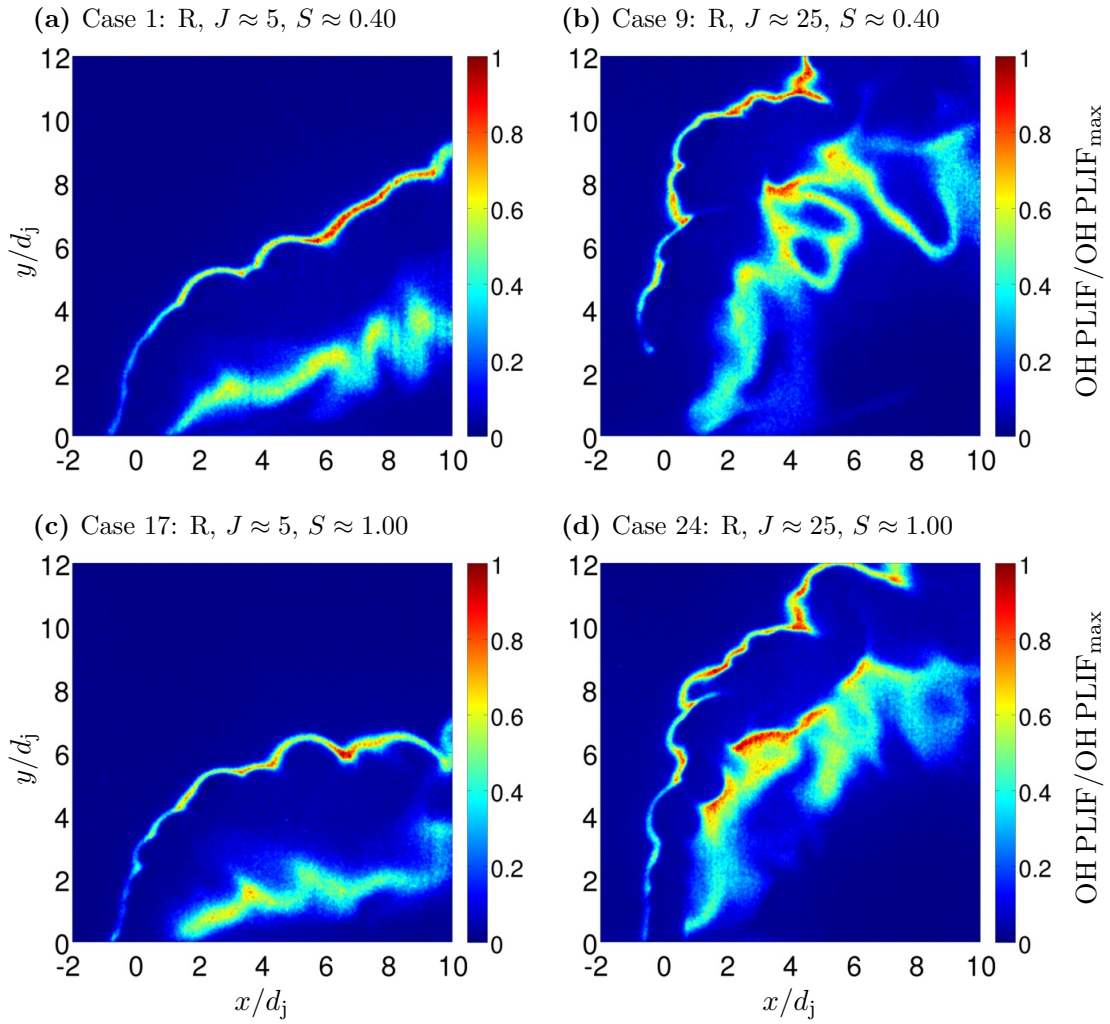

Figure 3.20: Instantaneous OH PLIF intensity images obtained for test conditions with four different combinations of J and S .

inside the shear layer vortices where large centrifugal forces ($a_{\text{centrifugal}} = \mathcal{O}(10^6\,\text{m/s}^2)$) tend to fling the ceramic particles radially outwards and away from the vortex core. Thus, strong Mie scattering signal in the jet near-field can be interpreted as an indicator of regions of the flow containing high concentrations of low temperature jet fluid with low-to-moderate vorticity. Following this line of reasoning, two important differences between the low J and high J cases can be deduced from the Mie scattering images. First, shear layer roll-up is suppressed on the leeward side of low J jets, as indicated by the lack of dark vortex cores on that side of the jet. The absence of strong shear layer vortices on the leeward side of the jet reduces mixing between the jet and the crossflow in that region, which ultimately inhibits

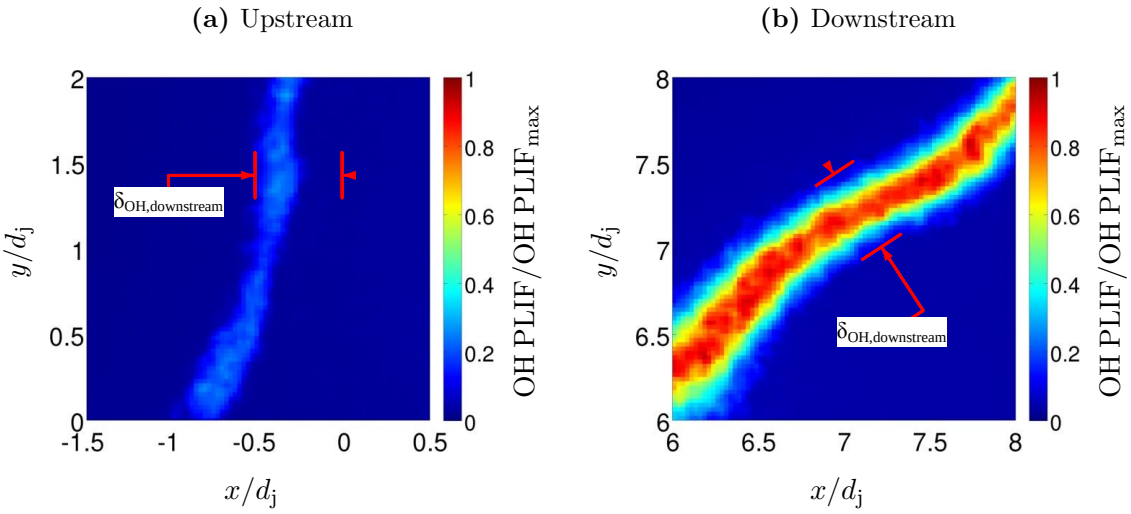

Figure 3.21: Enlarged view of the instantaneous OH PLIF intensity in the near-field and far-field of the windward flame branch of Figure 3.20a.

combustion. Secondly, a region of flow with seed density lower than either the jet or the crossflow is sandwiched between the jet potential core and the leeward OH PLIF signal in the low J jets. This observation confirms the previously made hypothesis in Section 3.1.4, based on time-averaged results, that the region immediately behind the jet potential core in the low J jets is filled with a non-flammable mixture of burnt combustion products. The high J jets, on the other hand, do not appear to trap combustion products immediately behind the leeward side of the jet but do contain strong shear layer vortices. Thus, near the jet injector, the leeward side conditions in high J jets are relatively more favorable for combustion than in low J jets. Note that this statement may not hold for low J cases that do not support an attached windward flame branch.

Additional consideration of the low S, high J case is merited to better understand the dynamics of the lifted windward flame branch. As seen in Figure 3.22b, the windward flame branch in this case is stabilized a few jet diameters downstream of the jet injector at a point slightly offset upstream of the location of maximum shear layer vorticity, while the leeward reaction zone remains attached at the backside of the jet. Closer inspection of additional instantaneous OH PLIF images reveals that the windward flame branch is also prone to local extinction at points located further downstream along the jet plume. Figure 3.24 presents a set of sequential OH PLIF images spanning 1.1ms of total time to illustrate

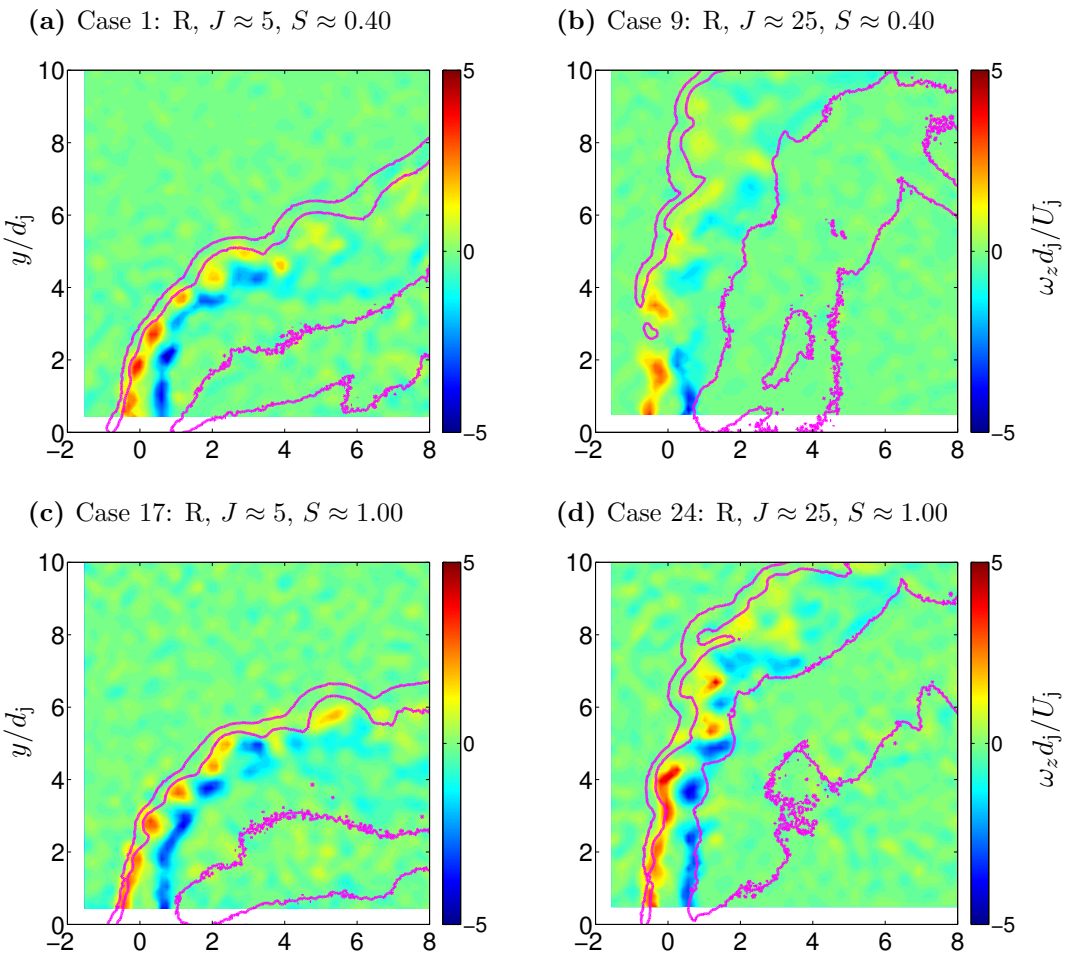

Figure 3.22: Non-dimensional instantaneous z-component of vorticity measured on the $z/d_\mathrm{j} = 0$ jet centerplane. (—): 10% OH PLIF intensity contour.

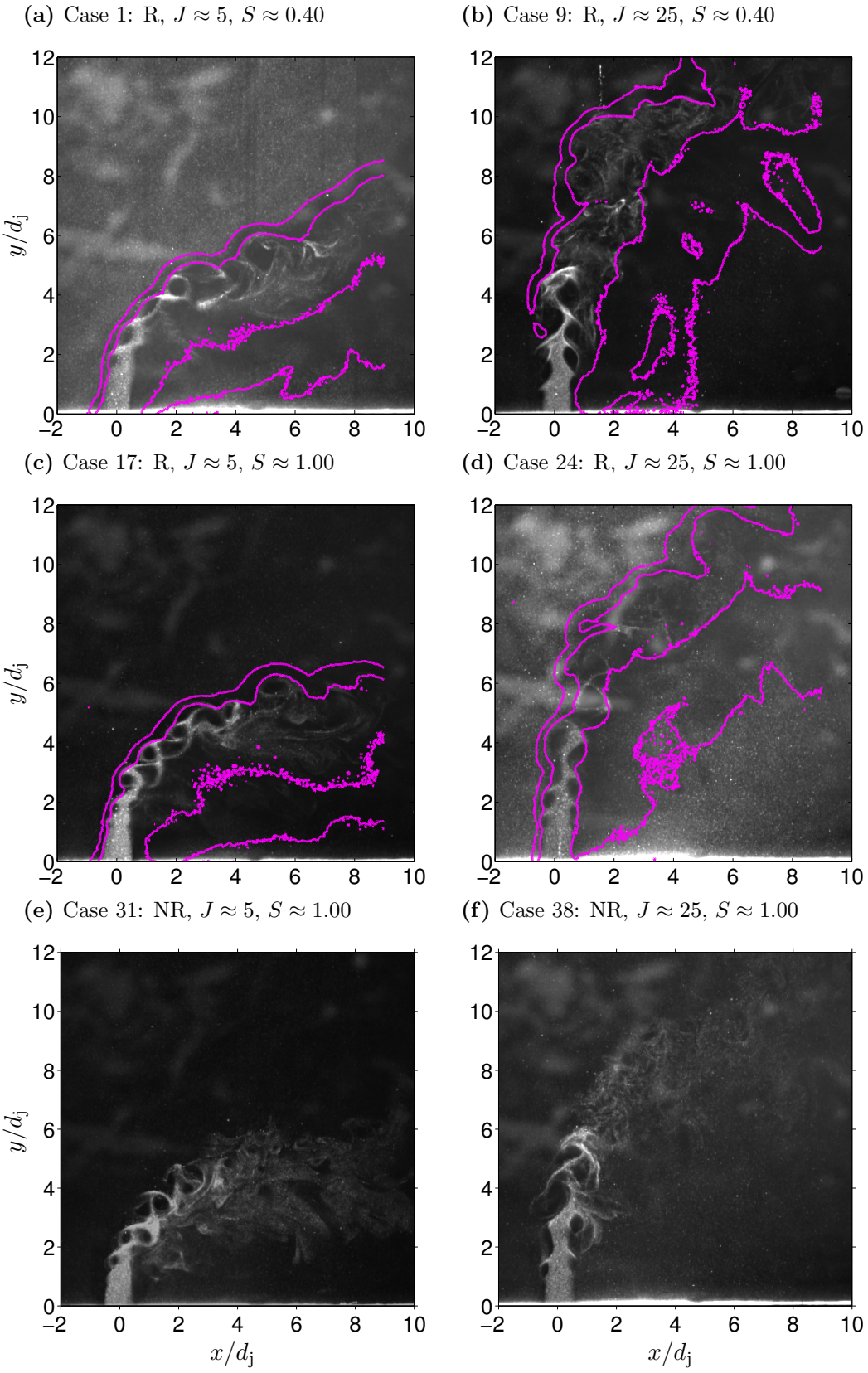

Figure 3.23: Instantaneous Mie scattering images obtained on the $z/d_j = 0$ jet centerplane. (—): 10% OH PLIF intensity contour.

this point. The local extinctions found along the windward flame branch can be short-lived and spatially localized, as seen in Figure 3.24a, or can persist for several milliseconds and span $4 - 5d_{\mathrm{j}}$ along the windward flame branch. Small, localized, flameless regions tend to rapidly disappear (i.e. within $\sim \Delta t$), presumably due to edge flame propagation. Edge flame propagation also plays a critical role in re-establishing a contiguous windward flame branch after larger extinction events, such as seen in Figures (d)-(j), but autoignition may also play an important role in these instances. In particular, the longer duration extinction events often contain localized, relatively large, uniform regions of high OH PLIF signal that appear quickly and are spatially removed from the main windward flame (see Figure 3.24i). Based on the present measurements alone, it is impossible to exclude the possibility that these localized reaction zones could be due to out-of-plane flame propagation rather than autoignition. Longer duration extinction events do, however, allow additional time for unreacted fuel and oxidizer to mix, which would increase the probability of an autoignition event occurring. The important role of autoignition in stabilizing the leeward reaction zone of JICF has also been cited by Micka & Driscoll [61] in their study of sonic CH_4/H_2 jets injected into a high-temperature $Ma = 0.70$ crossflow based on simultaneous CH_2O, OH, and CH PLIF studies. In their study, which was motivated by scramjet/ramjet applications, very high strain rates prohibited autoignition from occurring along the windward side of the jet even though the crossflow temperature $\sim$ 1370K was very high.

Edge tracking the windward flame branch, as demonstrated by the film reel in Figure 3.24, provides a means to quantify the flame liftoff distance, the likelihood of flame extinction at a given s/d_{j}, and the amount of time required for re-ignition to occur after an extinction event. A custom edge tracking routine based on a combination of intensity thresholding methods and gradient-based edge detection methods was developed for this purpose. The edge tracking routine was applied to each instantaneous OH PLIF image in the full data sequence ($\sim 10^4$ images) and a vector of pixel locations corresponding to the flame edge was stored. Note that edge tracking is only applied along the windward flame branch, and that the flame edge is defined as a thin interface separating the crossflow fluid from the region of high OH PLIF signal along the windward side of the jet. A flame brush image can be

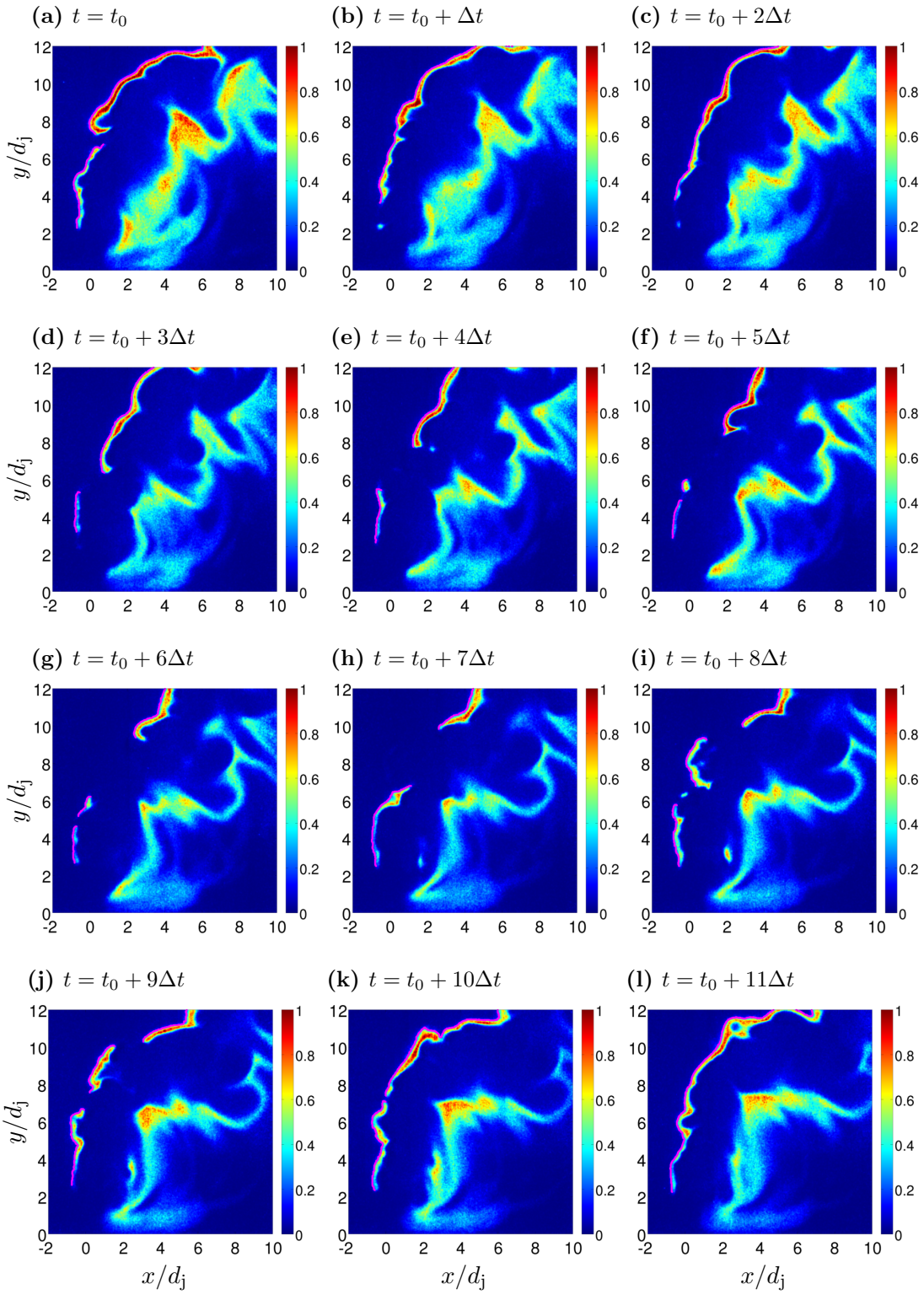

Figure 3.24: Sequence of instantaneous edge-tracked OH PLIF images illustrating flame front dynamics in a low S, high J jet (Case 9). $\Delta t = 1/10000$s. Colorbar corresponds to normalized OH PLIF signal from (a). (—): Instantaneous flame edge.

constructed by superimposing all the instantaneous flame edges on a dark background. A value of 1 is assigned to every point along each of the instantaneous flame edges such that the intensity of the flame brush image represents the total number of instantaneous flame edges that were located at a given pixel location over the duration of the measurement ($\sim$ 1s). Flame brush images for the four reacting JICF considered here are shown in Figure 3.25. As expected based on earlier results, the flame brush density is essentially zero below $y/d_{\mathrm{j}} = 2$ in the low S, high J case. The flame brush density in the other cases is highest at the jet injector, indicating attached flames. Note that the gradual increase in flame brush thickness as a function of distance along the jet trajectory closely resembles the increase in width of the mean OH PLIF signal on the windward side of the jet with downstream distance (see Figure 3.13). The key distinction is that the flame brush image is created by superposition of thin lines (thickness 1 pixel $\sim$ 0.06mm) and by definition does not account for changes in the flame thickness, which generally increases with s/d_{j}. Thus, flame motion (or flame flapping) is primarily responsible for broadening the mean OH PLIF signal on the windward side of the jet at downstream distances. Similarly, the high time-averaged OH PLIF signal near the jet injector in the windward shear layer of the low J jets exists not because the instantaneous OH PLIF signal is particularly high there (in actuality it is low), but rather because the windward flame branch does not flap as much at that location.

A mean windward flame edge location can be extracted from the flame brush density. This curve, denoted by the black dashed line in Figure 3.25, is defined as the locus of points with maximum flame density occurring along a set of lines normal to the time-averaged jet center streamline trajectory, which is shown by the dashed white line. While the mean flame edge is offset upstream by about $1d_{\mathrm{j}}$, it closely follows the jet trajectory in the high J cases. The mean flame edge deviates more from the jet trajectory in the low J cases but never by more than $2d_{\mathrm{j}}$ within the field of view. The number of extinction events for a given test condition can then be quantified by determining whether or not lines perpendicular to the mean flame edge intersect the instantaneous flame edges at a given s/d_{j}. Figure 3.26 illustrates this process using a subset of the flame edge normal lines actually used in the analysis. The solid white lines lie perpendicular to the mean flame edge and intersect the

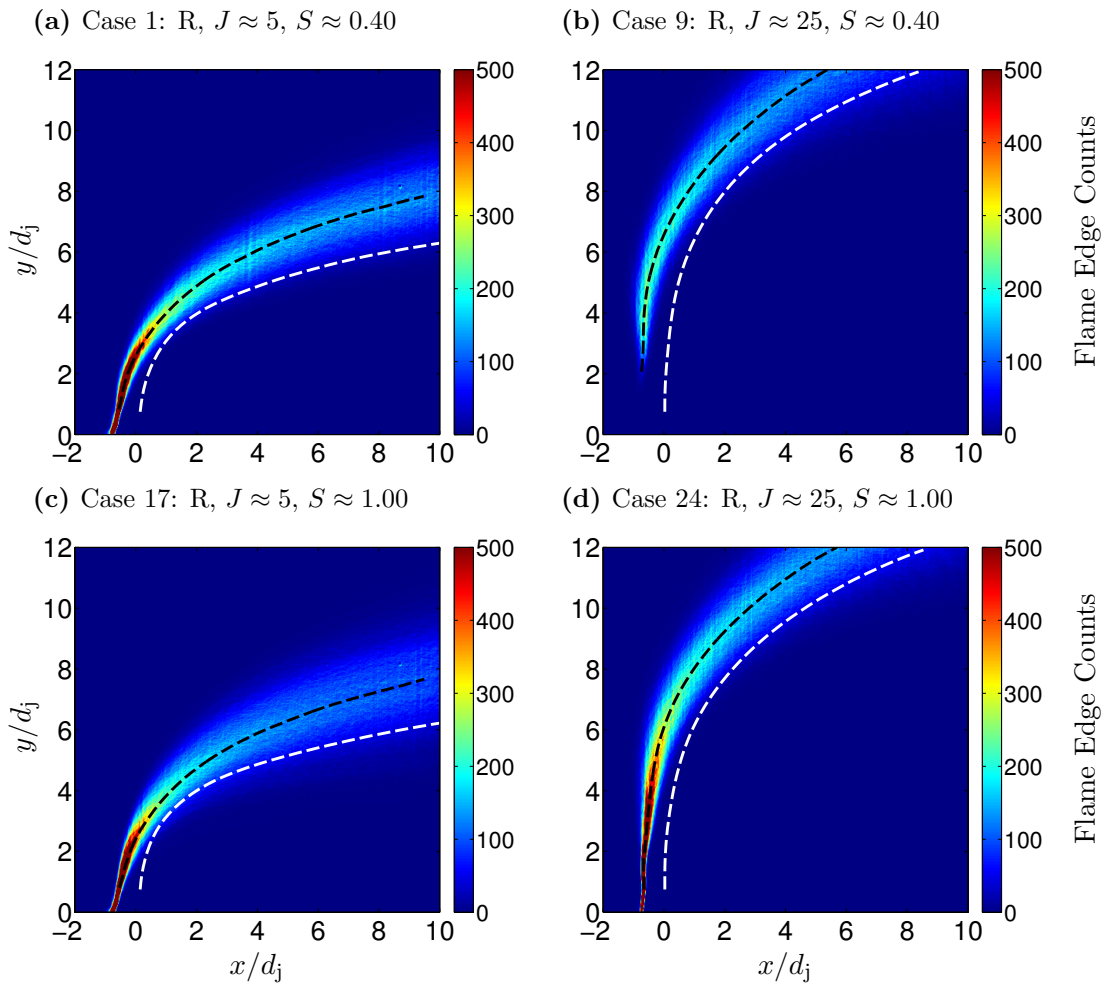

Figure 3.25: Windward flame edge brush extracted from edge-tracked OH PLIF reaction zone imaging. (---): Mean windward flame edge location. (▬ ▬): Jet center streamline trajectory.

mean flame edge at points, which are denoted by green dots, spaced 1 s/d_j apart. Points where the flame edge normal lines intersect the instantaneous flame edge, shown in magenta, are denoted by the green squares. Time instances where the flame edge normal line (e.g., the fifth normal line from the bottom) does not intersect the instantaneous flame edge are recorded as extinction events at the specified s/d_j.

Figure 3.27a plots the fraction of time during which the windward flame branch exists at a given s/d_j for the two high J cases. Equivalent results for the low J cases are not shown because the flame never experiences local extinction in those cases. The most noteworthy finding here is that the unity S, high J case does actually lift away from the jet injector part of the time, as evidenced by the absence of a windward flame about 30% of the time

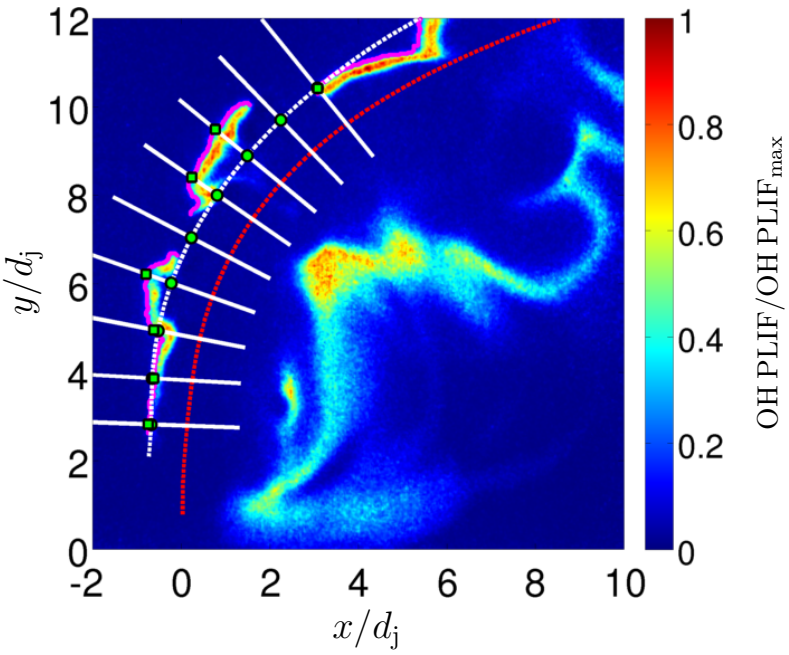

Figure 3.26: Illustration of windward flame edge tracking analysis.

at $s/d_j = 1$. Note that points below $s/d_j \sim 1$ are not resolved since the mean flame edge is not defined below $y/d_j = 0.75$. A windward flame exists about 90% of the time at $s/d_j = 5$ in the unity S case and is virtually always found for $s/d_j > 8$. The windward flame branch in the low S case, as expected, is much more likely to be extinguished at the same value of s/d_j, although the probability of a flame existing increases rapidly with s/d_j. Figure 3.27b shows the average duration of an extinction event along the windward flame branch for the two high J cases. Extinction events clearly persist longer in the low S case compared to the unity S case. The mean extinction event duration drops sharply with s/d_j near the jet injector, although more so in the low S case. The duration of extinction events plateaus and remains relatively constant beyond $s/d_j = 5$ for both the low S and the unity S cases. This observation suggests that extinction events near the jet injector (i.e., flame liftoff) last longer than extinction events that occur further downstream (i.e., holes in the flame). The duration of the extinction events is relatively long compared to the characteristic jet timescale, $\tau_j = d_j/U_j$. Recall that the passage frequency of the shear layer vortices is near $0.7St_j$, which indicates that on average many shear layer vortices will propagate past an extinguished region of the windward flame before re-ignition occurs. The wake vortices

shed at a lower frequency, with values in the literature in the $0.05 \leq St_{\mathrm{j}} \leq 0.2$ range [1], which leads to characteristic timescales that are comparable with the average lifetime of an extinction event in the downstream region. Despite their similar timescales, it is not proposed that a direct link between the wake vortices and windward flame extinctions. It is worth noting, however, that recent work by Schlatter et al. [44] has linked the wake vortices with a global mode of the jet that causes bulk oscillation of the jet column. This phenomena could provide a link between the wake vortices and the windward flame branch extinction events.

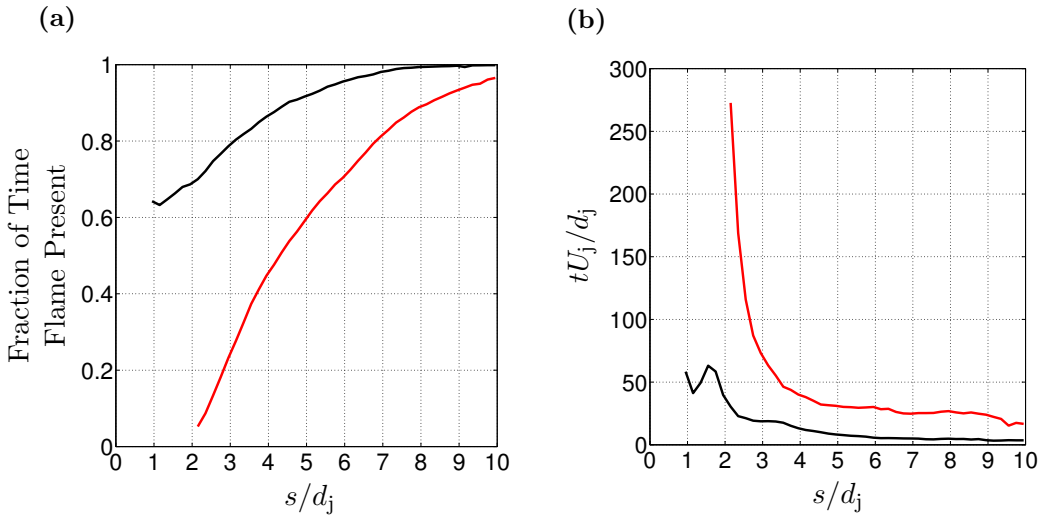

Figure 3.27: (a) Fraction of total measurement time during which a windward flame exists at a given arc length distance. (b) Average lifetime of a flame hole in the windward flame branch as a function of arc length distance along the jet center streamline. (—): Case 9, Reacting, high J, low S; (—): Case 24, Reacting, high J, unity S.

The duration of an extinction event can also be compared with the homogeneous ignition delay time, which is an important timescale in a vitiated flow. Accordingly, ignition delay times were computed for mixtures containing varying amounts of jet fluid and cross-flow fluid. These calculations were performed using a plug flow reactor in Chemkin, and the ignition delay time was defined as the residence time corresponding to the location of maximum $d\mathrm{x_H}/dt$, where $\mathrm{x_H}$ is the mole fraction of hydrogen atoms. Results for mixtures corresponding to both low S and unity S simulations are shown in Figure 3.28. The minimum ignition delay time occurs in very lean mixtures ($z \sim 0.2z_{\mathrm{st}}$), but does not vary significantly between the low and unity S cases. The mixture fraction corresponding to

the minimum ignition delay is known as the most reactive mixture fraction [58]. The ignition delay for a stoichiometric mixture is about 120μs, while the ignition delay for the most reactive mixture is about 50μs. For comparison, lines denoting the characteristic jet timescales, τ_{j}, for each of the four unforced, reacting cases are overlaid in Figure 3.28. The minimum ignition delay is less than or equal to τ_{j} in both of the low J cases. On the other hand, τ_{j} is about 50% smaller than the minimum ignition delay for the unity S case and is about half the minimum ignition delay for the low S, high J case. Since the fastest fluid mechanical timescales in a JICF (i.e., the SLV) are $\mathcal{O}(\tau_{\mathrm{j}})$, it is not surprising that local extinction becomes increasingly common for jets with combinations of J and S where τ_{j} is less than the minimum ignition delay.

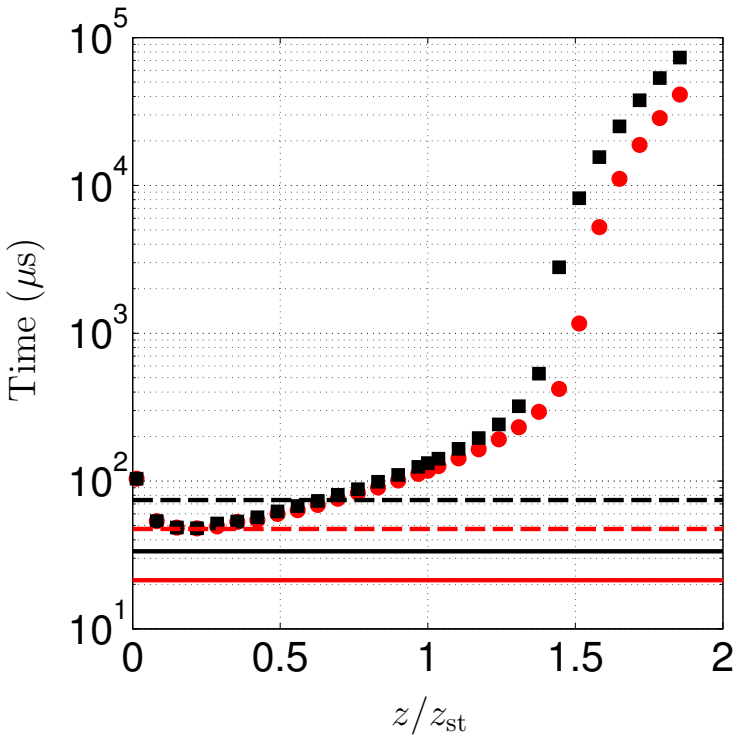

Figure 3.28: Homogeneous ignition delay times for low S and unity S jet fluid mixed with varying amounts of vitiated crossflow fluid. (●): Low S mixtures; (■): Unity S mixtures. Lines denote characteristic jet timescales. (---): Case 1, low S, low J; (—): Case 9, low S, high J; (---): Case 17, unity S, low J; (—): Case 24, unity S, high J.

3.3 Summary of Key Findings

This chapter investigated the flow structure and flame stabilization of jets injected into turbulent, vitiated crossflows. Time-resolved SPIV, OH PLIF, and dynamic pressure measurements were presented and used to characterize the time-averaged and unsteady dynamics of JICF. Non-reacting and reacting jets were studied for several combinations of J and S.

The important influence of the near-field pressure gradient was identified from the time-averaged velocity field data. Pressure forces cause a strong negative V velocity on the windward side of the jet and affect the leeward recirculation zone. The size, strength, and composition of the leeward recirculation zone depends on J and whether or not the jet is reacting. Low J jets never separate from the lower wall and have strong leeward recirculation zones, which, in the reacting case, are heavily diluted by entrainment of combustion products from the leeward side of the jet.

Velocity recovery in the wake is also sensitive to J, S, and combustion heat release. In low J situations, non-reacting, iso-density jets have smaller, more compact wake regions than reacting, low density jets. On the other hand, in high J cases, wake velocity recovery occurs preferentially in reacting, low S jets. These differences between low and high J jets were explained in terms of differences in the aerodynamic blockage due to the presence of the jet, differences in the jet trajectory, and differences in the heat release distribution between low and high J jets.

A new trajectory scaling law was proposed based on a modification of the scaling law developed by Muppidi & Mahesh [30] to account for the effect of combustion on jet penetration. The influence of combustion on the jet trajectory is treated as a modification of the near-field pressure gradient and a local flow acceleration. The revised scaling law provides improved collapse of trajectories measured in both non-reacting and reacting jets.

OH PLIF measurements indicate that the flame stabilization and reaction zone structure of jets injected into vitiated crossflows is markedly different than that of fuel jets injected into low-to-moderate temperature air crossflows. Vitiated crossflows promote near-field flame stabilization, which does not depend on premixing between the jet and crossflow fluid. In low J cases, the flame is strongly attached to the burner lip and wraps around

the circumference of the injector. A thin, non-premixed flame is located just outside the windward shear layer, which is wrinkled and distorted by the passage of high frequency shear layer vortices. A much thicker, more diffuse reaction zone is stabilized on the leeward side of the jet near the trailing edge of the leeward recirculation zone. The leeward reaction zone is offset from the leeward shear layer, presumably due to entrainment of combustion products into the leeward recirculation zone. The windward reaction zone in high J cases is characterized by a thin, non-premixed flame front, similar to what was observed in low J jets, but the much higher strain rates in the the high J cases lead to intermittent local extinction at small s/d_{j} and flame liftoff along the windward side of the jet. A lifted windward flame is generally found for JICF conditions where the timescale $d_{\mathrm{j}}/U_{\mathrm{j}}$ is less than the homogeneous ignition delay at the most reactive mixture fraction. In these cases, the flame is anchored by an attached reaction zone stabilized in the low velocity recirculation zone behind the jet potential core. Lastly, instantaneous OH PLIF results suggest that autoignition may also be important for flame stabilization and re-ignition along the windward side of high J jets.

CHAPTER IV

FORCED RESPONSE OF JETS IN VITIATED CROSSFLOW

Chapter 3 discussed jets injected into unforced, vitiated crossflows. This chapter investigates the forced response of jets injected into acoustically excited crossflows. Time-resolved SPIV, OH PLIF, and dynamic pressure measurements are presented for a set of JICF experiments where the crossflow was forced using a pair of loudspeakers. The forcing frequency and forcing amplitude are varied, while the key time-averaged JICF parameters, including J, S, Re_{j}, Re_{∞}, and T_{∞}, are matched to those used in the unforced experiments discussed in Chapter 3.

The chapter begins in Section 4.1 with a detailed characterization of the crossflow forcing conditions. The effect of crossflow forcing on the time-averaged and instantaneous jet trajectory is treated in Section 4.2. The modification of the leeward recirculation zone as a result of crossflow forcing is discussed in Section 4.3. Section 4.4 presents a detailed spectral analysis of the velocity and vorticity field response at the forcing frequency, f_{F}. The flame response and the effect of crossflow forcing on flame stabilization is treated in Section 4.5. The chapter concludes by presenting an analytical injector-coupled response model for predicting the fluctuating jet exit velocity, u'_{j}, which is critical to understanding the jet response in many situations.

4.1 Characterization of the Acoustically Forced Crossflow

This section presents dynamic pressure measurements and time-resolved SPIV measurements used to characterize the acoustically forced crossflow and the fluctuating jet exit velocity. The crossflow was excited by a pair of speakers mounted in the dilution section and driven near resonant frequencies of the facility. The resulting acoustic field inside the test section depends on both the frequency and amplitude of the excitation. Three different forcing frequencies, f_{F}, are considered in the present work: 177Hz, 250Hz, and 340Hz. Excitation amplitude, A_{F}, which is reported in terms of current supplied to the speakers, was

varied between 0.6A and 1.5A. The time-averaged JICF parameters in each of the forced experiments are identical to one of the six unforced experiments reported in Chapter 3. Hence, the parameter space in the forced experiments is defined by J, S, R/NR, f_{F}, and A_{F}.

A consistent labeling strategy is needed to study this broad parameter space. Figure 4.1 presents the labeling convention that will be used in the present work. The line style and line color represent the momentum flux ratio and the jet composition, respectively. Solid lines denote high J ($J \approx 25$) cases, while dashed lines denote low J ($J \approx 5$) cases. Reacting, low density ratio ($S \approx 0.40$) cases use red lines. Reacting, unity density ratio ($S \approx 1.00$) cases have black lines. Blue lines represent non-reacting, unity density ratio ($S \approx 1.00$) cases. Symbols describe the acoustic excitation. The frequency of excitation is given by the symbol shape, while the symbol color denotes the amplitude of excitation. Lines without any symbols are unforced cases.

Specifying the excitation frequency and excitation amplitude applied to the speakers is not, however, sufficient to characterize the oscillatory crossflow interacting with the jet in the test section. The standing wave patterns established inside the ducted reacting JICF facility are sensitive to the boundary conditions at the entrance and exit of the facility as well as the thermo-acoustic response of the vitiator. Accurately predicting the acoustic field, and the amplitude in particular, inside the facility based on the mean operating conditions and applied excitation is a difficult task. As an alternative, the two-microphone method [83, 84] was used in the present work to experimentally determine the acoustic pressure and velocity fields inside the test section during each experiment. A more detailed description of the two-microphone method and its application in the present facility was given previously in Chapter 2. The two-microphone method is well-suited for this application because the acoustic field is linear and one-dimensional. The forcing frequencies are well below cutoff for the duct, and the fluctuating pressure amplitude inside the duct never exceeds 0.25% of the mean pressure. Hence, the two-microphone method measurements were simultaneously acquired with the optical diagnostics during each experiment to provide an accurate depiction of the instantaneous acoustic field interacting with the jet.

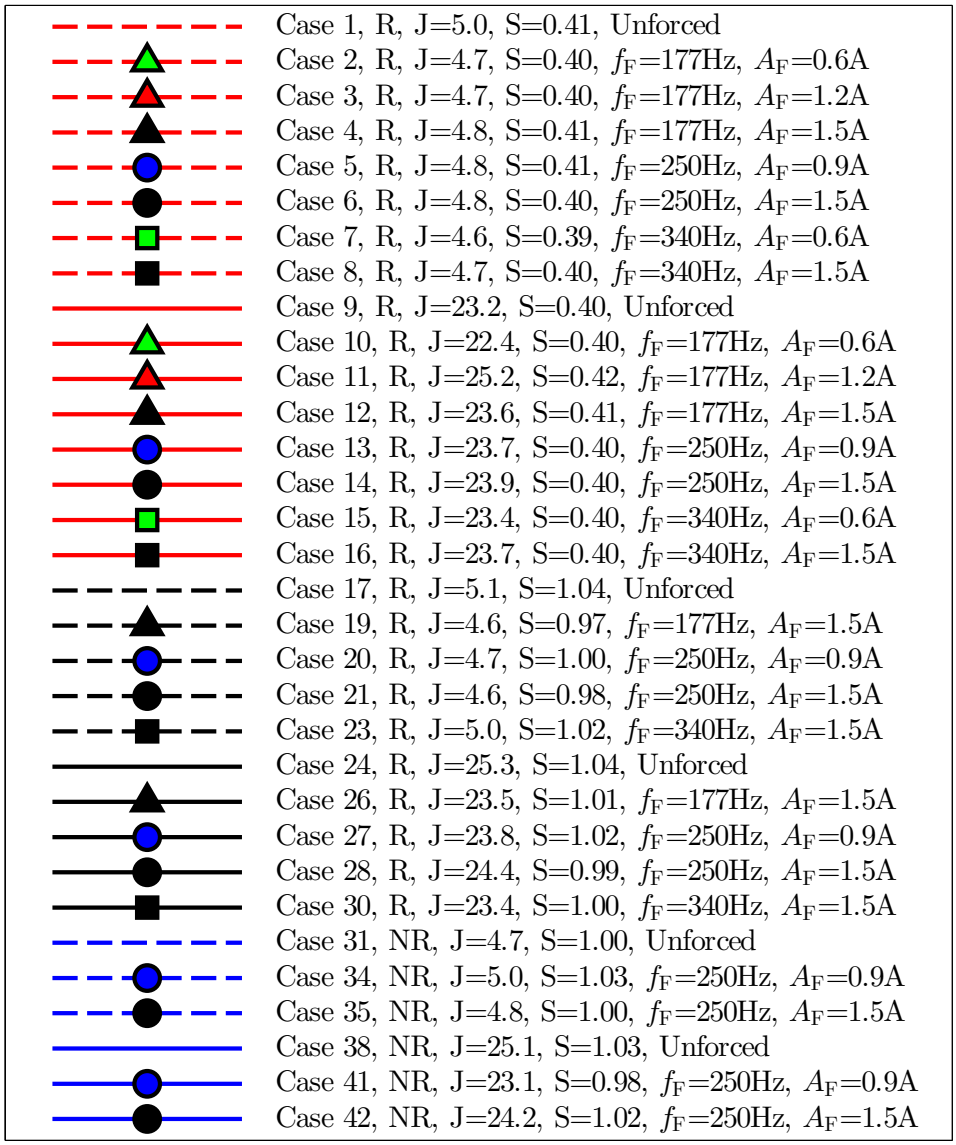

Figure 4.1: Legend of line styles used to represent different test conditions.

Representative pressure mode shapes determined using the two-microphone method are shown in Figure 4.2. As indicated by the line color, all the results plotted here correspond to reacting, low S cases. The excitation amplitude is 1.5A in each of the cases. The abscissa extends from $x = 0$, which is the location of the first pressure transducer, $P_{\infty,1}$, to the exit of the facility, which is denoted by $x = x_{\text{exit}}$. As anticipated, the oscillating pressure amplitude at the jet injector, whose location is denoted by $x = x_{\text{jet}}$, varies significantly as a function of frequency. This result reflects the different standing wave patterns established at each forcing frequency. The standing wave pattern for a given f_{F} depends on the acoustic boundary conditions of the facility, the heat release response of the vitiator, and the speaker response. For cases with fixed excitation amplitude, the fluctuating pressure amplitude at the jet injector, p'_{∞}, is largest when $f_{\text{F}} = 177$Hz and smallest for $f_{\text{F}} = 250$Hz. The jet injector is located near a pressure anti-node for both the 250Hz and 340Hz cases.

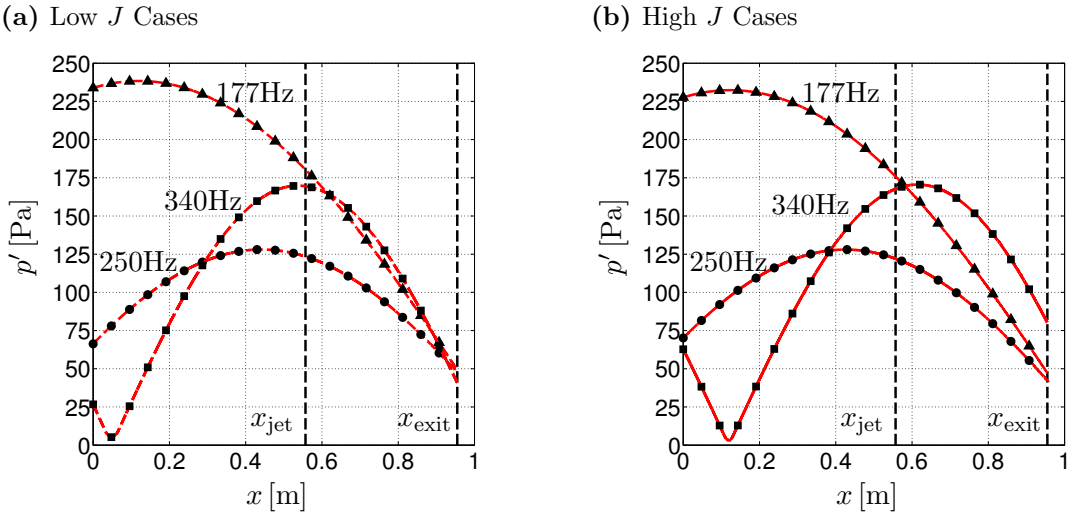

Figure 4.2: Acoustic pressure mode shape in the test section for low and high J jets forced at three different frequencies.

Figure 4.3 shows velocity mode shapes for the same set of forced reacting, low S test conditions whose pressure mode shapes were shown in Figure 4.2. The velocity mode shapes are nearly 90 degrees out of phase with the pressure modes (not exactly because of the mean flow). As a result, the jet injector sits near a velocity node for the 250Hz and 340Hz cases, and the fluctuating crossflow velocity amplitude at the jet injector, u'_{∞}, is negligibly small for cases forced at those frequencies regardless of excitation amplitude. Even for the 177Hz

cases, where the jet injector is located far from a velocity node, the fluctuating axial velocity, u'_∞, is less than 5% of the mean crossflow velocity, U_∞, and is even smaller relative to the mean jet exit velocity, U_j. Before continuing, it is important to make note of the x-axis scaling in Figures 4.2 and 4.3 to avoid any confusion about the physical configuration. Although the mode shapes appear to vary rapidly in the vicinity of the jet, the actual axial pressure/velocity gradients experienced by the jet are barely discernible because the acoustic wavelength at the forcing frequency, $\lambda_{\infty,\mathrm{F}}$, is very large relative to d_j. Recall that the speed of sound in the high-temperature, vitated crossflow gases is $c_\infty \approx 680\mathrm{m/s}$. This fact, combined with the low forcing frequencies, results in values for the acoustic wavelength in the range $2\mathrm{m} \leq \lambda_{\infty,\mathrm{F}} \leq 4\mathrm{m}$, while the jet diameter is $d_\mathrm{j} = 0.003175\mathrm{m}$. Thus, the range of the x and y coordinates corresponding to the entire visible area of the SPIV/OH PLIF measurements reported in this thesis (i.e., $-2 \leq x/d_\mathrm{j} \leq 10$ & $0 \leq y/d_\mathrm{j} \leq 12$) represents less than 2% of the acoustic wavelength. Therefore, the JICF can be considered acoustically compact in all the forced experiments.

(a) Low J Cases **(b)** High J Cases

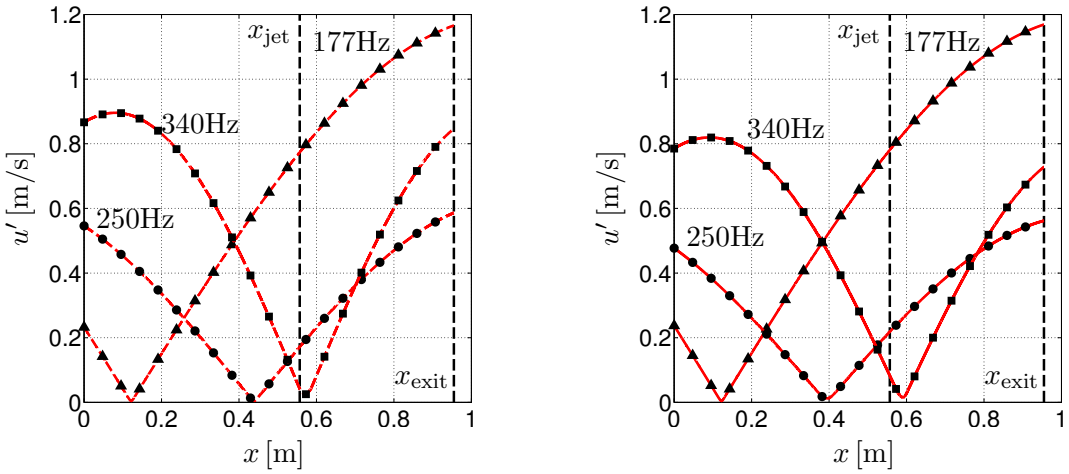

Figure 4.3: Acoustic velocity mode shape in the test section for low and high J jets forced at three different frequencies.

The two-microphone results presented thus far have focused on the influence of forcing frequency on the pressure and velocity mode shapes for reacting jets with a fixed (low S) mixture composition. Figure 4.4 presents two-microphone results for non-reacting and reacting jets with different mixture compositions that were forced using the same excitation

frequency, $f_F = 250$Hz, and excitation amplitude, $A_F = 1.5$A. The resulting pressure and velocity mode shapes show very little sensitivity to changes in mixture composition, and there is little difference between reacting and non-reacting cases. Notably, these results do not indicate that the jet *response* is independent of changes in jet mixture composition. Instead, they indicate that the crossflow acoustics are largely independent of changes to the jet composition and reactivity.

(a) Acoustic pressure mode

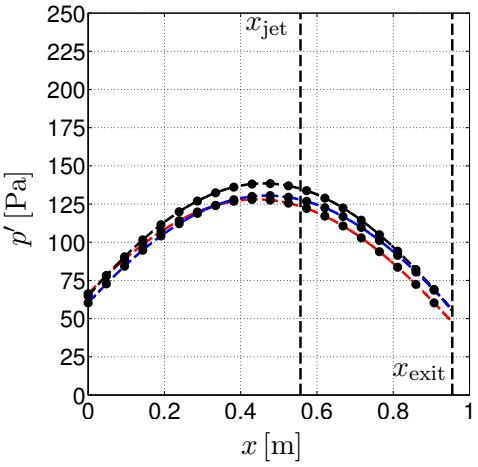

(b) Acoustic velocity mode

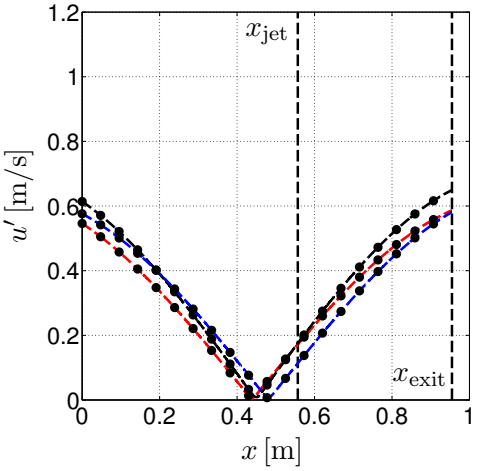

Figure 4.4: Acoustic pressure and velocity mode shapes in the test section for jets with different S forced at $f_F = 250$Hz and $A_F = 1.5$A.

The fluctuating crossflow velocity, u'_∞, can be interpreted as an asymmetric excitation of the jet, but based on the velocity mode shape results, u'_∞ is quite small compared to both U_∞ and U_j. However, in addition to the excitation of the jet by u'_∞, the fluctuating crossflow pressure induces a fluctuating jet exit velocity, u'_j, which can be much larger than u'_∞ in certain cases. u'_j can be interpreted as an axisymmetric excitation of the jet. The magnitude and phase of the fluctuating jet exit velocity depend on the amplitude of p'_∞ and the jet injector impedance, Z_j. Methods for modeling the injector impedance will be described in Section 4.6, but for the purposes of quantifying the applied forcing, the fluctuating jet exit velocity at the forcing frequency can be directly extracted from the time-resolved SPIV measurements using the expression

$$u'_j = [2S_{vv}(f_F)]^{1/2} \tag{4.1}$$

where $S_{vv}(f_F)$ is the component of the power spectra of the vertical velocity fluctuations at

the forcing frequency evaluated at $(x/d_\mathrm{j}, y/d_\mathrm{j}) = (0, 2)$. This location was selected instead of a location closer to the jet origin to minimize the error introduced by noisy near-wall power spectra estimates. The power spectra is approximated from the SPIV data using Welch's method [82] with five ensembles, 50% overlap, and 10^4 FFT bins. The effect due to the equivalent noise bandwidth of the Hanning windows applied to each ensemble in the Welch algorithm is also appropriately accounted for in the calculation of the power spectra. Unless otherwise noted, it may be assumed that the same methodology has been used to compute other power spectra reported throughout this chapter.

The magnitude of the vertical velocity fluctuations at the forcing frequency, $v'(f_\mathrm{F})$, for selected low S reacting jets is plotted in Figure 4.5 for x/d_j values in the range $-2 \leq x/d_\mathrm{j} \leq 2$. In each case, the fluctuating vertical velocity has been normalized by the mean jet exit velocity, U_j. $u'_\mathrm{j}/U_\mathrm{j}$ is defined as the value of $v'(f_\mathrm{F})/U_\mathrm{j}$ evaluated at $x/d_\mathrm{j} = 0$. It is noteworthy that the magnitude of $u'_\mathrm{j}/U_\mathrm{j}$ varies substantially with frequency for the low J cases. Regardless of the frequency of excitation, the magnitude of the fluctuating jet exit velocity due to the oscillating crossflow pressure is much larger in the low J cases than in the high J cases. Furthermore, $u'_\mathrm{j}/U_\mathrm{j}$ is essentially independent of frequency in the high J cases. The fluctuating jet exit velocity is, however, sensitive to changes in jet composition. This is illustrated in Figure 4.6, which presents $v'(f_\mathrm{F})/U_\mathrm{j}$ for cases with identical forcing but different jet composition. The results show that the same p'_∞ leads to larger values of $u'_\mathrm{j}/U_\mathrm{j}$ in the iso-density cases. The reacting iso-density jets also achieve larger $u'_\mathrm{j}/U_\mathrm{j}$ values compared to the non-reacting iso-density cases.

The values for $u'_\mathrm{j}/U_\mathrm{j}$ extracted from the SPIV measurements can be compared against the values for u'_∞/U_∞ determined using the two-microphone method to understand the relative importance of the fluctuating jet velocity and the fluctuating crossflow velocity in the forced response studies. This comparison is presented in Figure 4.7, where the symbols represent different forcing conditions (see Figure 4.1). The solid lines in the figures represent 1:1 and 5:1 relationships between $u'_\mathrm{j}/U_\mathrm{j}$ and u'_∞/U_∞. The 250Hz (circles) and 340Hz (squares) data lie well above the 1:1 line in all cases, which indicates that the response of jets forced at these frequencies is likely dominated by the fluctuating jet exit velocity. Similarly, $u'_\mathrm{j}/U_\mathrm{j}$ is much

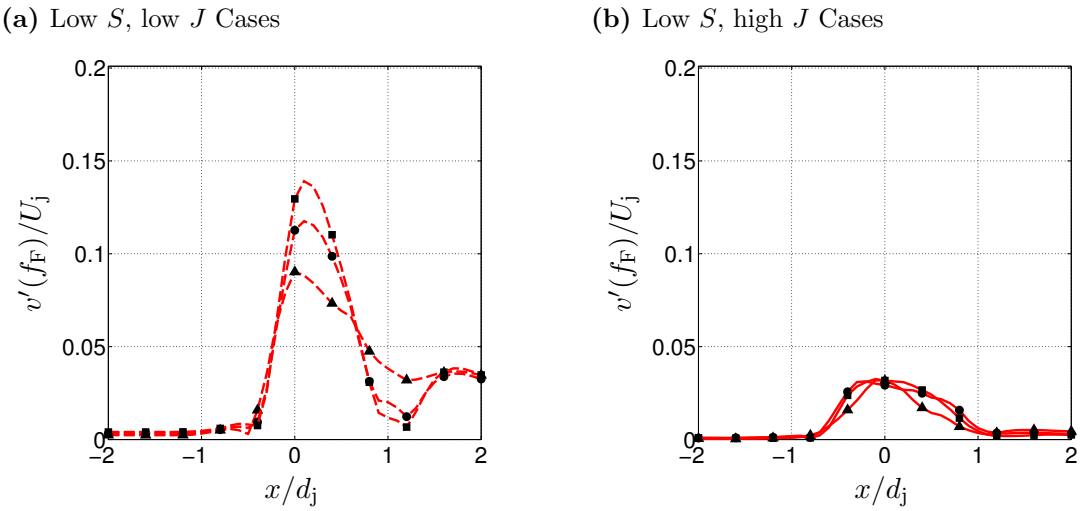

Figure 4.5: Fluctuating nozzle exit velocity measured using SPIV along the horizontal line $y/d_j = 2$ for jets forced at different frequencies. Forcing amplitude and density ratio held constant at $A_F = 1.5$A and $S = 0.40$, respectively.

larger than u'_∞/U_∞ in all the forced low J jets. The normalized jet and crossflow velocity fluctuations can, however, have more comparable magnitudes in the high J cases forced at 177Hz (triangles). This is caused by the very different velocity mode shape for the cases forced at 177Hz as well as the fact that the high J cases have smaller u'_j/U_j but essentially the same u'_∞/U_∞ as their lower J counterparts. It is worth noting that, even for the high J cases forced at 177Hz, u'_j is always much larger ($> 6\times$) than u'_∞ in absolute terms. For reference, the values for u'_j, u'_∞, p'_∞, u'_j/U_j, and u'_∞/U_∞ for all the forced response studies performed as part of this work are provided in Table B.1 in Appendix B. Many of the results presented in the remainder of this chapter will be normalized by either u'_j or u'_∞ as appropriate to isolate the JICF response from the magnitude of the applied forcing, which, as shown in this section, is a sensitive function of f_F, S, and J.

Before investigating the JICF response to the crossflow forcing, it is important to note that JICF response is inherently facility dependent. In particular, the magnitude and phase of the fluctuating jet exit velocity, u'_j, relative to the fluctuating crossflow velocity, u'_∞, depends on the acoustic mode shape and the jet injector impedance, Z_j. The acoustic pressure and velocity mode shapes are controlled by the facility boundary conditions and the thermoacoustic properties of the vitiator. The jet injector impedance, which controls the fluctuating jet exit velocity induced by the oscillatory crossflow pressure, depends on

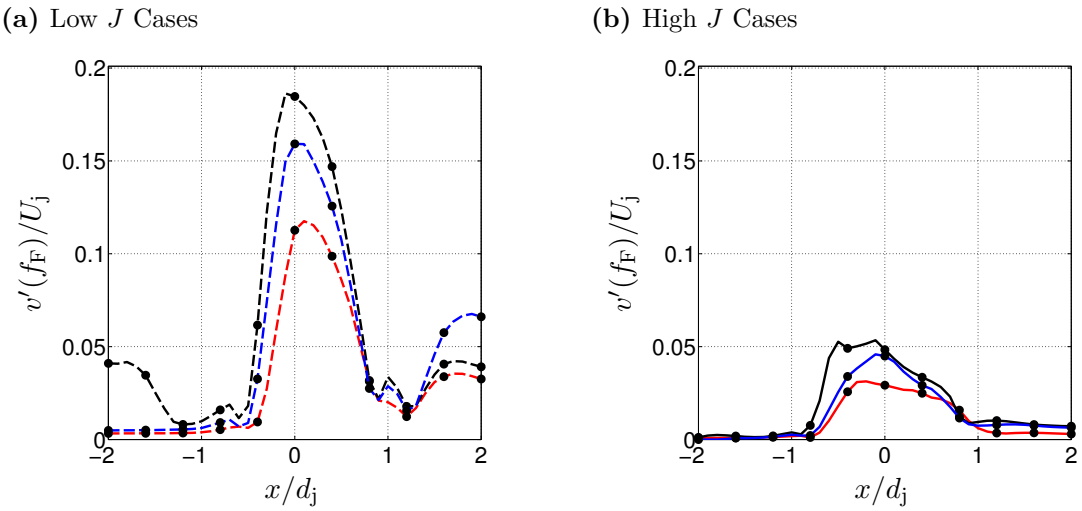

Figure 4.6: Fluctuating nozzle exit velocity measured using SPIV along the horizontal line $y/d_j = 2$ for jets with different mixture compositions. Forcing frequency and excitation amplitude held constant at $f_F = 250$Hz and $A_F = 1.5$A, respectively.

the acoustic boundary conditions and the nozzle geometry. Hence, a different JICF facility with different acoustic boundary conditions and/or a different jet injector design may exhibit different JICF response to crossflow forcing than that which is described in this thesis. For this reason, the asymmetric and axisymmetric excitation of the jet due to crossflow forcing have been carefully characterized for the present facility. The key point is that the facility geometry and boundary conditions must be considered prior to comparing results obtained in different studies of JICF response.

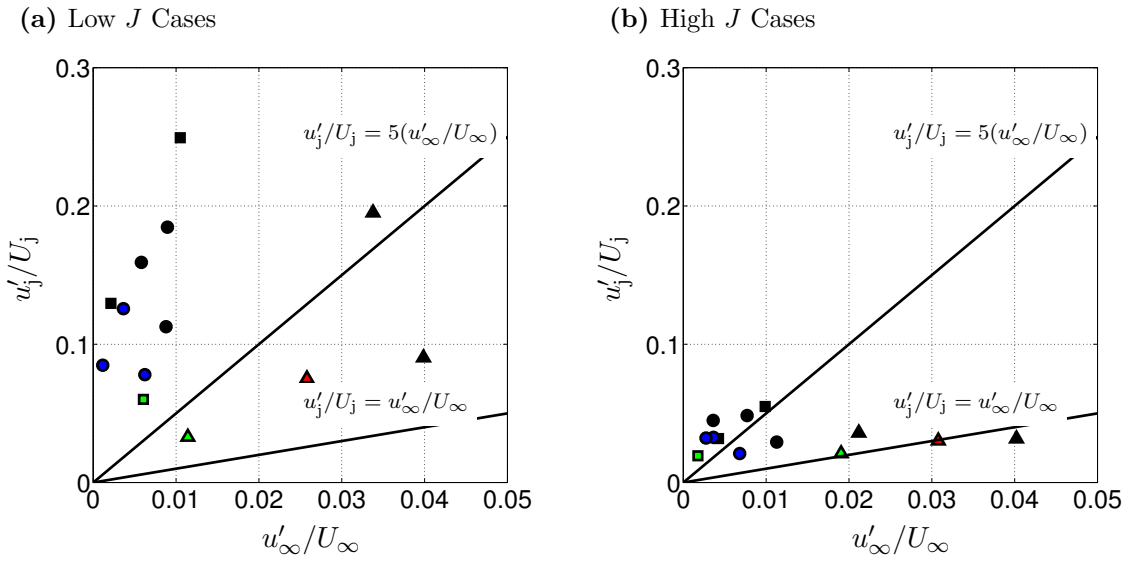

Figure 4.7: Scatter plot of u'_j/U_j versus u'_∞/U_∞ for forced cases.

4.2 Effect on Jet Trajectory

4.2.1 Time-Averaged Results

This section discusses the effect of crossflow forcing on the jet trajectory. Consistent with the unforced results presented in Chapter 3, the time-averaged jet trajectory is defined as the location of the mean jet center streamline and is extracted from SPIV measurements along the jet centerplane. Measured jet trajectories for all the test conditions examined as part of this work are shown in Figure 4.8. All the trajectories have been scaled by Rd_j. Each of the figures contains jet trajectory results for jets with the same combination of J and S subjected to crossflows excited at different forcing frequencies and forcing amplitudes. The unforced jet trajectory is shown in each case by the magenta curve. The results indicate that low frequency crossflow forcing only slightly increases jet penetration. This finding is in contrast to earlier studies, e.g., [67, 68, 73], that found increased penetration in jets forced at relatively high frequencies in the $0.2 \leq St_j \leq 0.7$ range. The likely explanation lies in differences in the response of JICF to low and high frequency forcing. In particular, increased penetration in JICF forced at high frequency is attributed to the formation and ejection of strong, coherent vortex rings from the jet injector [73]. On the other hand, low frequency forcing (i.e., $1/f_F \gg \tau_j$) does not result in vortex ring formation [77] and thus would not be expected to enhance penetration in the same manner.

The effect of low frequency forcing on the trajectory is slightly more pronounced, however, for lower J jets. Neither the frequency of excitation nor the amplitude of excitation appears to have a significant effect on the jet trajectory. Interestingly, the trajectory of the non-reacting jets is completely unaffected by crossflow forcing. This finding suggests that the slightly increased jet penetration in the forced, reacting cases is related to the effects of crossflow forcing on the near-field heat release. The discussion on flame stabilization effects due to crossflow forcing in Section 4.5 will present additional evidence that supports this hypothesis.

To facilitate comparison between jets with different J and S, the scaled trajectories for all the cases are re-plotted in Figure 4.9a. The observed trends with respect to J and S are consistent with those seen previously in the unforced results presented in Chapter 3. In particular, the forced, reacting jets penetrate further than the forced, non-reacting jets at the same J, and the standard Rd_{j} scaling fails to fully account for the J dependence, as evidenced by the over-penetration of the scaled high J jets. Re-scaling the forced trajectory data using the modified scaling law given in Section 3.1.2, as shown in Figure 4.9b, significantly improves the trajectory collapse.

Although crossflow forcing only slightly affects the time-averaged jet trajectory, the impact on other aspects of the time-averaged flow field is more significant. The time-averaged velocity magnitude for two pairs of unforced and forced jets with different J values are shown in Figure 4.10. The potential core of the forced, low J jet extends only half as far in the wall-normal direction. This significant shortening of the potential core is not apparent, however, in the forced high J cases. Since shortened potential core lengths are generally associated with reduced jet penetration [30, 36], it is noteworthy that the shortened potential core in the forced, low J case does not coincide with a reduction in jet penetration.

In unforced jets, the potential core length is closely related to the formation and growth rate of the shear layer vortices, which are the dominant near-field structure and largely control the rate of momentum transfer between the jet and the crossflow in that region. The shear layer dynamics are, in turn, a strong function of the jet exit velocity profile because of its influence on the shear layer thickness and initial vorticity distribution. New et al.

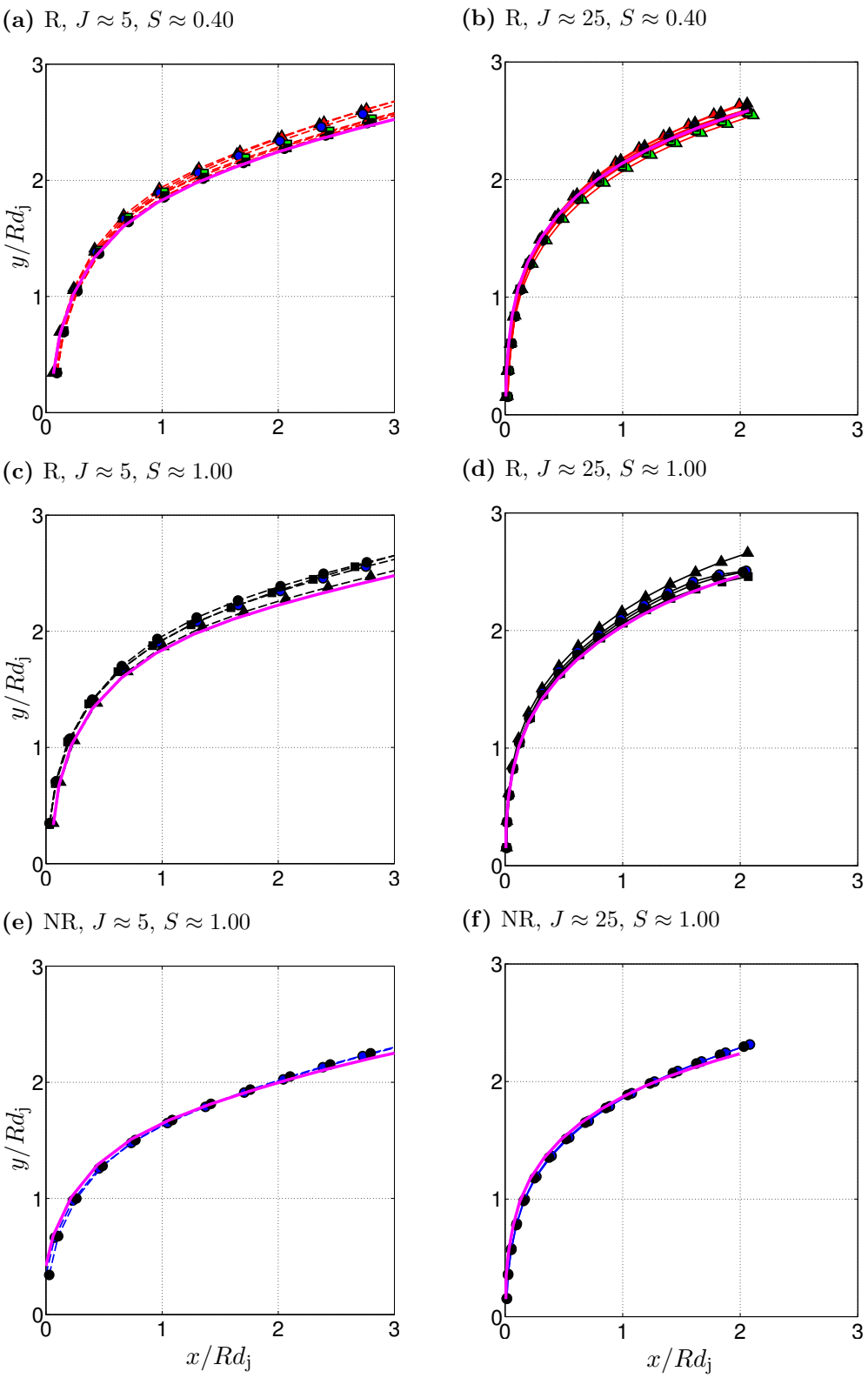

Figure 4.8: Time-averaged jet center streamline trajectories of jets with different S and J injected into acoustically excited crossflow. Solid magenta line denotes the unforced trajectory in each of the six subfigures corresponding to the R/NR, S, and J condition.

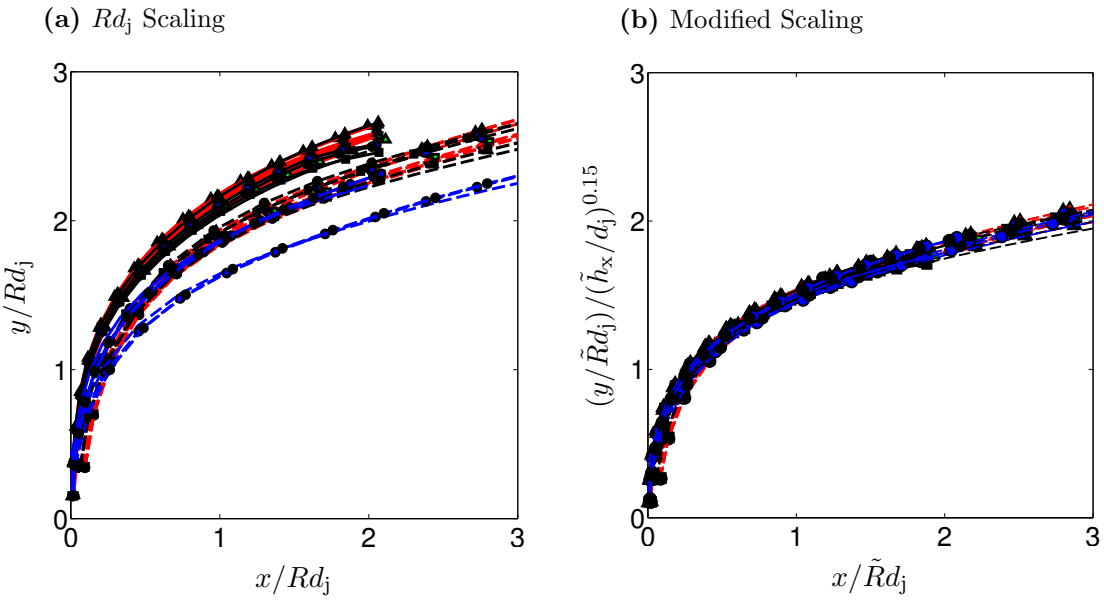

Figure 4.9: Jet center streamline trajectories for all unforced and forced JICF data acquired in the present work scaled using (a) standard Rd_j scaling and (b) the revised scaling law developed in Section 3.1.2.

[36] showed that jets with fully-developed jet exit velocity profiles experience reduced shear layer roll-up compared to jets with tophat velocity profiles, which have much thinner, more-concentrated vorticity layers. The fully-developed jets transferred less vertical momentum to the crossflow in the near-field and, as a result, penetrated further into the crossflow direction. It is important to note that the computation of J in these studies did properly account for the difference in jet momentum for jets with fixed mass flow rate but different velocity profiles. Thus, the increased penetration of jets with fully-developed velocity profiles was not simply a consequence of additional vertical momentum contained in a parabolic velocity profile versus a tophat velocity profile. Using this knowledge to interpret the present results suggests that the shear layer vortices, and thus the transfer of vertical momentum from the jet to the crossflow in the near-field, are not strongly affected by crossflow forcing, at least on a time-averaged basis. In other words, the effect of crossflow forcing on the shear layer vortices is not responsible for the shortened potential core in the forced, low J cases. Thus, it is reasonable to expect that a lower frequency mechanism must be responsible for the shortening of the potential core in the forced, low J case.

Additional evidence of the modification of the mean flow field due to forcing can be

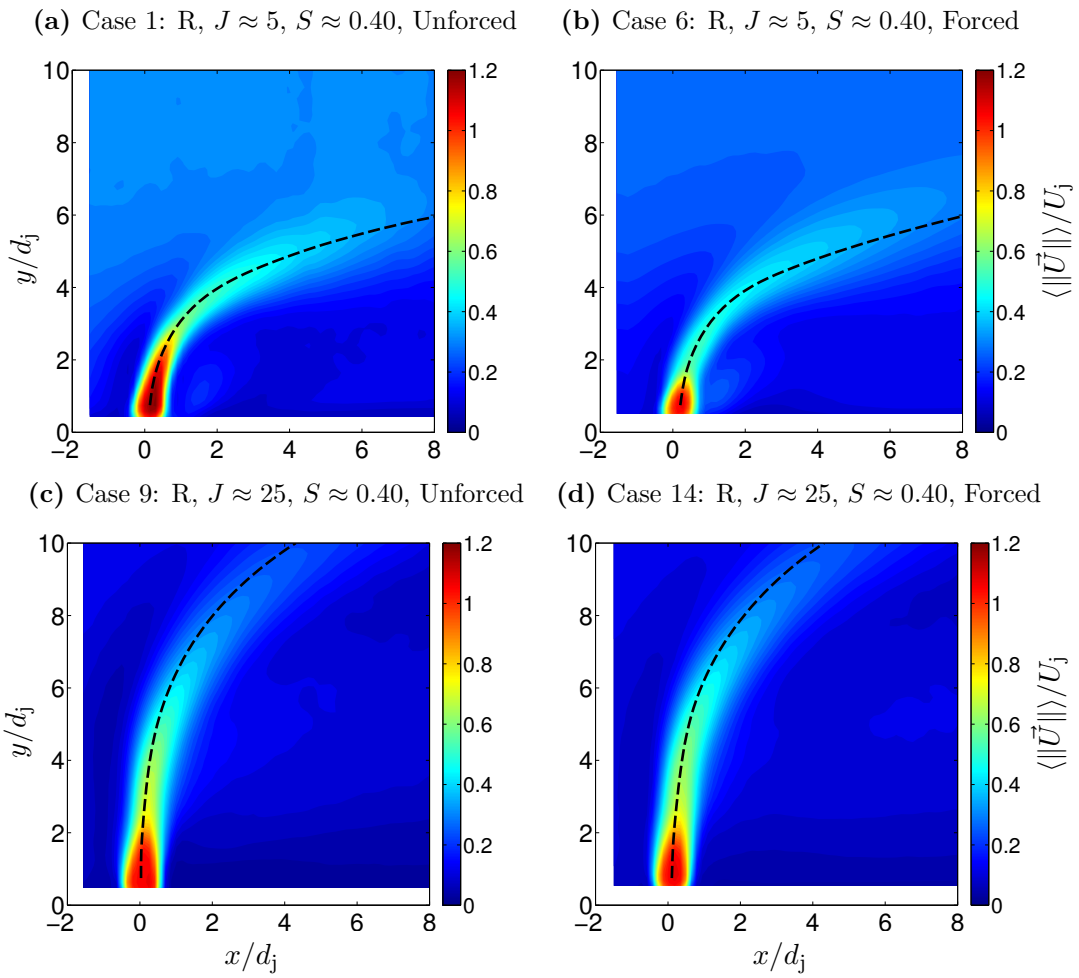

Figure 4.10: Contour plots of mean velocity magnitude for unforced and forced cases with low and high J. Forced conditions were $f_F = 250$Hz, $A_F = 1.5$A.

found in Figure 4.11, which plots the velocity magnitude along the jet center streamline. The significant difference in the streamwise decay of velocity magnitude for the unforced (no symbols) and forced cases (with symbols) in the near-field is immediately apparent. However, at $s/d_j \approx 6$ the velocity magnitudes of the unforced and forced low J cases again show good agreement. It is also noteworthy that there is very little difference between any of the forced low J cases, despite the significant variation in acoustic excitation frequency and amplitude. Not surprisingly, the decay of streamwise velocity magnitude in the high J cases is quite different relative to the low J cases. Specifically, there is almost no appreciable difference between the unforced high J cases and the forced high J cases.

The different response to crossflow forcing of the low and high J cases can be seen more clearly in the RMS velocity fields shown in Figure 4.12, where the test conditions are

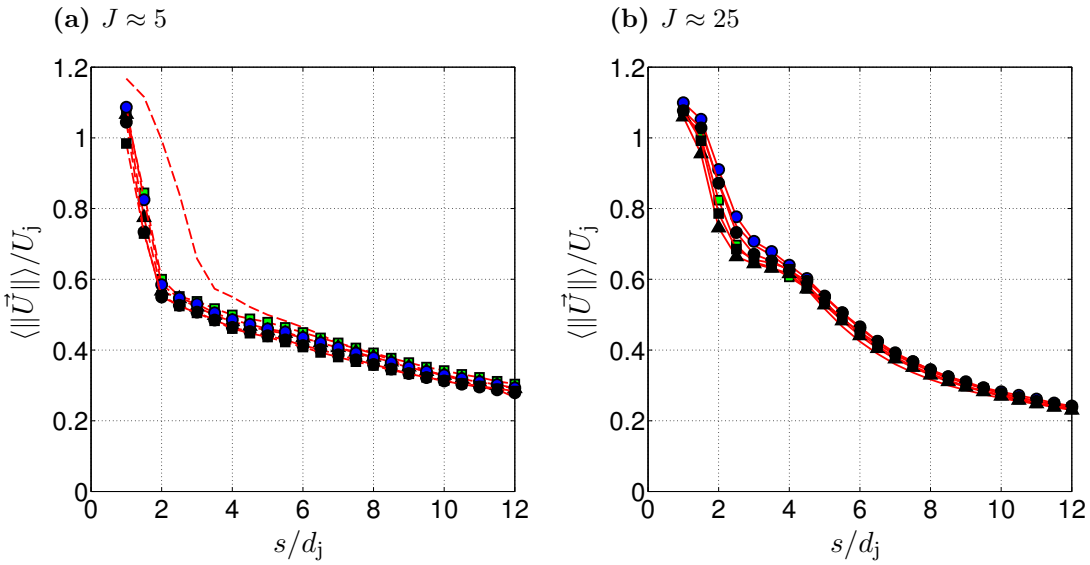

Figure 4.11: Decay of jet centerline velocity magnitude versus arc length for low and high J jets at different forcing conditions.

identical to those for the mean velocity fields shown in Figure 4.10. The location of the maximum RMS velocity fluctuations shifts in the low J cases between the unforced and forced jets. In the unforced case, the maximum RMS fluctuations occur in the shear layer near $(x/d_j, y/d_j) = (1, 3)$, while in the forced low J case, the maximum RMS fluctuation occurs in a concentrated region near the jet exit. In other words, the strongest velocity fluctuations in the unforced case are caused by the shear layer vortices, while the strongest velocity fluctuations in the forced case are due to the injector-coupled velocity response of the jet. However, the maximum RMS velocity fluctuation does not vary much, with values $\approx 0.30 U_j$ occurring in both the unforced and forced cases. It is also noteworthy that the RMS fluctuations in the shear layer are actually reduced relative to the unforced case. The difference between the unforced and forced cases is much less dramatic for the high J jets, although there is evidence of more intense fluctuations in the center of the jet closer to the injector in the forced case. This result is consistent with the fact that the relative magnitude of the injector-coupled response, u'_j/U_j, is much lower in the high J cases. In order to compare cases with different forcing conditions, the RMS velocity along the mean jet center streamline is plotted for both low and high J jets in Figure 4.13. There is again a clear difference between the unforced low J case and the forced low

J cases, but there is little difference between low J cases forced at different frequencies and amplitudes. As anticipated from the contour plots, the high J results show that while the spatial distribution of RMS velocity is not substantially altered, the peak amplitude of the RMS velocity is slightly increased at the same location where it peaked in the unforced case.

(a) Case 1: R, $J \approx 5$, $S \approx 0.40$, Unforced **(b)** Case 6: R, $J \approx 5$, $S \approx 0.40$, Forced

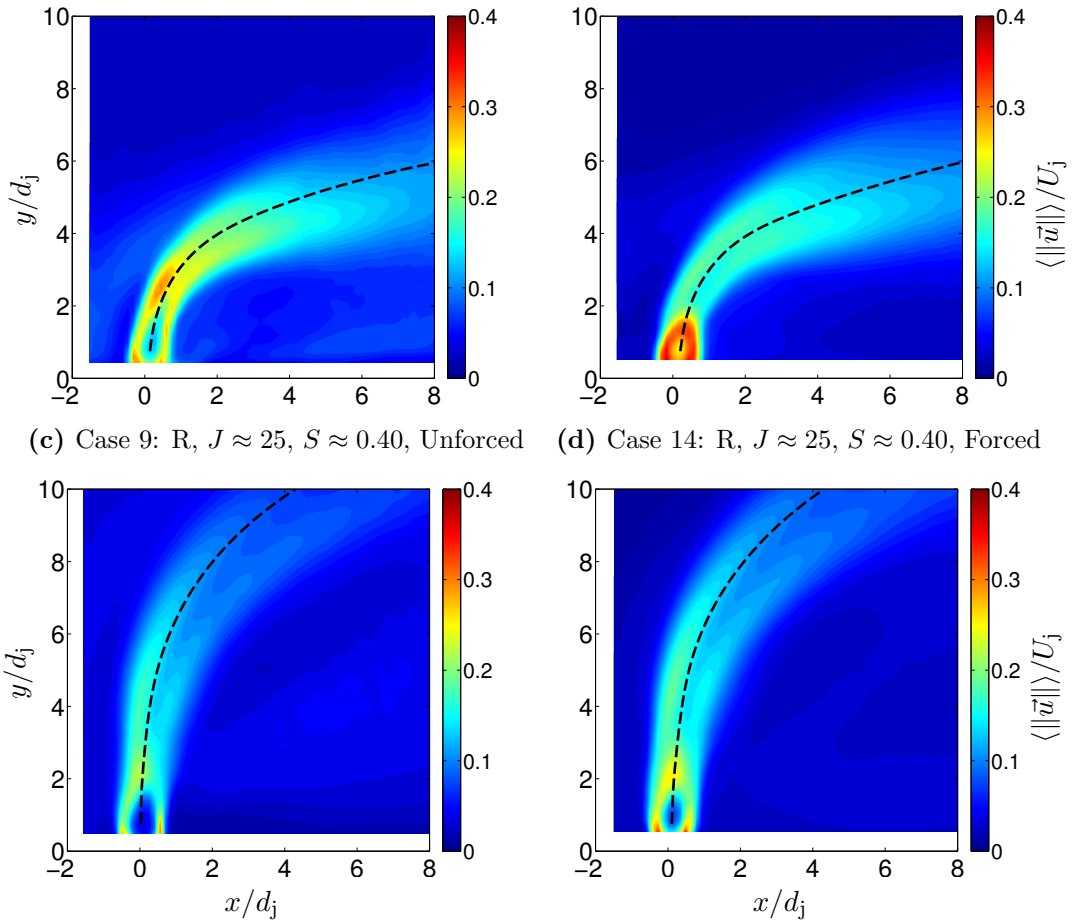

(c) Case 9: R, $J \approx 25$, $S \approx 0.40$, Unforced **(d)** Case 14: R, $J \approx 25$, $S \approx 0.40$, Forced

Figure 4.12: Contour plots of RMS velocity for unforced and forced cases with low and high J. Forced conditions were $f_{\mathrm{F}} = 250\mathrm{Hz}$, $A_{\mathrm{F}} = 1.5\mathrm{A}$.

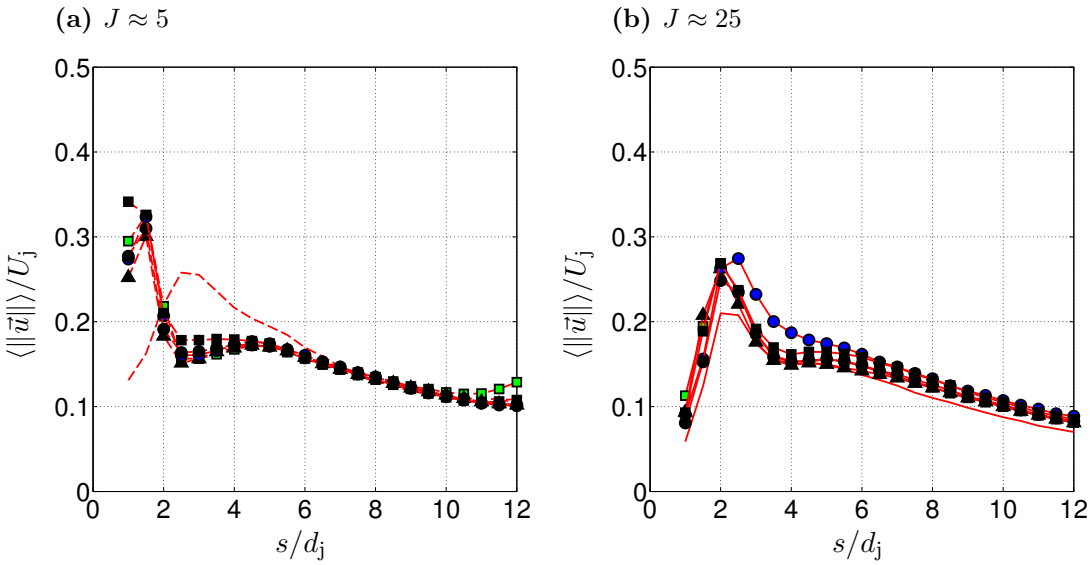

Figure 4.13: Decay of RMS velocity along the jet centerline as a function of arc length for low and high J jets at different forcing conditions.

4.2.2 Unsteady Results

Thus far only the time-averaged response of the jet to imposed crossflow forcing has been considered. It is important, however, to consider the unsteady response in order to fully appreciate the effect of crossflow forcing on the jet trajectory. Figure 4.14 presents a time sequence of instantaneous Mie scattering images superimposed by isocontours of the instantaneous OH PLIF field spanning one period of the acoustic pressure cycle at the forcing frequency for a forced, low J jet. Each instantaneous image in the sequence corresponds to a different phase value of the oscillating pressure signal at the forcing frequency, θ_{P_j}, measured inside the jet injector plenum (see Figure 2.5). A time trace of the raw pressure signal in the jet plenum, P_j, is shown in Figure 4.14e by the solid line, while the pressure signal at the forcing frequency is shown with a dotted line, which was determined using a Fourier decomposition. The phase (time) values corresponding to each of the instantaneous Mie scattering images are denoted by the blue and red dots along the reconstructed signal and the raw signal, respectively.

The key observation from the instantaneous Mie scattering images in Figure 4.14 is that the jet trajectory fluctuates significantly over the course of a single pressure cycle. While the jet extends furthest into the crossflow direction at $\theta_{P_j} = 0$, the penetration is at its

minimum near $\theta_{P_j} = \pi$ before recovering as the jet plenum pressure increases thereafter. It is also noteworthy that the contiguity of the jet is interrupted by the forcing, as evidenced by the "kink" in the jet seen at $\theta_{P_j} = 3\pi/4$ and $\theta_{P_j} = \pi$. This kink is a direct result of the time-varying jet exit velocity induced by the oscillating pressure drop between the jet plenum and the test section. A fluid element leaving the jet injector at a point when the pressure drop across the injector is at a maximum, e.g., near $\theta_{P_j} = 0$, has a higher exit velocity compared to a fluid element leaving at $\theta_{P_j} = \pi$. Neglecting the minor change in the crossflow momentum over the oscillation cycle, the fluid element with high exit velocity has both more momentum relative to the crossflow and a faster convection velocity compared to the fluid element leaving the injector half a period later. This leads to the formation of a kink in the instantaneous jet trajectory because the high velocity fluid tends to pull away from the lower velocity fluid trailing behind it.

The unsteady behavior of the jet also explains the shortening of the potential core observed previously in the forced, low J jets. The images in Figure 4.14 show that the unsteady jet exit velocity leads to a time-varying jet trajectory. This side-to-side jet flapping reduces the time-averaged centerline velocity of the jet but does not, however, significantly alter the time-averaged trajectory. Figure 4.15 presents additional Mie scattering images to explore the unsteady response of non-reacting and reacting low J jets with different S. The three test conditions selected are all forced at $f_F = 250$Hz and $A_F = 1.5$A. The different phase values again correspond to specific time instances during a single cycle of the oscillating jet plenum pressure at the forcing frequency. The jet flaps side-to-side in each case but the amplitude of the flapping depends on the specific test condition. In particular, the iso-density, reacting case (middle row) flaps with the largest amplitude while the non-reacting case appears to flap with the smallest amplitude. The difference in flapping amplitude between the two reacting cases is expected based on the larger injector-coupled velocity response of the iso-density jet, as discussed above in Section 4.1. Referencing Table B.1 shows that the normalized fluctuating jet exit velocity in the low S condition (Case 6) is $u'_j/U_j = 0.1127$, while it is $u'_j/U_j = 0.1847$ for the iso-density condition (Case 21). From a practical standpoint, the increased flapping of the iso-density case could be very

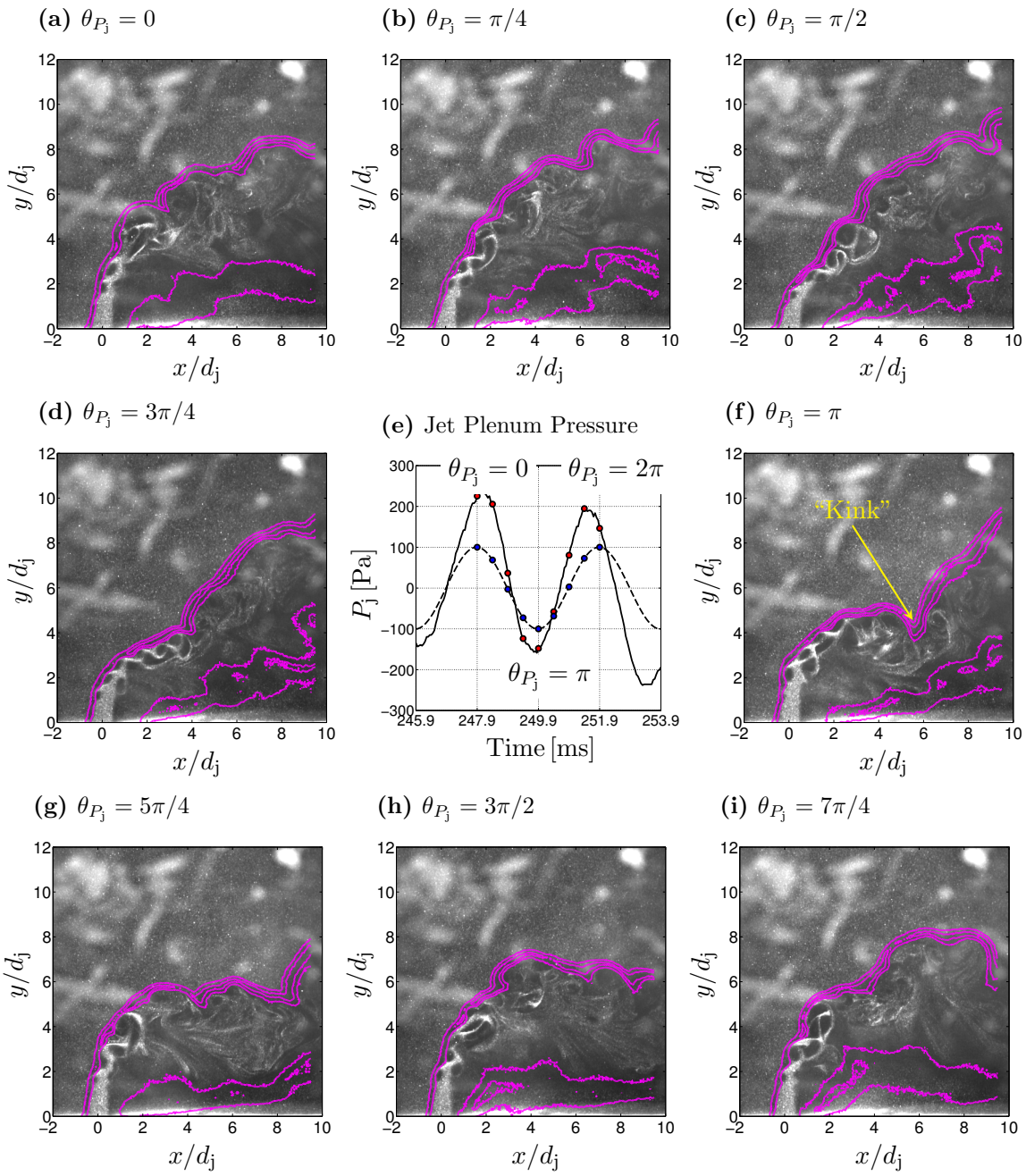

Figure 4.14: Time-sequence of instantaneous Mie scattering images spanning one acoustic forcing period for Case 6 (R, $J \approx 5$, $S \approx 0.40$, $f_F = 250$Hz, $A_F = 1.5$A). Phase values correspond to the jet plenum pressure signal. 10% and 50% OH PLIF contours shown in magenta.

undesirable because the leeward flame branch is pressed against the lower wall for portions of the forcing cycle, which undoubtedly increases heat transfer to the wall. Local extinction at the wall is also possible, which would lead to degraded emissions performance in a real system.

The relatively low amplitude flapping of the iso-density, non-reacting jet (Case 35) is, however, surprising since the normalized jet exit velocity fluctuation in this case is $u'_{\mathrm{j}}/U_{\mathrm{j}} = 0.1592$, which is much larger than in the reacting, low S case that flaps substantially. This observation suggests that the increased flapping amplitude seen in reacting jets is related to their time-varying near-field heat release. The extremely fast chemistry in vitiated crossflows means that combustion is largely mixing limited, while the low frequency jet flapping in the low J cases creates time instances when the jet stands more upright and time instances when the jet is pushed against the lower wall of the test section. Entrainment and mixing between the jet and the crossflow is enhanced when the jet stands more upright because crossflow fluid can more easily wrap around the jet core and flow into the leeward side of the jet. On the other hand, when the jet is pushed against the lower wall, as seen for Case 21 at $\theta_{P_{\mathrm{j}}} = \pi$, there is much less room for oxidizer in the crossflow to reach the fuel-rich jet fluid trapped against the lower wall. Thus, periodic modulation of the jet mixing leads to periodic heat release, which tends to augment the jet penetration when the jet exit velocity is already high while further suppressing penetration when jet exit velocity is low.

Before moving on to the high J cases, it is worth noting that the character of the shear layer vortices in Figure 4.15 varies with the phase of the oscillating pressure field, particularly in the iso-density, reacting case. At $\theta_{P_{\mathrm{j}}} = 0$ in Case 21, the windward shear layer is characterized by a train of regularly spaced vortices. A quarter period later at $\theta_{P_{\mathrm{j}}} = \pi/2$ there are no vortices anywhere along the windward shear layer. It is important to note that the characteristic timescale for the shear layer vortices, $\mathcal{O}(d_{\mathrm{j}}/U_{\mathrm{j}})$, is very fast compared to the timescale of the crossflow acoustics, $\mathcal{O}(1/f_{\mathrm{F}})$. This means that the jet flapping can be interpreted as a quasi-steady phenomena with respect to the shear layer dynamics. The lack of shear layer vortices at a point in the pressure cycle indicates that the instantaneous velocity field is less favorable for shear layer roll-up. Conversely, the

shear layer roll-up in the non-reacting case is not very sensitive to the phase of the pressure oscillation.

Figure 4.16 presents instantaneous Mie scattering images for high J jets at different points in the acoustic forcing cycle that are analogous to those shown previously for the low J jets. The forced high J jets flap in a similar manner to the low J jets but the amplitude of oscillation is much lower, at least within the field of view of the present experiments. The jet remains detached from the wall in all cases, and there is no evidence of the "kink" in the instantaneous jet trajectory that was seen in the lower J cases. The minimal flapping seen in the high J cases is consistent with the previous observation that neither the time-averaged velocity magnitude nor the RMS velocity of the high J cases varied significantly between unforced and forced jets. The relative flapping amplitude of different high J cases is difficult to discern from the Mie scattering images alone and can be better resolved by the instantaneous jet center streamline tracking procedure results discussed in the following paragraphs.

A quantitative method is needed to study the jet flapping phenomena described above. The method developed in this work relies on the time-resolved SPIV data to determine the instantaneous jet center streamline at each instant in time. A mean center streamline location can then be defined for each test condition based on the full set of instantaneous center streamlines, which will be referred to as a center streamline brush. An example of a center streamline brush is shown in Figure 4.17a. The contour map represents the number of instantaneous center streamlines located at each point over the entire duration of the experiment ($\approx$ 1.1 seconds), and the mean center streamline location is shown in white. As expected, the mean center streamline location computed using the set of instantaneous jet center streamlines is essentially identical to the mean jet center streamline extracted from the mean velocity field. The distance between the mean jet center streamline and the instantaneous jet center streamline at a given arc length distance, s/d_j, and time, t, along a line defined normal to the mean jet center streamline is defined as the jet center streamline perturbation distance, $\zeta_\mathrm{c} = \zeta_\mathrm{c}(s,t)$. A schematic illustrating the definition of ζ_c is available in Figure 4.17b. ζ_c contains all the spatio-temporal information needed to

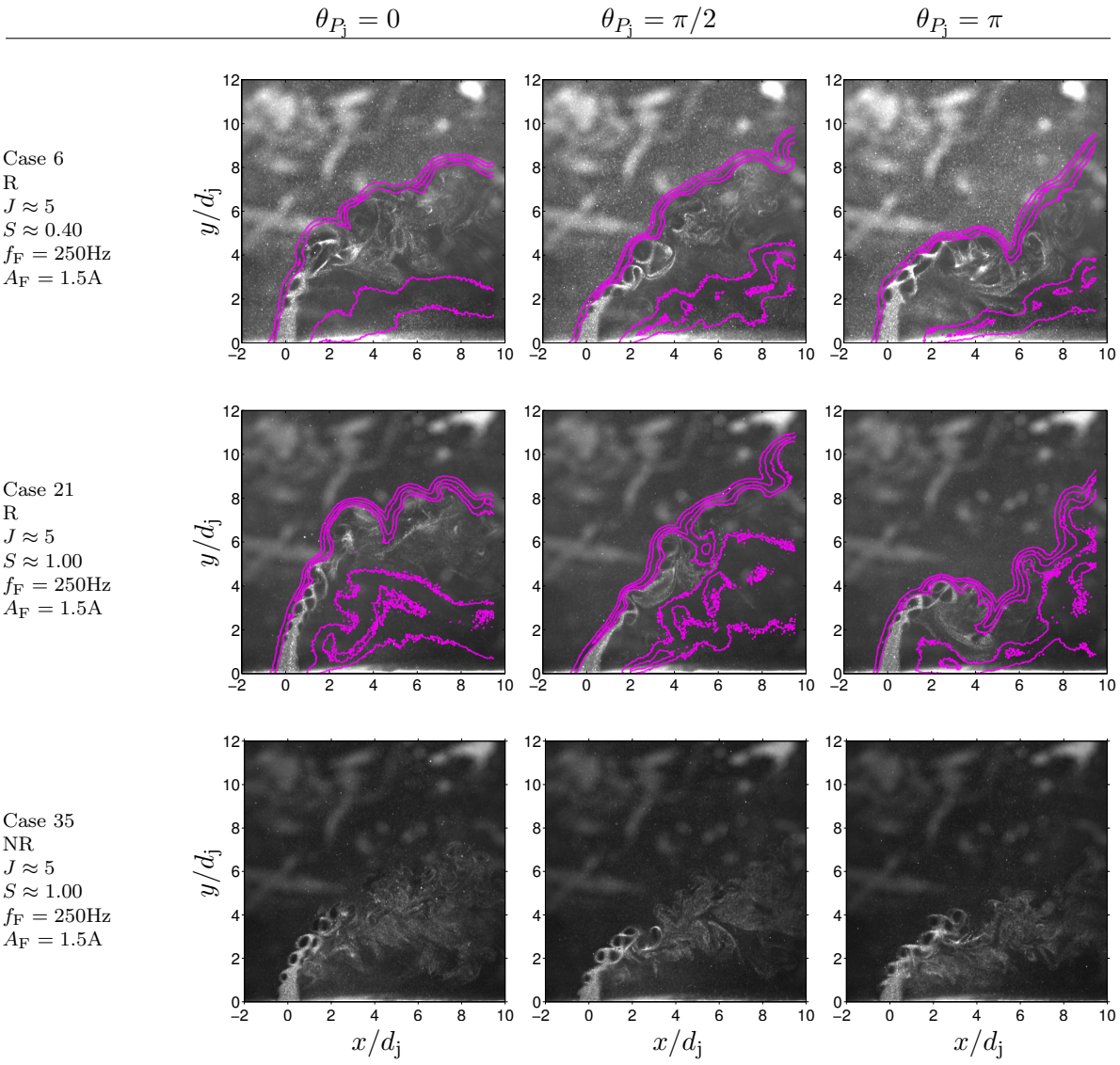

Figure 4.15: Instantaneous Mie scattering images at different phases of the acoustic pressure cycle inside the jet plenum for inert and reacting low J jets with different S. 10% and 50% OH PLIF contour lines superimposed in the reacting cases.

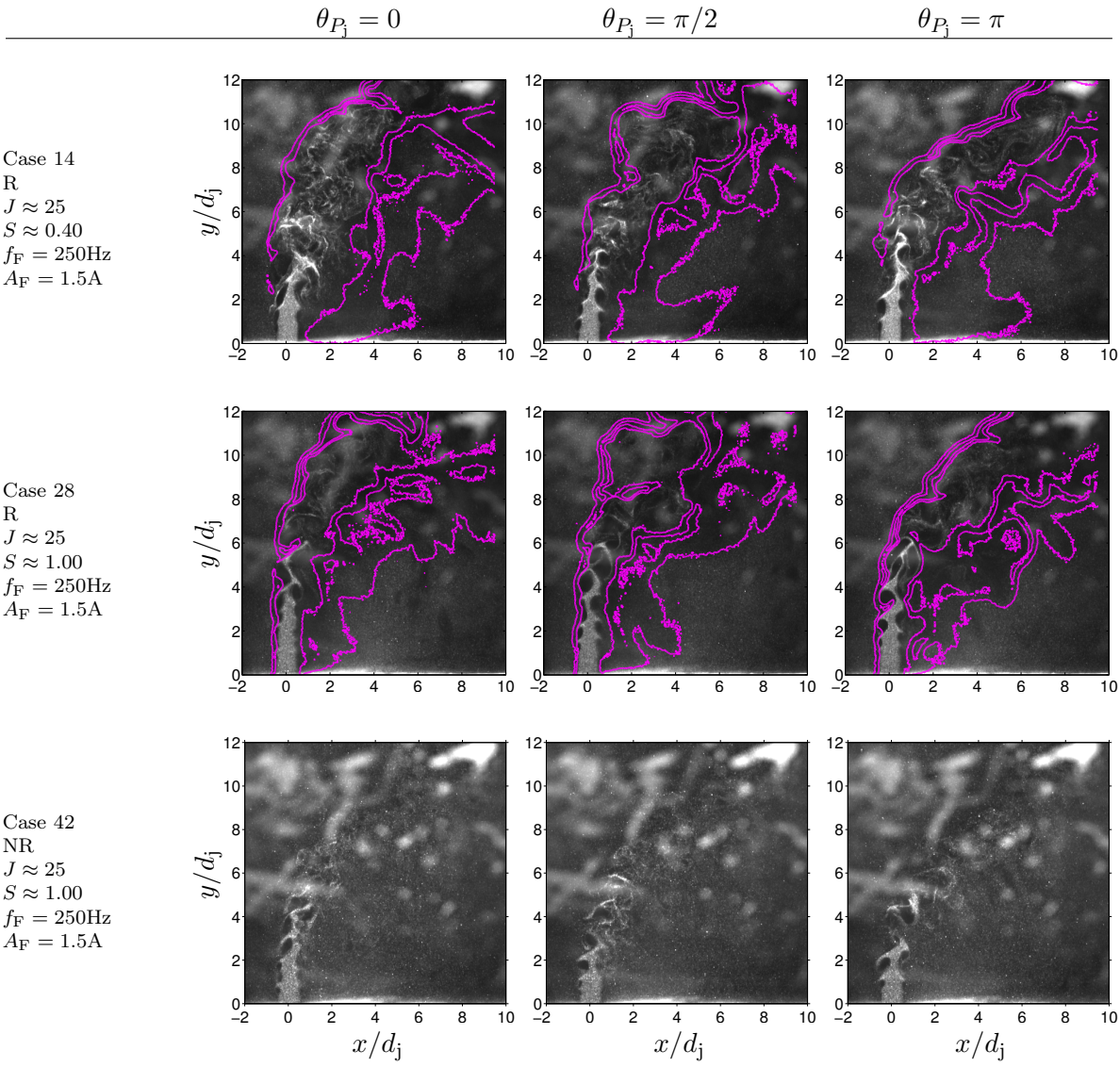

Figure 4.16: Instantaneous Mie scattering images at different phases of the acoustic pressure cycle inside the jet plenum for inert and reacting high J jets with different S. 10% and 50% OH PLIF contour lines superimposed in the reacting cases.

analyze and compare jet flapping for different test conditions.

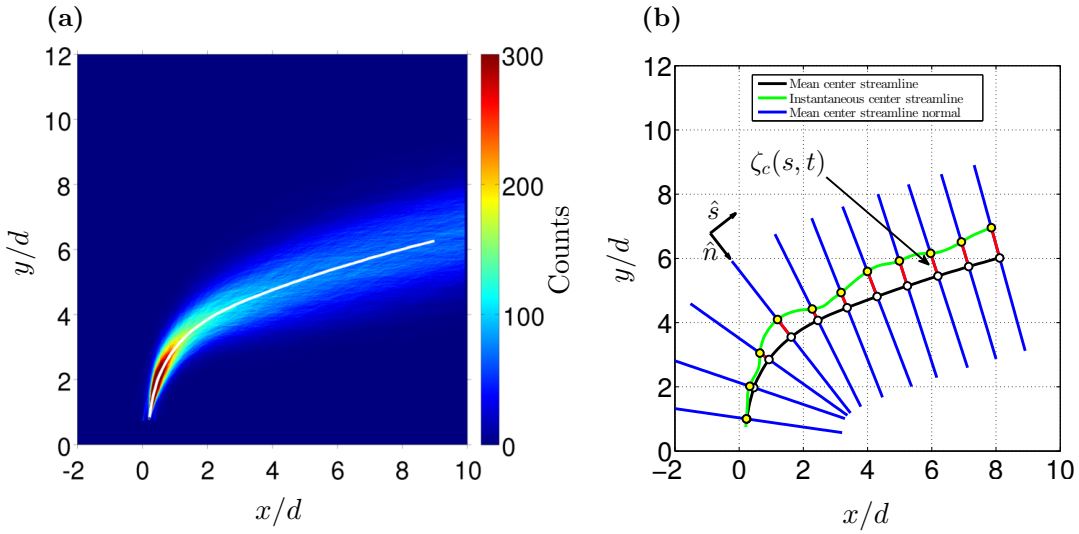

Figure 4.17: (a) Center streamline brush for Case 6 with mean center streamline location shown in white. (b) Sketch illustrating geometry for instantaneous center streamline perturbations.

Power spectra of center streamline perturbations normalized by the jet diameter are presented in Figure 4.18 for unforced and forced jets at two different J values. The spectra in the forced, low J case are dominated by perturbations at the forcing frequency, $f_{\mathrm{F}} = 250\mathrm{Hz}$, beyond $s/d_{\mathrm{j}} = 4$, and the amplitude of the perturbations at f_{F} increases sharply between $s/d_{\mathrm{j}} = 4$ and $s/d_{\mathrm{j}} = 10$. The forced, high J spectrum also has a sharp peak at the forcing frequency but the relative magnitude of the response at f_{F} compared to the background noise is much lower. It is important to note that the peaks in background noise are due to other naturally excited modes inside the combustor. The acoustic power in these natural modes is at least an order of magnitude smaller than that at the forcing frequency, as shown in Figure 2.8. Note that the ordinate scaling is not the same for the low J and high J cases because of their disparate amplitudes. The relatively robust response at frequencies other than f_{F} in the high J case is surprising since the crossflow acoustics are basically unchanged between the low J and high J cases. High J jets are, however, more resistant to injector coupling and have higher U_{j}, which leads to much lower $u'_{\mathrm{j}}/U_{\mathrm{j}}$ values compared to the low J cases. On the other hand, the value of u'_{∞}/U_{∞} does not change between the low and high J cases with the same applied crossflow forcing conditions. Thus, the

normalized crossflow velocity fluctuations, u'_∞/U_∞, are relatively more important in high J jets. As discussed in Section 4.1, the magnitude of u'_∞/U_∞ is a strong function of the velocity mode shape in the facility. Recall that the velocity mode shape for $f_\mathrm{F} = 250$Hz, which is the excitation frequency shown in Figure 4.18d, leads to a velocity node very near the jet injector, which does not occur at lower frequencies (e.g., see the mode shape for $f_\mathrm{F} = 177$Hz in Figure 4.3). Thus, the relatively high background noise seen in the low frequency regime of high J jets is a result of their resistance to injector-coupling, leading to an increase in the relative importance of the fluctuating crossflow velocity and thereby favoring lower frequencies oscillations that have larger u'_∞/U_∞.

To facilitate comparisons of jet flapping amplitude at different test and forcing conditions, the amplitude of the jet center streamline perturbations at the forcing frequency, $\zeta'_\mathrm{c}/d_\mathrm{j}$, is plotted as a function of s/d_j in Figure 4.19. ζ'_c is defined as

$$\zeta'_\mathrm{c}(s) = [2S_{\zeta_\mathrm{c}\zeta_\mathrm{c}}(s, f_\mathrm{F})]^{1/2} \tag{4.2}$$

where $S_{\zeta_\mathrm{c}\zeta_\mathrm{c}}(s, f_\mathrm{F})$ is the power spectrum of the jet center streamline perturbations evaluated at the forcing frequency for a specified arc length. Low J cases are shown on the left, while high J cases are on the right. Reacting, low S cases are in the top row, and reacting, iso-density cases are in the bottom row. These figures show that the amplitude of the jet flapping initially grows with increasing arc length in all cases. However, at higher s/d_j, the amplitude of jet flapping varies with f_F, J, and S. The relative amplitude of the jet flapping in the low J cases follows the trends observed in $u'_\mathrm{j}/U_\mathrm{j}$ as a function of frequency. For example, in the low J, low S cases in the upper left-hand corner, $u'_\mathrm{j}/U_\mathrm{j} = 0.0903$ for the 177Hz case while $u'_\mathrm{j}/U_\mathrm{j} = 0.1296$ for the 340Hz case. In other words, the larger $u'_\mathrm{j}/U_\mathrm{j}$ in the 340Hz case leads to larger jet flapping. This behavior is expected since the low J jets are dominated by injector-coupled response. Values of $u'_\mathrm{j}/U_\mathrm{j}$ for other cases can be found in Table B.1 and reliably predict the trends in jet flapping amplitude for low J jets in the range $s/d_\mathrm{j} < 6$.

The behavior of the low J jets in Figure 4.19 beyond $s/d_\mathrm{j} = 6$ cannot, however, be solely explained by the different values of $u'_\mathrm{j}/U_\mathrm{j}$ for different forcing conditions. In particular, $\zeta'_\mathrm{c}/d_\mathrm{j}$

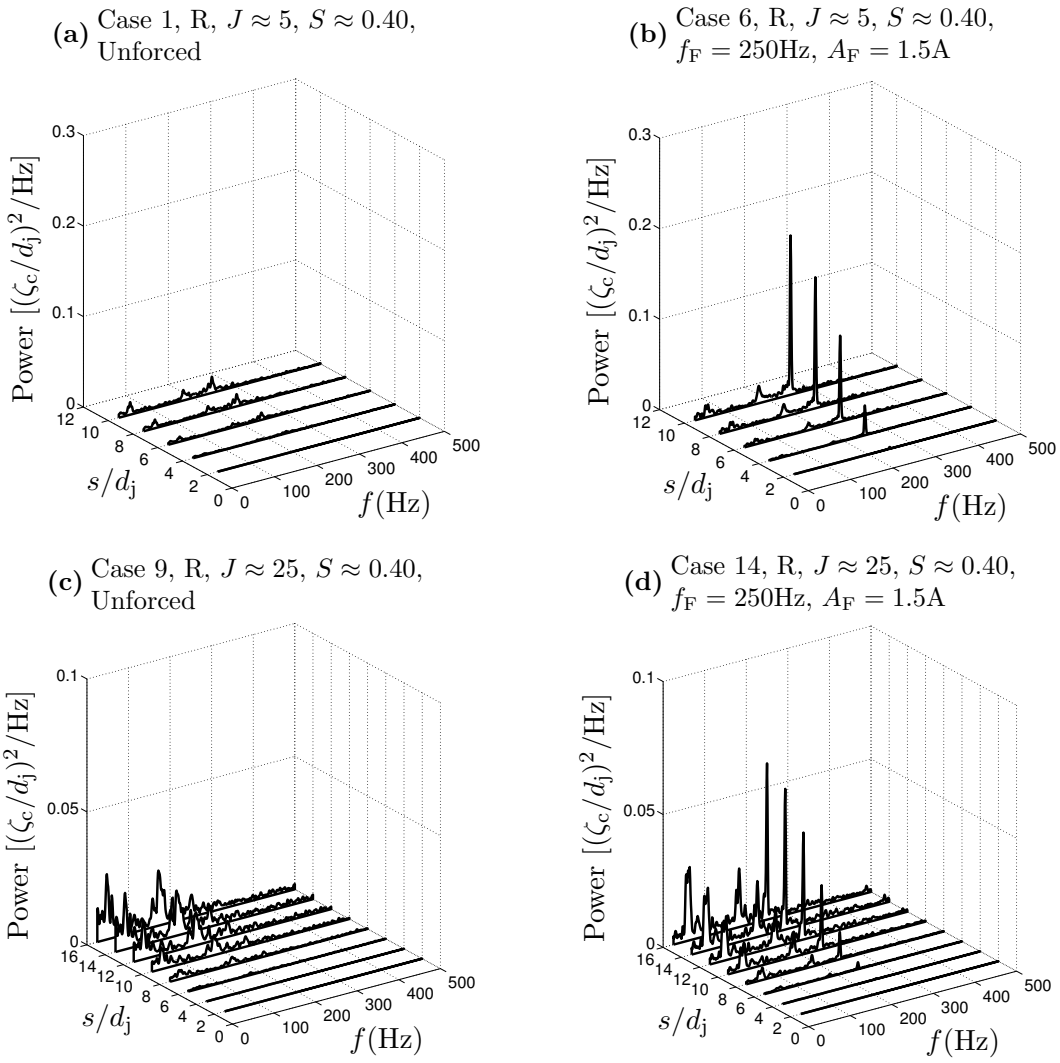

Figure 4.18: Power spectra of center streamline perturbations for (a,c) unforced and (b,d) forced jets.

saturates near $s/d_\mathrm{j} = 8$ for the 340Hz cases and is approaching saturation in the 250Hz cases by $s/d_\mathrm{j} = 10$. It is important to note that the saturation of the jet flapping amplitude is not due to wall confinement, as evidenced by the fact that the high J cases exhibit the same behavior even though they flap with lower amplitude and are far removed from any walls in the facility. Rather, this saturation phenomena is closely related to the "kink" in the instantaneous jet trajectory previously observed in Figure 4.15. Conceptually, jets flap further into the crossflow during time instances when the acoustic velocity at the jet exit augments the mean jet exit velocity, and jets penetrate less during time instances when the acoustic velocity at the jet exit opposes the mean jet exit velocity. From a Lagrangian perspective, the ability of a fluid element initially imparted with excess momentum at the jet exit to penetrate significantly further into the crossflow as it travels away from the jet injector is contingent not only on the excess momentum of the individual fluid element itself but also on the momentum of the fluid elements behind it. Equivalently, the instantaneous jet trajectory will continue to over-penetrate relative to the time-averaged jet trajectory as long as all the fluid in the jet plume exits the jet injector with velocity greater than U_j. The length of time during which this condition is met is directly related to the acoustic forcing period and is shorter for higher frequencies. Hence, the 340Hz cases saturate first in the present experiments, followed by the 250Hz cases, and the 177Hz cases, which do not saturate within the field of view. An interesting consequence of this saturation mechanism is that jets forced at lower frequencies can achieve larger absolute flapping amplitudes than jets forced at higher frequencies but having the same $u'_\mathrm{j}/U_\mathrm{j}$. This trend is clearly evident in the high J cases shown in Figure 4.19, where the lower frequency cases achieve larger flapping amplitudes than the 340Hz case.

Studying the phase of the jet center streamline perturbations provides additional insight into the jet response to the crossflow forcing that cannot be gained by solely analyzing the flapping amplitude. The phase angle of the jet center streamline perturbations, $\theta_{\zeta_\mathrm{c}}$, is determined as

$$\theta_{\zeta_\mathrm{c}}(s) = \angle\check{\zeta}_\mathrm{c}(s, f_\mathrm{F}) \cdot (180/\pi) \tag{4.3}$$

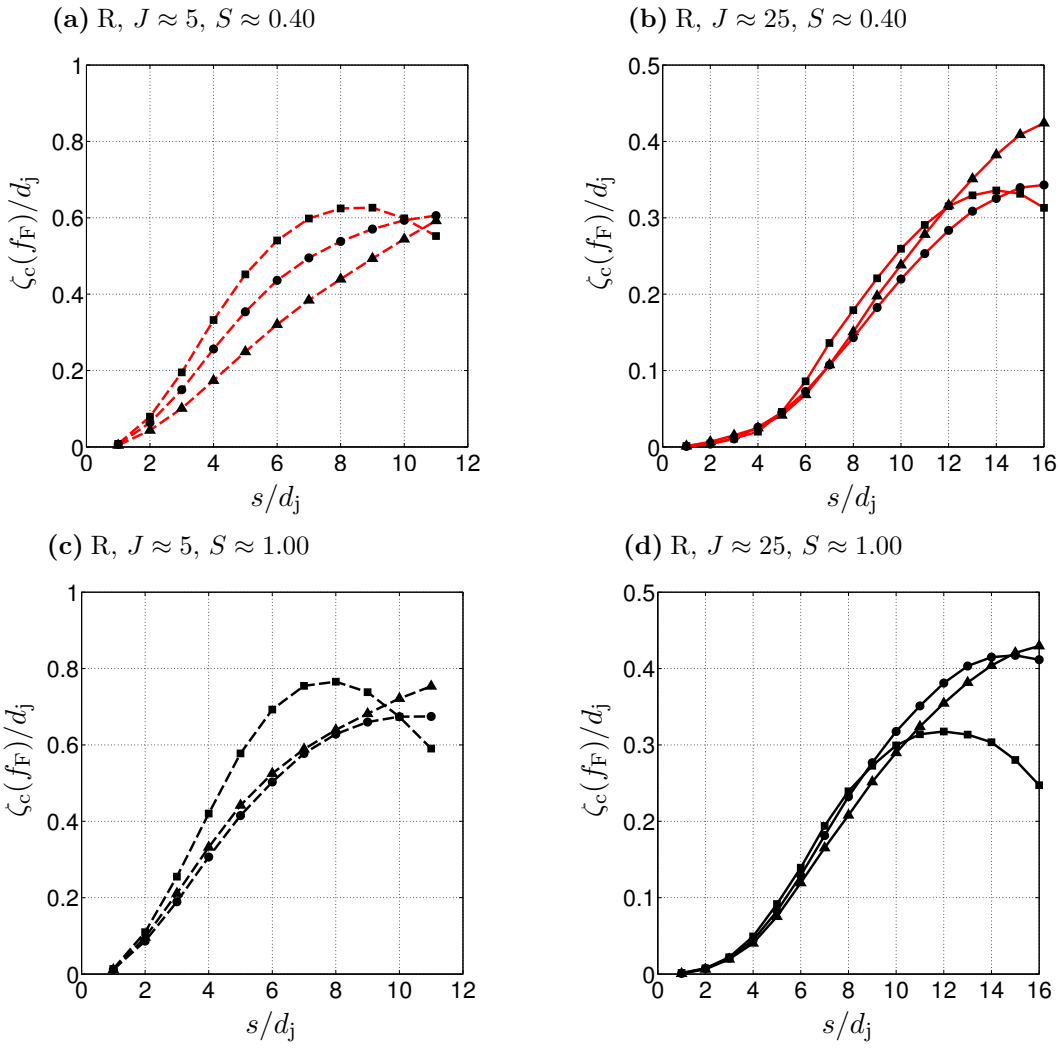

Figure 4.19: Comparison of center streamline perturbation amplitudes at different forcing frequencies and test conditions. (▲): f_F = 177Hz & A_F = 1.5A, (●): f_F = 250Hz & A_F = 1.5A, and (■): f_F = 340Hz & A_F = 1.5A.

where $\check{\zeta}_{\mathrm{c}}(s, f_{\mathrm{F}})$ is the component of the discrete Fourier transform of $\zeta_{\mathrm{c}}(s,t)$ at the forcing frequency, f_{F}, at a specified arc length distance, s. Since the sampling frequency of the SPIV is 10kHz, the FFT is computed using the first 10^4 elements of the signal (1 second of data) such that a frequency bin is located exactly at the forcing frequency in each case. Figure 4.20 shows the spatial variation of $\theta_{\zeta_{\mathrm{c}}}(s)$ for reacting, low J, iso-density jets forced at three different frequencies. The value of $\theta_{\zeta_{\mathrm{c}}}(s)$ in each figure has been offset by a constant such that $\theta_{\zeta_{\mathrm{c}}}(1d_{\mathrm{j}}) = 0$. Three reference lines are superimposed for each case in Figure 4.20. The blue line represents the phase roll-off for a perturbation oscillating at f_{F} and convecting along the jet center streamline with fixed convective velocity $U_{\mathrm{conv}} = (U_{\mathrm{j}} + U_{\infty})/2$, while the green line represents the phase roll-off for a perturbation convecting with the lower velocity $U_{\mathrm{conv}} = U_{\infty}$. The absolute value of the phase is arbitrary for both the blue and the green lines and thus has been offset from $\theta_{\zeta_{\mathrm{c}}}(s)$ to avoid confusion. The slope of the blue and green lines is fixed, however, by their respective convection velocities and thus can be compared against the slope of $\theta_{\zeta_{\mathrm{c}}}(s)$ to appreciate the relative convective velocity of the jet center streamline perturbations. The curved pink line represents the phase roll-off of a perturbation moving along the jet center streamline with convective velocity equal to the streamwise velocity along the mean center streamline, $U_{\mathrm{conv}} = U_{\hat{s}}(s)$. This is determined using the expression

$$\theta_{\hat{s}}(s) = \int_0^s -\frac{2\pi f_{\mathrm{F}}}{U_{\hat{\mathrm{s}}}(s^*)}\,\mathrm{d}s^* + \theta_O \tag{4.4}$$

where $U_{\hat{\mathrm{s}}}(s)$ is extracted directly from the SPIV results and θ_0 is an arbitrary constant that is adjusted to satisfy the relationship $\theta_{\hat{s}}(1d_{\mathrm{j}}) = \theta_{\zeta_{\mathrm{c}}}(1d_{\mathrm{j}})$.

The results shown in Figure 4.20 demonstrate that jet center streamline perturbations introduced by the crossflow forcing propagate in the streamwise direction at rates that depend on both f_{F} and s/d_{j}. In the lowest frequency case, the phase roll-off is nearly linear with a convection velocity close to $(U_{\mathrm{j}} + U_{\infty})/2$. In both of the higher frequency cases, the convection velocity decreases with increasing s/d_{j}. The convection velocity of the 340Hz case, in particular, drops to U_{∞} by $s/d_{\mathrm{j}} \approx 8$, which is the same streamwise location where the amplitude of the center streamline perturbations saturated. This agreement is

not a coincidence; it follows from the fact that the jet center streamline perturbations do not depend on the jet exit velocity once the continuity of the jet column is broken. From that point onward, the center streamline perturbations are apparently convected at the crossflow velocity. The transition in convective velocity can also be interpreted as a shift from jet-like behavior, where the expected convective velocity would be closer to U_{j}, to more wake-like behavior, where the expected convective velocity would be close to U_{∞}. Interestingly, previous researchers have shown that time-averaged JICF metrics such as the centerline concentration decay and centerline velocity decay of unforced JICF transition from jet-like scaling to wake-like scaling around $s/Jd_{\mathrm{j}} = 0.3$ [23]. The results presented in this section suggest that low frequency crossflow excitation may cause a similar transition in the unsteady dynamics of JICF.

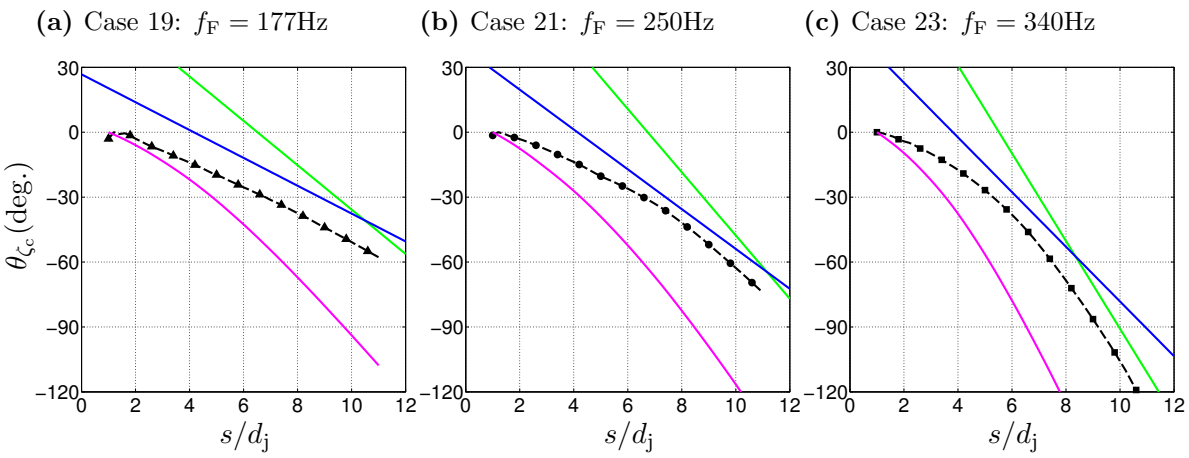

Figure 4.20: Phase of center streamline perturbations (---) oscillating at the forcing frequency as a function of arc length distance for reacting jets with $J = 5$, $S = 1.00$, and $A_{\mathrm{F}} =$ 1.5A. (—): Phase roll-off for a convective disturbance moving with the streamwise velocity, $U_{\mathrm{conv}} = U_{\hat{s}}(x, y)$. (—): Phase roll-off for a convective disturbance moving at the average of the jet and the crossflow velocity, $U_{\mathrm{conv}} = (U_{\mathrm{j}} + U_{\infty})/2$. (—): Phase roll-off for a convective disturbance moving at the crossflow velocity, $U_{\mathrm{conv}} = U_{\infty}$.

Figure 4.21 presents phase roll-off results for high J cases, similar to those discussed above for the low J cases. The mixture composition and crossflow forcing conditions are the same as in Figure 4.20. The results show that jet center streamline perturbations for high J cases behave very differently than in the low J cases. In general, perturbations convect at velocities much closer to the $U_{\hat{s}}(s)$ in the high J cases, as evidenced by the

similar slopes of the curves for $\theta_{\zeta_c}(s)$ (black) and $\theta_{\hat{s}}(s)$ (pink). The nearly constant value of θ_{ζ_c} for the 177Hz case below $s/d_j \approx 8$ suggests that perturbations are convecting at very high velocities in this region. This may be the result of jet center streamline perturbations due to u'_∞ rather than u'_j. Recall that u'_∞/U_∞ is proportionately more important in high J cases and the 177Hz case has the largest value of u'_∞/U_∞. Perturbations due to u'_∞ would appear to propagate at near infinite velocity since u'_∞ is essentially perpendicular to $\hat{s}$ near the jet injector. Within the field of view, the jet center streamline perturbations in the high J cases convect at velocities greater than U_∞, as seen by the fact that the $\theta_{\zeta_c}(s)$ curve is never parallel to the green line representing $U_{conv} = U_\infty$. Presumably, with a sufficiently large field of view, the convection velocity will approach U_∞ in the high J cases as well.

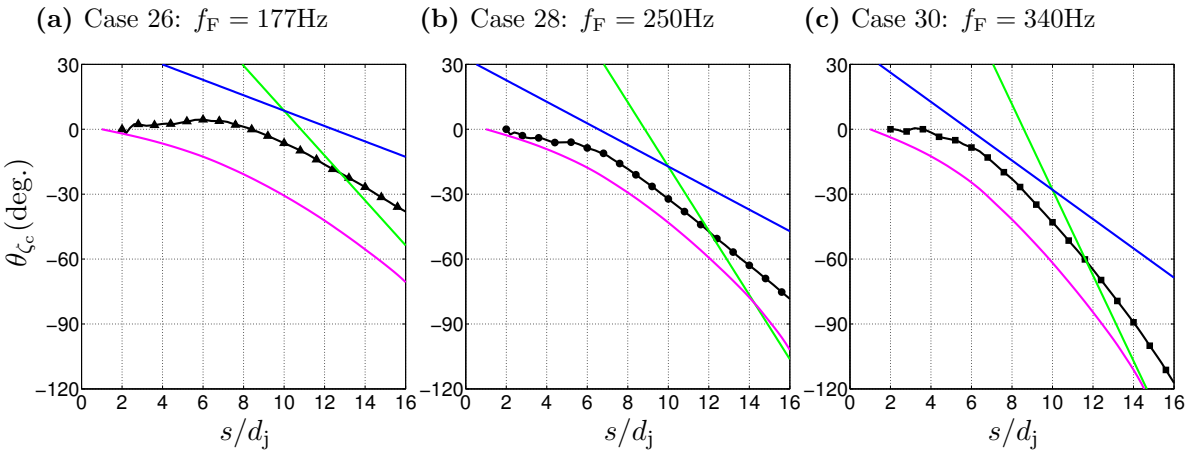

Figure 4.21: Phase of center streamline perturbations (—) oscillating at the forcing frequency as a function of arc length distance for reacting jets with $J = 25$, $S = 1.00$, and $A_F = 1.5$A. (—): Phase roll-off for a convective disturbance moving with the streamwise velocity, $U_{conv} = U_{\hat{s}}(x, y)$. (—): Phase roll-off for a convective disturbance moving at the average of the jet and the crossflow velocity, $U_{conv} = (U_j + U_\infty)/2$. (—): Phase roll-off for a convective disturbance moving at the crossflow velocity, $U_{conv} = U_\infty$.

4.3 Modification of the Leeward Recirculation Zone

The results presented in the previous section showed that acoustically forcing the crossflow causes jet flapping, which alters both the time-averaged and the unsteady behavior of JICF. This section investigates the effect of crossflow forcing on the recirculation region located on the leeward side of the jet. The leeward recirculation zone is a prominent structural feature of the JICF that plays a key role in flame stabilization, especially for jets with moderate

temperature crossflows [54, 87]. The size and strength (i.e., the magnitude of the reverse flow velocity) of the leeward recirculation zone were shown in Section 3.1 to be sensitive to changes in J, S, and the reactivity of the mixture. The leeward recirculation zone is also modified by crossflow forcing, as evidenced by the phase-averaged x-component velocity fields presented in Figure 4.22. The contour plots correspond to three different low J test conditions forced at $f_{\mathrm{F}} = 250\mathrm{Hz}$ and $A_{\mathrm{F}} = 1.5\mathrm{A}$. Similar to the results presented in Section 4.2, the phase values represent specific points along the acoustic pressure cycle measured in the jet plenum. The phase averaging is accomplished by collecting and averaging the subset of instantaneous U velocity field measurements that correspond to a specified phase value. The time-averaged jet trajectory is superimposed in each case to provide a spatial frame of reference.

The phase-averaged results for the reacting, low S case in the top row of Figure 4.22 show significant differences between the two different phase values. At $\theta_{P_{\mathrm{j}}} = 0$ the jet penetration is near a maximum and most of the high U velocity fluid lies above the mean jet center streamline. The recirculation region on the leeward side of the jet for $\theta_{P_{\mathrm{j}}} = 0$ is enlarged relative to the smaller recirculation region seen a half period later at $\theta_{P_{\mathrm{j}}} = \pi$. Similarly, the high U velocity fluid lies mostly below the mean jet center streamline at $\theta_{P_{\mathrm{j}}} = \pi$. Despite the smaller spatial extent, the magnitude of the reverse flow in the leeward recirculation zone is basically unchanged at $\theta_{P_{\mathrm{j}}} = \pi$. The change in the leeward recirculation zone is more noticeable in the reacting, iso-density case shown in the middle row of Figure 4.22. This result is not surprising since $u'_{\mathrm{j}}/U_{\mathrm{j}}$ is larger in the iso-density case, and the jet flaps with larger amplitude than in the low S case. The larger flapping amplitude leads to a leeward recirculation zone at $\theta_{P_{\mathrm{j}}} = \pi$ that is roughly half the size of the recirculation zone seen at $\theta_{P_{\mathrm{j}}} = 0$, although the peak negative flow velocity inside the recirculation zone is still relatively unaffected. On the other hand, the non-reacting, low J case, which is shown in the bottom row of Figure 4.22, is less sensitive to the crossflow forcing. The U velocity distribution changes slightly between $\theta_{P_{\mathrm{j}}} = 0$ and $\theta_{P_{\mathrm{j}}} = \pi$ in this case, but the leeward recirculation zone is essentially unchanged. This finding is consistent with the results of Section 4.2, which showed that non-reacting jets are less sensitive to crossflow forcing than

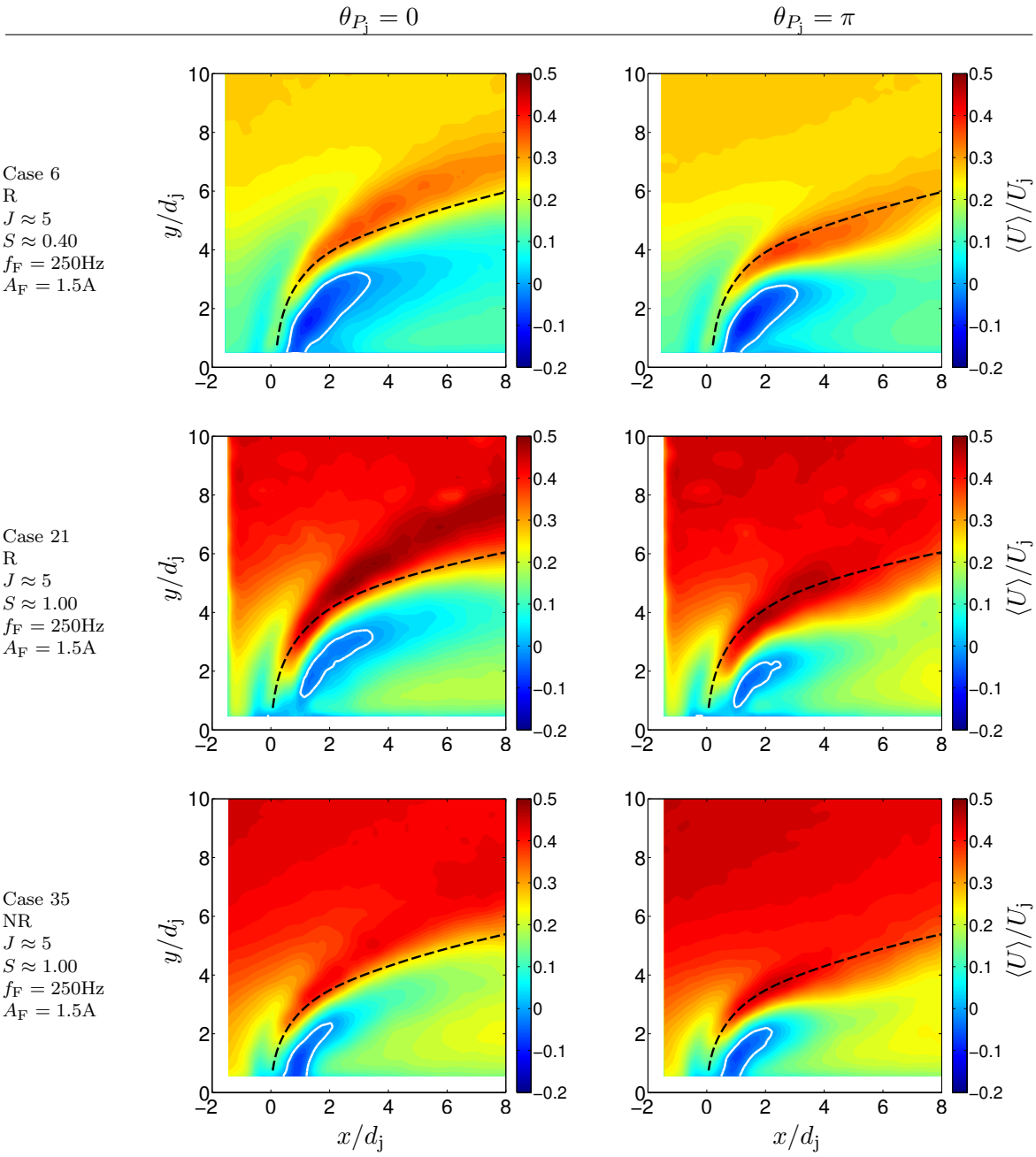

Figure 4.22: Phase-averaged non-dimensional axial velocity in low J cases with identical forcing. Selected phase values correspond to time instances of high ($\theta_{P_j} = 0$) and low ($\theta_{P_j} = \pi$) jet plenum pressure, P_j. (---): Mean jet center streamline trajectory. (▬): $U = 0$ contour.

reacting jets with the same u'_j/U_j.

The periodic modulation of the spatial extent of the leeward recirculation zone in the reacting jets is noteworthy since a reduction in the size of the leeward recirculation zone has been shown by Kolla et al. [53] to precede global flame blowoff in reacting JICF stabilized in a 750K crossflow. In that study, the reduction in the size of the leeward recirculation zone was the result of gradually reducing the jet injection angle from 90° to 70°. Flame blowoff occurred when the injection angle approached 75° because the significantly diminished leeward recirculation zone in the angled injection case did not provide the same low velocity, well-mixed region responsible for flame stabilization in the 90° injection case. Flame blowoff does not occur in the present experiments because of the much higher crossflow temperature, $T_\infty = 1200$K. The modification of the leeward recirculation zone due to crossflow forcing is, however, likely to interfere with flame stabilization in jets injected into low-to-moderate temperature crossflows.

Phase averaged $\langle U \rangle$ velocity fields for high J cases are presented in Figure 4.23. Generally speaking, the leeward recirculation zone of high J jets is less sensitive to the phase value of the pressure cycle. This result could be anticipated based on the lower jet flapping amplitudes seen in the high J cases. The leeward recirculation zone in high J jets is much more sensitive to differences in S than to differences in the acoustic pressure phase. However, similar to the low J results, the leeward recirculation zone in the non-reacting case is basically independent of the phase of the pressure cycle, which further supports the argument in Section 4.2 that combustion is partially responsible for enhancing jet flapping in forced cases.

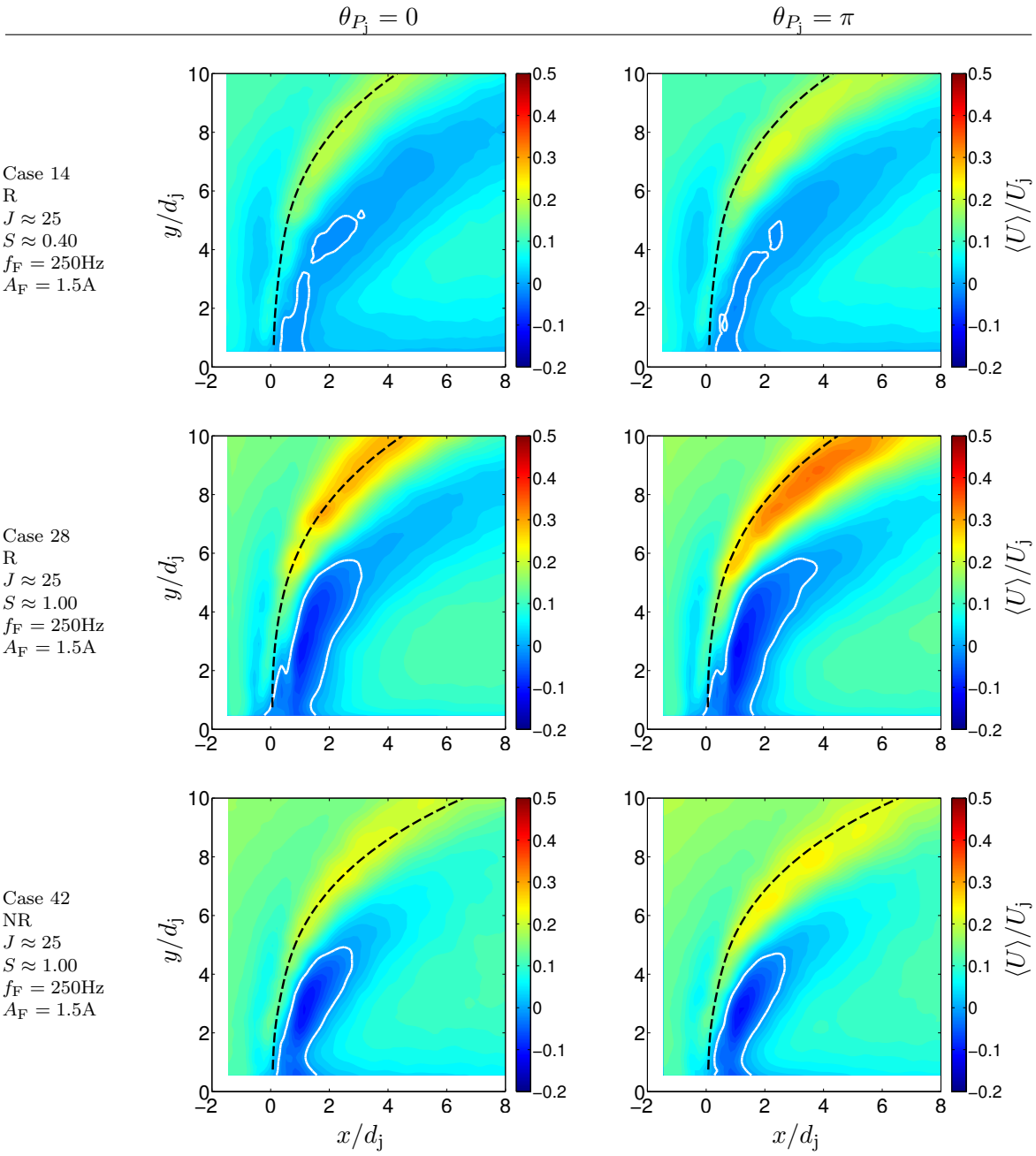

Figure 4.23: Phase-averaged non-dimensional axial velocity in high J cases with equivalent forcing. Selected phase values correspond to time instances of high ($\theta_{P_j} = 0$) and low ($\theta_{P_j} = \pi$) jet plenum pressure, P_j. (---): Mean jet center streamline trajectory. (▬): $U = 0$ contour.

4.4 Unsteady Velocity and Vorticity Field Response

The results shown in Sections 4.2 and 4.3 demonstrated the significant effect that crossflow forcing can have on structural features of the JICF, including the jet trajectory and the size of the leeward recirculation zone. This section provides a more detailed examination of the forced response of JICF at the forcing frequency based on spectral analysis of the oscillatory velocity and vorticity fields. To facilitate comparison between cases with different J values, a coordinate system defined relative to the trajectory of the mean jet center streamline is used instead of the standard cartesian coordinates. A schematic illustrating the definition of the streamwise and normal component directions with respect to the standard cartesian grid is shown in Figure 4.24 for a representative case.

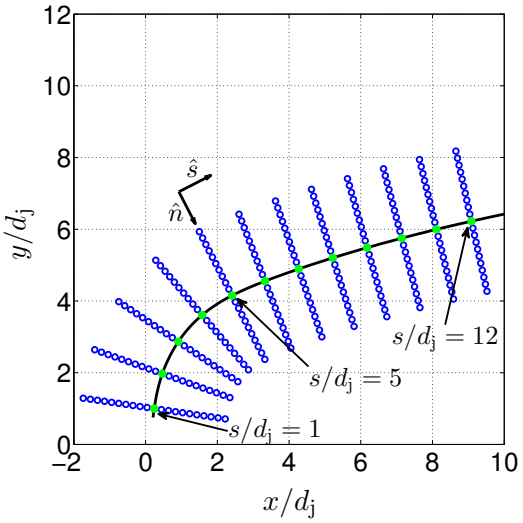

Figure 4.24: Illustration demonstrating the definition of the streamwise and normal component directions with respect to the standard cartesian grid. (—): Mean jet center streamline.

As discussed in Section 4.1, crossflow forcing excites the jet both through an injector-coupled mechanism and through the direct action of the fluctuating crossflow velocity. The injector-coupled mechanism is dominant, however, in most cases. Therefore, the crossflow forcing acts on the jet primarily through the introduction of an axisymmetric velocity disturbance, u'_j, at the jet exit. The spatial evolution of these initially streamwise disturbances can be understood by examining Figure 4.25, which presents waterfall plots of the fluctuating streamwise velocity at the forcing frequency for six different test conditions. In each

case, $u'_{\hat{s}}(f_F)$ is defined as

$$u'_{\hat{s}}(s, n, f_F) = [2S_{U_{\hat{s}}U_{\hat{s}}}(s, n, f_F)]^{1/2} \tag{4.5}$$

where $S_{U_{\hat{s}}U_{\hat{s}}}(s, n, f_F)$ is the component of the power spectrum of the streamwise velocity, $U_{\hat{s}}(s, n, t)$, evaluated at the forcing frequency. The waterfall plots of $u'_{\hat{s}}(f_F)$ for each test condition are normalized by the corresponding value of u'_j. To simplify the notation, $u'_{\hat{s}}(f_F)$ will be referred to simply as $u'_{\hat{s}}$ since it is understood that the fluctuations of interest are those at the forcing frequency. As shown in Figure 4.24, the s/d_j coordinate is zero at the jet exit and increases in the streamwise direction. The n/d_j coordinate is zero along the jet center streamline and takes positive values on the leeward side of the jet, i.e., in the downstream direction, and negative values on the windward side of the jet.

The results show interesting and non-intuitive spatial evolution patterns for the fluctuating streamwise velocity. $u'_{\hat{s}}/u'_j$ is essentially symmetric near the jet injector, which is expected based on the predominately axisymmetric excitation. The extent to which $u'_{\hat{s}}/u'_j$ remains symmetric varies, however, with J. The low J cases lose their symmetry by $s/d_j \approx 2$, while the high J cases retain their symmetry until $s/d_j \approx 5$. The evolution of $u'_{\hat{s}}/u'_j$ in the low and high J cases diverges significantly after the streamwise perturbations lose their symmetry with respect to the mean jet center streamline.

In the low J cases, the peak magnitude of $u'_{\hat{s}}/u'_j$ on the windward side (i.e., $n/d_j < 0$), declines sharply beyond $s/d_j \approx 2$, and the location of the peak shifts further away from the jet centerline. The magnitude of $u'_{\hat{s}}/u'_j$ on the leeward side increases sharply around the same point where the windward fluctuations begin to decay. Further downstream, $u'_{\hat{s}}/u'_j$ continues to decline on the windward side, while the magnitude of $u'_{\hat{s}}/u'_j$ saturates on the leeward side and diffuses in the normal direction. Interpreting these results requires recognizing the two different mechanisms responsible for generating streamwise velocity fluctuations. The first mechanism, which is most important near the jet injector, is directly related to u'_j. Injector-coupling causes a fluctuating exit velocity, u'_j, and those perturbations are simply convected by the mean flow, which is in the streamwise direction. The second mechanism is related to jet flapping and becomes dominant once the jet begins to deflect into the crossflow

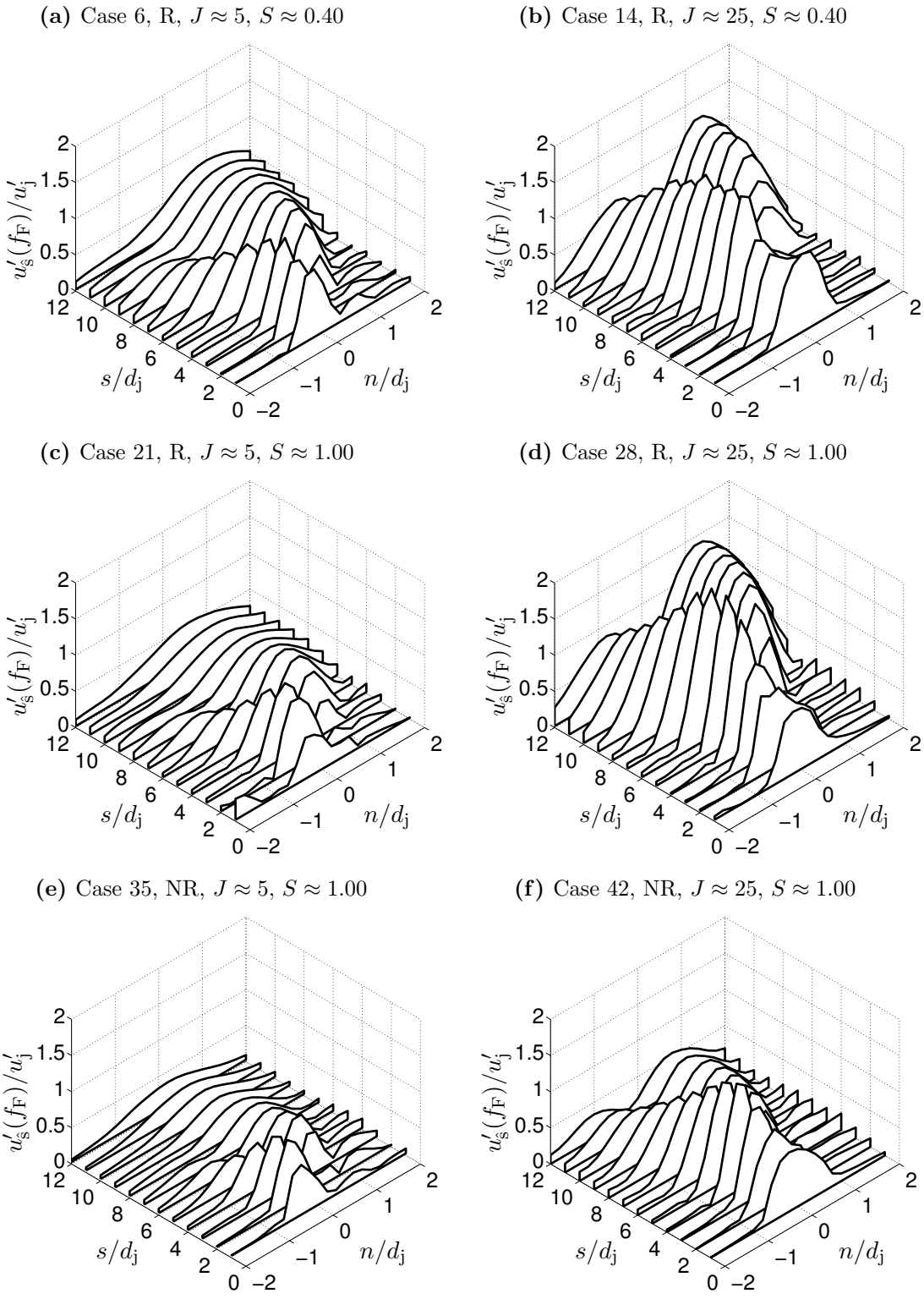

Figure 4.25: Waterfall plots of streamwise velocity fluctuations at the forcing frequency extracted along lines defined normal to the mean jet center streamline trajectory. Forcing frequency and amplitude held constant for all cases ($f_F = 250$Hz, $A_F = 1.5$A).

direction, near $s/d_j \approx 2$ in the low J cases. Jet flapping, which is ultimately caused by u'_j as well, contributes to the fluctuating streamwise velocity because the high momentum jet fluid periodically flaps into regions of the flow with lower velocity, i.e., the crossflow on the windward side and the wake of the jet on the leeward side.

The strongly asymmetric response of $u'_{\hat{s}}/u'_j$ between the windward and leeward sides of the low J jets is also a consequence of the jet flapping dynamics. On the windward side, the the crossflow velocity is larger than it is on the leeward side and is traveling in a direction roughly parallel with the jet after the initial deflection. On the other hand, the leeward side of the jet is characterized by much lower velocities and a complex, three-dimensional wake flow that does not closely follow the jet trajectory. Thus, larger values for $u'_{\hat{s}}/u'_j$ are found on the leeward side of the jet because the variation in streamwise velocity is larger in that region. This line of reasoning also explains why the peak values for $u'_{\hat{s}}/u'_j$ on the leeward side of low J jets vary for cases with different S and for non-reacting versus reacting jets. It is important to remember that heat release was shown in Section 3.1 to delay velocity recovery in the wake region of reacting jets relative to non-reacting jets with the same J and S. Thus, a larger fluctuating streamwise velocity results when the jet core flaps into the lower velocity reacting wake compared to that of a non-reacting jet. Similarly, the location of peak $u'_{\hat{s}}/u'_j$ at downstream locations is shifted towards the leeward side in reacting jets, whereas the distribution of $u'_{\hat{s}}/u'_j$ has become symmetric again in the non-reacting jet by $s/d_j = 12$.

The spatial distribution of $u'_{\hat{s}}/u'_j$ is quite different in the high J cases shown in Figure 4.25. As mentioned previously, the streamwise velocity fluctuations remain roughly symmetric about the jet centerline until larger values of s/d_j in the high J cases. This observation is a direct consequence of the delayed deflection of high J jets relative to their lower J counterparts. Interestingly, the magnitude of these nominally symmetric streamwise velocity fluctuations grows with increasing s/d_j until $s/d_j \approx 5$. Beyond that point of initial jet deflection, $u'_{\hat{s}}/u'_j$ increases sharply on the leeward side of the jet as the jet flapping mechanism discussed in the low J cases becomes increasingly important. However, the decay of $u'_{\hat{s}}/u'_j$ on the windward side of the jet is much less dramatic than was seen in

the low J cases because the velocity difference between the jet and the crossflow remains large in high J jets until further downstream. Furthermore, velocity recovery occurs much more quickly in the wake of the high J jets since, unlike low J jets, they fully separate from the lower wall. This difference explains why the spatial distribution of $u'_{\hat{s}}/u'_{j}$ is much more symmetric in high J jets at larger values of s/d_j. Similarly, the low $u'_{\hat{s}}/u'_{j}$ values found along the jet centerline in the high J cases reflect the fact that the jet never flaps sufficiently to cause a large fluctuation in the streamwise velocity. Thus, the streamwise velocity fluctuations are essentially confined to the shear layers in the high J cases. It is also worth noting that the peak value of $u'_{\hat{s}}/u'_{j}$ is nearly twice as large in the high J cases. While the larger velocity difference between the jet and the crossflow is partially responsible for this behavior, it does not fully account for the more significant growth in $u'_{\hat{s}}/u'_{j}$ in high J jets before any deflection into the crossflow direction has occurred. It is also possible that the spatial growth rate for these long wavelength disturbances is significantly larger in the high J jets, but a more likely explanation is that the earlier deflection and much larger jet flapping amplitude in the low J jets interferes with the spatial amplification of disturbances at the jet exit.

The effect of changing S and the presence/absence of combustion has already been shown to modify the spatial distribution of $u'_{\hat{s}}/u'_{j}$ in low J jets because of associated differences in wake velocity recovery. To better understand the role of mixture composition on the streamwise velocity response, Figure 4.26 presents plots of $u'_{\hat{s}}/u'_{j}$ versus n/d_j for three different jet mixture compositions, including two reacting cases and one inert case, at low and high J. Near the jet injector at $s/d_j = 2$ the jet response is independent of changes in S and the presence/absence of combustion when normalized with respect to u'_{j}. The situation changes significantly further downstream at $s/d_j = 8$. The low J results on the leeward side of the jet for $s/d_j = 8$ support the arguments made previously concerning the relationship between wake velocity recovery and $u'_{\hat{s}}/u'_{j}$. The differences on windward side of the low J jets with different mixture compositions can only be understood by considering both the jet flapping amplitude and the mean velocity difference, $U_j - U_\infty$, between the jet and the crossflow. The reacting, low S jet has the largest response because its flapping

amplitude is comparable to the other reacting case (with unity S) but $U_j - U_\infty$ is almost twice as large in the low S case. Conversely, both the non-reacting and reacting jets with unity S have identical $U_j - U_\infty$ but the reacting jet flaps with larger amplitude, which leads to larger values for $u'_{\hat{s}}/u'_j$.

The influence of mixture composition on $u'_{\hat{s}}/u'_j$ in the high J jets is more complex. In particular, the streamwise velocity response at $s/d_j = 8$ is largest for the reacting, unity S case, which was not the case at low J and can not be explained using the same arguments based on jet flapping amplitude and velocity differences. It is also noteworthy that the shape of the $u'_{\hat{s}}/u'_j$ profile is almost identical for the reacting and non-reacting unity S cases while the magnitude varies by a factor of two. The similarity of the profiles, and especially the fixed locations of the peak $u'_{\hat{s}}/u'_j$ values, suggests that differences in jet flapping cannot be responsible for the large difference in $u'_{\hat{s}}/u'_j$ since the velocity difference does not vary for these unity S cases. One plausible explanation, which will be explored in Chapter 5, is that the shear layers of the non-reacting jets are more effective at dissipating streamwise fluctuations than their reacting counterparts.

In addition to the aforementioned dependence on mixture composition, the variation in streamwise velocity response due to changes in excitation frequency is also of interest. To investigate the frequency dependence, Figure 4.27 plots $u'_{\hat{s}}/u'_j$ versus n/d_j at selected s/d_j values for jets with fixed mixture composition forced at 177Hz, 250Hz, and 340Hz. When normalized by u'_j, the response of the low J jets is nearly independent of frequency, except for slight differences in the 177Hz case. The low J cases forced at 250Hz and 340Hz are indistinguishable, while the response of the 177Hz case is skewed towards the leeward side of the jet. The deviation in the 177Hz case is presumably related to the larger u'_∞/U_∞ for that case compared to the other two forcing frequencies. It is also important to remember that the mean velocities on the leeward side of the jet, particularly near the jet injector, are low and, thus, are more sensitive to crossflow velocity fluctuations that are negligibly small compared to either U_∞ or U_j.

The streamwise velocity response of the high J jets is more sensitive to differences in excitation frequency. As shown in Figure 4.27, there is little effect on $u'_{\hat{s}}/u'_j$ due to excitation

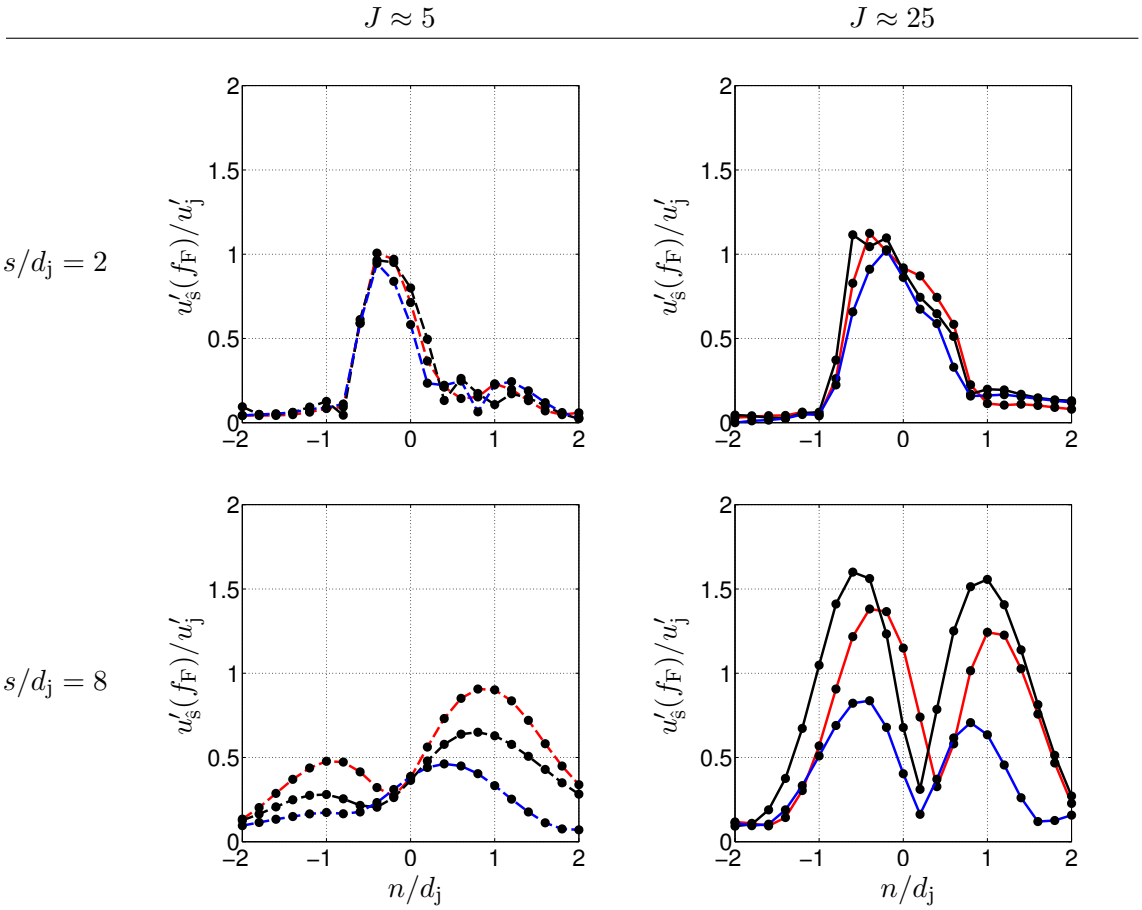

Figure 4.26: Comparison of streamwise velocity fluctuations at the acoustic forcing frequency for jets with different J and S. Forcing frequency, $f_\mathrm{F} = 250$Hz, and forcing amplitude, $A_\mathrm{F} = 1.5$A, held constant in all cases. Results extracted along lines defined normal to the mean jet center streamline trajectory and centered at $s/d_\mathrm{j} = 2$ and $s/d_\mathrm{j} = 8$. (—/---): R, $S = 0.40$, (—/---): R, $S = 1.00$, (—/---): NR, $S = 1.00$.

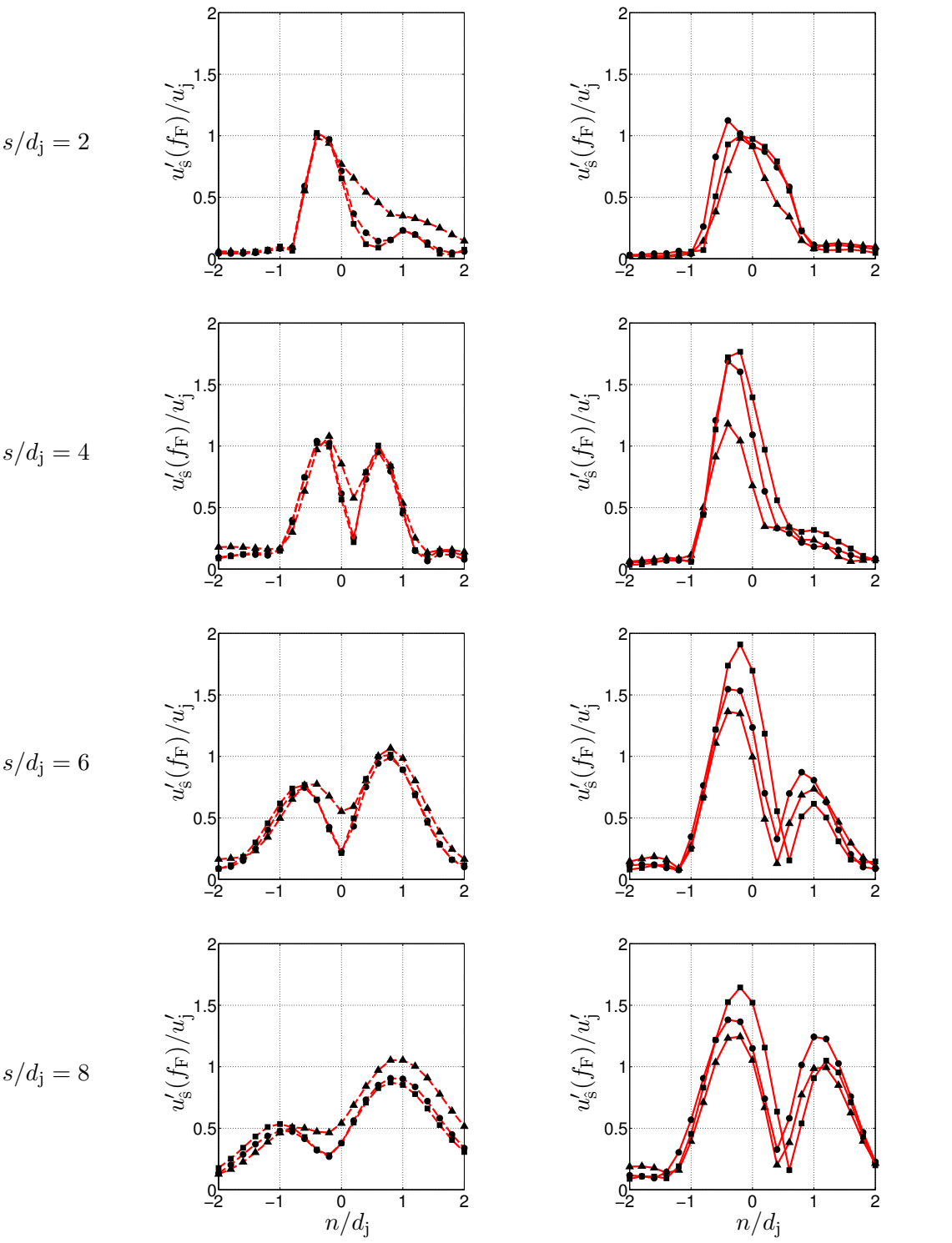

Figure 4.27: Comparison of streamwise velocity fluctuations at different f_F for jets with fixed J and S. Results extracted along lines defined normal to the mean jet center streamline trajectory. Forcing amplitude, $A_F = 1.5$A, held constant for all cases. (▲): $f_F = 177$Hz & $A_F = 1.5$A, (●): $f_F = 250$Hz & $A_F = 1.5$A, and (■): $f_F = 340$Hz & $A_F = 1.5$A.

frequency at $s/d_\mathrm{j} = 2$, but by $s/d_\mathrm{j} = 4$, the streamwise velocity response in the 340Hz case is 50% larger than it is in the 177Hz case. The peak value of $u'_\hat{\mathrm{s}}/u'_\mathrm{j}$ for all three excitation frequencies, however, is located in the windward shear layer near $n/d_\mathrm{j} = -0.5$. The response at 340Hz remains dominant along the windward side of the jet through $s/d_\mathrm{j} = 8$, while the frequency response on the leeward side of the jet does not show the same trend. It is important to note that the streamwise velocity fluctuations have been normalized by u'_j in Figure 4.27, and the flapping amplitude of high J jets excited at different frequencies did not vary below $s/d_\mathrm{j} = 8$. Thus, the frequency dependent response of $u'_\hat{\mathrm{s}}/u'_\mathrm{j}$ in the windward shear layer does not appear to be a consequence of initial excitation amplitude or jet flapping amplitude.

The structural response of jets in acoustically excited crossflow can be further examined by considering the unsteady vorticity field, which is presented in Figure 4.28. It shows waterfall plots of the spatial distribution of the fluctuating z-component of the vorticity at the forcing frequency. The fluctuating vorticity, ω'_z is defined as

$$\omega'_z(s, n, f_\mathrm{F}) = [2S_{\omega_z\omega_z}(s, n, f_\mathrm{F})]^{1/2} \tag{4.6}$$

in a similar manner as was done for $u'_\hat{\mathrm{s}}$ (see Equation (4.5)), where $S_{\omega_z\omega_z}(s, n, f_\mathrm{F})$ is the power spectra of the z-component of the vorticity, $\omega_z(s, n, t)$, evaluated at the forcing frequency. ω'_z is normalized by the forced response timescale $d_\mathrm{j}/u'_\mathrm{j}$ to eliminate the influence of the injector impedance.

After recognizing a few key points that differentiate the unsteady vorticity response from the velocity response, the interpretation of ω'_z follows directly from the arguments previously used to understand $u'_\hat{\mathrm{s}}$. More specifically, the sign of the mean vorticity field is positive in the windward shear layer and negative in the leeward shear layer. Thus, when considering the effect of jet flapping on ω'_z, it is important to remember that a given point on the jet centerline may oscillate between positive and negative values of instantaneous vorticity whereas only the magnitude of the positive streamwise velocity fluctuated in this study. Similarly, a point on the windward side of the jet located sufficiently far from the mean jet centerline will only experience magnitude fluctuations of the positive values of

instantaneous vorticity.

Returning to the waterfall plots shown in Figure 4.28, the preceding discussion on sign changes in the instantaneous vorticity field due to jet flapping explains the tri-peaked response in ω_z'. The largest values are found along the mean jet centerline since the vorticity periodically oscillates between positive and negative values at those locations when the jet flaps. Smaller values of ω_z' are found in the shear layers where the oscillation amplitude is smaller. All three peaks in ω_z' decay with increasing s/d_j because the fluctuating vorticity magnitude due to jet flapping decreases as the velocity difference between the jet and the crossflow decreases. Locations close to the injector in the high J cases are an exception, and ω_z' is double-peaked in those regions since jet flapping is negligibly small. The high J jets maintain larger values of $\omega_z' d_\mathrm{j}/u_\mathrm{j}'$ further downstream because the velocity difference, $U_\mathrm{j} - U_\infty$, is greater than in the low J cases.

Profiles of ω_z' extracted at selected streamwise locations for jets with the same forcing conditions but different mixture compositions are plotted in Figures 4.29 and 4.30, for low and high J jets, respectively. The normalized values of ω_z' in low J jets are insensitive to changes in mixture composition in the near-field, but mixture composition becomes more important further downstream. Similar to the results shown for $u_\hat{\mathrm{s}}'/u_\mathrm{j}'$, the response is strongest in the low S reacting case, which has a larger jet velocity and delayed wake velocity recovery. The vorticity response in the high J jets, shown in Figure 4.30, is sensitive to changes in mixture composition at all s/d_j. Among the high J jets, the response is again strongest in the reacting, unity S case, presumably for the same reasons that $u_\hat{\mathrm{s}}'/u_\mathrm{j}'$ achieved a maximum for those conditions.

The evolution of vortical disturbances along the shear layers can be further investigated by considering the phase of the fluctuating vorticity at the forcing frequency. The phase angles of the z-component vorticity fluctuations in the windward and leeward shear layers, $\theta_{\omega_z,\mathrm{WSL}}$ and $\theta_{\omega_z,\mathrm{LSL}}$, respectively, are defined as

$$\theta_{\omega_z,\mathrm{WSL}}(s_\mathrm{WSL}) = \angle\breve{\omega}_{z,\mathrm{WSL}}(s_\mathrm{WSL}, f_\mathrm{F}) \cdot (180/\pi) \tag{4.7}$$

$$\theta_{\omega_z,\mathrm{LSL}}(s_\mathrm{LSL}) = \angle\breve{\omega}_{z,\mathrm{LSL}}(s_\mathrm{LSL}, f_\mathrm{F}) \cdot (180/\pi) \tag{4.8}$$

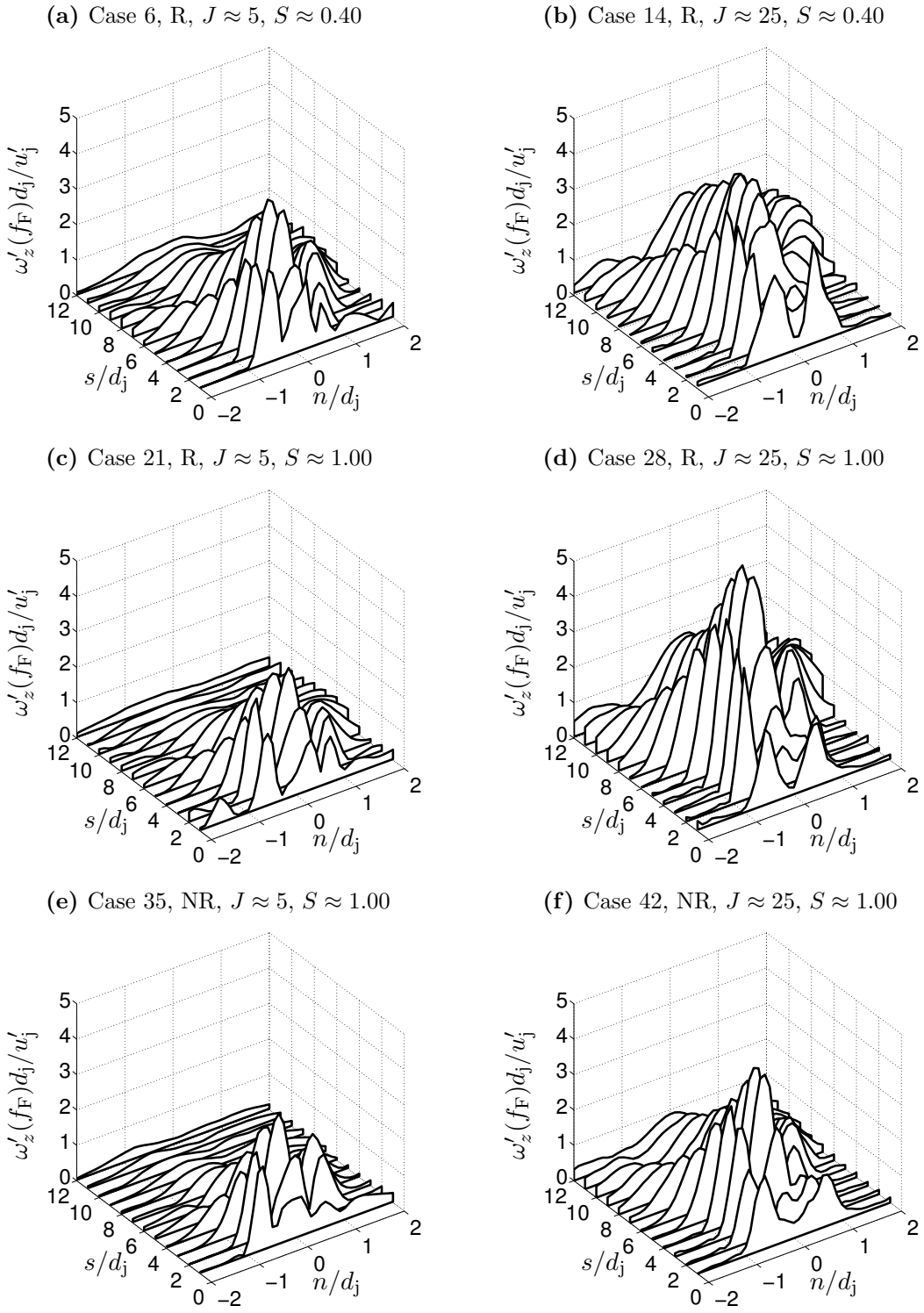

Figure 4.28: Waterfall plots of z-component vorticity fluctuations at the forcing frequency extracted along lines defined normal to the mean jet center streamline trajectory. Forcing frequency and amplitude held constant for all cases ($f_\mathrm{F} = 250\mathrm{Hz}$, $A_\mathrm{F} = 1.5\mathrm{A}$).

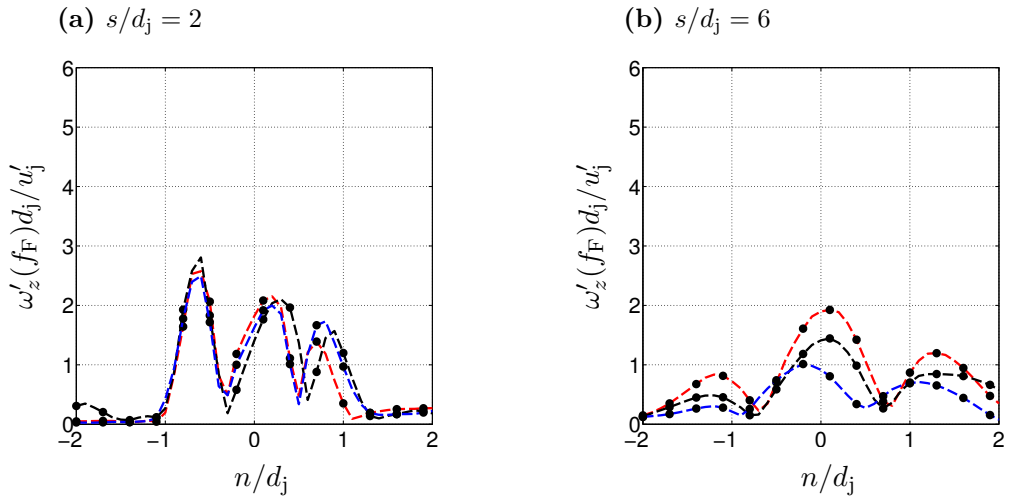

Figure 4.29: z-component vorticity fluctuations at the forcing frequency extracted along lines defined normal to the mean jet center streamline trajectory for inert and reacting low J jets with different S. (---): R, $S = 0.40$, (---): R, $S = 1.00$, (---): NR, $S = 1.00$.

where $\breve{\omega}_{z,\mathrm{WSL}}$ and $\breve{\omega}_{z,\mathrm{LSL}}$ are the components of the discrete Fourier transforms of ω_z at the forcing frequency, f_F, at specified arc length distances, s_WSL and s_LSL, along the mean windward and leeward shear layer trajectories, respectively. The mean windward and leeward shear layer trajectories were defined in Section 3.1.3 as the locus of points of maximum and minimum mean ω_z along lines defined normal to the mean jet trajectory. Phase angle results for low and high J jets forced at three different frequencies are shown in Figures 4.31 and 4.32, respectively. In each subfigure, the phase angles for both the windward and leeward shear layer vorticity are offset by a constant such that $\theta_{\omega_z,\mathrm{WSL}} = 0$ at $s_\mathrm{WSL}/d_\mathrm{j} = 2$. As a result, the phase of the leeward shear layer vorticity at $s_\mathrm{LSL}/d_\mathrm{j} = 2$ is roughly $-180°$ in each case.

The low J results presented in Figure 4.31 show that vortical disturbances in both the windward and leeward shear layers convect at velocities close to the mean streamwise velocity along the jet centerline. The phase angle difference between the windward and leeward shear layers remains constant at approximately 180° until $s_\mathrm{SL}/d_\mathrm{j} = 8$. The phase angle results become noisy and irregular beyond that point, presumably due to the increasingly three-dimensional vorticity field at downstream locations. The phase angle results for high J jets shown in Figure 4.32 are much noisier even in the near-field but are generally consistent with the low J results. Vortical disturbances in the windward shear layer propagate at

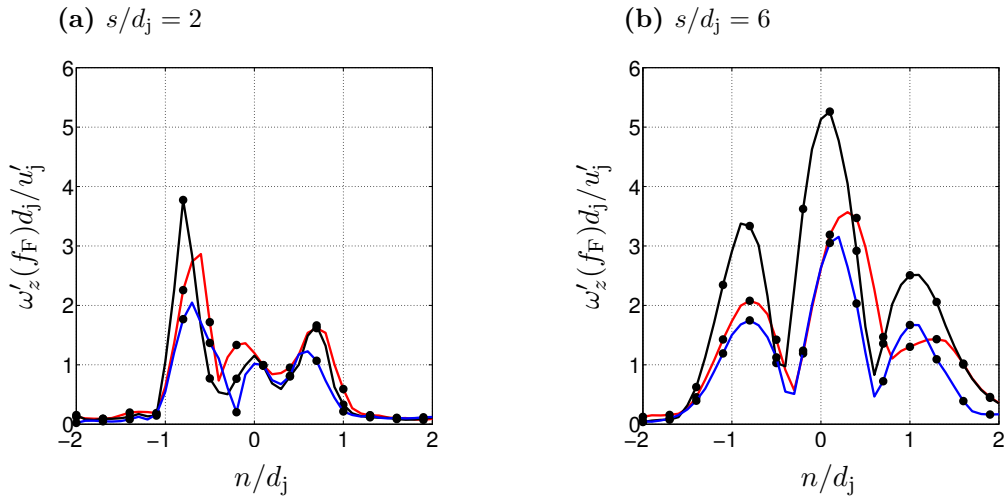

Figure 4.30: z-component vorticity fluctuations at the forcing frequency extracted along lines defined normal to the mean jet center streamline trajectory for inert and reacting high J jets with different S. (—): R, $S = 0.40$, (—): R, $S = 1.00$, (—): NR, $S = 1.00$.

a velocity close to the mean streamwise velocity along the jet centerline and the fluctuating vorticity in the leeward shear layer is 180° out-of-phase with the windward shear layer.

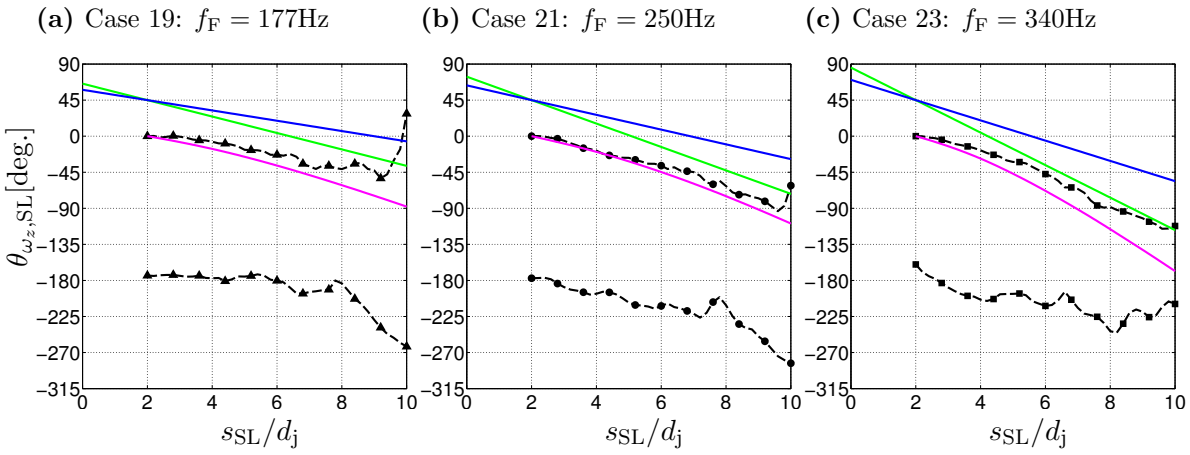

Figure 4.31: Phase roll-off of fluctuating vorticity in the windward and leeward shear layers at the forcing frequency (---) as a function of arc length distance for reacting jets with $J = 5$, $S = 1.00$, and $A_F = 1.5$A. (—): Phase roll-off for a convective disturbance moving with the streamwise velocity, $U_{conv} = U_{\hat{s}}(s, n)$. (—): Phase roll-off for a convective disturbance moving at the average of the jet and the crossflow velocity, $U_{conv} = (U_j + U_\infty)/2$. (—): Phase roll-off for a convective disturbance moving at the crossflow velocity, $U_{conv} = U_\infty$.

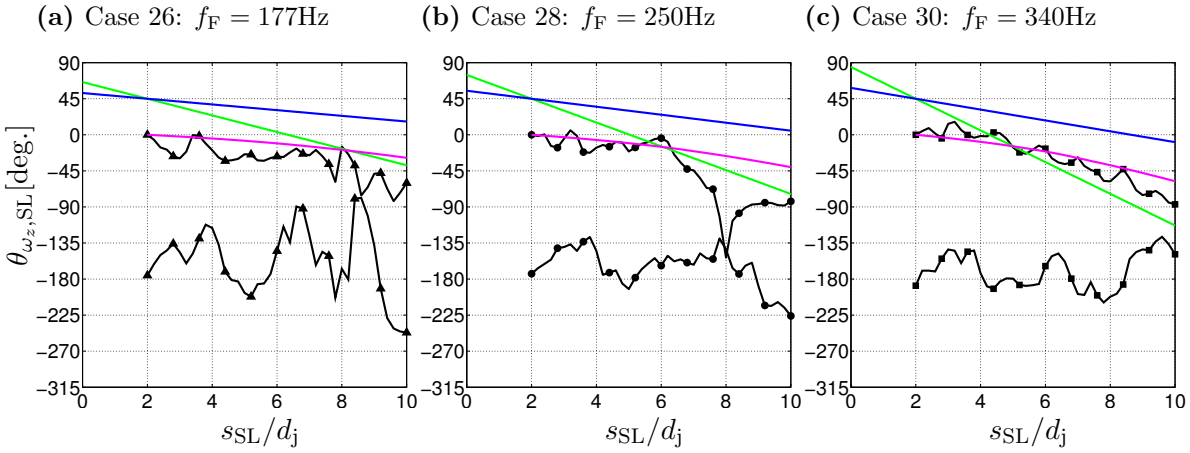

Figure 4.32: Phase roll-off of fluctuating vorticity in the windward and leeward shear layers at the forcing frequency (---) as a function of arc length distance for reacting jets with $J = 25$, $S = 1.00$, and $A_F = 1.5$A. (—): Phase roll-off for a convective disturbance moving with the streamwise velocity, $U_{conv} = U_{\hat{s}}(x, y)$. (—): Phase roll-off for a convective disturbance moving at the average of the jet and the crossflow velocity, $U_{conv} = (U_j + U_\infty)/2$. (—): Phase roll-off for a convective disturbance moving at the crossflow velocity, $U_{conv} = U_\infty$.

4.5 Reaction Zone Dynamics and Flame Stabilization Effects

Staged fuel combustion systems, which often utilize JICF-type fuel injectors, are a key motivation for this work. As discussed in the introduction, the crossflow is inherently unsteady in these systems due to the presence of coherent acoustic oscillations. Results presented earlier in this chapter showed that low frequency, low amplitude crossflow acoustics can significantly alter the behavior of JICF. In particular, low frequency crossflow forcing induces periodic jet flapping, whose magnitude strongly depends on such JICF parameters as J and S. This section investigates the flame response to crossflow acoustic forcing and explores the similarities and differences between the flame response and the flow response.

Instantaneous OH PLIF images extracted at different phase values of the acoustic pressure cycle in the jet plenum, θ_{P_j}, are shown in Figure 4.33. Lines of constant n/d_j spanning the range $-3 \leq n/d_j \leq 3$ in $1d_j$ intervals are superimposed to provide a spatial frame of reference. The results indicate that the instantaneous location of the windward and leeward reaction zones depends on the phase of the pressure oscillation. The thin, windward flame front flaps away from the jet centerline (shown by white line with red dots) towards negative values of n/d_j for $\theta_{P_j} = 0$. Conversely, for $\theta_{P_j} = \pi$, the windward flame flaps towards positive n/d_j. This behavior is consistent with the response of a non-premixed flame exposed to an oscillatory flow in the fast chemistry limit. In other words, the windward flame front follows the time-varying stoichiometric mixture fraction contour, which is controlled by the jet flapping. The leeward reaction zone is broader and more diffuse than the windward flame front, and its dynamics are more difficult to characterize, particularly for high J test conditions. In general, the location of the leeward reaction zone is less sensitive to changes in θ_{P_j} compared to the windward flame front. As discussed in Chapter 3, the leeward reaction zone is heavily diluted with combustion products and is characterized by lower scalar dissipation rates. Based on this observation, it is hypothesized that the mixture fraction field on the leeward side of the jet is less sensitive to changes in the instantaneous jet trajectory and thus the location of the leeward reaction zone does not move as much as the windward flame front.

Spectral analysis of the time-resolved OH PLIF fields is used to further explore the

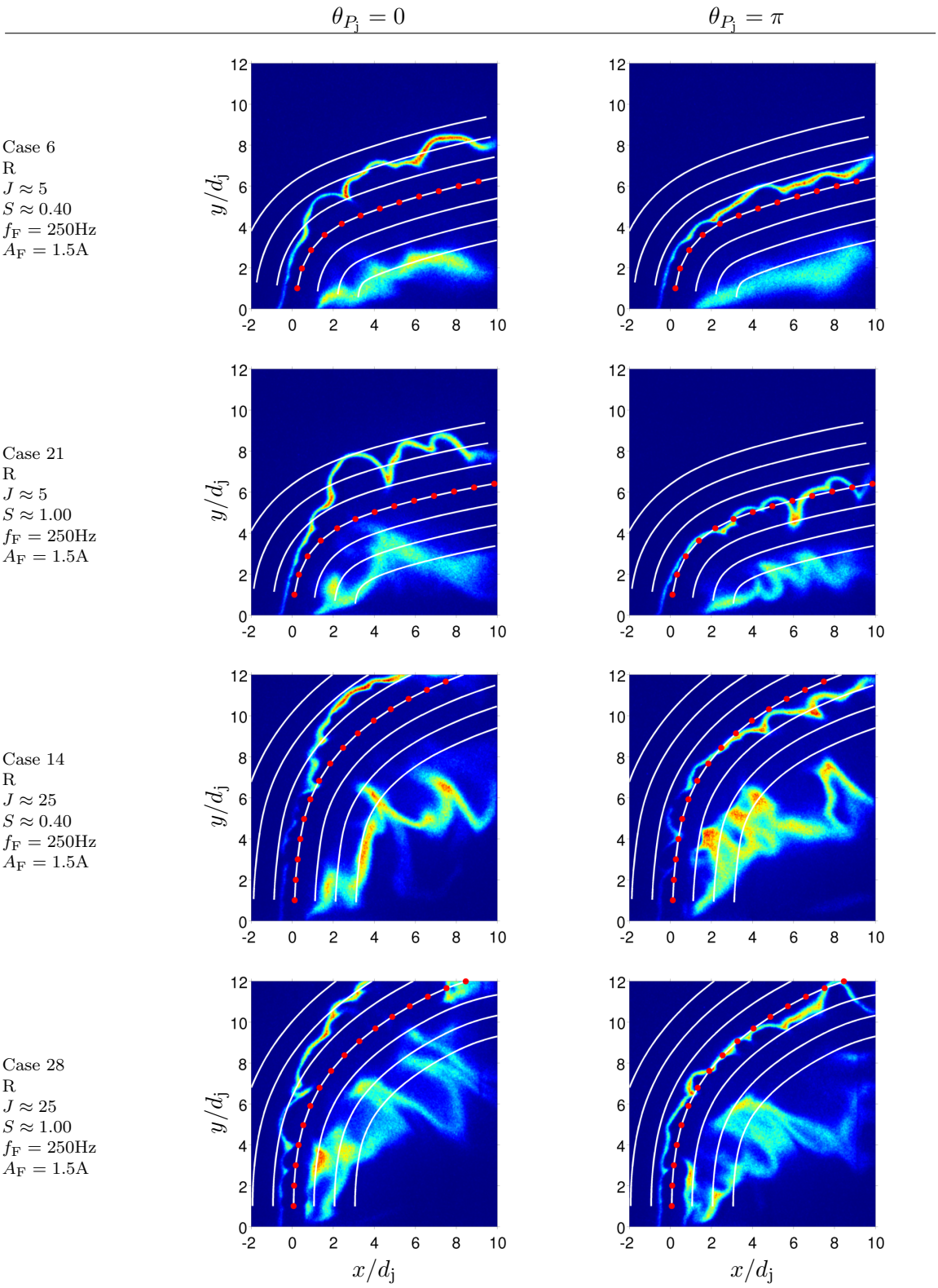

Figure 4.33: Instantaneous OH PLIF images at different phases of the acoustic pressure cycle inside the jet plenum for jets with different J and S. (▬): Lines of constant n/d_j. Mean jet center streamline indicated by red dots.

reaction zone response at the forcing frequency. Waterfall plots of the spatial distribution of OH PLIF power at the forcing frequency are presented in Figure 4.34. The power is near zero along the jet centerline since the predominately non-premixed reaction zones are confined to the edges of the jet. The windward side of the jet is generally characterized by a double-peaked response, while the leeward side contains a single, broad response peak. The double-peaked response on the windward side of the jet is consistent with a thin flamelet periodically flapping back and forth about a mean flame location at the forcing frequency. The broad, single-peaked response on the leeward side of the jet is a result of the very different reaction zone structure in that region.

The leeward side response at the forcing frequency in the low S, low J case (see Figure 4.34a) is particularly surprising. In this case, the magnitude of the leeward side response is almost double that of the windward side response despite the fact that the instantaneous OH PLIF signal is stronger on windward side of the low J jets (see Figure 4.33). Furthermore, the location of the windward flame front is more sensitive to the periodic jet flapping compared to the leeward reaction zone. These observations lead one to expect large OH PLIF fluctuations at the forcing frequency on the windward side of the jet rather than on the leeward side. This discrepancy can be explained by reconsidering the instantaneous OH PLIF images for the low S, low J cases shown in Figure 4.33. Note that the windward flame front is wrinkled and distorted by smaller scale structures, while the leeward reaction zone is not. These small scale structures are caused by the shear layer vortices, whose passage frequency is much higher than f_{F}. Thus, the superposition of random displacements due to the SLV reduces the periodicity associated with jet flapping on the windward side of the jet.

Flame edge tracking is used to analyze the spatiotemporal dynamics of the windward flame front. The mean flame edge location in the forced response cases is determined using the same procedure discussed previously for the unforced cases in Section 3.2.2. More specifically, an edge finding algorithm is used to identify the instantaneous location of the windward flame front at each instant in time. The complete set of instantaneous flame edges are then superimposed to create a flame brush image. The mean flame edge location

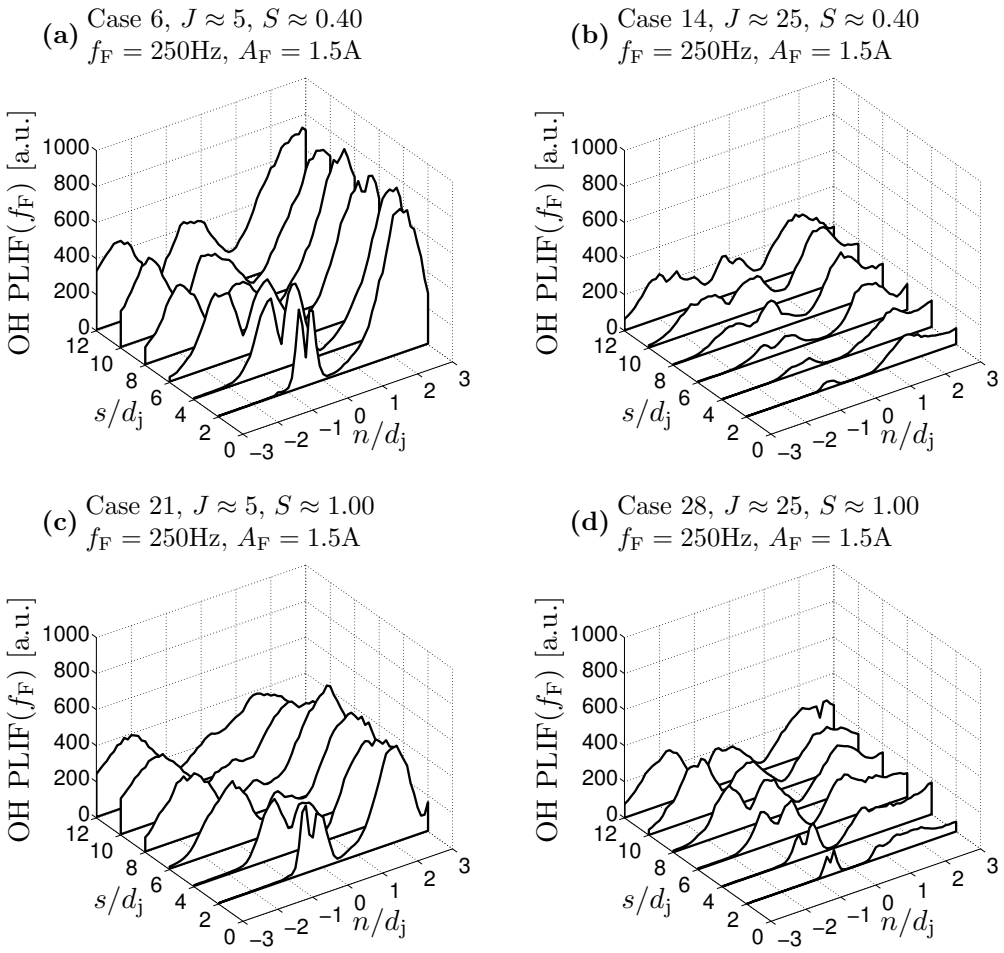

Figure 4.34: Spatial distribution of the fluctuating power of the OH PLIF signal at the forcing frequency extracted along trajectory normal lines for jets with different J and S. Forcing frequency and amplitude held constant for all cases.

is defined as the locus of points of maximum flame brush density along a set of evenly spaced lines defined normal to the time-averaged jet center streamline trajectory. Finally, the instantaneous flame edge perturbation, $\zeta_f(s,t)$, is defined as the normal distance between the mean flame edge and an instantaneous flame edge at a specified arc length, s, and time, t. A schematic illustrating the definition of the flame edge perturbation is shown in Figure 4.35.

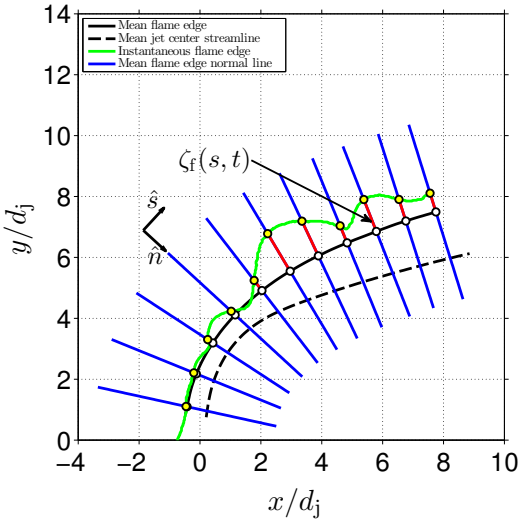

Figure 4.35: Illustration of instantaneous flame edge perturbation tracking.

Spectral analysis of the flame edge perturbations provides additional insight into the response of the windward flame front at the forcing frequency. Figure 4.36 shows waterfall plots of the power spectral density of ζ_f at different streamwise positions for unforced (left-hand side) and forced (right-hand side) cases. The results are very similar to the power spectral density estimates given previously in Figure 4.18 for the jet center streamline perturbations, ζ_c. The spectra is dominated by the component at the forcing frequency in forced, low J case, and the power at f_F increases sharply with increasing s in the low J case. The power is much less concentrated at the forcing frequency in the high J cases, and, similar to the jet center streamline perturbation spectra for high J cases, the low frequency background noise is again strong. The similarity between the jet center streamline perturbation spectra and the flame edge perturbation spectra suggests that the same mechanism is responsible; namely, jet flapping due to injector-coupled velocity response.

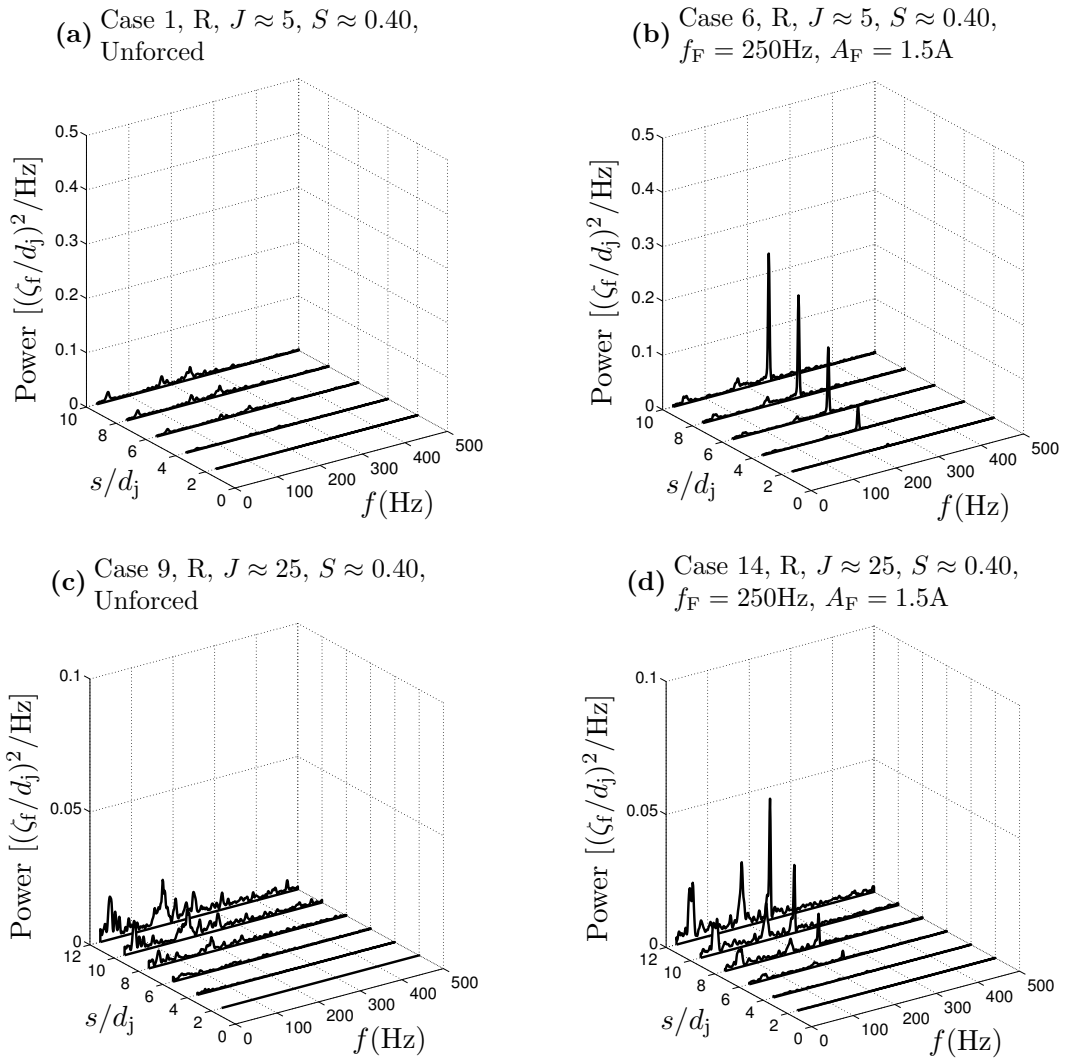

Figure 4.36: Power spectra of windward flame edge perturbations for (a,c) unforced and (b,d) forced jets.

The sensitivity of the flame edge flapping to changes in J and S is evaluated by extracting the amplitude of the flame edge perturbations at the forcing frequency, $\zeta'_{\mathrm{f}}(s, f_{\mathrm{F}})$, which is defined as

$$\zeta'_{\mathrm{f}}(s, f_{\mathrm{F}}) = [2S_{\zeta_{\mathrm{f}}\zeta_{\mathrm{f}}}(s, f_{\mathrm{F}})]^{1/2} \tag{4.9}$$

where $S_{\zeta_{\mathrm{f}}\zeta_{\mathrm{f}}}(s, f_{\mathrm{F}})$ is the component of the power spectra of $\zeta_{\mathrm{f}}(s,t)$ evaluated at the forcing frequency. Figure 4.37 plots $\zeta'_{\mathrm{f}}(s, f_{\mathrm{F}})$ for jets with four different combinations of J and S. Three different forcing frequencies are considered for each combination of J and S. Similar to the previously discussed ζ'_{c} results, ζ'_{f} increases with increasing arc length distance and the sensitivity of ζ'_{f} to changes in J and S is well-predicted by the relative magnitude of the fluctuating jet exit velocity, $u'_{\mathrm{j}}/U_{\mathrm{j}}$ (see Table B.1). Thus, ζ'_{f} is larger in low J cases and in iso-density cases because the injector-coupled response is strongest for those conditions. Interestingly, the amplitude of ζ'_{f} is consistently about 25% larger than ζ'_{c} at the same arc length distance, s/d_{j}. The most noticeable difference between ζ'_{f} and ζ'_{c} is, however, that ζ'_{f} does not saturate in the higher frequency cases. These differences indicate that the mixture fraction field, and in particular the location of the stoichiometric mixture fraction contour, does not exactly follow the instantaneous (flapping) jet trajectory. Rather, ζ'_{f} depends on both the jet flapping and the mixing between the jet and the crossflow. It is hypothesized that while the jet/crossflow mixing, and by extension ζ'_{f}, is increasingly dominated by the crossflow rather than the jet at downstream locations, ζ'_{c} is always controlled by the contiguity of the jet column. This would explain why ζ'_{c} saturates once the jet contiguity is broken in the high frequency cases while ζ'_{f} does not.

Scatter plots of $\zeta_{\mathrm{f}}(s,t)$ versus $\zeta_{\mathrm{c}}(s,t)$ are shown in Figure 4.38 for two different forced test conditions to further explore the connection between center streamline perturbations and flame edge perturbations. The correlation between ζ_{f} and ζ_{c} depends on both streamwise position and J. The flame perturbations and centerline perturbations are highly correlated in low J jets at streamwise locations near the jet injector. Conversely, ζ_{f} and ζ_{c} are much less correlated at downstream locations and in higher J jets. In other words, flame perturbations and centerline perturbations are well-correlated where the flow field is dominated by jet

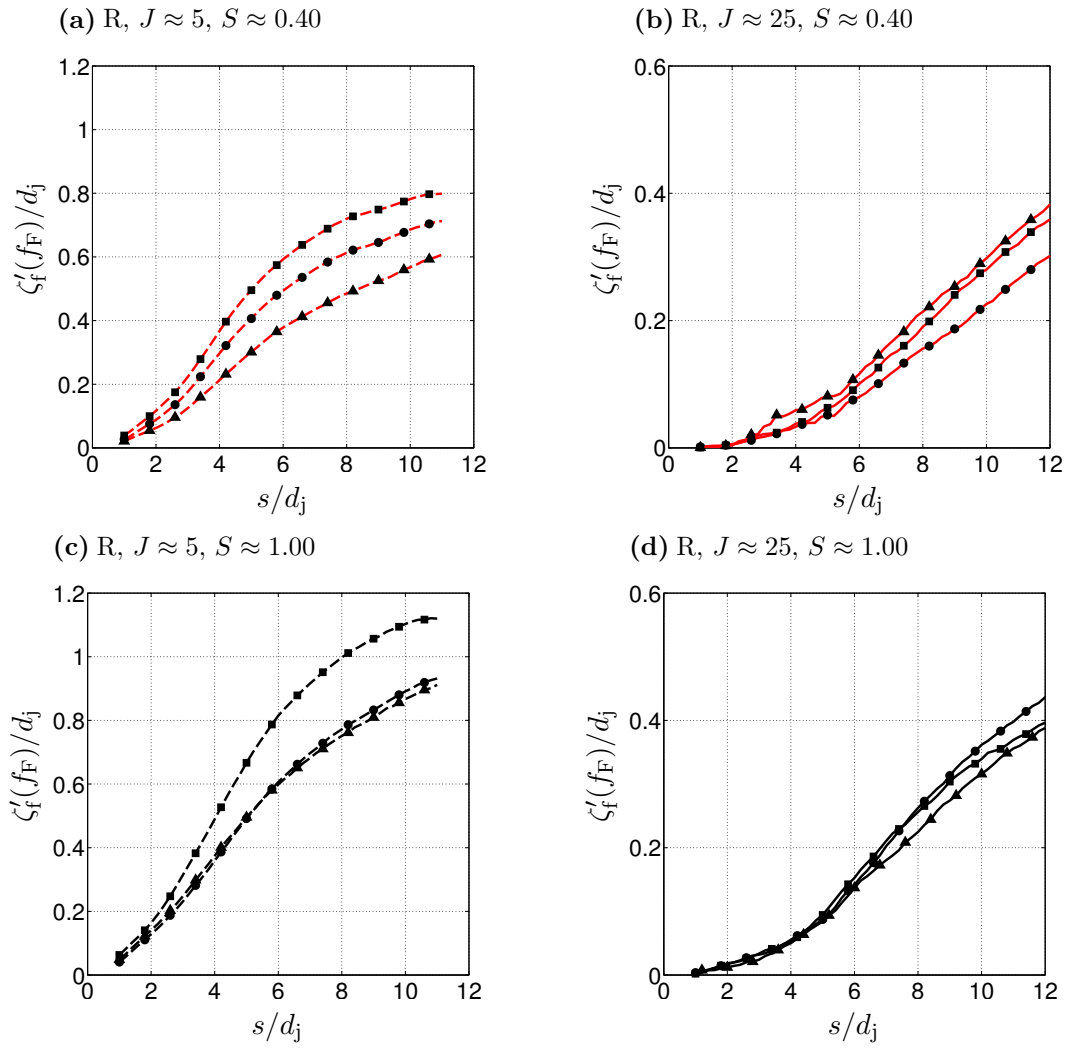

Figure 4.37: Comparison of windward flame edge perturbation amplitudes as a function of arc length for different forcing frequencies and test conditions. Forcing amplitude, $A_{\mathrm{F}} = 1.5\mathrm{A}$, held constant in all cases shown. (▲): $f_{\mathrm{F}} = 177\mathrm{Hz}$ & $A_{\mathrm{F}} = 1.5\mathrm{A}$, (●): $f_{\mathrm{F}} = 250\mathrm{Hz}$ & $A_{\mathrm{F}} = 1.5\mathrm{A}$, and (■): $f_{\mathrm{F}} = 340\mathrm{Hz}$ & $A_{\mathrm{F}} = 1.5\mathrm{A}$.

flapping. The correlation decays at downstream locations in the low J cases because the flow field is increasingly controlled by the crossflow rather than the jet injector dynamics. The high-frequency shear layer vortices tend to reduce the correlation between ζ_f and ζ_c in all cases because only ζ_f responds at the SLV passage frequencies. The impact of the shear layer vortices on the correlation between ζ_f and ζ_c is, however, much larger in the high J cases because the jet flapping amplitude is lower.

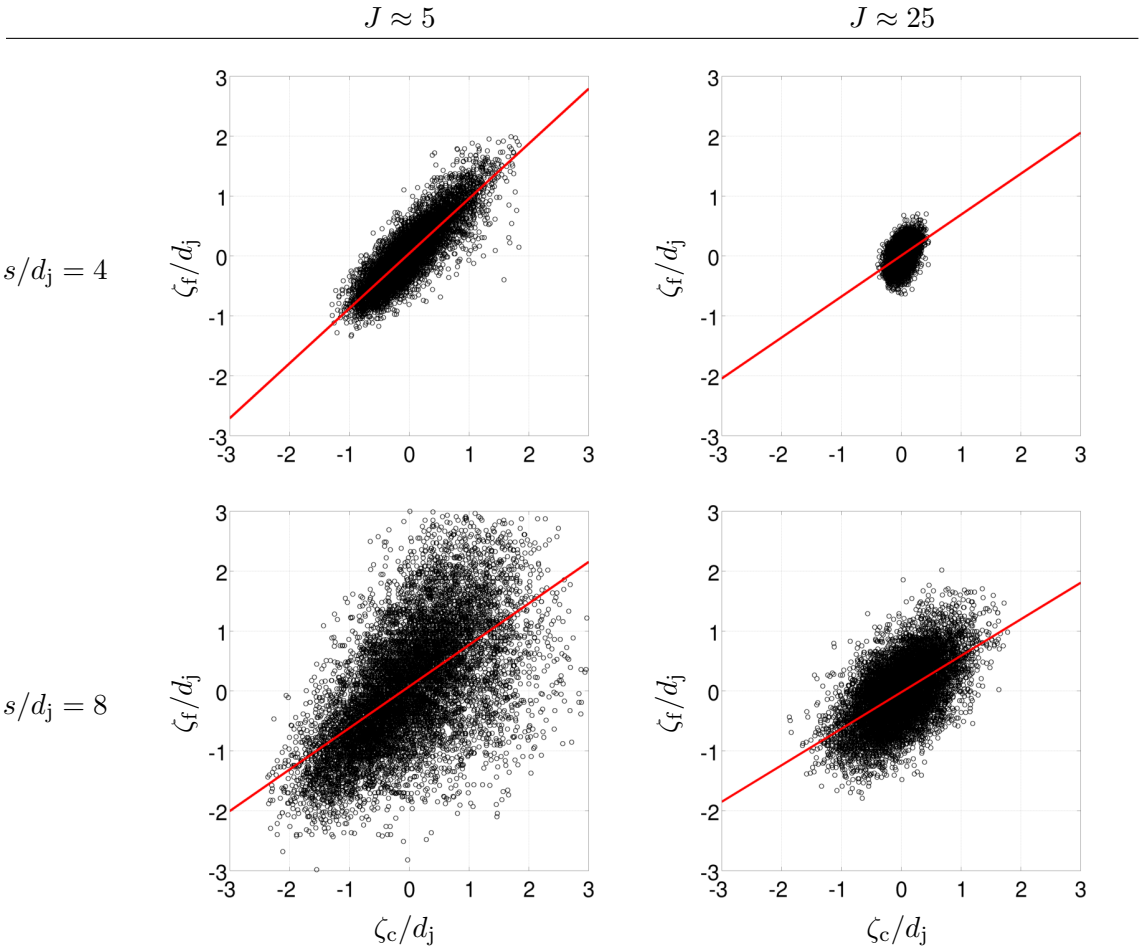

Figure 4.38: Scatter plots of instantaneous windward flame edge perturbations and center streamline perturbations for iso-density reacting jets with two different J values. Forcing frequency and amplitude fixed at $f_F = 250$Hz and $A_F = 1.5$A in both cases. (—): Linear fit to the data.

Differences between the flow response and the flame response to crossflow forcing are further investigated by considering the phase velocity for flame perturbations fluctuating at the forcing frequency. The phase of the flame edge perturbations at the forcing frequency,

$\theta_{\zeta_f}(s)$, is defined as

$$\theta_{\zeta_f}(s) = \angle\check{\zeta}_f(s, f_F) \cdot (180/\pi) \tag{4.10}$$

where $\check{\zeta}_f(s, f_F)$ is the component of the discrete Fourier transform of $\zeta_f(s,t)$ at f_F. Figure 4.39 plots θ_{ζ_f} for three low J cases with different forcing frequencies. In each case, lines representing the phase roll-off for disturbances fluctuating at the forcing frequency but convecting with different reference velocities are superimposed, as was done previously in the plots of θ_{ζ_c}. The results indicate that flame edge perturbations in low J jets convect at the mean crossflow velocity, U_∞, independent of the forcing frequency and independent of arc length distance. This is contrary to the results for θ_{ζ_c}, which showed that the convection velocity of center streamline perturbations varied both with f_F and with s/d_j. Recall that the behavior of the center streamline perturbations was explained in terms of the loss of jet contiguity at higher forcing frequencies. The results for θ_{ζ_f}, on the other hand, support the earlier hypothesis that flame edge perturbations are controlled by the crossflow dynamics rather than the jet dynamics. This finding is in good agreement with the recent work by Micka & Driscoll [61] on unforced reacting JICF, which showed that flame length in reacting JICF scales with the crossflow velocity rather than the jet velocity. The crossflow velocity scaling indicates "wake-like" mixing phenomena between the jet and the crossflow.

Figure 4.40 shows corresponding results for the phase of flame edge perturbations at the forcing frequency in high J jets. As anticipated, the behavior of θ_{ζ_f} is quite different in the high J cases. In particular, θ_{ζ_f} depends on f_F and s/d_j, which is similar to the trends observed for center streamline perturbations but contrary to the low J flame edge perturbation results discussed above. As shown in Figure 4.40, flame edge perturbations convect at the mean jet center streamwise velocity in the $f_F = 177$Hz case. At higher frequencies, the convection velocity gradually approaches U_∞ with increasing arc length distance. This behavior is identical to that observed previously for the jet center streamline perturbations and was explained in terms of the jet flapping dynamics, which suggests that the flame edge perturbations are controlled by the jet rather the crossflow in high J cases. This follows intuitively from the fact that high J jets remain "jet-like" for a larger range of

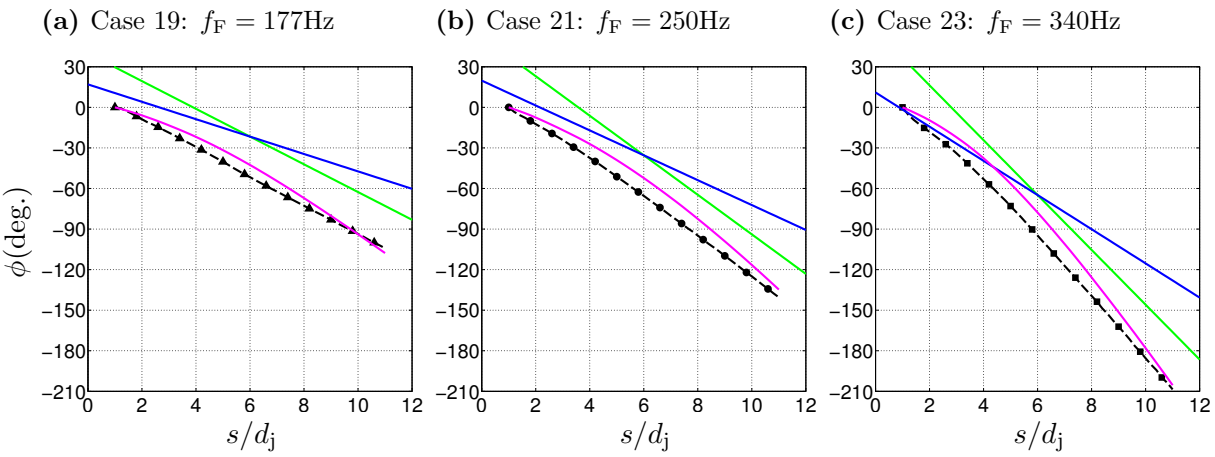

Figure 4.39: Phase roll-off of windward flame edge perturbations (---) at the forcing frequency as a function of arc length distance for reacting jets with $J = 5$, $S = 1.00$, and $A_F = 1.5$A. (—): Phase roll-off for a convective disturbance moving with the streamwise velocity, $U_{conv} = U_{\hat{s}}(x, y)$. (—): Phase roll-off for a convective disturbance moving at the average of the jet and the crossflow velocity, $U_{conv} = (U_j + U_\infty)/2$. (—): Phase roll-off for a convective disturbance moving at the crossflow velocity, $U_{conv} = U_\infty$

s/d_j values.

The discussion of flame front dynamics up to this point has focused on the flame edge perturbations, $\zeta_f(s,t)$, which are defined normal to the mean flame edge in the $\hat{n}$-direction. An underlying assumption in that analysis is that a flame is present at all arc length distances. This assumption is uniformly valid for low J jets because the flame is always attached to the injector lip. In high J jets, however, the flame can be either attached to the burner or lifted, as discussed for unforced jets in Section 3.2.2. This raises an interesting question: is the flame stabilization affected by crossflow forcing in high J jets?

To investigate the effect of crossflow forcing on flame stabilization, the number of extinction events as a function of s/d_j is quantified by processing $\zeta_f(s,t)$ to determine the fraction of time during which a flame is present. Figure 4.41 presents the fraction of time a flame is present versus s/d_j for low S and unity S jets forced at different frequencies. The unforced result discussed previously is superimposed for comparison purposes. Crossflow forcing significantly increases the fraction of time a flame is present at lower s/d_j values. In other words, crossflow forcing reduces the liftoff height in forced JICF relative to unforced JICF and promotes flame stabilization near the jet injector. Furthermore, the results show that

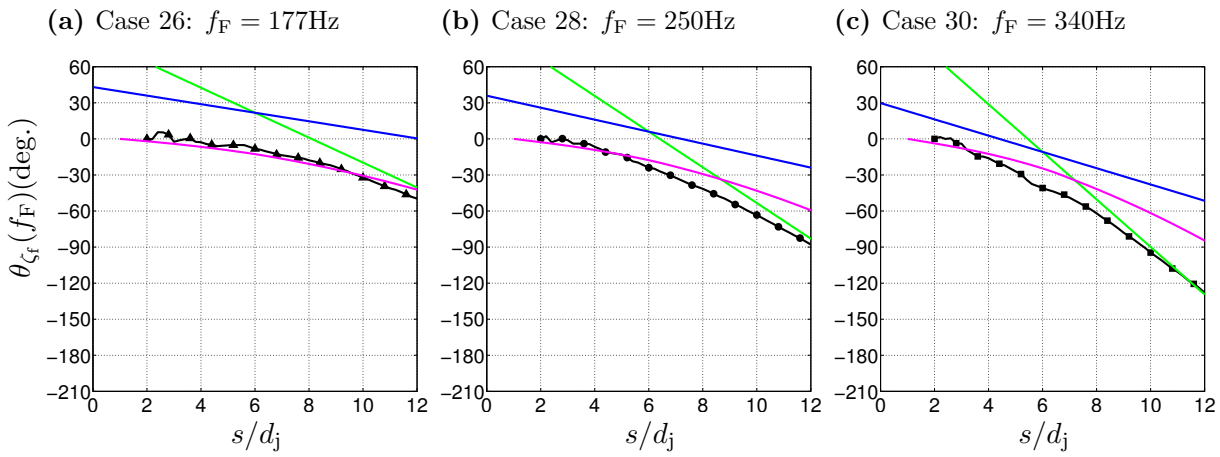

Figure 4.40: Phase roll-off of windward flame edge perturbations (—) at the forcing frequency as a function of arc length distance for reacting jets with $J = 25$, $S = 1.00$, and $A_F = 1.5$A. (—): Phase roll-off for a convective disturbance moving with the streamwise velocity, $U_{conv} = U_{\hat{s}}(x, y)$. (—): Phase roll-off for a convective disturbance moving at the average of the jet and the crossflow velocity, $U_{conv} = (U_j + U_\infty)/2$. (—): Phase roll-off for a convective disturbance moving at the crossflow velocity, $U_{conv} = U_\infty$

higher frequency forcing is more effective for promoting flame stabilization. The fraction of time a flame is present can vary by almost 40% between unforced and forced cases.

The mechanism by which crossflow forcing promotes flame stabilization is also of interest. The crossflow forcing induces a fluctuating jet exit velocity, u'_j, which leads to a harmonically varying strain rate field in the jet shear layers. It is plausible that flame stabilization occurs during the portion of the acoustic pressure cycle associated with low strain rate in the jet shear layer. The flame would persist until the strain rate increased sufficiently to cause local extinction. In this situation, flame stabilization would be directly related to the phase of the acoustic pressure cycle, and hysteresis would be anticipated based on the harmonically oscillating strain rate field. To investigate this possibility, the fraction of time during which a flame is present is re-computed conditional on the phase of the acoustic pressure cycle inside the jet plenum, θ_{P_j}. Results for low S and unity S cases are presented in Figure 4.42 for two different s/d_j values. These results illustrate that the fraction of time a flame is present in the forced cases does not depend on the phase of the acoustic pressure cycle. Thus the time-varying jet exit velocity is not directly responsible for the improved flame stabilization in the forced jets. Instead, the improved flame stabilization appears to be the

result of enhanced mixing in the near-field due to acoustic excitation of the jet shear layer.

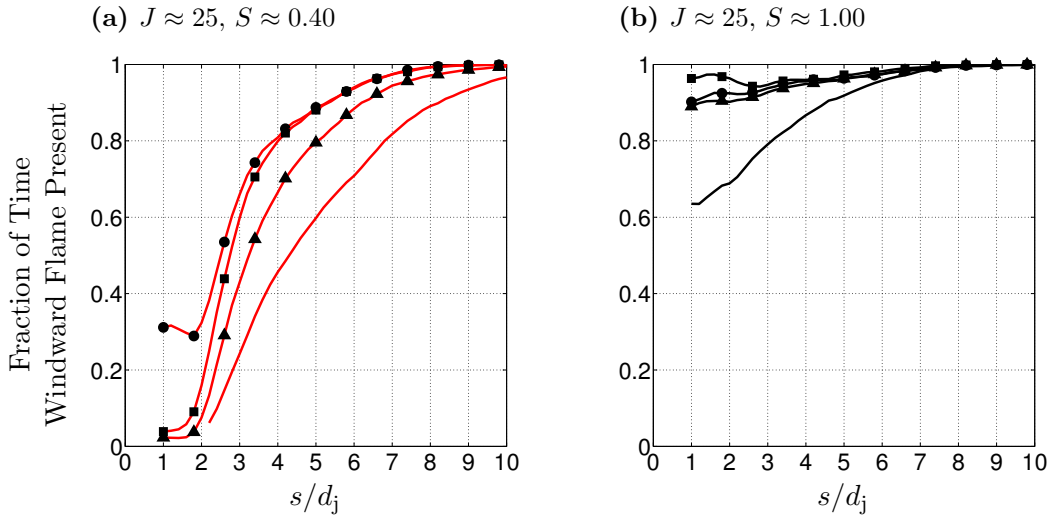

Figure 4.41: Fraction of time a flame is present on the windward edge of the jet as a function of arc length for unforced and forced high J jets with different S. Forcing amplitude, $A_F = 1.5$A, held constant in all the forced cases.

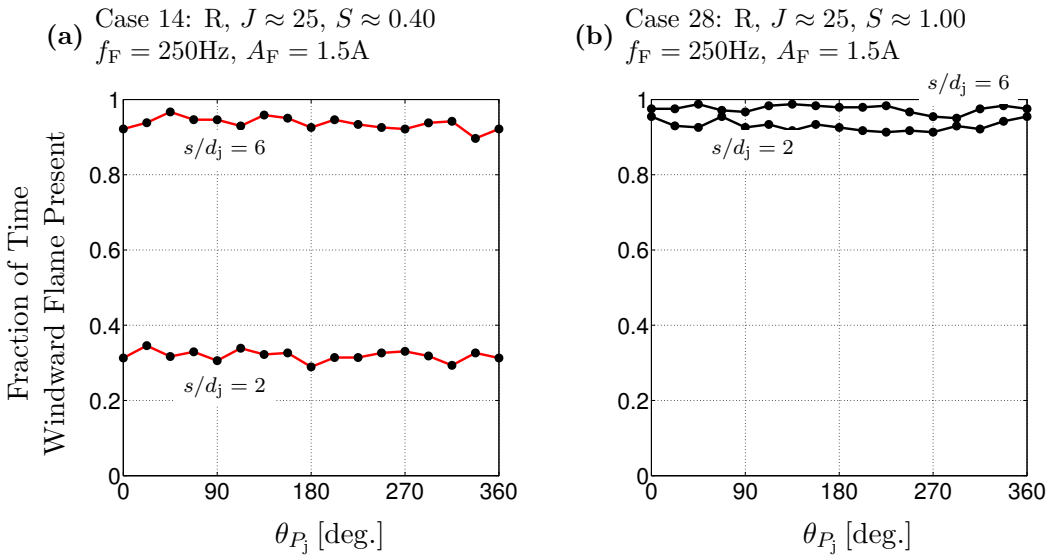

Figure 4.42: Fraction of time a flame is present on the windward side of the jet at different phase values of the acoustic pressure cycle measured in the jet supply plenum.

4.6 Injector-Coupled Response Model

The SPIV, OH PLIF, and dynamic pressure measurements reported earlier in this chapter indicate that the primary response mechanism in a JICF exposed to crossflow forcing is jet flapping. Jet flapping occurs because the instantaneous momentum balance between the jet

and the crossflow is altered when an oscillatory pressure field in the test section induces a fluctuating jet exit velocity, u'_j. The magnitude of u'_j/U_j, which is a strong function of J and S (see Section 4.1), largely controls the jet flapping amplitude. Recall, for example, that the flapping amplitude of low J jets far exceeds that of high J jets because u'_j/U_j is much larger for low J jets. In addition to predicting flapping amplitude, u'_j is also the appropriate normalization factor for comparing the forced response of jets with different J and S.

Thus, knowledge of u'_j is critical to understanding the response of jets injected into acoustically excited crossflows. In the present work, u'_j was extracted from time-resolved SPIV measurements, as discussed in Section 4.1. This approach is straightforward and accurate but might not be convenient or even be possible in other situations, such as industrial test facilities and high pressure experiments. An alternative, analytical approach to determining u'_j is presented here. The analytical method avoids the difficulties associated with SPIV measurements and, more importantly, makes it easy to perform parametric studies for jets with different injector geometry, different crossflow pressures, and different J and S.

The goal of the analytical model is to predict the dependence of u'_j/U_j upon the fluctuating pressure at the jet injector, p'_∞. In other words, the goal is to model the acoustic impedance of the jet supply system, Z_j. A diagram illustrating the geometry of the jet supply system is provided in Figure 4.43. The model extends from the jet exit back to the choked orifice at the entrance to the small jet plenum, which is the closest location to the jet exit with a well-defined acoustic boundary condition.

Linear, one-dimensional acoustic wave propagation is assumed because all the frequencies of interest are well below the cutoff frequency and $p'_\infty/p_\infty \ll 1$. The influence of the jet supply system on the crossflow acoustic field is neglected because the area of the jet, A_j, is much smaller than the area of the test section duct, A_{TS}. In other words, the fluctuating crossflow pressure at the jet injector, p'_∞, is imposed on the jet supply system by the crossflow. The impedance of the jet supply system determines the value of u'_j but does not substantially modify the acoustic pressure field in the test section. This assumption is very good in the present case but could be relaxed for other situations (e.g., cases with larger A_j or multiple jets) by incorporating an acoustic model for the crossflow region. Mean flow

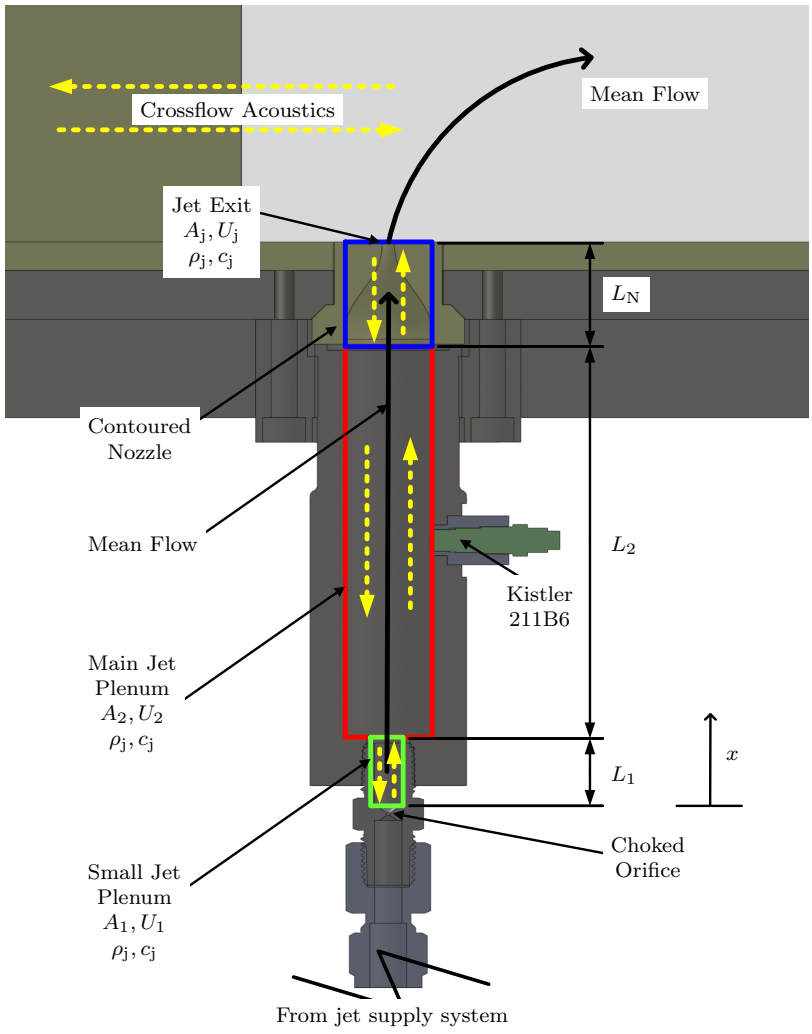

Figure 4.43: A schematic of the geometry and variables used in the injector-coupled response model.

effects are included in the model because they provide an important source of damping, particularly for high J jets. The gas density and the speed of sound in the jet supply system are ρ_j and c_j, respectively.

For modeling purposes, the jet supply system is divided into three different sections, which, as shown in Figure 4.43, include the small jet plenum (green), the main jet plenum (red), and the contoured nozzle (blue). The model development begins in the small jet plenum, which is treated using standard one-dimensional, linear acoustics with mean flow effects. Therefore, the acoustic pressure in the small jet plenum, $p_1'(x,t)$, can be written as the superposition of a left and a right traveling wave,

$$p_1'(x,t) = a_1 \exp(ik_1^+ x - i\omega t) + b_1 \exp(-ik_1^- x - i\omega t) \tag{4.11}$$

where $\omega = 2\pi f$ is the radial frequency, k_1^+ is the wavenumber in the positive x-direction, k_1^- is the wavenumber in the negative x-direction, and a_1 and b_1 are complex-valued constant coefficents. k_1^+ and k_1^- are defined in terms of the mean velocity in the small plenum, U_1, as

$$k_1^+ = \frac{\omega}{c_\mathrm{j} + U_1} \qquad k_1^- = \frac{\omega}{c_\mathrm{j} - U_1} \tag{4.12}$$

Switching to the frequency domain by taking the Fourier transform of Equation (4.11) gives

$$\breve{p}_1'(x) = a_1 \exp(ik_1^+ x) + b_1 \exp(-ik_1^- x) \tag{4.13}$$

The acoustic velocity in the small plenum is written as

$$\breve{u}_1'(x) = \frac{1}{\rho_\mathrm{j} c_\mathrm{j}} \left(a_1 \exp(ik_1^+ x) - b_1 \exp(-ik_1^- x) \right) \tag{4.14}$$

and the acoustic impedance at $x = L_1$ is

$$Z_1(L_1) = \left(\frac{-\rho_\mathrm{j} c_\mathrm{j}}{A_1} \right) \frac{a_1 \exp(ik_1^+ L_1) + b_1 \exp(-ik_1^- L_1)}{a_1 \exp(ik_1^+ L_1) - b_1 \exp(-ik_1^- L_1)} \tag{4.15}$$

where L_1 is the length of the small jet plenum. Applying the choked boundary condition at $x = 0$, i.e., $\breve{u}_1'(0) = 0$, immediately shows that the reflection coefficient is $R_1(0) = a_1/b_1 = 1$ at the sonic orifice. Substituting this result into Equation (4.15) cancels out the unknown

a_1 and b_1 coefficients and leads to the simplified impedance expression at $x = L_1$

$$Z_1(L_1) = \left(\frac{-\rho_j c_j}{A_1}\right) \frac{\exp(ik_1^+ L_1) + \exp(-ik_1^- L_1)}{\exp(ik_1^+ L_1) - \exp(-ik_1^- L_1)} \tag{4.16}$$

The acoustic field in the main jet plenum (denoted by subscript 2) can be treated in a similar manner as was done for the small jet plenum. The acoustic pressure, $\breve{p}_2'(x)$, and acoustic velocity, $\breve{u}_2'(x)$, in the main plenum are written as

$$\begin{aligned} \breve{p}_2'(x) &= a_2 \exp(ik_2^+(x - L_1)) + b_2 \exp(-ik_2^-(x - L_1)) \\ \breve{u}_2'(x) &= \frac{1}{\rho_j c_j} \left(a_2 \exp(ik_2^+(x - L_1)) - b_2 \exp(-ik_2^-(x - L_1))\right) \end{aligned} \tag{4.17}$$

where k_2^+ and k_2^- are analogous to the expressions given in Equation (4.12), except that U_1 is replaced by the mean velocity in the main plenum, U_2. a_2 and b_2 are complex-valued, constant coefficients. Using Equation (4.17), the acoustic impedance at $x = L_1$ is formulated in terms of main plenum variables as

$$Z_2(L_1) = \left(\frac{\rho_j c_j}{A_2}\right) \frac{a_2/b_2 + 1}{a_2/b_2 - 1} \tag{4.18}$$

Enforcing the continuity of pressure and volume velocity at $x = L_1$ then gives

$$Z_1(L_1) = \left(\frac{-\rho_j c_j}{A_2}\right) \frac{a_2/b_2 + 1}{a_2/b_2 - 1} \tag{4.19}$$

which can be rearranged to obtain an expression for a_2/b_2 in terms of $Z_1(L_1)$

$$\frac{a_2}{b_2} = \frac{Z_1(L_1) - \frac{\rho_j c_j}{A_2}}{Z_1(L_1) + \frac{\rho_j c_j}{A_2}} \tag{4.20}$$

The acoustic impedance in the main plenum at $x = L_1 + L_2$ can then be given in terms of the coefficient ratio a_2/b_2, which is known from Equation (4.20), as

$$Z_2(L1 + L_2) = \frac{-\breve{p}_2'(L_1 + L_2)}{A_2 \breve{u}_2'(L_1 + L_2)} = \left(-\frac{\rho_j c_j}{A_2}\right) \frac{(a_2/b_2)\exp(ik_2^+ L_2) + \exp(-ik_2^- L_2)}{(a_2/b_2)\exp(ik_2^+ L_2) - \exp(-ik_2^- L_2)} \tag{4.21}$$

Since the objective of the injector-coupled response model is to find an expression for u_j' in terms of p_∞', a model for the acoustic impedance of the contoured nozzle is required to relate $\breve{p}_2'(L_1 + L_2)$ to p_∞'. To first order, the contoured nozzle acts as a sudden area contraction with mean flow. Acoustic energy is dissipated by the separating shear layer at the jet exit. The relevant physics are well-accounted for by the model developed by

Cummings & Eversman [89] for acoustically compact subsonic nozzles. Their model treats the nozzle flow as irrotational and incompressible, which are good assumptions for low Mach number flows in acoustically compact regions. In the present experiments, the mean flow Mach number is $Ma_{\mathrm{j}} < 0.15$ and the acoustic wavelength in the jet plenum is $\lambda_{\mathrm{j,F}} >> L_{\mathrm{N}}$. It is important to note that, although the jet shear layer is certainly not irrotational, the boundary layer is not actually responsible for most of the acoustic energy losses at the jet exit. Rather, the acoustic loss results when the pressure drop required to accelerate the flow through the nozzle is not recovered by the separating flow. Thus, neglecting the boundary layer, Cummings & Eversman [89] used the unsteady Bernoulli equation to treat the acoustic loss in the inviscid region, which resulted in the following expression for the nozzle impedance:

$$Z_{\mathrm{N}} = \frac{\check{p}'_2(L_1+L_2) - p'_\infty}{A_2\check{u}'_2(L_1+L_2)} = \left(\frac{\rho_{\mathrm{j}}c_{\mathrm{j}}}{A_{\mathrm{j}}}\right)\left[\frac{i2\pi f\delta_{\mathrm{N}}}{c_{\mathrm{j}}} + Ma_{\mathrm{j}}\left(1-\left(\frac{A_{\mathrm{j}}}{A_2}\right)^2\right)\right] \tag{4.22}$$

where δ_{N} is the "mass end correction" of the nozzle and $Ma_{\mathrm{j}} = U_{\mathrm{j}}/c_{\mathrm{j}}$ is the mean flow Mach number at the jet exit. Ingard [90] measured δ_{N} for sudden area contractions and provided the empirical model

$$\delta_{\mathrm{N}} = 0.48A_{\mathrm{j}}^{1/2}\left(1-1.25\frac{d_{\mathrm{j}}}{d_2}\right) \tag{4.23}$$

where d_2 is the diameter of the main jet plenum. The radiation impedance at the nozzle exit is neglected since the jet exits into a confined test section. An expression for the fluctuating velocity at the inlet to the contoured nozzle, $\check{u}'_2(L1+L2)$, is then obtained by solving Equation (4.21) for $\check{p}'_2(L_1+L_2)$ and substituting into Equation (4.22),

$$\check{u}'_2(L_1+L_2) = \left(\frac{1}{A_2}\right)\left(\frac{-p'_\infty}{Z_2(L_1+L_2)+Z_{\mathrm{N}}}\right) \tag{4.24}$$

Applying the incompressible continuity equation at inlet and exit of the contoured nozzle shows that

$$A_{\mathrm{j}}U_{\mathrm{j}} = A_2U_2 \tag{4.25}$$

$$A_{\mathrm{j}}u'_{\mathrm{j}} = A_2\check{u}'_2(L_1+L_2) \tag{4.26}$$

Substituting into Equation (4.24) yields an expression for u'_{j} where the only remaining unknown quantity is p'_{∞},

$$u'_{\mathrm{j}} = \left(\frac{1}{A_{\mathrm{j}}}\right)\left(\frac{-p'_{\infty}}{Z_2(L_1+L_2)+Z_{\mathrm{N}}}\right) \tag{4.27}$$

which is the desired result and will be referred to as the injector-coupled response model from this point onwards.

The model shows that the fluctuating jet exit velocity, u'_{j}, is directly proportional to the magnitude of the fluctuating crossflow pressure, p'_{∞}, and is inversely proportional to the acoustic impedance of the jet supply system. The total acoustic impedance of the jet supply system, $Z_{\mathrm{j}} = Z_2(L_1+L_2)+Z_{\mathrm{N}}$, appears in the denominator of Equation (4.27) and contains both reactive and resistive elements. Both Z_2 and Z_{N} contribute to the system reactance, but for the injector geometry of interest here, the fluid volume in the main jet plenum is the dominant reactive element. Similar to a Helmholtz resonator, the stiffness of the system is also a strong function of c_{j}, which is an important consideration for jets with very different S and will be addressed below in more detail. The system resistance, on the other hand, comes almost entirely from the mean flow acceleration through the nozzle, which leads to a loss of acoustic energy since the pressure drop through the nozzle is not recovered after the jet separates. This effect is captured in the second term of Equation (4.22), which shows that the acoustic resistance scales with Ma_{j}. Physically, the acoustic resistance is larger in high Ma_{j} jets, or equivalently higher J jets, because more acoustic energy is lost when the flow separates at the jet injector. Intuitively, one expects that a given p'_{∞} should induce a smaller u'_{j} when p'_{∞} is small compared to the pressure drop across the nozzle. Furthermore, the steady Bernoulli equation shows that the pressure drop across the nozzle scales with U_{j}^2. Thus, high J jets have a larger pressure drop and a lower u'_{j} than a corresponding low J jet exposed to the same p'_{∞}.

It is important to note, however, that non-linear effects can introduce an additional, amplitude-dependent resistive component in Z_{N} whose magnitude scales with u'_{j}. This non-linear effect is accounted for in the model recently developed by Scarborough [91], which could be substituted for Equation (4.22). However, non-linear effects only become significant

when flow reversal occurs at the nozzle [91]. Since the present work concerns only jets with positive outflow, i.e., $U_\mathrm{j} + u'_\mathrm{j} > 0$, the non-linear effects can be safely neglected.

The performance of the injector-coupled response model is evaluated by comparing the values predicted by Equation (4.27) with the values of u'_j measured using SPIV, which were discussed in Section 4.1. The values for p'_∞, which are required to evaluate the injector response model, are determined using the two-microphone measurements described previously (see Table B.1). Figure 4.44 shows a scatter plot comparing the model predictions of $u'_\mathrm{j}/U_\mathrm{j}$ with the measured values. All the forced response cases considered in the present work are plotted. As outlined in the legend at the beginning of this chapter (see Figure 4.1), the shape and color of the symbols denotes the frequency and amplitude of excitation, respectively. The agreement between the model and the measurements is quite good considering the simplicity of the model. In agreement with the measured data, the predicted values for $u'_\mathrm{j}/U_\mathrm{j}$ can vary by up to an order of magnitude for jets with different J and S exposed to the same crossflow forcing.

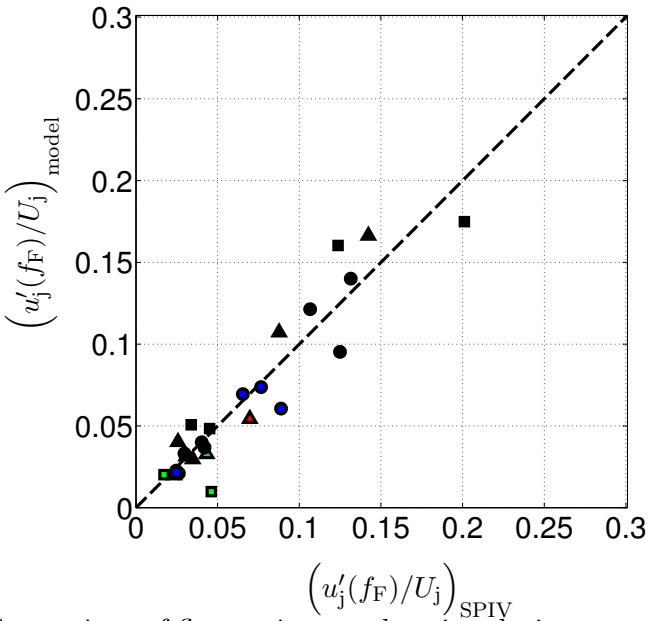

Figure 4.44: Comparison of fluctuating nozzle exit velocity measured using SPIV versus values predicted based on the injector-coupled response model given in Equation (4.27).

The good agreement between the injector coupled response model and the experiments suggests that the model can be utilized to study the jet response to crossflow forcing in

situations for which experimental results are not available. For example, Figure 4.45 shows the predicted dependence of u'_j/U_j upon the forcing frequency in the $0 \leq f_F \leq 1000$Hz range in low and high J jets. Three different mixture compositions are considered, each of which corresponding to a subset of the experimental data. The physio-chemical properties of interest for each mixture are given in Table 4.1.

The low J results presented in Figure 4.45a indicate that u'_j/U_j can vary by up to 25% for jets with different mixture composition. In particular, u'_j/U_j is noticeably lower for low S jets. As alluded to earlier, this effect is primarily related to the 50% increase in c_j for $S = 0.40$ jets relative to $S = 1.00$ jets. Equation (4.21) shows that higher values of c_j increase the stiffness of the jet plenum, which, in turn, reduces the magnitude of u'_j/U_j. One might also expect u'_j/U_j to drop in low S jets because low S jets have higher U_j for the same J. This is not, however, the case because the critical parameter for jet resistance is Ma_j, which is essentially unchanged for jets with the same J in the present work. Furthermore, the specific acoustic impedance, $\rho_j c_j$, is actually smaller in the low S cases despite their higher speed of sound.

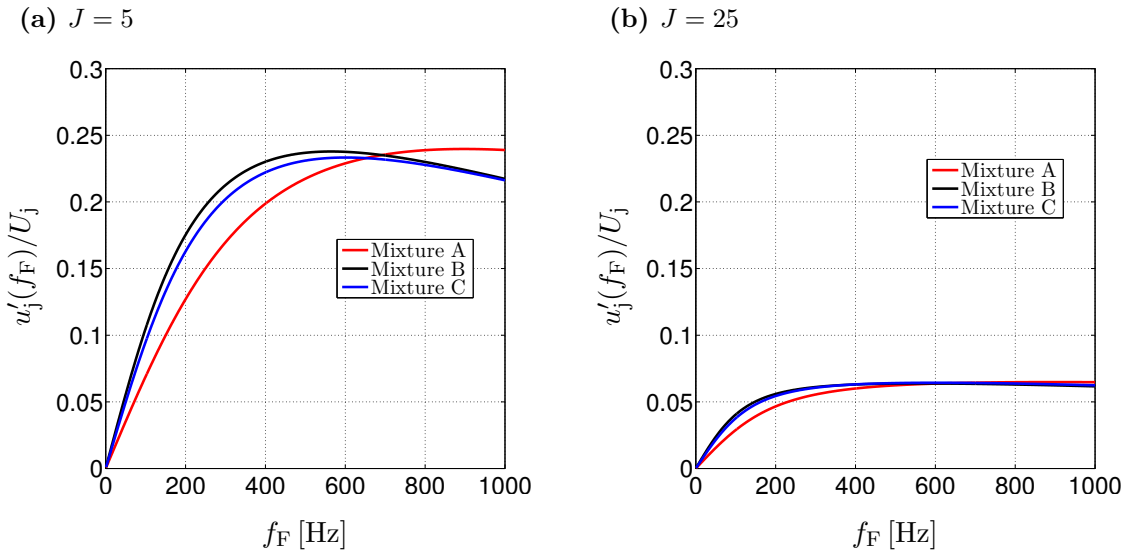

Figure 4.45: Predicted nozzle exit velocity response at the forcing frequency due to an imposed $p'_\infty = 200\,\text{Pa}$ pressure oscillation at the jet injector inlet.

The high J results shown in Figure 4.45b generally show the same trends as the low J results with respect to mixture composition but, as expected, the amplitude of u'_j/U_j is

Table 4.1: Different mixture compositions used to study the sensitivity of the injector-coupled response to changes in the jet gases.

Mixture	Cases	S	NR/R	x_{H_2}	x_{N_2}	x_{He}	ρ_j [kg/m^3]	c_j [m/s]
A	$1 \rightarrow 16$	R	0.40	0.7000	0.0087	0.2913	0.1152	1135
B	$17 \rightarrow 30$	R	1.00	0.7000	0.1849	0.1151	0.2880	714
C	$31 \rightarrow 42$	NR	1.00	0.0000	0.1270	0.8730	0.2880	760

much lower than in the low J cases. The frequency response of both the low and high J results merits, however, some additional consideration. The model predicts a sharp increase in u'_j/U_j at low frequencies. Shortly thereafter the injector-coupled response reaches a peak at an intermediate frequency value and then the response slowly declines as frequency is increased further. The location of the peak response depends on both the mixture composition and J. The nearly linear increase in u'_j/U_j with increasing frequency does not persist as long in the high J cases. The increase in u'_j/U_j with frequency in the low frequency regime is noteworthy in the context of the present experiments because the response at $f_F = 177$Hz and $f_F = 340$Hz, which are the limiting values explored in the experiments, varies by as much as a factor of two in the low J cases.

The frequency response of the jet supply system can be better understood by focusing on the frequency-dependent terms in Z_j; namely, the predominately reactive impedance of the main plenum (see Equation (4.21)) and the "mass end correction" in Z_N. u'_j/U_j increases with frequency initially because the reactive part of Z_2 increases sharply with frequency and has the opposite sign of the reactive part of Z_N. The peak response occurs when the reactive part of the Z_j reaches a minimum although the non-negligible resistance associated with the mean flow negates the possibility of sharp resonance peak. Increasing f_F beyond the frequency for maximum u'_j/U_j diminishes the response because the reactive part of Z_N continues to increase. From a physical perspective, u'_j/U_j increases initially because higher frequencies lead to a greater phase offset between the pressure inside the jet supply plenum and p'_∞. Larger instantaneous pressure differences lead to larger u'_j/U_j. The increased response is eventually offset, however, because the impedance of the nozzle steadily increases with frequency due to increased mass entrainment. Lastly, it is important to note that the present model is only valid for acoustically compact nozzles where the flow

can be considered incompressible. Thus, the model cannot be used at very high frequencies where the acoustic variables may significantly change over short distances; e.g., inside the nozzle. Fortunately, c_j is quite high for the conditions of interest in this study and L_N is very small.

The discussion of injector-coupled response up to this point focused exclusively on the jet injector geometry used in the experiments. The need to carefully consider the injector-coupled response in jets injected into oscillatory crossflows is not, however, unique to the work presented here. Furthermore, the acoustic modeling approach applied here can easily be adapted to other injector geometries used in JICF applications. As an example, Figure 4.46 presents a comparison of the injector-coupled response for three different injector configurations. Figure 4.46a corresponds to the jet supply system used in the experiments, while Figures 4.46b and 4.46c correspond to simple, straight tube injectors of different lengths. The inlet to each of the straight tube injectors is choked, as was the jet supply system used in the current experiments. The frequency dependence of $u'_\mathrm{j}/U_\mathrm{j}$ is very different for each of the injectors. It is important to note, however, that the y-axis scaling is different in Figure 4.46b. $u'_\mathrm{j}/U_\mathrm{j}$ is actually much lower in the short, straight tube injector compared to the jet supply system used in the present work, presumably because the much smaller volume results in a much "stiffer" injector. Increasing the length of the straight tube injector by a factor of two can lead, however, to a resonance condition with very large $u'_\mathrm{j}/U_\mathrm{j}$ for f_F near resonance, as depicted in Figure 4.46c. It should be noted that switching from the present jet supply system to a short, straight tube injector is not without trade-offs. For instance, JICF using straight tube injectors will have fully-developed jet exit velocity profiles, which have been shown to dramatically alter the shear layer dynamics of JICF [36] as well as the jet trajectory [30].

(a) Jet supply system used in the experimental measurements.

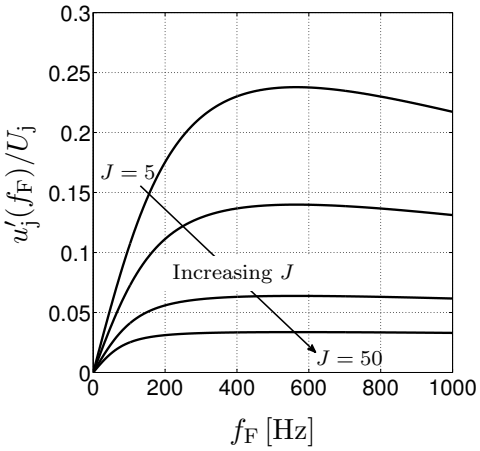

(b) Simple, straight tube injector with $d = d_j$ and $l = 127\,\text{mm}$. Note the y-axis limits.

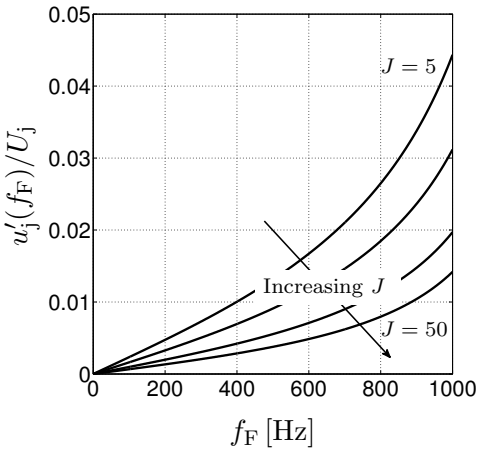

(c) Simple, straight tube injector with $d = d_j$ and $l = 254\,\text{mm}$

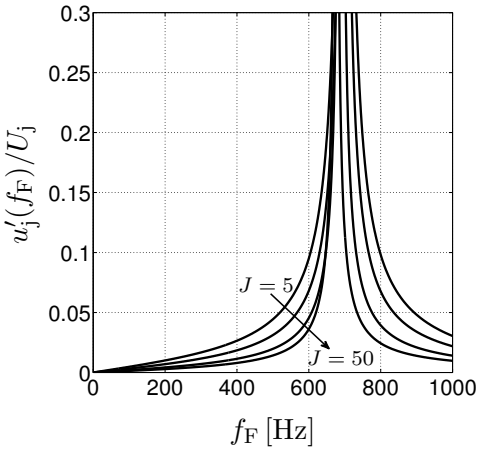

Figure 4.46: Predicted nozzle exit velocity response at the forcing frequency for three different injector configurations when exposed to the same $p'_\infty = 200\,\text{Pa}$ pressure oscillation at the jet injector inlet.

4.7 Summary of Key Findings

This chapter investigated the behavior of jets injected into forced, vitiated crossflows. Low frequency ($f_{\mathrm{F}} < 500$Hz), low amplitude ($p'_\infty/p_\infty < 0.0025$) crossflow forcing significantly alters the time-averaged and instantaneous dynamics of JICF. Crossflow forcing results in both axisymmetric and asymmetric excitation of the jet. Injector-coupling between the fluctuating crossflow pressure, p'_∞, and the jet injector leads to axisymmetric excitation, which manifests itself as a fluctuating jet exit velocity, u'_{j}, while the fluctuating crossflow velocity, u'_∞, is directly responsible for asymmetric excitation of the jet. The relative magnitude of the axisymmetric versus asymmetric excitation depends on the acoustic mode shape as well as key JICF parameters, such as J, S, and Ma_{j}. The injector-coupled response is dominant in low J jets, which have larger u'_{j} and lower U_{j}, leading to values of $u'_{\mathrm{j}}/U_{\mathrm{j}}$ as high as 0.20 in the present work. Higher J jets also experience injector coupling but $u'_{\mathrm{j}}/U_{\mathrm{j}}$ is much lower.

Crossflow forcing reduces the length of the time-averaged jet potential core and increases the RMS velocity near the jet exit. The time-averaged jet trajectory is not affected, even in cases with high $u'_{\mathrm{j}}/U_{\mathrm{j}}$. The instantaneous jet trajectory, on the other hand, varies significantly over the course of each pressure cycle. Jet penetration increases when the phase difference between the pressure in the jet plenum and the crossflow pressure produces a larger pressure drop across the nozzle, and penetration decreases when the pressure drop across the nozzle is small. This phenomena results in periodic jet flapping at the forcing frequency.

The amplitude of the jet flapping scales with $u'_{\mathrm{j}}/U_{\mathrm{j}}$, which explains why iso-density jets and low J jets flap with larger amplitude when compared against low S jets and high J jets exposed to the same crossflow forcing. Non-reacting jets flap with smaller amplitudes than reacting jets with comparable $u'_{\mathrm{j}}/U_{\mathrm{j}}$. In all cases, jet flapping amplitude grows with increasing arc length distance at low s/d_{j} but saturates further downstream at a location that depends on the frequency of excitation. Saturation occurs because of a loss of jet contiguity, which happens at smaller s/d_{j} for higher f_{F}. The fluctuating velocity and vorticity fields at the forcing frequency are dominated by the jet flapping dynamics,

particularly for low J jets. Normalization by u'_{j} collapses the velocity response of jets with different J and S in the near-field but additional structural dependencies of JICF with respect to J and S lead to differences in the response at downstream locations.

Jet flapping causes the location of the windward and leeward reaction zones to periodically oscillate between positions closer to and further from the lower wall. The amplitude of the windward flame displacement at f_{F} increases with increasing arc length distance, but unlike the instantaneous jet trajectory, the flame flapping amplitude shows no signs of saturating at downstream locations. Differences between the phase velocity of the center streamline perturbations and the windward flame edge perturbations indicate that they are controlled by different physical processes. In particular, the flame perturbations propagate at velocities much closer to the crossflow velocity, and since mixing is usually the rate-controlling process for a flame in a vitiated flow, this suggests that wake-like processes control the mixing between the jet and the crossflow. Crossflow forcing also enhances mixing in the jet near-field, leading to earlier flame stabilization and less local extinction events in high J jets.

Lastly, an analytical model is developed that predicts the dependence of the magnitude of $u'_{\mathrm{j}}/U_{\mathrm{j}}$ upon J, S, Ma_{j}, and f_{F}. The model predictions are in good agreement with the values of $u'_{\mathrm{j}}/U_{\mathrm{j}}$ measured by SPIV and, thus, can be used to understand the sensitivity of $u'_{\mathrm{j}}/U_{\mathrm{j}}$ to changes in injector geometry, J, S, Ma_{j}, and f_{F}.

CHAPTER V

DENSITY RATIO EFFECTS ON SHEAR LAYER DYNAMICS

The important influence of density ratio on the dynamics of JICF is a recurring theme of this work. SPIV and OH PLIF results presented in Chapter 3 illustrated the important influence of density ratio, S, on the time-averaged and instantaneous structure of unforced JICF. Chapter 4 showed that the response of JICF to crossflow forcing also depends on S, which was primarily attributed to differences in the injector-coupled response of fixed J jets with different S. This chapter focuses specifically on the effect of S on the shear layer dynamics of JICF. Results from SPIV measurements, Mie scattering flow visualization, and OH PLIF imaging are used to investigate the effect of density ratio on the shear layer vortices, and by extension, the scalar and momentum transport in the near-field.

The remainder of the chapter is organized as follows. Section 5.1 presents centerline velocity measurements in unforced jets with different S that demonstrate the significant and sometimes counter-intuitive effect of density ratio on the near-field momentum transport. Mie scattering images in Section 5.2 highlight the effect of changes in S on the size, structure, and spatial development of the shear layer vortices. Vortex tracking is used to quantify the shear layer growth rate in non-reacting and reacting cases with different S. Concepts from linear stability theory are used in Section 5.3 in conjunction with findings from previous studies on other density-stratified open shear flows to interpret unexpected trends observed in the shear layer growth rates of reacting, density-stratified JICF. Finally, Section 5.4 explores the effect of crossflow forcing on shear layer growth rates in density-stratified JICF.

5.1 Effect on the Mean Flow Field

The discussion in Chapter 3 identified the important influence of density ratio, S, on the time-averaged structure of reacting JICF. Varying S in reacting jets with the same J leads to differences in the aerodynamic blockage experienced by the crossflow due to the presence

of the jet as well as differences in flame stabilization. Furthermore, jets with different S have different wake velocity recovery rates and different shear layer vorticity decay rates. In an effort to understand the S dependence observed in reacting JICF, the combustion-induced dilatation for jets with different S was investigated, but the results showed that the dilatation is largely controlled by the vitiated crossflow and, thus, could not explain the sensitivity to changes in S. This finding led to the hypothesis that changing S alters the near-field mixing rate between the jet and the crossflow, leading to greater near-field heat release that significantly alters the near-field flow structure in certain cases.

In addition to altering the amount of near-field heat release, the jet/crossflow mixing rate also controls the momentum transport between the jet and the crossflow. Unlike scalar transport, however, the momentum transport between the jet and the crossflow can be investigated directly using SPIV results. In fact, for non-reacting jets with the same J, the JICF trajectory, which is defined in terms of the mean jet center streamline and is discussed extensively in Chapter 3, can be considered a first-order measure of the rate of momentum transport between the jet and the crossflow. Jets that lose their wall-normal momentum and acquire streamwise momentum from the crossflow at higher rates will more rapidly deflect into the crossflow direction. The situation is, however, more complex in reacting JICF. Near-field heat release causes dilatation and local flow acceleration, which can act as a local momentum source and alter the exchange of momentum between the jet and the crossflow. In reacting cases with the same J, the jet trajectory reflects both the rate of momentum transport between the jet and the crossflow and the effect of combustion heat release.

Thus, the rate of momentum transport between the jet and the crossflow can not be inferred solely from jet trajectory measurements in reacting JICF. The time-averaged centerline velocity decay is, however, a more useful metric by which to understand the influence of S on momentum transport between the jet and the crossflow. The OH PLIF images shown in Chapter 3 indicate that reactions do not occur along the jet centerline until at least $s/d_{\mathrm{j}} \approx 8$. Therefore, the centerline velocity decay is not directly affected by combustion; it is controlled by the rate at which the jet exchanges momentum with the crossflow. Figure

5.1 shows the centerline velocity decay for low and high J jets with different S. Following the labeling convention defined in Figure 4.1 and used throughout the thesis, the line style and line color denote the value of J and the mixture composition, respectively.

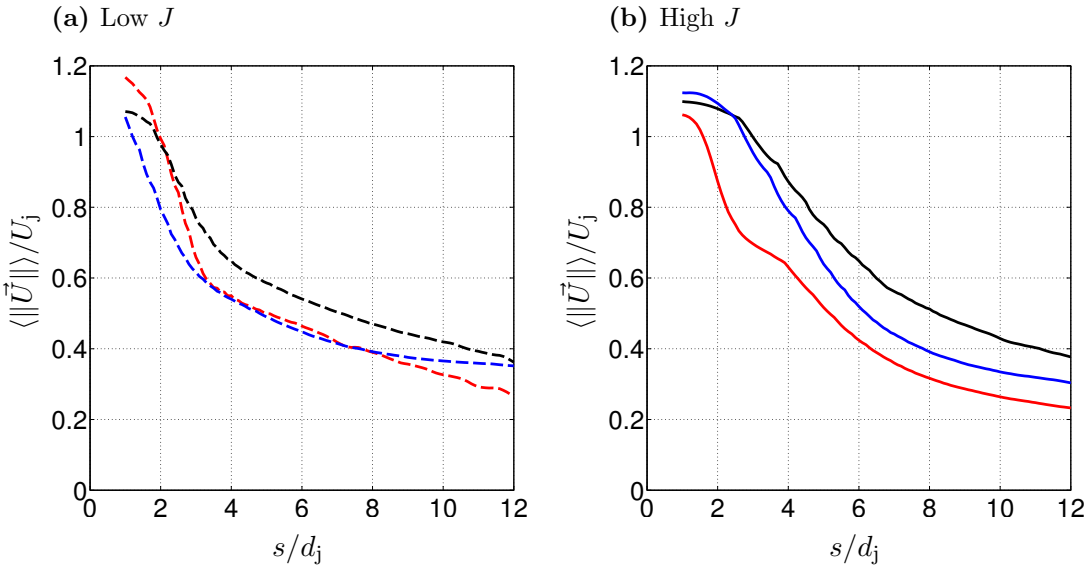

Figure 5.1: Decay of velocity magnitude along the jet centerline as a function of arc length distance ($n/d_j = 0$) for unforced cases with different mixture compositions. (—/---): R, $S = 0.40$, (—/---): R, $S = 1.00$, (—/---): NR, $S = 1.00$.

The results presented in Figure 5.1 indicate that S and the presence/absence of combustion strongly affects centerline velocity decay. The more rapid decay of centerline velocity in the non-reacting, iso-density cases compared to their reacting, iso-density counterparts is not surprising since reacting cases penetrate further into the crossflow. The more interesting result is that reacting jets with different S have very different centerline velocity decay. To understand the significance of this result, it is important to remember that the trajectory of reacting jets was shown in Chapter 3 to be insensitive to changes in S. On the other hand, a jet with faster centerline velocity decay is expected to deflect more rapidly into the crossflow direction. However, this is clearly not the case for reacting jets with different S. The hypothesis described earlier in this section offers a plausible explanation for this non-intuitive result; namely, the sensitivity of the near-field mixing rate to differences in S leads to differences in the amount of combustion heat release, which, in turn, affects the jet trajectory. More specifically, the penetration of reacting, low S jets is similar to that of

reacting, unity S jets (as shown in Figure 3.5) because their faster centerline velocity decay is associated with increased jet/crossflow mixing, leading to more combustion-induced aerodynamic blockage and flow acceleration in the near-field. In other words, the more rapid centerline velocity decay in reacting, low S jets is offset by the additional near-field heat release in those cases.

The slope of the centerline velocity with respect to s/d_j in Figure 5.1 provides additional insight into the jet structure. In particular, the slope does not vary with S beyond $s/d_\mathrm{j} \approx 4$ for the reacting cases. This is true in both low and high J jets. In other words, the effect of S on the centerline velocity decay is primarily a near-field effect. This result suggests that the shear layer vortices, which are the dominant coherent structure in the near-field of JICF, play an important role in the response of JICF to changes in S.

The influence of S on the near-field dynamics is also apparent in the centerline RMS velocity fields plotted in Figure 5.2. In low J jets, the centerline RMS velocity increases sharply with increasing s/d_j near the jet exit before reaching a peak and then gradually decaying. The reacting, unity S case reaches the largest peak RMS value but the location of the peak is approximately $s/d_\mathrm{j} = 3$ in both of the low J reacting cases. Beyond $s/d_\mathrm{j} = 3$, the centerline RMS velocity in both of the reacting cases decays at the same rate, which is similar to the far-field behavior observed previously for centerline velocity decay. The centerline RMS velocity profiles show more variation in the high J cases. In particular, the RMS velocity in the reacting, low S case increases much faster near the jet injector and exhibits a narrow peak at $s/d_\mathrm{j} \approx 2$, which is not seen in the other cases. On the other hand, the centerline RMS velocity in the reacting, high J, unity S case steadily increases towards a broad peak at $s/d_\mathrm{j} \approx 5$ and then gradually decays. However, the far-field decay of RMS velocity is similar in both of the reacting, high J cases, which resembles the behavior seen previously in the low J jets.

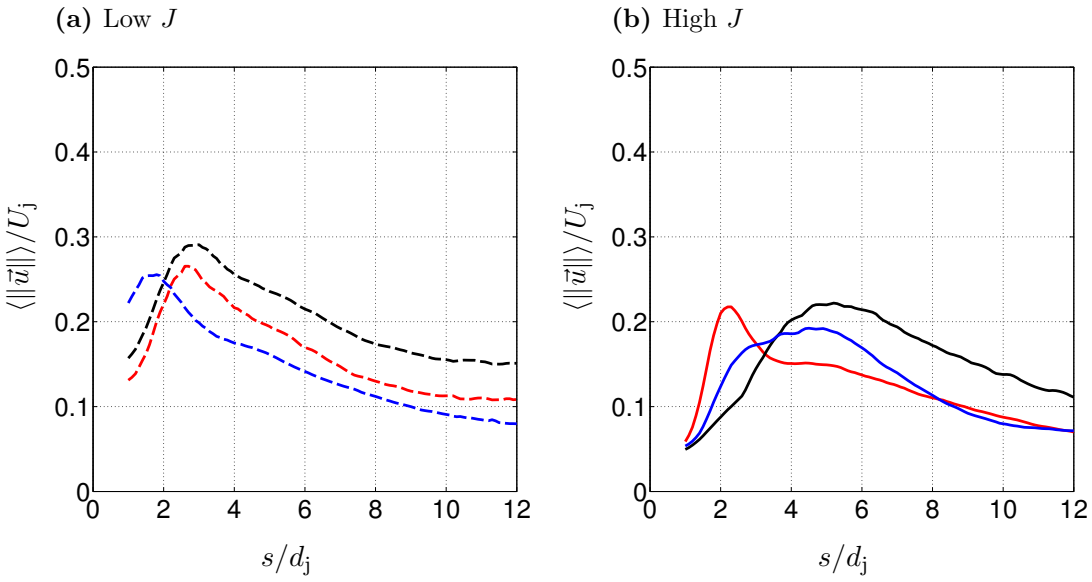

Figure 5.2: RMS velocity as a function of arc length distance along the jet centerline ($n/d_j = 0$) for unforced cases with different mixture compositions. (—/---): R, $S = 0.40$, (—/---): R, $S = 1.00$, (—/---): NR, $S = 1.00$.

5.2 Effect on Size and Structure of the Shear Layer Vortices

The time-averaged results presented in Section 5.1 support the hypothesis that differences in S affect the scalar and momentum transport of reacting JICF. The differences in scalar and momentum transport are, however, largely confined to the jet near-field, as evidenced by the fact that the decay of both the mean and the fluctuating centerline velocity does not vary with S beyond $s/d_j \approx 4$. Thus, it is reasonable to assume that the shear layer vortices, which are the dominant coherent vortical structure in the JICF near-field, must be responsible for the differences in scalar and momentum transport observed in jets with different S. The remainder of this section explores the sensitivity of the shear layer vortices to changes in S based on results and analysis of instantaneous Mie scattering images and OH PLIF measurements.

Although the passage frequency of the shear layer vortices is much too high to resolve using the SPIV system, the size, shape, and spatial distribution of the shear layer vortices can be readily determined from instantaneous Mie scattering images. Representative Mie scattering images for six different unforced test conditions with different J and S are shown in Figure 5.3. The contrast has been adjusted in each image to highlight the jet structure.

Instantaneous OH PLIF results are superimposed in the reacting cases to indicate the location of the windward and leeward reaction zones. The magenta isolines correspond to 10% and 50% of the maximum corrected OH PLIF signal. The mean jet center streamline trajectory is shown with the dashed white line, and the small red dots indicate $1d_j$ increments of arc length distance. The white dots surrounded by the neon green ellipses indicate the centroid and outer perimeter, respectively, of the shear layer vortex located at $s/d_j = 2 \pm 0.25$ in each case. The significance of the neon green ellipses will be addressed in detail after the instantaneous Mie scattering images are discussed.

The Mie scattering results presented in Figure 5.3 show that the size and spatial distribution of the shear layer vortices strongly depend on J, S, and the presence/absence of combustion. The low J results in the left hand column of Figure 5.3 are considered first. The windward shear layer of the non-reacting, low J case shown in Figure 5.3e is characterized by a train of regularly spaced shear layer vortices, which form close to the jet injector on the windward side of the jet and grow rapidly with increasing s/d_j along the first few jet diameters. A smaller shear layer vortex is also present on the leeward side of the jet near $s/d_j = 2$. The delayed shear layer roll-up on the leeward side of the jet is presumably a consequence of the lower strain rate in that region. Interestingly, the shear layer roll-up along the windward side of the jet in the reacting, low S case (Figure 5.3a) is broadly consistent with that observed in the non-reacting, iso-density case. More specifically, shear layer vortices again form near the exit of the jet injector, grow rapidly with increasing s/d_j, and ultimately breakdown into turbulence near $s/d_j \approx 4$. Furthermore, the size of the shear layer vortex located near $s/d_j = 2$ (shown in neon green) is comparable in both the reacting, low S case and the non-reacting, iso-density case. The spacing between individual vortices is, however, larger in the reacting case. Since U_j is higher in the reacting, low S case (for fixed J), the increased vortex spacing in that case would be expected if the underlying instability mechanism responsible for the shear layer roll-up in both cases was characterized by the same St_j scaling. The shear layer roll-up in the other reacting case ($S \approx 1.00$), which is shown in Figure 5.3c, is very different and does not resemble either the

reacting, low S case or the non-reacting, iso-density case. In particular, the shear layer roll-up along the windward side of the reacting, iso-density jet is significantly delayed relative to the other low J cases. No vortices are visible below $s/d_{\mathrm{j}} = 2$ in the reacting, iso-density case, and the vortices that are present at larger s/d_{j} are much smaller than those found in the other low J cases at similar arc length distances.

As previously seen in the low J cases, the size of the shear layer vortices in the high J jets (shown in the right column of Figure 5.3) depends on S and the presence/absence of combustion. In particular, the shear layer vortices in the reacting, low S case are similar to those observed in the non-reacting, iso-density case. The shear layer roll-up in the high J reacting, iso-density case (Figure 5.3d) is, however, noticeably different than the other high J cases. In this case, a train of small shear layer vortices is evident along both the windward and leeward sides of the jet. Furthermore, the size of the shear layer vortices increases more slowly with s/d_{j} in the reacting, iso-density case.

The most noticeable difference between the low and high J cases is the more pronounced shear layer roll-up on the leeward side of the high J jets. The strong shear layer roll-up on both sides of the jet can lead to "pinching" of the jet column when the windward and leeward shear layer vortices collide, as seen in the non-reacting, iso-density case shown in Figure 5.3f. It is also worthwhile to note that the windward flame is lifted away from the jet injector in the low S, high J case (see Figure 5.3b). Thus, the windward shear layer in that case develops initially without the influence of the high temperature reaction zone sandwiched between the jet fluid and the stagnating crossflow fluid. On the other hand, the other three reacting conditions are all characterized by an attached windward flame. The significance of this result with respect to the shear layer development will be addressed in more detail in the next section.

Vortex tracking is used to quantify the differences in shear layer vortex size observed in Figure 5.3. Vortices are identified with the help of a custom Matlab GUI that randomly selects 250 Mie scattering images out of the full set of $\sim 10,000$ images. The GUI displays the near-field region of each Mie scattering image one at a time and allows the user to manually select a set of 4 points around the circumference of the vortex located closest to

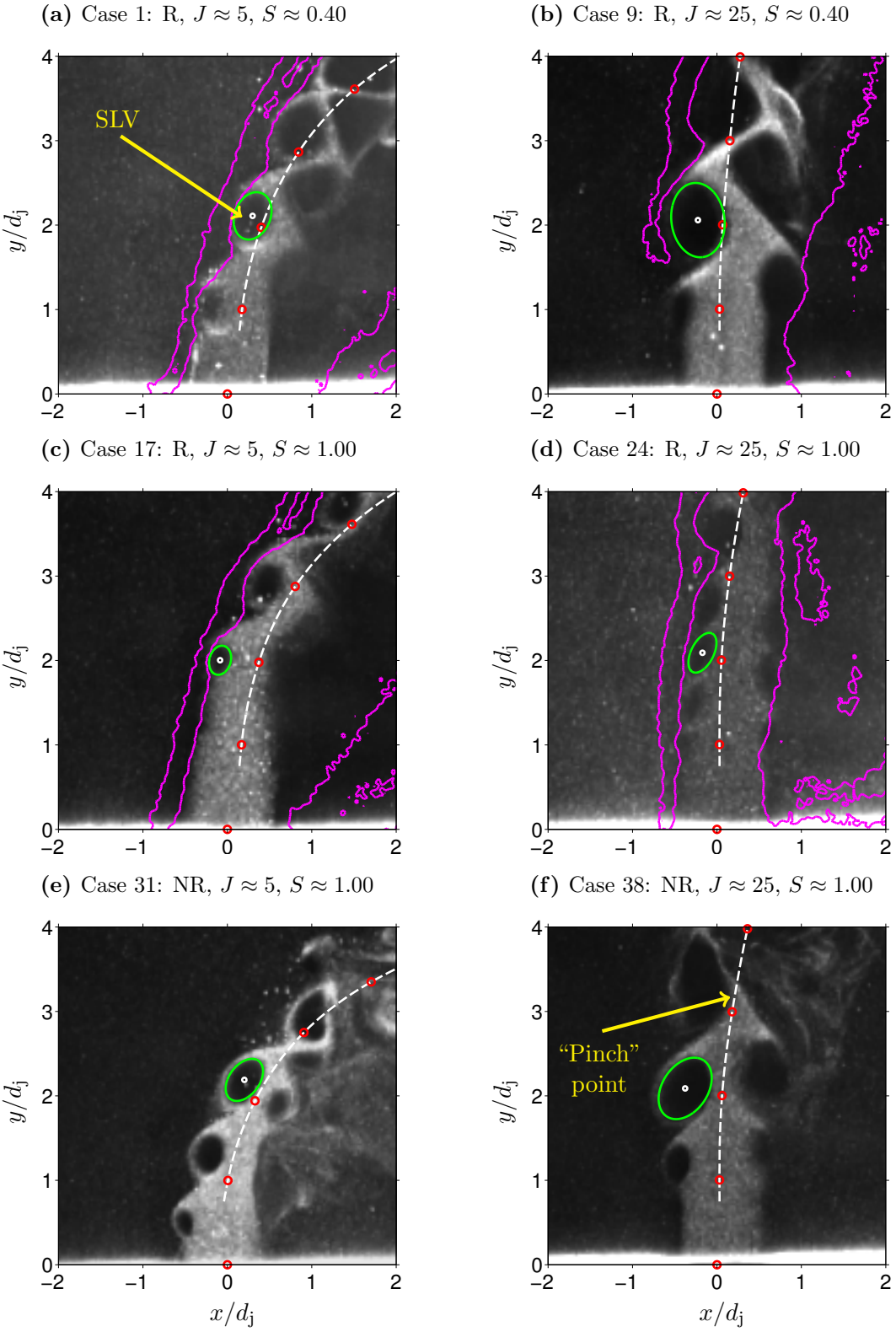

Figure 5.3: Mie scattering flow visualization of the near-field region of R/NR jets with different J and S illustrating the formation and growth of shear layer vortices. (—): 10% and 50% OH PLIF contour lines. (▬ ▬): Mean jet center streamline trajectory. (○): Points spaced $1d_j$ apart along the mean jet center streamline.

$s/d_\mathrm{j} = 2$. The user-specified points are then used to calculate the location of the vortex centroid and to parameterize an equation for the ellipse that best approximates the circumference of the vortex. The neon green ellipses drawn in Figure 5.3 were identified using this approach. Since the size and structure of the shear layer vortices varies with s/d_j, only vortices located at $s/d_\mathrm{j} = 2 \pm 0.25$ were recorded. After identifying a set of 250 vortices for each case, statistical properties such as the mean shear layer vortex area, Σ, and RMS area fluctuation, Σ', are computed. The sample size of 250 Mie scattering images was selected after performing a convergence study to insure that the statistical properties of interest, i.e., Σ and Σ', did not vary by more than 5% when the vortex tracking procedure was applied repeatedly to different randomly selected sets of images from the same dataset. Histograms showing the distribution of shear layer vortex sizes, Σ, normalized by the area of the jet, A_j, are shown in Figure 5.4. Each histogram is computed using 20 bins evenly distributed between 0 and the maximum observed vortex size for a given J value, which was $0.4A_\mathrm{j}$ in the low J cases and $0.8A_\mathrm{j}$ in the high J cases. Hence, the x-axis scaling in Figure 5.4 is different for the low and high J cases.

Comparing the distributions of shear layer vortex size for different test conditions in Figure 5.4 reinforces the qualitative observations made based on the instantaneous Mie scattering images in Figure 5.3. As anticipated based on the instantaneous images, the mean shear layer vortex size is larger in high J cases than in the low J cases. For jets with the same J, Σ/A_j is largest for reacting, low S cases. Σ/A_j varies by a factor of two between reacting cases with different S for both low and high J jets. The size of the shear layer vortices in non-reacting cases lies in between that of the reacting, iso-density cases and the reacting, low S cases. The distribution of Σ/A_j is much narrower in the reacting, iso-density cases. The reacting, low S cases have the broadest distribution of Σ/A_j and the largest fluctuations.

The values for Σ/A_j and Σ'/A_j in each case are presented in Table 5.1. The detailed test conditions as well as the mean vortex centroid location are also shown for reference. The last column in Table 5.1, which is labeled "No SLV," refers to the fraction of instantaneous Mie scattering images encountered during the vortex tracking procedure for that case that

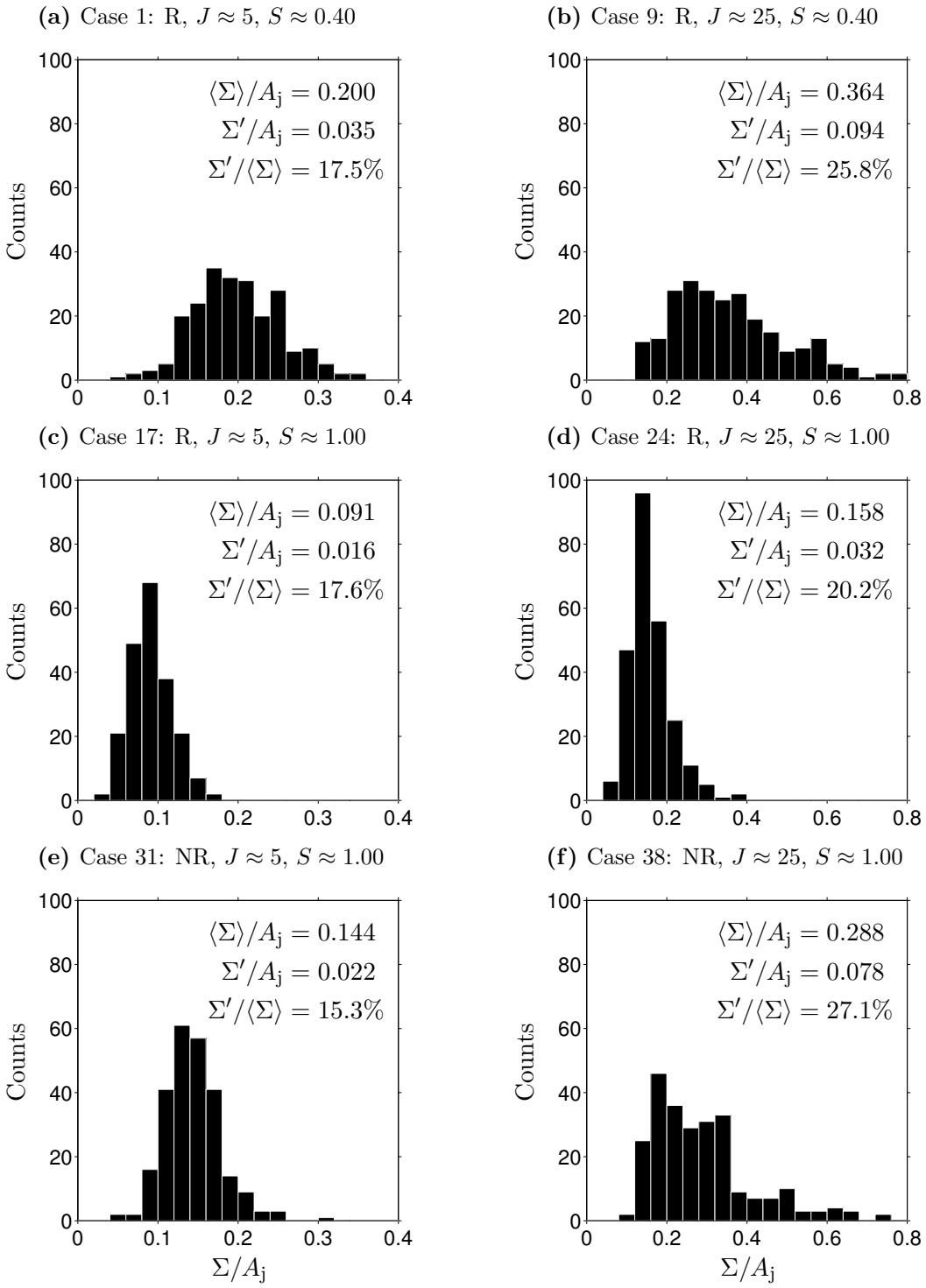

Figure 5.4: Histograms of shear layer vortex size, Σ, for unforced cases with different J and S. Σ measured at $s/d_\mathrm{j} = 2 \pm 0.25$ for 250 randomly selected samples in each case.

did not exhibit shear layer roll-up on the windward side of the jet. An example of the "No SLV" condition taken from the reacting, low J, iso-density case is shown in Figure 5.5. The reacting, low J iso-density test condition was the only case where shear layer roll-up was not observed for a non-negligible percentage of the instantaneous images. To avoid biasing the results, images without shear layer vortices were not, however, used in the calculation of Σ/A_j and Σ'/A_j. Lastly, it is important to note that even when shear layer roll-up does not occur, as in Figure 5.5, evidence of the windward shear layer instability is still seen in the wave-like deformation of the jet/crossflow interface.

Table 5.1: Size of shear layer vortices in unforced cases with different J and S.

Case	R/NR	J	S	Re_j	$\langle\Sigma\rangle/A_\mathrm{j}$	Σ'/A_j	$(x/d_\mathrm{j}, y/d_\mathrm{j})_\Sigma$	No SLV (%)
1	R	5.05	0.41	1980	0.200	0.035	(0.16, 2.17)	0.80
9	R	23.23	0.40	4420	0.364	0.094	(-0.25,2.08)	0.00
17	R	5.08	1.04	2590	0.091	0.016	(0.22,2.20)	15.20
24	R	25.32	1.04	5750	0.158	0.032	(-0.21,2.11)	0.00
31	NR	4.74	1.00	1920	0.144	0.022	(0.19,2.02)	0.00
38	NR	25.14	1.03	4270	0.288	0.078	(-0.30,2.11)	0.00

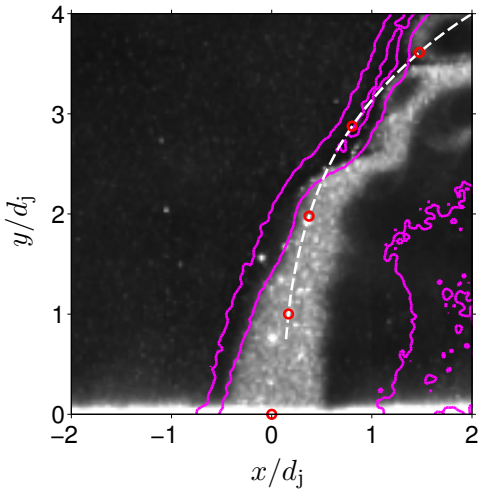

Figure 5.5: Instantaneous Mie scattering image extracted from the reacting, low J, iso-density case where shear layer roll-up does not occur. (—): 10% and 50% OH PLIF contour lines. (▬): Mean jet center streamline trajectory. (○): Points spaced $1d_\mathrm{j}$ apart along the mean jet center streamline.

5.3 Phenomenological Model Based on Shear Layer Stability Concepts

Section 5.2 illustrated the significant effect of J, S, and presence/absence of combustion on the formation and spatial growth rate of the shear layer vortices. This section presents a more in-depth discussion of the underlying physical processes responsible for the differences in size, structure, and evolution of the shear layer vortices in reacting JICF with different J and S. Concepts from linear stability theory and results from previously reported experimental studies on the stability of density-stratified open shear flows are reviewed in the context of the present work and are used to develop a framework for understanding the shear layer dynamics of reacting, variable density JICF.

As discussed in Section 1.4, the windward shear layer of the JICF is convectively unstable for all the values of J and S considered in the present study. Thus, the windward shear layer acts as a "noise amplifier" for incident flow disturbances, which in this case are broadband fluctuations continuously supplied by the turbulent, vitiated crossflow. Since the amplification of incident disturbances is a strong function of frequency, disturbances near the preferred mode of the shear layer quickly become dominant. The disturbance amplitude initially increases exponentially with increasing arc length distance, but non-linear mechanisms quickly takeover further downstream, leading to wave-breaking, amplitude saturation, and eventually, breakdown into turbulence. In addition to the amplification of external perturbations by the windward shear layer as a result of the convective instability, it is known that the interaction of multiple shear layers, as is the case in a jet flow, can fundamentally alter the stability of the flow [38]. Jet and wake flows, for example, can contain pockets of local absolute instability, which can lead to global instability of the flow. A globally unstable flow behaves as a self-excited oscillator, whose instability persists even in the absence of external excitation. Megerian et al. [7] recently demonstrated that a non-reacting, iso-density JICF transitions to a globally unstable regime when J is reduced below a critical $J_{\text{critical}} \approx 10$ value.

Assuming for the moment that the non-reacting results [7–9] are also valid in the reacting case, the important implication for the present study is that the low J and high J jets

lie on opposite sides of the global stability threshold. Thus, the underlying physical mechanism responsible for the shear layer vortices is not the same. Shear layer vortices in the convectively unstable high J cases result from amplification of disturbances present in the crossflow. Conversely, in the low J cases, the flow has a built-in "wave-maker," i.e., a pocket of local absolute instability, which supplies initial disturbances that are subsequently amplified by the downstream flow. Low J JICF in the globally unstable regime are characterized by strong narrow-band shear layer spectra, which, in contrast to the shear layer spectra seen in convectively unstable JICF, do not change with s/d_{j} in the near-field. The recent acetone PLIF measurements reported by Getsinger [92] link the strong periodicity of the globally unstable JICF shear layer to the observation of long sequences of regularly spaced shear layer vortices. Mie scattering images from the present experiments on non-reacting and reacting JICF with low J exhibit similar behavior, as seen in Figure 5.6a. Getsinger [92] also showed that high J JICF, which are not believed to be globally unstable, often exhibit vortex pairing in the windward shear layer, a phenomenon that is not observed in low J JICF. A representative high J case demonstrating vortex pairing in the near-field is shown in Figure 5.6b. While a detailed study of the convective versus global instability of reacting JICF is beyond the scope of the present work, it is important to remember that the physical mechanism controlling the formation and evolution of the shear layer vortices is fundamentally different in low J and high J jets.

In addition to the sensitivity to changes in J, the stability of the JICF shear layer, and therefore the shear layer growth rate, also depends on the jet-to-crossflow density ratio, S [9]. The important influence of density ratio on shear layer stability is well-established in several other common open shear flows, including axial jets, axisymmetric wakes, and counter-current mixing layers. Axial jets where the jet fluid has low density relative to the ambient fluid exhibit increased absolute instability growth rates, as shown by Sreenivasan et al. [93] and Yu & Monkewitz [94]. Raynal et al. [95] showed that low molecular weight jets and heated jets have different shear layer growth rates because differences in the mass transport and heat transport near the jet injector lead to differences in the density gradient felt by the shear layer. The importance of the relative positions of the density and velocity

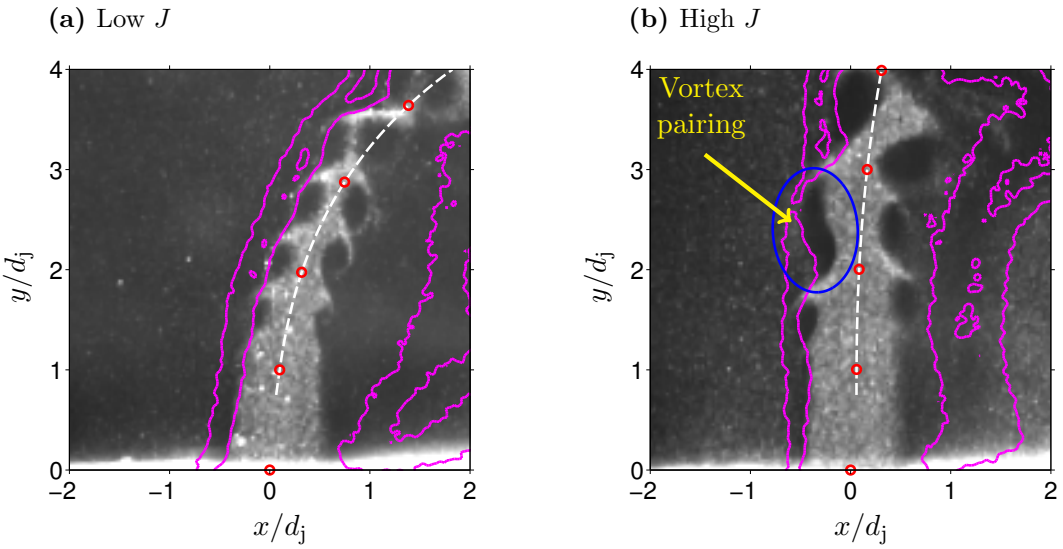

Figure 5.6: Mie scattering flow visualization illustrating differences in the evolution of shear layer vortices in low and high J cases. $S \approx 1.00$ in both images. (—): 10% and 50% OH PLIF contour lines. (▬ ▬): Mean jet center streamline trajectory. (○): Points spaced $1d_j$ apart along the mean jet center streamline.

gradients was also reported in a recent study on the wake characteristics of a turbulent, bluff-body stabilized premixed flame [20]. More specifically, offsets between the density and velocity gradients increased absolute instability growth rates in the wake flow, which was primarily attributed to modifications of the baroclinic vorticity production processes. On the other hand, the absolute instability growth rate in jet flows is decreased when the density layer is offset from the shear layer. The largest shear layer growth rates in axial jets with fixed S are achieved when steep, step-like changes in density are located in high shear regions of the flow [96].

The preceding discussion on density ratio effects in shear flows provides some insight into the very different shear layer growth rates observed in the instantaneous Mie scattering images discussed in Section 5.2. In particular, the strong shear layer roll-up and rapid increase in vortex size observed in the low S cases is consistent with the results of stability studies on low density axial jets, which showed that those cases have the most unstable shear layers and thus the largest growth rates. On the other hand, the studies discussed above do not explain why shear layer roll-up in the reacting, iso-density jet is dramatically suppressed in comparison to the non-reacting, iso-density jet.

However, the location of the windward flame front, which is clearly indicated by the

OH PLIF contour lines in Figure 5.3, provides a clue as to why the shear layer growth rates are so different for the non-reacting and reacting iso-density cases. Specifically, a non-premixed flame sits in the shear layer formed between the stagnating crossflow and the high velocity jet fluid. The flame increases the temperature in that region, leading to significant dilatation, an increase in the fluid viscosity, and local flow acceleration. Although the reduction in effective Reynolds number due to increased viscosity can be important in some cases, the primary mechanism responsible for altering the shear layer stability in moderate-to-high Reynolds number flows is the modification of the density gradient within the shear layer [20]. Clemens & Paul [59] found that the reduction in shear layer growth rates for reacting versus non-reacting co-axial jets was very similar to the reduction in shear layer growth rate for axial jets injected into lower density co-flows. Similarly, in their studies of bluff-body stabilized premixed flames, Erickson & Soteriou [80] and Emerson et al. [20] found that higher reactant preheat temperatures destabilized the reacting wake, because of the reduction in the density of the reactants relative to the burnt products in the wake. The general equivalence principle developed by Tacina & Dahm [97] successfully extended scaling laws for shear layer growth rate in density-stratified non-reacting flows to reacting flows, which reinforces the notion that combustion heat release primarily affects shear layer growth rates through the same physical mechanism at work in density-stratified non-reacting flows.

Hence, it is reasonable to believe that the dramatic difference in shear layer growth rates seen in the present experiments for non-reacting versus reacting iso-density JICF is a consequence of the combustion-induced density gradient in the reacting case. To further explore this line of reasoning, Figure 5.7 presents sketches illustrating the effect of combustion on the shear layer density stratification for cases with different jet mixture composition. The flame thickness, δ_{f}, in the reacting cases is assumed to be $\delta_{\mathrm{f}} \sim 1\mathrm{mm}$ and is drawn to scale accordingly in Figure 5.7 with respect to d_{j}. The density of the flame zone, which is denoted in the sketches by different shades of pink for the two reacting cases, is approximated as the equilibrium product density, ρ_{ad}, for a stoichiometric mixture of jet fluid and vitiated crossflow fluid. As discussed previously in Chapter 3 (see Table 3.2), ρ_{ad} varies by only

$\sim 6\%$ between the low S and unity S cases in spite of the 250% change in ρ_{j}, which is primarily due to the low stoichiometric mixture fraction, z_{st}, for flames stabilized in vitiated crossflows.

In light of the combustion-induced density stratification outlined in Figure 5.7, it is clear that S alone is not sufficient to characterize the shear layer structure in a reacting JICF. The relevant density gradient in terms of shear layer stability, i.e., the density gradient experienced by the jet shear layer, is better characterized by the jet-to-reaction zone density ratio, $S_{\mathrm{j,ad}}$, rather than the jet-to-crossflow density ratio, S. This is in contrast to the situation in non-reacting JICF where the density gradient is well-characterized by S. Thus, the effective density ratio can be very different in non-reacting and reacting jets with the same S. In the present experiments, $S_{\mathrm{j,ad}}$ is roughly 2 in the reacting case with $S = 1.00$. From a stability standpoint, the reacting, $S = 1.00$ case is actually a dense jet rather than an iso-density jet. Shear flows where the high velocity fluid is dense relative to the low velocity fluid tend to be very stable. This observation is in excellent agreement with the suppressed shear layer roll-up observed in the reacting, $S = 1.00$ case. Re-examining the density stratification in the reacting, low S case shows that the effective density ratio in the shear layer is actually very close to unity despite the fact that $S = 0.40$. From this perspective, it is not surprising that the shear layer roll-up in the non-reacting, iso-density case closely resembles that of the reacting, low S case.

It is worth noting that the combustion-induced density stratification mechanism described above is different than the physical mechanism responsible for altering the wake stability characteristics in a bluff-body stabilized premixed flame. The flame in the premixed wake is essentially a thin boundary separating (relatively) cold reactants from hot combustion products recirculated into the wake. The location of the flame relative to the shear layer is very important in that situation [20] as well, but the thickness of the flame itself is not generally an important consideration in predicting the stability of the flow. Conversely, in the present experiments, the ratio of the flame thickness to the momentum thickness of the jet is $\delta_{\mathrm{f}}/\theta_{\mathrm{j}} > 1$ and $\delta_{\mathrm{f}}/d_{\mathrm{j}} = \mathcal{O}(1)$. Thus, the density of the reaction zone itself becomes important in characterizing the shear layer stability. An interesting question

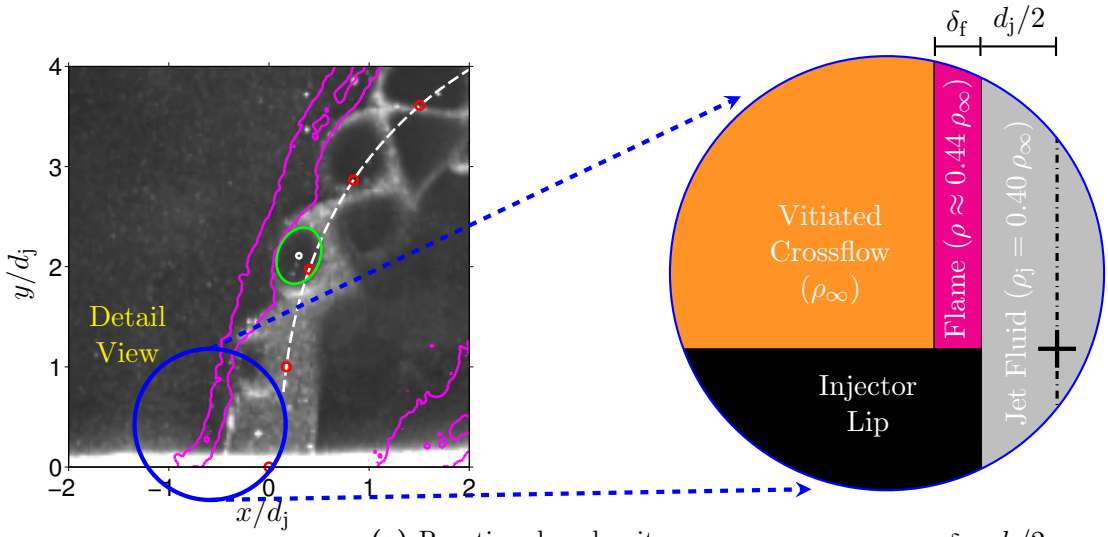

(a) Reacting, low density case.

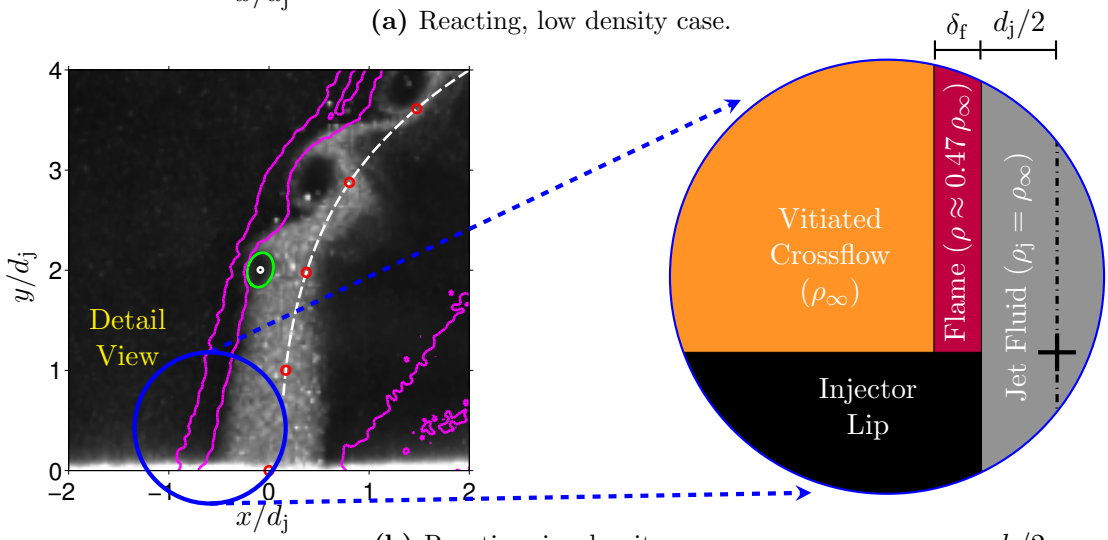

(b) Reacting, iso-density case.

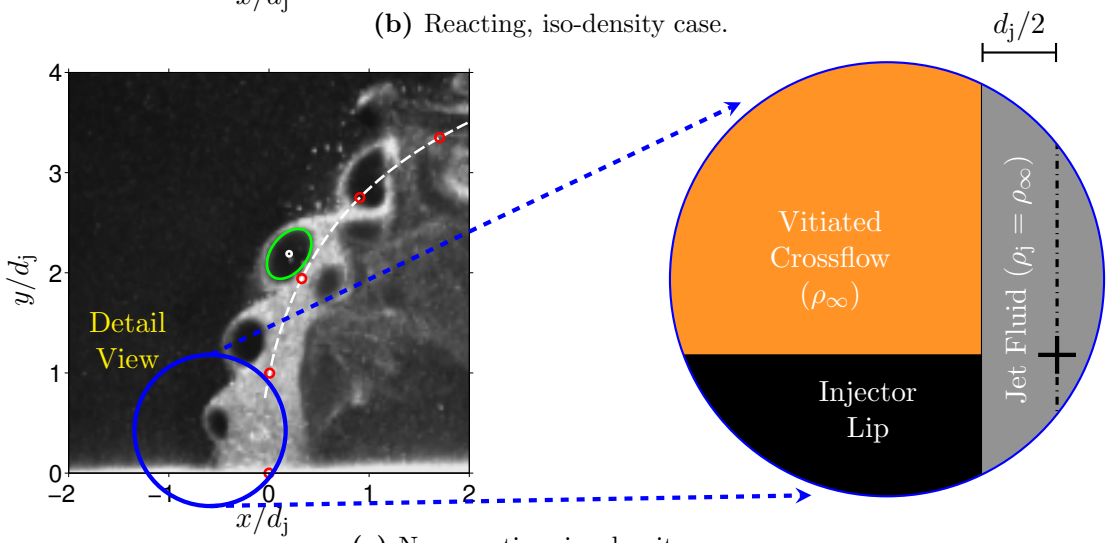

(c) Non-reacting, iso-density case.

Figure 5.7: Sketches illustrating the density stratification in non-reacting and reacting JICF with attached windward flames.

to consider, and a motivation for future work, is what happens to the shear layer stability in a reacting JICF as d_j is increased to the point where $\delta_f/\theta_j \ll 1$.

Finally, the role of flame stabilization in the windward shear layer is an important, and unexplored, factor that influences the shear layer stability. For example, reacting jets in low-to-moderate temperature air crossflows stabilize a flame on the leeward side of the jet in a well-mixed, low velocity region removed from the lower wall [29, 54, 98]. The windward shear layer near the jet-exit region may be essentially isothermal under these conditions, and the shear layer stability is much more likely to resemble that of a non-reacting JICF than a jet injected into a vitiated, high-temperature crossflow with a strongly attached flame near the jet-exit region. A third, more complex situation occurs when a lifted flame stabilizes in the windward shear layer, as was intermittently observed for the low S, high J test conditions in the present experiments. A diagram illustrating the density stratification for this situation is provided in Figure 5.8. Since the flame is lifted away from the injector lip, the initial shear layer development is characterized only by ρ_j and ρ_∞. The density gradient is, however, modified by the presence of the reaction zone further downstream after flame stabilization occurs. It should also be noted that the location of flame stabilization tends to be highly intermittent in these situations, which may partially account for the broadened shear layer vortex size distribution seen in Figure 5.4. Interestingly, the physical situation depicted in Figure 5.8 closely resembles the lifted flame configuration studied theoretically in the recent work by Nichols et al. [99]. Those authors found that axial (streamwise) confinement of the shear layer due to flame stabilization can be destabilizing, potentially leading to situations where resonant streamwise modes have larger growth rates than the usual shear layer modes.

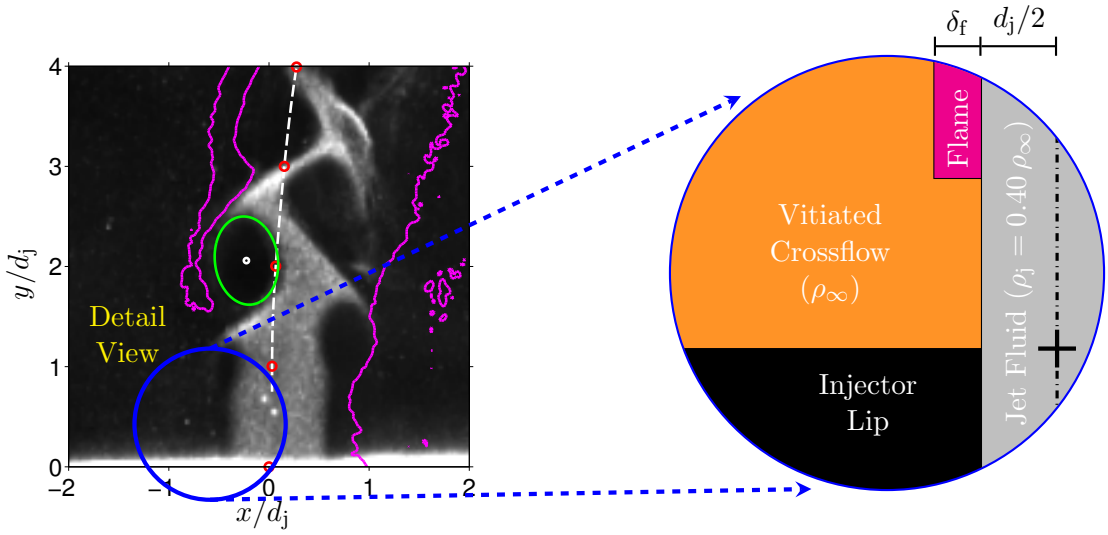

Figure 5.8: Sketch illustrating the density stratification in a high J, low S case with a lifted windward flame.

5.4 Role of Crossflow Acoustics

The results presented in Chapter 4 demonstrated that crossflow forcing can significantly alter both the instantaneous and the time-averaged features of JICF. The extent to which crossflow forcing modifies the flow depends on both J and S, which is due primarily to the influence of J and S on u'_j/U_j. As discussed throughout this chapter, J and S also affect the formation and evolution of the shear layer vortices. Section 5.3 used hydrodynamic stability concepts to explain why changes in the size and structure of the shear layer vortices occur as a result of changes in J and S. A logical extension of that work, and the focus of the present section, is to consider the influence of low frequency crossflow forcing on the formation and evolution of the shear layer vortices.

The shear layer stability concepts discussed in Section 5.3 indicate that the windward shear layer of the JICF amplifies velocity perturbations. In the forced response cases, the shear layer is perturbed both by the fluctuating crossflow velocity, u'_∞, and the injector-coupled fluctuating jet exit velocity, u'_j. However, the acoustic forcing frequencies, f_F, are very low ($f_F < 377$Hz) compared to the frequency of shear layer's fundamental mode, f_M. The hot-wire measurements performed by Getsinger et al. [9] on variable density ratio non-reacting JICF showed that f_M lies in the range $0.50 \leq St_j \leq 0.90$. Assuming similar Strouhal scaling in the present measurements gives dimensional frequencies for the fundamental mode

in the range 6.6kHz $\leq f_{\mathrm{M}} \leq$ 43.1kHz. Although Getsinger et al. [9] showed that f_{M} is in general a function of both J and S, the key point with respect to the present experiments is that $f_{\mathrm{M}} \gg f_{\mathrm{F}}$. In other words, the characteristic timescale of the shear layer vortices is much shorter than the acoustic period of the crossflow forcing.

The drastic difference between f_{M} and f_{F} suggests that the effect of crossflow forcing on the shear layer vortices can be interpreted from a quasi-steady perspective. More precisely, the rate at which the crossflow forcing alters the JICF is very slow compared to the characteristic timescale of the shear layer. Thus, the shear layer vortices adjust to the changing crossflow very rapidly, and the shear layer dynamics are affected primarily because the crossflow acoustics modify the JICF velocity field in a quasi-steady manner. The effect of this slow modification of the velocity field due to crossflow forcing is similar to changing the "base-flow" in a linear stability analysis. Since the shear layer growth rate is sensitive to changes in the magnitude and location of the velocity gradient, it is reasonable to expect that quasi-steady modulation of the velocity field may significantly alter the shear layer stability.

The time-averaged effect of crossflow forcing on the shear layer dynamics can be appreciated by comparing Figure 5.9, which plots the mean jet centerline velocity decay for six different forced cases, against the unforced results presented in Figure 5.1. Overall, the mean centerline velocity decay in the forced cases is qualitatively similar to that of the unforced cases. The centerline velocity decay is fastest in the non-reacting, iso-density cases, particularly in comparison to the reacting, iso-density case. Furthermore, the two reacting cases with different S behave very differently in the near-field but exhibit almost identical centerline velocity decay rates beyond $s/d_{\mathrm{j}} \approx 4$. The most noticeable difference between the unforced and forced centerline velocity decay measurements is that the agreement between the reacting, low S case and the non-reacting iso-density case is significantly improved for forced high J test conditions. The improved agreement relative to the unforced case may be a consequence of the fact that crossflow forcing promotes near-field flame stabilization in the reacting, high J cases. Thus, consistent with the discussion in Section 5.3, the density stratification of the reacting, low S case may more closely match that of the non-reacting,

iso-density case because crossflow forcing promotes near-field flame stabilization.

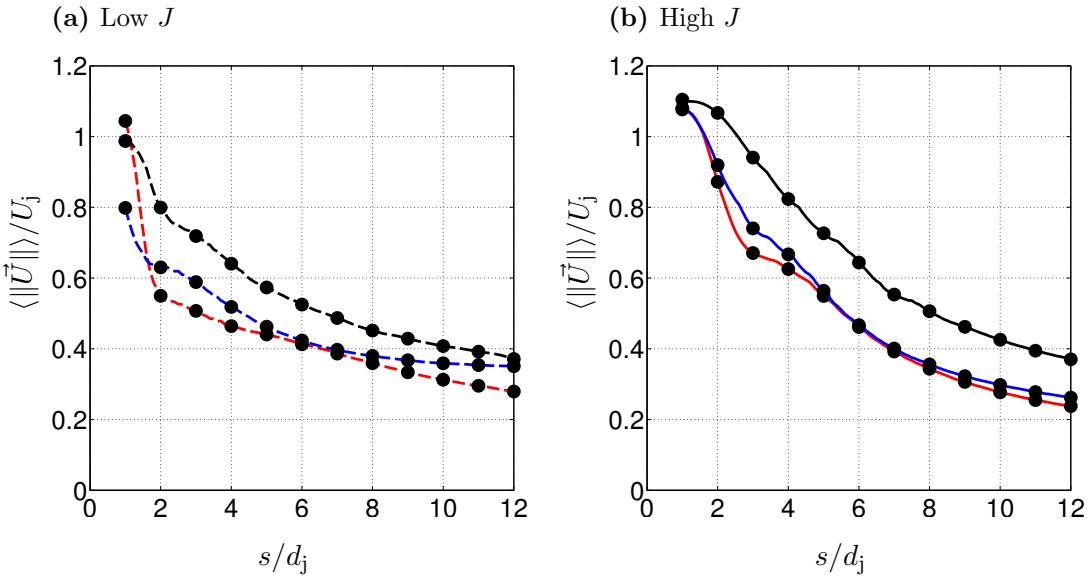

Figure 5.9: Decay of velocity magnitude along the jet centerline as a function of arc length distance ($n/d_j = 0$) for forced cases with different mixture compositions. Forcing frequency and excitation amplitude held constant in all cases at $f_F = 250$Hz and $A_F = 1.5$A, respectively. (—/---): R, $S = 0.40$, (—/---): R, $S = 1.00$, (—/---): NR, $S = 1.00$.

The centerline RMS velocity is plotted in Figure 5.10 for the same set of six forced test conditions considered above. As in the unforced cases shown previously in Figure 5.2, the forced centerline RMS velocity measurements indicate that S significantly affects the near-field ($s/d_j < 6$) behavior but has only a minimal influence on the far-field dynamics. The peak centerline RMS velocity in each of the three low J cases does shift closer to the jet injector in the forced cases compared to the unforced cases, an effect which was previously linked to the strong injector-coupled response in low J jets. Consistent with the unforced results, the reacting, iso-density cases always have the largest centerline RMS velocities at downstream locations. On the other hand, the centerline RMS velocities in both the non-reacting, iso-density cases and the reacting, low S cases decay much more rapidly in the near-field. The slope of the centerline RMS velocity curves does not vary beyond $s/d_j \approx 4$ in the low J cases and $s/d_j \approx 6$ in the high J cases. This observation again points to the influence of the shear layer vortices, which are most important in the near-field but do not persist into the far-field.

Vortex tracking is used to further quantify the influence of crossflow forcing on the

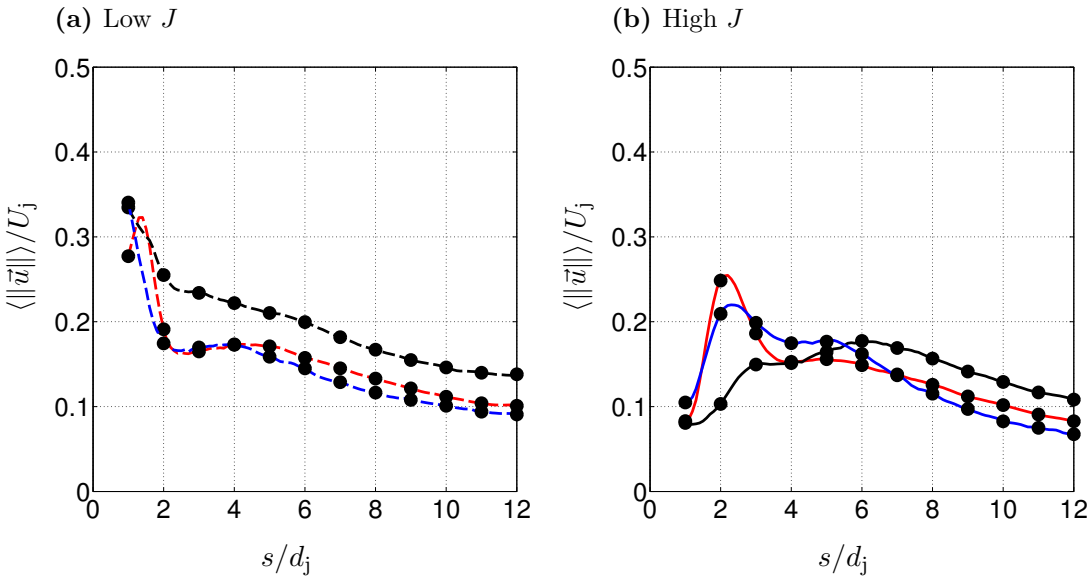

Figure 5.10: RMS velocity as a function of arc length distance along the jet centerline ($n/d_j = 0$) for forced cases with different mixture compositions. Forcing frequency and excitation amplitude held constant in all cases at $f_F = 250$Hz and $A_F = 1.5$A, respectively. (—/---): R, $S = 0.40$, (—/---): R, $S = 1.00$, (—/---): NR, $S = 1.00$.

shear layer growth rate. The methodology is identical to that described previously for the unforced cases. Histograms of the shear layer vortex size for the six forced cases are shown in Figure 5.11. Additional statistical quantities computed using the vortex tracking procedure are reported in Table 5.2. Interestingly, the mean shear layer size, $\langle \Sigma \rangle$, decreased relative to the unforced cases for five out of the 6 combinations of J and S considered, indicating that at least on average crossflow forcing tends to inhibit the shear layer growth rate. This effect was most pronounced in the reacting, low S cases, which saw a nearly 25% decrease in mean shear layer vortex size compared to the unforced cases. Both the non-reacting and reacting iso-density cases displayed much more modest decreases in mean shear layer vortex size. Interestingly, the mean shear layer vortex size in the low J reacting, iso-density case, which had the largest u_j'/U_j, actually increased slightly compared to the corresponding unforced case. This result should not be overstated, however, since instantaneous images with no shear layer roll-up were not included in the mean shear layer vortex size calculation. The percent of instantaneous images without shear layer roll-up actually increased in the forced case, as indicated by the "No SLV" column in Table 5.2. However, similar to the unforced results, the low J reacting, iso-density case was the only test condition where shear layer

roll-up was not observed for a significant percentage of the randomly selected Mie scattering images.

Table 5.2: Size of shear layer vortices in forced cases with different J and S. In each case, forcing frequency and excitation amplitude are fixed at $f_{\mathrm{F}} = 250\mathrm{Hz}$ and $A_{\mathrm{F}} = 1.5\mathrm{A}$, respectively.

Case	R/NR	J	S	Re_{j}	$\langle\Sigma\rangle/A_{\mathrm{j}}$	Σ'/A_{j}	$(x/d_{\mathrm{j}}, y/d_{\mathrm{j}})_{\Sigma}$	No SLV (%)
6	R	4.78	0.40	1980	0.154	0.027	(0.26,2.15)	1.20
14	R	23.89	0.40	4400	0.282	0.081	(-0.24,2.15)	0.00
21	R	4.63	0.98	2550	0.096	0.016	(0.23,2.16)	22.40
28	R	24.44	0.99	5760	0.148	0.035	(-0.34,2.04)	0.00
35	NR	4.82	1.00	1920	0.143	0.021	(0.25,2.07)	2.00
42	NR	24.24	1.02	4290	0.246	0.60	(-0.22,2.06)	0.00

Since the histograms in Figure 5.11 were constructed using randomly selected Mie scattering images, they contain no phase information with respect to the crossflow forcing. On the other hand, the results presented in Chapter 4 showed that the JICF flow field can change dramatically over the course of a single acoustic pressure cycle. Based on the quasi-steady hypothesis stated previously, the shear layer should respond rapidly to changes in the JICF flow field caused by the crossflow forcing. Thus, it is plausible that shear layer growth rates may be sensitive to the phase of the acoustic pressure cycle. To investigate this possibility, a modified vortex tracking procedure that considers only images acquired at the same phase of the acoustic pressure cycle (as measured in the jet injector plenum) is applied to two of the forced cases. Representative instantaneous Mie scattering images for two different phases of the acoustic pressure cycle are shown in Figure 5.12. The difference in shear layer roll-up, or lack thereof, in the low J case is readily apparent. Strong shear layer roll-up occurs at $\theta_{P_{\mathrm{j}}} = 0$ when the jet exit velocity is high, but no shear layer roll-up occurs half a period later at $\theta_{P_{\mathrm{j}}} = \pi$. Conversely, the high J jets show no meaningful difference in shear layer roll-up at the two different phases of the acoustic pressure cycle. Histograms computed using the phase-resolved vortex tracking procedure are shown in Figure 5.13. As anticipated based on the Mie scattering images, the mean shear layer vortex size is significantly reduced in the low J case at $\theta_{P_{\mathrm{j}}} = \pi$. Furthermore, Table 5.3 shows that the "No SLV" condition is much more common at $\theta_{P_{\mathrm{j}}} = \pi$ than at $\theta_{P_{\mathrm{j}}} = 0$. The phase-resolved histograms in the high J case, on the other hand, are virtually identical.

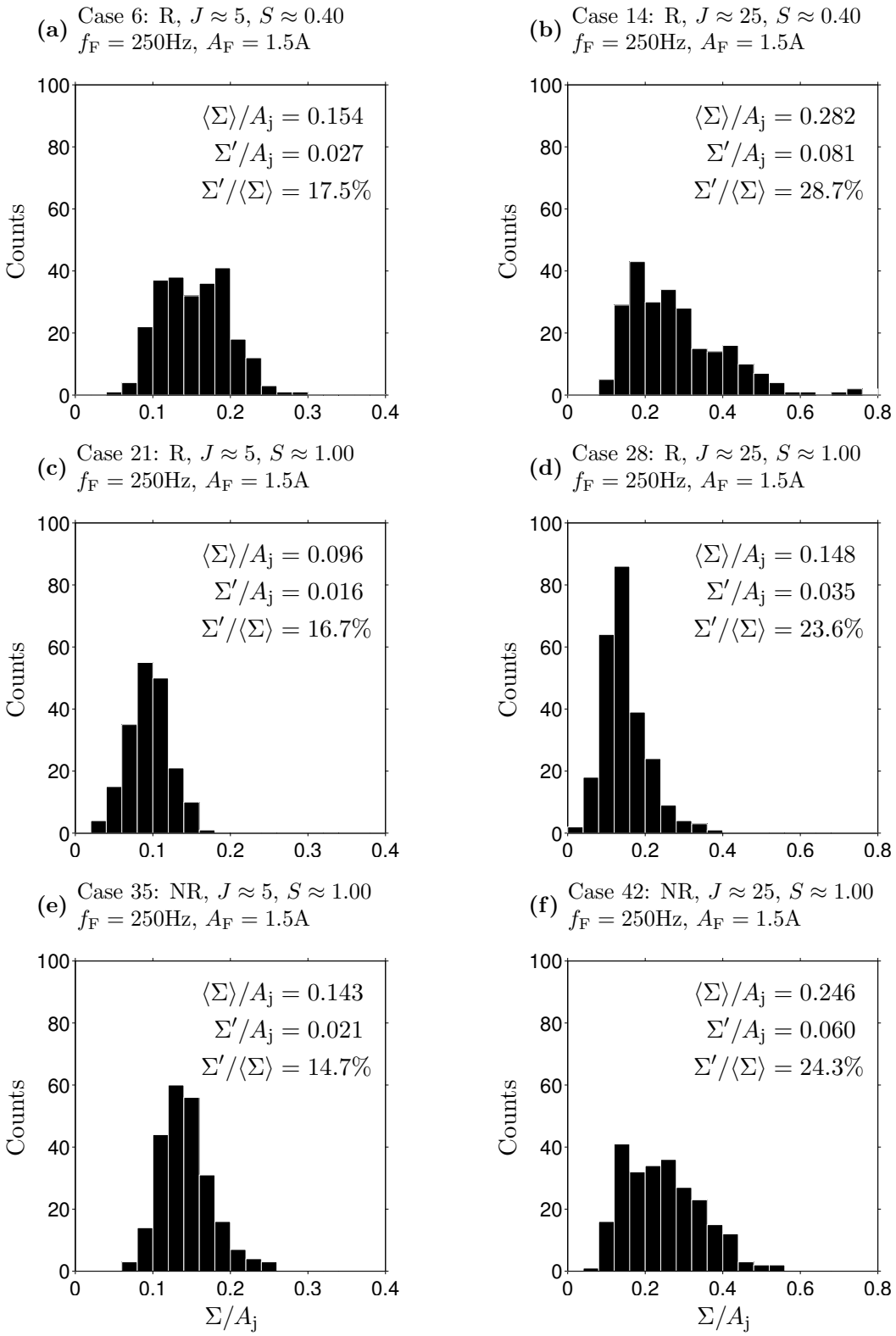

Figure 5.11: Histograms of shear layer vortex size, Σ, for forced cases with different J and S. Σ measured at $s/d_j = 2 \pm 0.25$ for 250 randomly selected samples in each case. Forcing frequency and excitation amplitude fixed at $f_F = 250$Hz and $A_F = 1.5$A, respectively, in all cases.

Thus, it appears that the shear layer growth rate is only significantly affected when $u'_{\mathrm{j}}/U_{\mathrm{j}}$ is sufficiently large to alter the phase-averaged velocity field. In other words, cases where the jet flaps significantly are likely to have very different shear layer growth rates at different points in the acoustic pressure cycle.

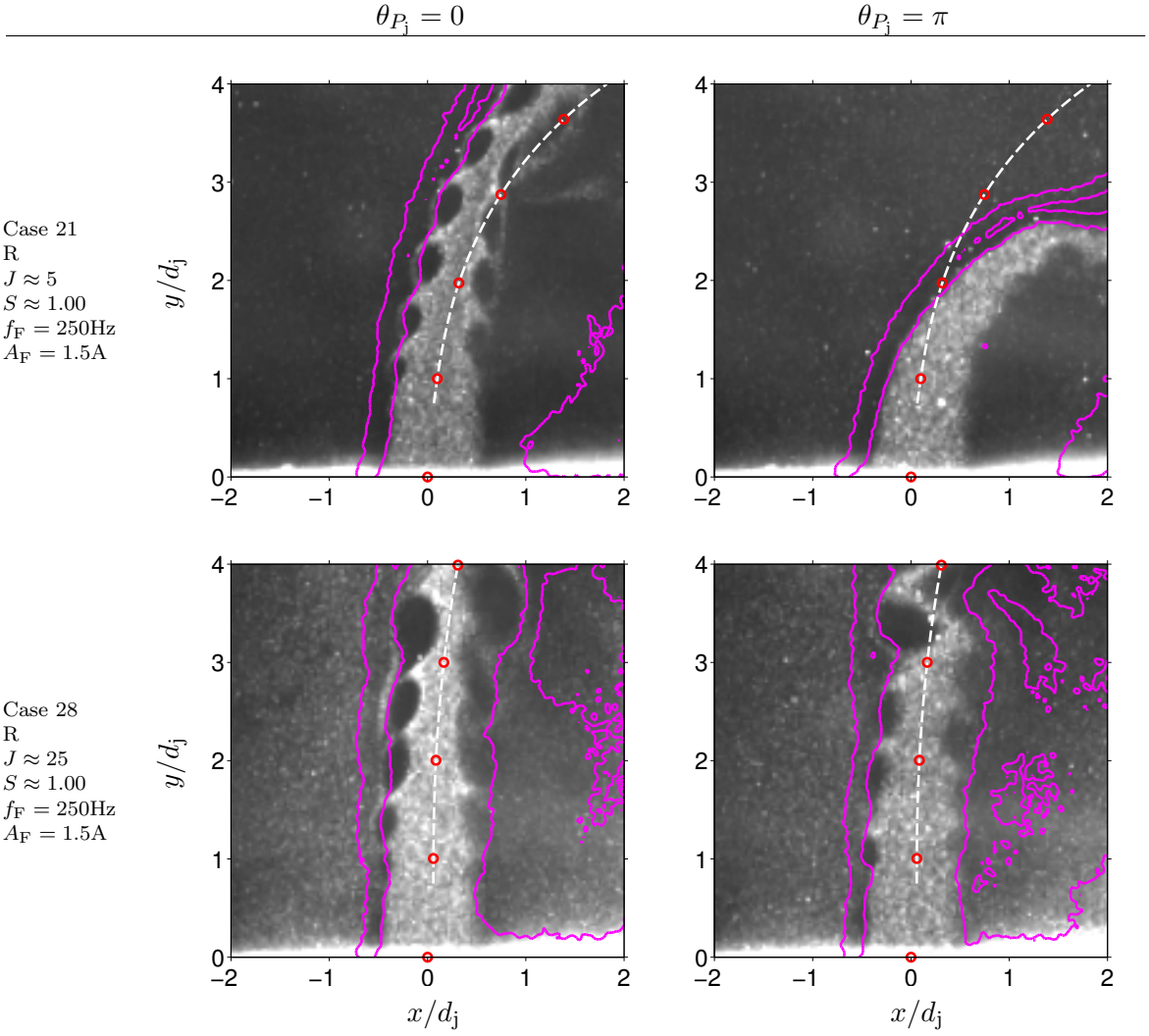

Figure 5.12: Mie scattering flow visualization of shear layer vortices in low and high J jets at different points during the acoustic pressure cycle. Forcing frequency, $f_{\mathrm{F}} = 250\mathrm{Hz}$, and forcing amplitude, $A_{\mathrm{F}} = 1.5\mathrm{A}$, held constant in all cases. (—): 10% and 50% OH PLIF contour lines. (▬ ▬): Mean jet center streamline trajectory. (○): Points spaced $1d_{\mathrm{j}}$ apart along the mean jet center streamline.

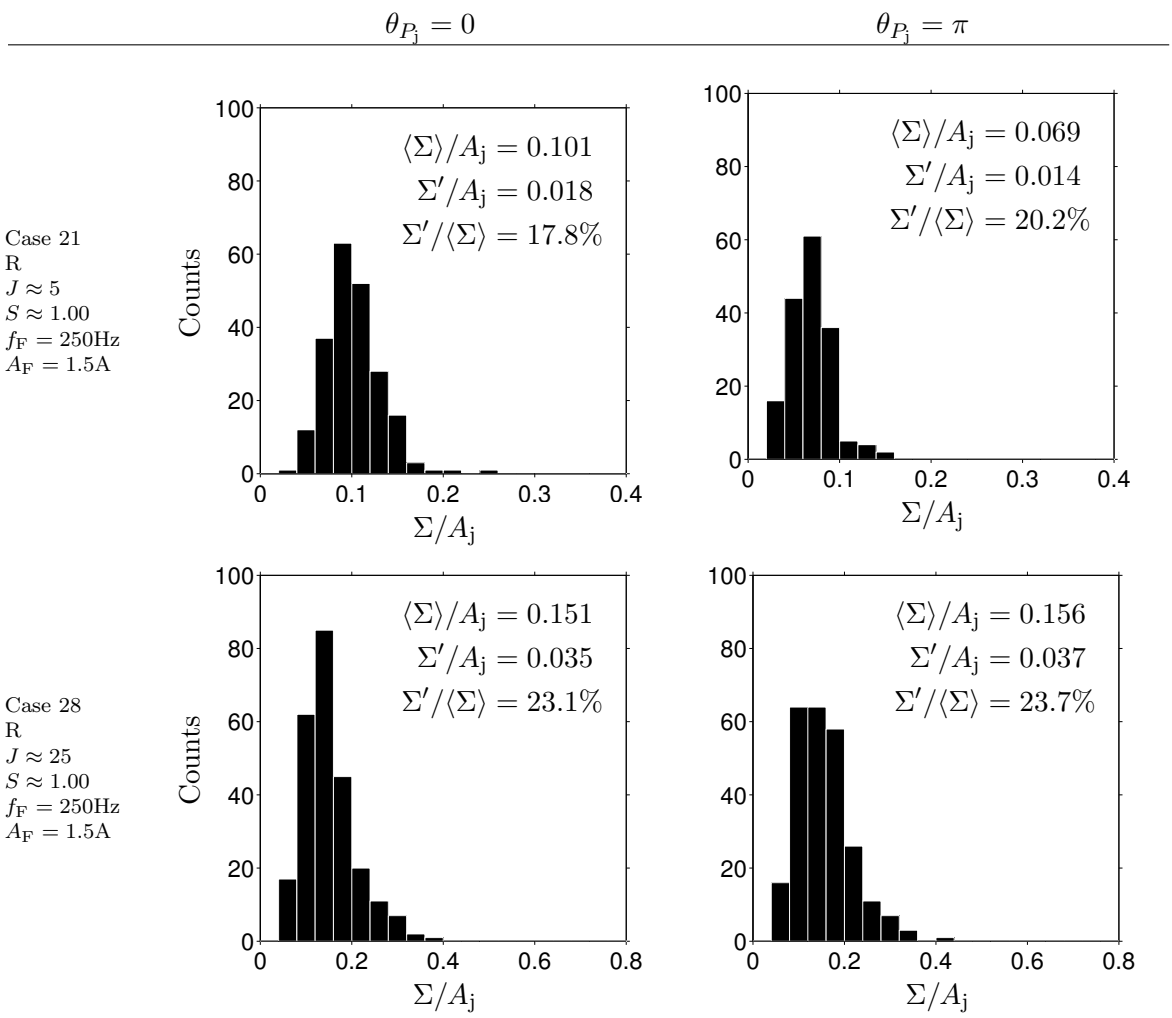

Figure 5.13: Histograms of shear layer vortex size, Σ/A_j, at different points during an acoustic pressure cycle. Σ measured at $s/d_j = 2 \pm 0.25$ for 250 randomly selected samples in each case. Forcing frequency and excitation amplitude fixed at $f_F = 250$Hz and $A_F = 1.5$A, respectively, in all cases. Note that different x-axis scaling has been used for Case 21 and Case 28.

Table 5.3: Size of shear layer vortices in forced cases with different J and S at different points in the acoustic pressure cycle measured in the jet injector. For both cases, forcing frequency and excitation amplitude are fixed at $f_{\mathrm{F}} = 250\mathrm{Hz}$ and $A_{\mathrm{F}} = 1.5\mathrm{A}$, respectively.

Case	$\theta_{P_{\mathrm{j}}}$(rad)	R/NR	J	S	Re_{j}	$\langle\Sigma\rangle/A_{\mathrm{j}}$	Σ'/A_{j}	$(x/d_{\mathrm{j}}, y/d_{\mathrm{j}})_{\Sigma}$	No SLV (%)
21	0	R	4.63	0.98	2550	0.101	0.018	(0.15,2.19)	6.40
21	π	R	4.63	0.98	2550	0.069	0.014	(0.20,2.14)	27.20
28	0	R	24.44	0.99	5760	0.151	0.035	(-0.33,2.05)	0.00
28	π	R	24.44	0.99	5760	0.156	0.037	(-0.33,2.05)	0.00

5.5 Summary of Key Findings

This chapter focused on the important influence of density stratification on the shear layer dynamics of reacting JICF. Comparing SPIV measurements of the centerline velocity magnitude and the centerline RMS velocity indicates that momentum and scalar transport in the JICF near-field are significantly altered for jets with different mixture composition and jets with/without combustion heat release. The results show that centerline velocity decay in non-reacting, iso-density jets more closely resembles the behavior of reacting, low S jets than that of reacting, iso-density jets. This counter-intuitive result suggests that the S parameter is not sufficient to characterize the behavior of reacting JICF. Furthermore, the fact that the observed differences in centerline velocity decay were largely confined to the jet near-field highlights the need to understand density stratification effects on the shear layer vortices in reacting JICF.

Subsequent analysis of simultaneous Mie scattering flow visualization and OH PLIF imaging indicates that the size, structure, and evolution of shear layer vortices strongly depends on J, S, and the presence/absence of combustion. Non-reacting, iso-density jets and reacting, low S jets experience strong shear layer roll-up near the jet exit, and under those conditions, shear layer vortices tend to grow rapidly with increasing arc length distance. However, shear layer vortices in the reacting, iso-density case are significantly smaller and in certain instances shear layer roll-up does not occur at all in reacting, low J, iso-density jets.

A vortex tracking procedure is used to determine the distribution of shear layer vortex sizes in jets with different J and S. The results show the mean shear layer vortex size is larger in high J cases than in low J cases when mixture composition is fixed, although

variability in the shear layer vortex size is also increased in high J jets. Mean shear layer vortex sizes in reacting, low S jets and non-reacting, iso-density jets are significantly larger than those measured under reacting, iso-density conditions.

Shear layer stability concepts are used to interpret the observed differences in shear layer growth rates for cases with different mixture composition and cases with/without combustion. The presence of an attached flame in the windward shear layer is shown to substantially alter the density stratification in reacting JICF. A simple phenomenological model is proposed to explain why shear layer roll-up is suppressed in the reacting, iso-density cases. The ratio of the jet fluid density relative to the reaction zone density is identified as an important parameter affecting the stability of the shear layer, at least when $\delta_{\mathrm{f}} = \mathcal{O}(d_{\mathrm{j}})$.

Lastly, the effect of crossflow forcing on the shear layer dynamics is investigated. Based on a timescale separation argument between the relatively slow acoustic period and the high frequency shear layer dynamics, the effect of the crossflow forcing on the shear layer roll-up is interpreted from a quasi-steady perspective. Vortex tracking results show that the modified velocity field in the forced cases leads to reduced shear layer growth rates. Furthermore, the shear layer growth rate is related to the phase of the acoustic pressure cycle because the quasi-steady velocity gradient can change substantially over the course of an acoustic period. This effect is minimal in high J jets, which do not experience significant injector-coupling, but can be very significant in low J cases with much stronger jet flapping.

CHAPTER VI

CONCLUSIONS AND RECOMMENDATIONS

The application of the jet in crossflow for secondary fuel injection in staged-fuel combustion systems motivated this work. The high-temperature, vitiated air crossflow in these systems is inherently unsteady and characterized by coherent acoustic fluctuations. The primary objective of this study was to understand the effect of near-field heat release and crossflow acoustics on JICF dynamics. For this purpose, the flow structure and flame stabilization of unforced and forced JICF with different J and S were experimentally characterized using simultaneous time-resolved SPIV measurements, OH PLIF reaction zone imaging, and dynamic pressure measurements. This chapter summarizes the key contributions of this work, draws conclusions about the role of crossflow acoustics on JICF dynamics, and provides recommendations for future work.

6.1 Summary of Findings

The first major contribution of this study is a detailed characterization of the flow structure and flame stabilization of unforced jets injected into high temperature, vitiated air crossflow. Results presented in this thesis demonstrated that, contrary to the behavior of reacting jets stabilized in low-to-moderate temperature air crossflow, vitiated crossflows tend to support attached flames anchored at the exit of the jet injector. These attached flames result in significant near-field heat release, which produces large volumetric dilatation, local flow acceleration, and modification of the local mixture fraction field due to entrainment of combustion products.

Furthermore, the effect of near-field heat release on JICF dynamics depends on both J and S. Low J jets ($J \approx 5$) are characterized by attached flames that wrap around the periphery of the jet. OH PLIF results indicate that the windward side of the jet is characterized by a thin, non-premixed flame located between the stagnating crossflow and the windward shear layer. On the other hand, the leeward side of the jet is characterized

by a broad, diffuse reaction zone that is located further downstream from the jet centerline and well outside the leeward shear layer. In addition to differences in the scalar dissipation rate on the windward and leeward sides of the jet, the entrainment of combustion products generated by the windward flame front into the leeward recirculation zone of low J jets plays an important role in determining the structure of the leeward reaction zone. Comparing non-reacting and reacting low J jets shows that the presence of the leeward reaction zone delays velocity recovery in the wake region of low J jets.

High J jets (e.g., $J \approx 25$) experience larger near-field strain rates, which lead to intermittent liftoff of the windward flame branch for the test conditions investigated in this work. The leeward reaction zone remained, however, anchored at the base of the jet near the jet injector lip at all times. The structure of the windward flame front in the high J cases resembles the thin, non-premixed flame seen previously in the low J jets, but the flame front is significantly wrinkled and distorted by the shear layer vortices. Pockets of local extinction also occur in small regions along the windward shear layer and, on average, these regions of local extinction persist much longer than the characteristic timescale of the shear layer vortices. Both autoignition and edge flame propagation appear to be important in the re-ignition process. As seen in the low J jets, the leeward reaction zone in the high J jets is noticeably thickened in comparison to the windward reaction zone. However, unlike the low J jets, the leeward reaction zone closely follows the contour of the leeward shear layer. This difference is attributed to the fact that high J jets separate from the lower wall of the test section, thus reducing the probability that combustion products will be trapped in the wake of the jet and allowing more oxidizer from the crossflow to mix with the fuel-rich jet fluid.

Combustion increases the penetration of both low and high J jets. Conventional Rd_{j} scaling methods are not able to fully-collapse measured jet trajectories in non-reacting and reacting cases. The increased penetration of reacting jets is attributed to two effects: (i) the effect of combustion heat release on the aerodynamic blockage of the crossflow due to the presence of the jet and (ii) the effect of near-field flow acceleration as a result of combustion-induced dilatation. An extension of the scaling law developed by Muppidi & Mahesh [30] is

proposed to account for the effect of combustion on jet penetration. Significantly improved trajectory collapse is achieved by applying the modifed scaling law to the present results. The modified scaling law suggests that the effect of near-field heat release on jet trajectory is most important in jets where $\delta_f/d_j \sim \mathcal{O}(1)$.

The second major contribution of this study is a description of the jet response to low frequency crossflow forcing. Results obtained from simultaneous time-resolved SPIV measurements and OH PLIF reaction zone imaging showed that relatively low amplitude crossflow acoustic forcing can dramatically alter the time-averaged and instantaneous behavior of JICF. Low frequency crossflow acoustics provide both asymmetric and axisymmetric excitation of JICF. The fluctuating crossflow velocity, u'_∞, induces a bulk, asymmetric (transverse) velocity response. On the other hand, the fluctuating crossflow pressure, p'_∞, induces a time-varying pressure drop across the jet injector, which leads to a fluctuating jet exit velocity, u'_j, that axisymmetrically excites the jet. This axisymmetric excitation of the jet is referred to as injector-coupling to emphasize the similarity with behavior previously observed in liquid rocket instability research.

The relative importance of the asymmetric versus axisymmetric excitation depends on the magnitude of u'_∞/U_∞ and u'_j/U_j, which, in turn, depend on the acoustic mode shape and such JICF parameters as J, S, and Ma_j. Low J jets are characterized by much larger u'_j and smaller U_j, which results in large values of u'_j/U_j. Thus, the injector-coupled response mechanism tends to dominant low J jets, as evidenced by the significant periodic jet flapping observed in low J jets. This periodic jet flapping significantly alters the mean and RMS velocity fields, reduces the extent of the time-averaged jet core, and causes the mean centerline velocity to decay more rapidly than in corresponding unforced jets.

The amplitude of the jet flapping in low J jets scales with u'_j/U_j. This explains why iso-density jets flap with larger amplitudes than low S jets exposed to identical crossflow acoustics. The jet flapping amplitude, measured as the distance of the instantaneous jet center streamline from the mean jet center streamline, initially increases with increasing arc length distance, s, but eventually saturates further downstream. The arc length distance at which saturation occurs depends on the frequency of excitation. The flapping amplitude

saturates closer to the jet exit in jets forced at higher frequencies.

Jet flapping is much less pronounced in high J jets compared to low J jets because identical crossflow forcing results in much lower values of $u'_{\mathrm{j}}/U_{\mathrm{j}}$ in the high J cases. Larger values of U_{j} in high J jets increase the resistive part of the jet injector impedance, which reduces injector-coupling and leads to much smaller $u'_{\mathrm{j}}/U_{\mathrm{j}}$. On the other hand, the magnitude of u'_{∞}/U_{∞} is essentially unchanged in high J jets and thus is relatively more important in high J jets than in low J jets. While crossflow forcing only moderately affects the time-averaged velocity field in high J jets, crossflow forcing significantly increases the probability of windward flame attachment in high J jets and reduces the probability of local extinction occurring further downstream.

While the acoustic forcing conditions in the present experiments were designed to simulate the acoustic environment inside a staged-fuel combustor, it is important to note that the forced response mechanisms reported in this thesis could also be important in other JICF applications involving acoustically perturbed crossflows. JICF injectors designed for low pressure drop, such as those utilized in premixing zones of lean premixed gas turbines and in the film cooling of combustor liners, are particularly susceptible to strong injector-coupled response. Hence, future experimental and computational studies on reacting JICF should carefully consider and characterize crossflow acoustics before drawing conclusions based on those results. Fortunately, linear acoustic modeling, as described in Section 4.6, can effectively predict the magnitude of $u'_{\mathrm{j}}/U_{\mathrm{j}}$ in different JICF configurations.

The third major contribution of this work is the identification of near-field heat release as an important factor affecting the shear layer stability of reacting JICF. This thesis presented time-averaged results that demonstrated the significant and counter-intuitive effect of combustion on near-field momentum transport in density stratified, reacting JICF. Instantaneous Mie scattering flow visualization and vortex tracking suggest that the differences in momentum transport are due to combustion-induced modification of the shear layer growth rate. Shear layer roll-up is significantly reduced in reacting, iso-density jets compared to non-reacting, iso-density jets. On the other hand, shear layer roll-up in reacting, low S jets closely resembles that of non-reacting, iso-density jets. These findings indicate that the

effect of density stratification on the shear layer stability of reacting JICF cannot be parameterized solely based on the density ratio, S. It is suggested that the jet-to-reaction zone density ratio, $S_{\mathrm{j,ad}}$, is an important parameter in determining the shear layer growth rate of reacting JICF. Thus, the location of flame stabilization in the windward shear layer and the thickness of the reaction zone relative to the jet diameter, $\delta_{\mathrm{f}}/d_{\mathrm{j}}$, are also important parameters in determining the shear layer stability of reacting JICF.

Lastly, in addition to the contributions discussed above, this thesis provides extensive, well-characterized experimental results that can be compared with high-fidelity simulations. A detailed list of the investigated experimental test conditions is provided in Table 2.3.

6.2 Recommendations for Future Work

6.2.1 Additional Studies on Flame Stabilization Mechanisms

While this thesis has described the flame stabilization of jets injected into high-temperature (T_∞ = 1200K), vitiated air crossflow, additional research is needed to understand the significant differences noted with respect to the flame stabilization of jets injected into low-to-moderate temperature air crossflows. In particular, studies that continuously varied the crossflow temperature, T_∞, while holding other parameters such as J, S, and Re_{j} constant would provide insight into how the flame stabilization mechanism changes as a function of Da. Such a study could be performed in the present facility, but it is important to note that the temperature of the crossflow cannot be varied in a vitiated facility without also affecting the crossflow composition (i.e., z_{st}) as well as the crossflow acoustics.

In addition to improving the understanding of flame stabilization in reacting JICF, studies that systematically varied the crossflow temperature would also be applied to investigate the validity of the modified trajectory scaling law proposed in Chapter 3. Recall that the physical reasoning behind the modified trajectory scaling law for reacting jets assumes that the flame remains attached to the jet injector. This assumption is important because *near-field* combustion heat release is responsible for increasing the aerodynamic blockage of the crossflow due to the presence of the jet and for locally accelerating the jet fluid. Based on that reasoning, it is reasonable to expect that the penetration of reacting jets becomes

similar to the penetration of non-reacting jets once the crossflow temperature drops to sufficiently low levels that cause the flame to significantly detach from the jet injector. At that point, the non-reacting form of the modified trajectory scaling law may be a better indicator of the reacting jet trajectory. Additional research is needed, however, to understand if and when this transition occurs.

This study raises interesting and important questions about the role of autoignition in the flame stabilization of reacting JICF. Although lifted windward flames are generally observed when the homogeneous autoignition delay time becomes comparable to the characteristic fluid mechanical timescale of the jet, it is not clear that autoignition processes are actually responsible for flame stabilization. For instance, the OH PLIF results in the present study indicate that a thin, non-premixed flame is anchored in the windward shear layer. PLIF studies targeting radical species that are important in autoignition chemistry would be particularly valuable. Since detection of autoignition precursors is difficult in H_2 systems, CH_4 may be a more practical fuel choice for these studies. Alternatively, direct numerical simulations with detailed H_2 chemistry are feasible for the jet and crossflow Reynolds numbers considered in this study and would also be very valuable for investigating the role of autoignition. In particular, DNS results can reveal information about the mixture fraction field and the scalar dissipation rate that are critical to understanding flame stabilization processes but are difficult to measure.

6.2.2 Additional Forced Response Studies

The present work identified periodic jet flapping as the primary response mechanism for a jet exposed to low frequency crossflow forcing. This finding is largely due to the fact that u'_j/U_j was generally much larger than u'_∞/U_∞. Additional experiments should be performed, however, to determine whether the response mechanism changes when u'_∞/U_∞ is large relative to u'_j/U_j. This situation would occur, for example, if the jet injector was located at a pressure node. Hence, studies that systematically varied the position of the jet injector relative to the acoustic pressure/velocity mode shape would provide additional insight into JICF response mechanisms.

The role of the jet injector impedance in the forced response of JICF should also be investigated further. Recall that the amplitude of the jet flapping in the present study scaled with the magnitude of $u'_{\mathrm{j}}/U_{\mathrm{j}}$, which depended on the jet injector impedance and the amplitude of the fluctuating crossflow pressure at the exit of the jet. Additional experiments should be performed to verify that changes to the jet injector impedance have the predicted effect on jet flapping amplitude. For example, a straight tube injector with the same overall length as the contoured nozzle assembly used in present work should have a much larger injector impedance and, thus, should significantly reduce jet flapping. Such conclusions should be experimentally verified while holding all other important JICF parameters fixed. A particularly attractive means to vary the jet injector impedance "on-the-fly" during experiments would be to use a fuel system tuner similar to the one described by Scarborough [91].

Since the present work only investigated the forced response along the jet centerplane, additional studies are needed to fully characterize the jet response. Time-resolved SPIV and OH PLIF measurements in the $y-z$ plane would be particularly useful to understand the effect of crossflow forcing on the counter-rotating vortex pair, which is an important structure that strongly affects mixing in the far-field. $x-z$ plane measurements at small y/d_{j} values would elucidate the effect of crossflow forcing on the wake vortices, which shed asymmetrically on the leeward side of the jet. Furthermore, OH PLIF measurements in the $x-z$ plane would provide useful information about how the reaction zone varies around the periphery of the jet in the near-field.

6.2.3 Hydrodynamic Stability Analysis of Reacting JICF

The results presented in this thesis indicate that near-field heat release can significantly alter the hydrodynamic stability of reacting JICF. A focused study of the shear layer stability of reacting JICF is needed, however, to better understand the underlying physics. Since the temperature of the crossflow is a critical parameter affecting the location of flame stabilization, it is imperative that future stability studies investigate high temperature crossflows. However, the complexity of the reacting JICF presents a number of challenges for

experimental and theoretical stability studies.

Experimental approaches are hampered primarily by a shortage of diagnostic tools with sufficient spectral bandwidth that can be used in high temperature flows. While non-reacting stability studies have historically relied on hot-wire measurements, this author is not aware of any diagnostic tool for reacting flows that approaches the accuracy and spectral bandwidth of a hot-wire. New approaches are needed to alleviate this problem. Although the capability of high-speed cameras and lasers is remarkable and steadily improving, there is much work to do before time-resolved SPIV can be used to directly study the shear layer stability of a reacting JICF. Notably, seeding particles that can withstand high temperatures are dense and thus have difficulty tracking very high frequency (i.e., $\mathcal{O}(50\text{kHz})$) dynamics. Although shrinking the diameter of the seed particles is possible, a better approach may be to increase the size of the jet and thereby reduce the fundamental mode frequency of the shear layer. It is important to remember, however, that increasing the jet diameter will increase jet penetration as well as Re_{j}.

Alternatively, theoretical studies on the stability of reacting JICF could explain why and how near-field heat release affects the shear layer stability. A major difficulty with this approach is prescribing a base flow for the complex, three-dimensional JICF. Recent global stability analyses, such as the work by Schlatter et al. [44], have, however, overcome this difficulty for non-reacting JICF. Although adding heat release will significantly increase the computational cost, it may be possible to learn a great deal about the shear layer stability in the reacting JICF by using a reduced-order combustion model in conjunction with a numerical global stability code. Additionally, parallel stability studies on axial jets with attached flames should be performed to gain insight about how near-field heat release and density stratification affect jet shear layers.

APPENDIX A

FLOW MEASUREMENT UNCERTAINTY

This appendix presents an error analysis of the flow measurements used in the operation of the reacting JICF facility. The first section describes the uncertainty associated with the sub-critical orifice assemblies used to meter the primary air, primary fuel, and secondary air. This is followed by an analysis of the uncertainty in the critical orifice assemblies used to meter the three jet gases. Finally, the uncertainties in key JICF parameters such as J and S are derived and tabulated.

A.1 Sub-critical Orifice Meter Assemblies

The mass flow rate measured by a subcritical orifice assembly can be expressed as

$$\dot{m}_{\mathrm{sub-critical}} = A_2 \cdot C_D \cdot Fa \cdot Y1 \cdot \left(\frac{2P(\Delta P)MW}{\bar{R}T(1-\beta^4)} \right)^{1/2} \tag{A.1}$$

where A_2 is the area of the orifice restriction, C_D is the discharge coefficient, Fa is the thermal expansion factor, $Y1$ is the compressibility factor, P is the upstream static pressure, $\Delta P = P_1 - P_2$ is the differential pressure, $\bar{R}$ is the universal gas constant, MW is the molecular weight of the flowing gas, and $\beta = d_2/d_1$ is the ratio of the orifice diameter to the pipe bore diameter.

The measured quantities in Equation (A.1) are P, ΔP, and T. C_D is a tabulated value but is assumed to have a bias error of $\pm 1\%$ in order to account for uncertainty in the orifice/ pipe diameter and the inherent uncertainty associated with approximating the flow through a sharp-edged orifice. The coefficients Fa and $Y1$ are very nearly 1 and contribute negligible uncertainty to the measurement. The uncertainty in MW is also neglected. Following the ASME measurement uncertainty guidelines outlined by Abernethy et al. [100], the total uncertainty in $\dot{m}_{\mathrm{sub-critical}}$ can be expressed as

$$\dot{m}_{\mathrm{sub-critical}} = f(P, \Delta P, T, C_D). \tag{A.2}$$

Partial derivatives of Equation (A.1) are used to determine the sensitivity factors corresponding to the independent variables in Expression (A.2). The sensitivity factors are as follows:

$$\Theta_P = \frac{\partial \dot{m}_{\text{sub-critical}}}{\partial P} = A_2 \cdot C_D \cdot Fa \cdot Y1 \cdot \left(\frac{P^{-1/2}}{2}\right) \cdot \left(\frac{2(\Delta P)MW}{\bar{R}T(1-\beta^4)}\right)^{1/2}$$

$$\Theta_{\Delta P} = \frac{\partial \dot{m}_{\text{sub-critical}}}{\partial \Delta P} = A_2 \cdot C_D \cdot Fa \cdot Y1 \cdot \left(\frac{(\Delta P)^{-1/2}}{2}\right) \cdot \left(\frac{2PMW}{\bar{R}T(1-\beta^4)}\right)^{1/2}$$

$$\Theta_T = \frac{\partial \dot{m}_{\text{sub-critical}}}{\partial T} = A_2 \cdot C_D \cdot Fa \cdot Y1 \cdot \left(\frac{-T^{-3/2}}{2}\right) \cdot \left(\frac{2P(\Delta P)MW}{\bar{R}(1-\beta^4)}\right)^{1/2}$$

$$\Theta_{C_D} = \frac{\partial \dot{m}_{\text{sub-critical}}}{\partial C_D} = A_2 \cdot Fa \cdot Y1 \cdot \left(\frac{2P(\Delta P)MW}{\bar{R}T(1-\beta^4)}\right)^{1/2}. \tag{A.3}$$

The total bias error in $\dot{m}_{\text{sub-critical}}$ is given by

$$B_{\dot{m}_{\text{sub-critical}}} = \left(\sum(\Theta_i B_i)\right)^{1/2} \tag{A.4}$$

and the total precision error is

$$S_{\dot{m}_{\text{sub-critical}}} = \left(\sum(\Theta_i S_i)\right)^{1/2} \tag{A.5}$$

where Θ_i are the sensitivities from Equation (A.3), S_i are the corresponding precision errors of the raw measurements, and B_i are the bias errors of the raw measurements. The values for S_i and B_i in the present experiments are tabulated in Table A.1. Finally, the cumulative

Table A.1: Bias and precision error in raw measurements contributing to error in mass flow rates measured using sub-critical orifice meter assemblies.

	B_i	S_i
P	$7400\,\text{N/m}^2$	$3747\,\text{N/m}^2$
ΔP	$124.6\,\text{N/m}^2$	$25.19\,\text{N/m}^2$
T	$0.0\,\text{K}$	$2.2\,\text{K}$
C_D	0.01	0.00

uncertainty in $\dot{m}_{\text{sub-critical}}$ is

$$E_{\dot{m}_{\text{sub-critical}}} = \left(B^2_{\dot{m}_{\text{sub-critical}}} + (tS_{\dot{m}_{\text{sub-critical}}})^2\right)^{1/2} \tag{A.6}$$

where t is the Student t value. In this case, the t value for 95% confidence is equal to 2 since the number of samples is much greater than 30 for all of the measurements. The total bias

error and precision error in $\dot{m}_{\text{sub-critical}}$ as a percent of the measured value are 1.74% and 0.19%, respectively. Thus, the total uncertainty in $\dot{m}_{\text{sub-critical}}$ as a percent of the measured value is 1.79%.

A.2 Critical Orifice Meter Assemblies

The mass flow rate through a critical orifice assembly can be expressed as

$$\dot{m}_{\text{critical}} = \frac{P_0 C_D A_0}{(RT_0)^{1/2}} F(\gamma, Ma) \tag{A.7}$$

where P_0 is the stagnation pressure, T_0 is the stagnation temperature, A_0 is the area of the critical orifice, $R = \bar{R}/MW$ is the gas constant, C_D is a discharge coefficient, and F is given by

$$F(\gamma, Ma) = \sqrt{\gamma} Ma \left(1 + \frac{\gamma - 1}{2} Ma^2\right)^{-\frac{\gamma+1}{2(\gamma-1)}} \tag{A.8}$$

where γ is the ratio of specific heats and Ma is the Mach number at the throat. Critical orifice meters require sonic flow at the throat such that $Ma = 1$ and $F = F(\gamma, 1)$. The only measured quantities in Equation (A.7) are P_0 and T_0, but the uncertainty due to C_D is also considered here. The supply plenum upstream of the critical orifice is assumed to be large and nearly stagnant such that P_0 and T_0 are equivalent to the static pressure and temperature. Following the procedure used previously for the sub-critical orifice assemblies, the sensitivity factors for $\dot{m}_{\text{critical}}$ are

$$\begin{aligned}
\Theta_{P_0} &= \frac{\partial \dot{m}_{\text{critical}}}{\partial P_0} = \frac{C_D A_0}{(RT_0)^{1/2}} F(\gamma, Ma) \\
\Theta_{T_0} &= \frac{\partial \dot{m}_{\text{critical}}}{\partial T_0} = \frac{P_0 C_D A_0}{R^{1/2}} \left(\frac{-T_0^{-3/2}}{2}\right) F(\gamma, Ma) \\
\Theta_{C_D} &= \frac{\partial \dot{m}_{\text{critical}}}{\partial C_D} = \frac{P_0 A_0}{(RT_0)^{1/2}} F(\gamma, Ma).
\end{aligned} \tag{A.9}$$

The bias and precision error in the measurement of $\dot{m}_{\text{critical}}$ are estimated using Equations (A.4) and (A.5), respectively. The requisite bias and precision errors of the sensors used in the critical orifice meters are tabulated in Table A.2. Substituting the raw measurement uncertainty values from Table A.2 into Equations (A.4) and (A.5) gives bias and precision error in the critical mass flow meters as a percent of the measured value equal to 1.32% and

Table A.2: Bias and precision error in raw measurements contributing to error in mass flow rates metered using critical orifice meter assemblies.

	B_i	S_i
P_0	$3953\,\mathrm{N/m^2}$	$2000\,\mathrm{N/m^2}$
T_0	$0.0\,\mathrm{K}$	$2.2\,\mathrm{K}$
C_D	0.01	0.00

0.51%, respectively. The cumulative uncertainty in $\dot{m}_{\mathrm{critical}}$ for a 95% confidence interval is thus 1.67%, again taking $t = 2$ based on the large sample size.

A.3 Uncertainty in Key JICF Parameters

The uncertainties associated with $\dot{m}_{\mathrm{sub-critical}}$ and $\dot{m}_{\mathrm{critical}}$ propagate uncertainty into key JICF parameters that are based either directly or indirectly on the measurement of mass flow rate in the jet and/or crossflow. The crossflow is most strongly influenced by uncertainty in the vitiator air and vitiator fuel flow rate, which directly affects the vitiator equivalence ratio and ultimately T_∞, ρ_∞, U_∞, S , and J . Uncertainty in the mass flow rates of the constituent gases in the jet gas mixture leads to uncertainty in parameters such as ρ_j, U_j, S and J .

In the interest of brevity, all the steps required to analyze the uncertainty of the many JICF parameters of interest are not shown here. Instead, a brief summary of the process is given and the final results, which were computed using a Matlab script, are tabulated in Table A.3. The uncertainty analysis of each of the JICF parameters proceeds using the same Taylor series expansion approach used to analyze the error in $\dot{m}_{\mathrm{sub-critical}}$ and $\dot{m}_{\mathrm{critical}}$. The order of the analysis starts with the most basic JICF parameters and then uses the computed uncertainty for those basic parameters to analyze the uncertainty of the more complex JICF parameters. For example, the uncertainties for S , U_j, and U_∞ are each computed before the uncertainty in $J = SU_\mathrm{j}^2/U_\infty^2$ can be determined. All of the constituent uncertainties can ultimately be related to a combination of mass flow rates measured by either sub-critical or critical orifice assemblies, whose error is known based on the analysis in Sections A.1 and A.2.

A few additional comments are needed to explain the assumptions underlying the tabulated uncertainties in Table A.3. In particular, the uncertainty in T_∞ requires a slight modification of the usual uncertainty analysis. Note that T_∞ depends on the adiabatic flame temperature of vitiator, which is primarily a function of the vitiator equivalence ratio, ϕ.The uncertainty in ϕ can be determined using the usual Taylor series approach but an analytical expression for the adiabatic flame temperature as a function of ϕ cannot be easily formed and thus the sensitivity of T_∞ with respect to the uncertainty in ϕ cannot be directly evaluated. To circumvent this problem, the present calculations used a custom Matlab/Chemkin routine, similar to the one used to select test conditions, to evaluate the

Table A.3: Estimated uncertainty in calculated JICF parameters for 95% confidence intervals. All errors given as a percent of the nominal value. Error estimates computed at test conditions corresponding to Cases 1-8 in Table 2.3.

	Bias Error(%)	Precision Error (%)	Total Uncertainty (%)
$\dot{m}_\mathrm{j}$	0.87	0.34	1.10
$\dot{m}_\infty$	1.42	0.15	1.45
ρ_j	1.32	0.90	2.24
ρ_∞	1.58	0.22	1.63
T_j	0.67	0.74	1.62
T_∞	1.58	0.22	1.63
U_j	2.26	0.97	2.97
U_∞	3.28	0.26	3.32
ϕ	2.48	0.26	2.53
Re_j	2.74	1.32	3.80
Re_∞	6.24	0.77	6.43
S	2.06	0.93	2.77
J	8.23	2.21	9.34

uncertainty in T_∞ based on the computed bias and precision error in ϕ. The resulting bias and precision error in T_∞ as a function of ϕ were 18.9K and 2.6K, respectively.

Lastly, note that the values in Table A.3 correspond to test conditions for Cases 1-8 (see Table 2.3). Although the mean crossflow condition is fixed for all the experiments reported in this thesis, the jet condition does vary for different test cases. Accordingly, the uncertainty in JICF parameters such as S and J will vary slightly for different test cases. The variance is not significant, however, and thus the values in Table A.3 provide a good estimate for the uncertainty at all the test conditions.

APPENDIX B

ACOUSTIC FORCING CONDITIONS

Table B.1: Acoustic forcing parameters for each test condition considered in the present work. Crossflow parameters measured using the two-microphone method. SPIV used to determine jet parameters.

Case	R/NR	J	S	f_{F} [Hz]	A_{F} [A]	p'_{∞} [Pa]	u'_{∞} [m/s]	u'_{j} [m/s]	u'_{∞}/U_{∞}	$u'_{\mathrm{j}}/U_{\mathrm{j}}$
1	R	5.05	0.41	n/a	n/a	n/a	n/a	n/a	n/a	n/a
2	R	4.72	0.40	177	0.6	55.5	0.22	2.21	0.0114	0.0329
3	R	4.69	0.40	177	1.2	91.5	0.50	5.02	0.0258	0.0751
4	R	4.84	0.41	177	1.5	180.3	0.77	6.00	0.0399	0.0903
5	R	4.83	0.41	250	0.9	95.0	0.12	5.21	0.0062	0.0780
6	R	4.78	0.40	250	1.5	123.5	0.17	7.58	0.0088	0.1127
7	R	4.60	0.39	340	0.6	10.45	0.12	4.05	0.0061	0.0601
8	R	4.67	0.40	340	1.5	169.5	0.04	8.67	0.0021	0.1296
9	R	23.23	0.40	n/a	n/a	n/a	n/a	n/a	n/a	n/a
10	R	22.40	0.40	177	0.6	87.0	0.38	3.10	0.0191	0.0209
11	R	25.19	0.42	177	1.2	138.0	0.59	4.49	0.0308	0.0302
12	R	23.59	0.41	177	1.5	175.9	0.78	4.69	0.0402	0.0317
13	R	23.75	0.40	250	0.9	76.8	0.13	3.11	0.0068	0.0209
14	R	23.89	0.40	250	1.5	122.0	0.22	4.37	0.0113	0.0292
15	R	23.38	0.40	340	0.6	66.6	0.03	2.88	0.0018	0.0193
16	R	23.67	0.40	340	1.5	167.7	0.08	4.75	0.0043	0.0318
17	R	5.08	1.04	n/a	n/a	n/a	n/a	n/a	n/a	n/a
18	n/a	n/a	n/a	n/a	n/a	n/a	n/a	n/a	n/a	n/a
19	R	4.64	0.97	177	1.5	198.8	0.66	8.42	0.0338	0.1951
20	R	4.68	1.00	250	0.9	58.4	0.07	5.32	0.0036	0.1257
21	R	4.63	0.98	250	1.5	135.0	0.18	7.86	0.0090	0.1847
22	n/a	n/a	n/a	n/a	n/a	n/a	n/a	n/a	n/a	n/a
23	R	4.97	1.02	340	1.5	149.5	0.20	10.55	0.0105	0.2493
24	R	25.32	1.04	n/a	n/a	n/a	n/a	n/a	n/a	n/a
25	n/a	n/a	n/a	n/a	n/a	n/a	n/a	n/a	n/a	n/a
26	R	23.49	1.01	177	1.5	103.3	0.41	3.38	0.0212	0.0359
27	R	23.77	1.02	250	0.9	71.4	0.07	3.07	0.0037	0.0327
28	R	24.44	0.99	250	1.5	117.7	0.15	4.62	0.0077	0.0484
29	n/a	n/a	n/a	n/a	n/a	n/a	n/a	n/a	n/a	n/a
30	R	23.38	1.00	340	1.5	146.6	0.19	5.23	0.0099	0.0550
31	R	4.74	1.00	n/a	n/a	n/a	n/a	n/a	n/a	n/a
32	n/a	n/a	n/a	n/a	n/a	n/a	n/a	n/a	n/a	n/a
33	n/a	n/a	n/a	n/a	n/a	n/a	n/a	n/a	n/a	n/a
34	NR	5.02	1.03	250	0.9	72.4	0.02	3.60	0.0012	0.0848
35	NR	4.82	1.00	250	1.5	127.9	0.11	6.82	0.0058	0.1592
36	n/a	n/a	n/a	n/a	n/a	n/a	n/a	n/a	n/a	n/a
37	n/a	n/a	n/a	n/a	n/a	n/a	n/a	n/a	n/a	n/a
38	NR	25.14	1.03	n/a	n/a	n/a	n/a	n/a	n/a	n/a
39	n/a	n/a	n/a	n/a	n/a	n/a	n/a	n/a	n/a	n/a
40	n/a	n/a	n/a	n/a	n/a	n/a	n/a	n/a	n/a	n/a
41	NR	23.08	0.98	250	0.9	71.6	0.05	3.06	0.0027	0.0322
42	NR	24.24	1.02	250	1.5	132.4	0.07	4.27	0.0036	0.0449
43	n/a	n/a	n/a	n/a	n/a	n/a	n/a	n/a	n/a	n/a
44	n/a	n/a	n/a	n/a	n/a	n/a	n/a	n/a	n/a	n/a

REFERENCES

[1] Fric, T. F. & Roshko, A., 1994 Vortical structure in the wake of a transverse jet. *Journal of Fluid Mechanics* **279**, 1–47.

[2] Schlüter, J. U. & Schönfeld, T., 2000 LES of jets in cross flow and its application to a gas turbine burner. *Flow, Turbulence and Combustion* **65**, 177–203.

[3] Moin, P. & Apte, S., 2006 Large-eddy simulation of realistic gas turbine combustors. *AIAA Journal* **44** (4), 698–708.

[4] Güthe, F., Hellat, J. & Flohr, P., 2009 The reheat concept: the proven pathway to ultralow emissions and high efficiency and flexibility. *Journal of Engineering for Gas Turbines and Power* **131** (2), 21503.

[5] Galeazzo, F. C. C., Prathap, C., Kern, M., Habisreuther, P., Zarzalis, N., Beck, C., Krebs, W. & Wegner, B., 2012 Investigation of a flame anchored in crossflow stream of vitiated air at elevated pressures. In *Proceedings of ASME Turbo Expo 2012*. ASME, Copenhagen, Denmark, 9.

[6] Kelso, R., Lim, T. & Perry, A., 1996 An experimental study of round jets in cross-flow. *Journal of Fluid Mechanics* **306**, 111–144.

[7] Megerian, S., Davitian, J., de B. Alves, L. S. & Karagozian, A. R., 2007 Transverse-jet shear-layer instabilities. part 1. experimental studies. *Journal of Fluid Mechanics* **593**, 93–129.

[8] Davitian, J., Getsinger, D., Hendrickson, C. & Karagozian, A., 2010 Transition to global instability in transverse-jet shear layers. *Journal of Fluid Mechanics* **661**, 294–315.

[9] Getsinger, D. R., Hendrickson, C. & Karagozian, A. R., 2012 Shear layer instabilities in low-density transverse jets. *Experiments in fluids* **53** (3), 783–801.

[10] Muppidi, S. & Mahesh, K., 2008 Direct numerical simulation of passive scalar transport in transverse jets. *Journal of Fluid Mechanics* **598**, 335–360.

[11] Karagozian, A. R., 2010 Transverse jets and their control. *Progress in Energy and Combustion Science* **36**, 531–553.

[12] Mahesh, K., 2013 The interaction of jets with crossflow. *Annual Review of Fluid Mechanics* **45** (1), 379–407.

[13] Prathap, C., Galeazzo, F. C. C., Kasabov, P., Habisreuther, P., Zarzalis, N., Beck, C., Krebs, W. & Wegner, B., 2012 Analysis of NOX formation in an axially staged combustion system at elevated pressure conditions. *Journal of Engineering for Gas Turbines and Power* **134** (3), 031507–031507.

[14] Ivanova, E. M., Noll, B. E., Griebel, P., Aigner, M. & Syed, K., 2012 Numerical simulations of turbulent mixing and autoignition of hydrogen fuel at reheat combustor operating conditions. *Journal of Engineering for Gas Turbines and Power* **134** (4), 041504.

[15] Putnam, A. A., 1971 *Combustion Driven Oscillations in Industry.* Fuel and Energy Science Series, Elsevier, New York, NY.

[16] Culick, F. E. & Yang, V., 1995 Overview of combustion instabilities in liquid-propellant rocket engines. *Liquid Rocket Engine Combustion Instability* **169**, 3–37.

[17] Lieuwen, T. C. & Yang, V., 2005 Combustion instabilities in gas turbine engines(operational experience, fundamental mechanisms and modeling). *Progress in astronautics and aeronautics* .

[18] Keller, J. ., Vaneveld, L., Korschelt, D., Hubbard, G. L., Ghoniem, A. F., Daily, J. W. & Oppenheim, A. K., 1982 Mechanism of instabilities in turbulent combustion leading to flashback. *AIAA Journal* **20** (2), 254–262.

[19] Balachandran, R., Ayoola, B. O., Kaminski, C. F., Dowling, A. P. & Mastorakos, E., 2005 Experimental investigation of the nonlinear response of turbulent premixed flames to imposed inlet velocity oscillations. *Combustion and Flame* **143** (1), 37–55.

[20] Emerson, B., O'Connor, J., Juniper, M. & Lieuwen, T., 2012 Density ratio effects on reacting bluff-body flow field characteristics. *Journal of Fluid Mechanics* **706**, 1–32.

[21] Thumuluru, S. K. & Lieuwen, T. C., 2009 Characterization of acoustically forced swirl flame dynamics. *Proceedings of the Combustion Institute* **32** (2), 2893–2900.

[22] Demare, D. & Baillot, F., 2004 Acoustic enhancement of combustion in lifted nonpremixed jet flames. *Combustion and flame* **139** (4), 312–328.

[23] Smith, S. & Mungal, M., 1998 Mixing, structure and scaling of the jet in crossflow. *Journal of Fluid Mechanics* **357**, 83–122.

[24] Kamotani, Y. & Greber, I., 1972 Experiments on a turbulent jet in a cross flow. *AIAA Journal* **10** (11), 1425–1429.

[25] Su, L. K. & Mungal, M. G., 2004 Simultaneous measurements of scalar and velocity field evolution in turbulent crossflowing jets. *Journal of Fluid Mechanics* **513**, 1–45.

[26] Pratte, S. D. & Baines, W. D., 1967 Profiles of the round turbulent jet in a cross flow. *Journal of Hydraulics Division, ASCE* **92**, 53–64.

[27] Broadwell, J. E. & Breidenthal, R. E., 1984 Structure and mixing of a transverse jet in incompressible flow. *Journal of Fluid Mechanics* **148**, 405–412.

[28] Margason, R. J., 1993 Fifty years of jet in cross flow research. In *72nd AGARD Fluid Dynamics Panel Meeting and Symposium on Computational and Experimental Assessment of Jets in Cross Flow.* Winchester, U.K., 7–34.

[29] Hasselbrink Jr., E. F. & Mungal, M. G., 2001 Transverse jets and jet flames. Part 1. Scaling laws for strong transverse jets. *Journal of Fluid Mechanics* **443**, 1–25.

[30] Muppidi, S. & Mahesh, K., 2005 Study of trajectories of jets in crossflow using direct numerical simulations. *Journal of Fluid Mechanics* **530**, 81–100.

[31] Shan, J. W. & Dimotakis, P. E., 2006 Reynolds-number effects and anisotropy in transverse-jet mixing. *Journal of Fluid Mechanics* **566**, 47–96.

[32] Kelso, R. & Smits, A., 1995 Horseshoe vortex systems resulting from the interaction between a laminar boundary layer and a transverse jet. *Physics of Fluids* **7** (1), 153–158.

[33] Andreopoulos, J., 1985 On the structure of jets in a crossflow. *Journal of Fluid Mechanics* **157**, 163–197.

[34] Sykes, R., Lewellen, W. & Parker, S., 1986 On the vorticity dynamics of a turbulent jet in a crossflow. *Journal of Fluid Mechanics* **168**, 393–413.

[35] Muppidi, S. & Mahesh, K., 2006 Two-dimensional model problem to explain counter-rotating vortex pair formation in a transverse jet. *Physics of Fluids (1994-present)* **18** (8), 085103.

[36] New, T., Lim, T. & Luo, S., 2006 Effects of jet velocity profiles on a round jet in cross-flow. *Experiments in Fluids* **40**, 859–875.

[37] Huerre, P. & Monkewitz, P., 1985 Absolute and convective instabilities in free shear layers. *Journal of Fluid Mechanics* **159**, 151–168.

[38] Huerre, P. & Monkewitz, P. A., 1990 Local and global instabilities in spatially developing flows. *Annual Review of Fluid Mechanics* **22**, 473–537.

[39] Poinsot, T. J., Trouve, A. C., Veynante, D. P., Candel, S. M. & Esposito, E. J., 1987 Vortex-driven acoustically coupled combustion instabilities. *Journal of Fluid Mechanics* **177**, 265–292.

[40] Broadwell, J. E. & Mungal, M. G., 1991 Large-scale structures and molecular mixing. *Physics of Fluids A: Fluid Dynamics (1989-1993)* **3** (5), 1193–1206.

[41] Catrakis, H. J., Aguirre, R. C., Ruiz-Plancarte, J., Thayne, R. D., McDonald, B. A. & Hearn, J. W., 2002 Large-scale dynamics in turbulent mixing and the three-dimensional space–time behaviour of outer fluid interfaces. *Journal of Fluid Mechanics* **471**, 381–408.

[42] Chandler, G. J., 2010 *Sensitivity analysis of low-density jets and flames.* Ph.D. thesis, University of Cambridge.

[43] Bagheri, S., Schlatter, P., Schmid, P. J. & Henningson, D. S., 2009 Global stability of a jet in crossflow. *Journal of Fluid Mechanics* **624**, 33–44.

[44] Schlatter, P., Bagheri, S. & Henningson, D., 2011 Self-sustained global oscillations in a jet in crossflow. *Theoretical and Computational Fluid Dynamics* **25**, 129–146.

[45] Monkewitz, P. A. & Sohn, K. D., 1988 Absolute instability in hot jets. *AIAA Journal* **26** (8), 911–916.

[46] Kyle, D. M. & Sreenivasan, K. R., 1993 The instability and breakdown of a round variable-density jet. *Journal of Fluid Mechanics* **249**, 619–664.

[47] Juniper, M. P., Li, L. K. B. & Nichols, J. W., 2009 Forcing of self-excited round jet diffusion flames. *Proceedings of the Combustion Institute* **32** (1), 1191–1198.

[48] Mahalingam, S., Cantwell, B. J. & Ferziger, J. H., 1991 Stability of low-speed reacting flows. *Physics of Fluids A: Fluid Dynamics (1989-1993)* **3** (6), 1533–1543.

[49] Lesshafft, L. & Marquet, O., 2010 Optimal velocity and density profiles for the onset of absolute instability in jets. *Journal of Fluid Mechanics* **662**, 398.

[50] Hasselbrink Jr., E. F. & Mungal, M. G., 2001 Transverse jets and jet flames. Part 2. Velocity and OH field imaging. *Journal of Fluid Mechanics* **443**, 27–68.

[51] Rehm, J. E. & Clemens, N. T., 1999 The large-scale turbulent structure of non-premixed planar jet flames. *Combustion and flame* **116** (4), 615–626.

[52] Han, D. & Mungal, M., 2003 Simultaneous measurements of velocity and CH distribution. part ii: deflected jet flames. *Combustion and Flame* **133**, 1–17.

[53] Kolla, H., Grout, R. W., Gruber, A. & Chen, J. H., 2012 Mechanisms of flame stabilization and blowout in a reacting turbulent hydrogen jet in cross-flow. *Combustion and Flame* **159** (8), 2755–2766.

[54] Grout, R., Gruber, A., Kolla, H., Bremer, P.-T., Bennett, J., Gyulassy, A. & Chen, J., 2012 A direct numerical simulation study of turbulence and flame structure in transverse jets analysed in jet-trajectory based coordinates. *Journal of Fluid Mechanics* **1** (1), 1–33.

[55] Sullivan, R., Wilde, B., Noble, D. R., Periagaram, K., Seitzman, J. M. & Lieuwen, T. C., 2012 Unsteady flame–wall interactions in a reacting jet injected into a vitiated cross-flow. *Proceedings of the Combustion Institute* .

[56] Galeazzo, F., Donnert, G., Habisreuther, P., Zarzalis, N., Valdes, R. J. & Krebs, W., 2011 Measurement and simulation of turbulent mixing in a jet in crossflow. *Journal of Engineering for Gas Turbines and Power* **133**, 1–10.

[57] Mörtberg, M., Blasiak, W. & Gupta, A. K., 2007 Experimental investigation of flow phenomena of a single fuel jet in cross-flow during highly preheated air combustion conditions. *Journal of engineering for gas turbines and power* **129** (2), 556–564.

[58] Mastorakos, E., 2009 Ignition of turbulent non-premixed flames. *Progress in Energy and Combustion Science* **35** (1), 57–97.

[59] Clemens, N. T. & Paul, P. H., 1995 Effects of heat release on the near field flow structure of hydrogen jet diffusion flames. *Combustion and Flame* **102** (3), 271–284.

[60] Gupta, A. K., 2004 Thermal characteristics of gaseous fuel flames using high temperature air. *Journal of Engineering for Gas Turbines and Power* **126** (1), 9–19.

[61] Micka, D. J. & Driscoll, J. F., 2012 Stratified jet flames in a heated (1390k) air cross-flow with autoignition. *Combustion and Flame* **159** (3), 1205–1214.

[62] Schmitt, D., Kolb, M., Weinzierl, J., Hirsch, C. & Sattlemayer, T., 2013 Ignition and flame stabilization of a premixed jet in hot cross flow. In *Proceedings of ASME Turbo Expo 2013: Turbine Technical Conference and Exposition*. San Antonio, TX, 3–7.

[63] Poinsot, T. & Veynante, D., 2005 *Theoretical and Numerical Combustion*. RT Edwards, Inc.

[64] Demayo, T. N., Leong, M. Y. & Samuelson, G. S., 2003 Assessing jet-induced spatial mixing in a rich, reacting crossflow. *Journal of Propulsion and Power* **19** (1), 14–21.

[65] Wu, J. M., Vakili, A. D. & Yu, F. M., 1988 Investigation of the interacting flow of nonsymmetric jets in crossflow. *AIAA journal* **26** (8), 940–947.

[66] Johari, H., Pacheco-Tougas, M. & Hermanson, J. C., 1999 Penetration and mixing of fully modulated turbulent jets in crossflow. *AIAA Journal* **37** (7), 842–850.

[67] Eroglu, A. & Breidenthal, R. E., 2001 Structure, penetration, and mixing of pulsed jets in crossflow. *AIAA Journal* **39** (3), 417–423.

[68] Narayanan, S., Barooah, P. & Cohen, J., 2003 Dynamics and control of an isolated jet in crossflow. *AIAA Journal* **41** (12), 2316–2330.

[69] Johari, H., 2006 Scaling of fully pulsed jets in crossflow. *AIAA Journal* **44** (11), 2719–2725.

[70] Crow, S. C. & Champagne, F. H., 1971 Orderly structure in jet turbulence. *Journal of Fluid Mechanics* **48** (03), 547–591.

[71] Ho, C.-M. & Huerre, P., 1984 Perturbed free shear layers. *Annual Review of Fluid Mechanics* **16** (1), 365–422.

[72] MCloskey, R. T., King, J. M., Cortelezzi, L. & Karagozian, A. R., 2002 The actively controlled jet in crossflow. *Journal of Fluid Mechanics* **452**, 325–335.

[73] Sau, R. & Mahesh, K., 2010 Optimization of pulsed jets in crossflow. *Journal of Fluid Mechanics* **653**, 365–390.

[74] Muldoon, F. & Acharya, S., 2010 Direct numerical simulation of pulsed jets-in-crossflow. *Computers & Fluids* **39**, 1745–1773.

[75] Marr, K., Clemens, N. & Ezekoye, O., 2012 Mixing characteristics and emissions of strongly-forced non-premixed and partially-premixed jet flames in crossflow. *Combustion and Flame* **159** (2), 707 – 721.

[76] Kremer, D., am Ende, M., Mustakis, J. & am Ende, D., 2007 A numerical investigation of a jet in oscillating crossflow. *Physics of Fluids* **19**, 1–14.

[77] Zhang, L., Yang, V. & Sung, H.-G., 2012 Flow dynamics and mixing of a turbulent gaseous jet into oscillating crossflow. In *50th AIAA Aerospace Sciences Meeting including the New Horizons Forum and Aerospace Exposition*. American Institute of Aeronautics and Astronautics, 0970.

[78] O'Connor, J. & Lieuwen, T., 2011 Disturbance field characteristics of a transversely excited burner. *Combustion Science and Technology* **183** (5), 427–443.

[79] Motheau, E., Lederlin, T., Florenciano, J. L. & Bruel, P., 2012 Les investigation of the flow through an effusion-cooled aeronautical combustor model. *Flow, turbulence and combustion* **88** (1-2), 169–189.

[80] Erickson, R. & Soteriou, M., 2011 The influence of reactant temperature on the dynamics of bluff body stabilized premixed flames. *Combustion and Flame* **158** (12), 2441 – 2457.

[81] Eckbreth, A. C., 1996 *Laser Diagnostics for Combustion Temperature and Species*, volume 3. CRC Press.

[82] Welch, P. D., 1967 The use of fast fourier transform for the estimation of power spectra: a method based on time averaging over short, modified periodograms. *IEEE Transactions on audio and electroacoustics* **15** (2), 70–73.

[83] Seybert, A. F. & Ross, D. F., 1977 Experimental determination of acoustic properties using a two-microphone random-excitation technique. *The Journal of the Acoustical Society of America* **61** (5), 1362–1370.

[84] Chung, J. Y. & Blaser, D. A., 1980 Transfer function method of measuring induct acoustic properties. i. theory. *The Journal of the Acoustical Society of America* **68** (3), 914–921.

[85] Bodén, H. & Åbom, M., 1986 Influence of errors on the two-microphone method for measuring acoustic properties in ducts. *The Journal of the Acoustical Society of America* **79** (2), 541–549.

[86] Pope, S. B., 2000 *Turbulent Flows*. Cambridge University Press.

[87] Steinberg, A., Sadanandan, R., Dem, C., Kutne, P. & Meier, W., 2012 Structure and stabilization of hydrogen jet flames in cross-flows. *Proceedings of the Combustion Institute* .

[88] Grout, R., Gruber, A., Yoo, C. & Chen, J., 2011 Direct numerical simulation of flame stabilization downstream of a transverse fuel jet in cross-flow. *Proceedings of the Combustion Institute* **33** (1), 1629–1637.

[89] Cummings, A. & Eversman, W., 1983 High amplitude acoustic transmission through duct terminations: Theory. *Journal of Sound and Vibration* **91** (4), 503–518.

[90] Ingard, U., 1953 On the theory and design of acoustic resonators. *The Journal of the Acoustical Society of America* **25** (6), 1037–1061.

[91] Scarborough, D. E., 2010 *An Experimental and Theoretical Investigation of a Fuel System Tuner for the Suppression of Combustion Driven Oscillations.* Ph.D. thesis, Georgia Institute of Technology.

[92] Getsinger, D., 2012 *Shear Layer Instabilities and Mixing in Variable Density Transverse Jet Flows.* Ph.D. thesis, University of California, Los Angeles.

[93] Sreenivasan, K., Raghu, S. & Kyle, D., 1989 Absolute instability in variable density round jets. *Experiments in Fluids* **7** (5), 309–317.

[94] Yu, M.-H. & Monkewitz, P. A., 1990 The effect of nonuniform density on the absolute instability of two-dimensional inertial jets and wakes. *Physics of Fluids A: Fluid Dynamics (1989-1993)* **2** (7), 1175–1181.

[95] Raynal, L., Harion, J.-L., Favre-Marinet, M. & Binder, G., 1996 The oscillatory instability of plane variable-density jets. *Physics of Fluids (1994-present)* **8** (4), 993–1006.

[96] Hallberg, M. P. & Strykowski, P. J., 2006 On the universality of global modes in low-density axisymmetric jets. *Journal of Fluid Mechanics* **569**, 493–507.

[97] Tacina, K. M. & Dahm, W. J. A., 2000 Effects of heat release on turbulent shear flows. part 1. a general equivalence principle for non-buoyant flows and its application to turbulent jet flames. *Journal of Fluid Mechanics* **415**, 23–44.

[98] Lyra, S., Wilde, B., Kolla, H., Seitzman, J. M., Lieuwen, T. C. & Chen, J. H., 2014 Structure and stabilization of hydrogen-rich transverse jets in a vitiated turbulent flow. *Combustion and Flame* **In Review**, XX–XX.

[99] Nichols, J. W., Chomaz, J.-M. & Schmid, P. J., 2009 Twisted absolute instability in lifted flames. *Physics of Fluids (1994-present)* **21** (1), 015110.

[100] Abernethy, R. B., Benedict, R. P. & Dowdell, R. B., 1985 Asme measurement uncertainty. *Journal of Fluids Engineering* **107** (2), 161–164.